SEISMIC PROTECTION
OF
BUILDING FRAMED STRUCTURES
WITH
BUCKLING RESTRAINED BRACES

Teză destinată obţinerii
titlului ştiinţific de doctor inginer
la
Universitatea Politehnica Timişoara
în domeniul INGINERIE CIVILĂ
de către

Ing. Ciprian-Ionuț Zub

Conducător ştiinţific: acad.prof.univ.dr.ing. Dan Dubină
Referenţi ştiinţifici: conf.univ.dr.ing. Atsusi Sato
prof.univ.dr.ing. Radu Sorin Văcăreanu
prof.univ.dr.ing. Cosmin-Gruia Chiorean

Ziua susţinerii tezei: 26.11.2018

Seriile Teze de doctorat ale UPT sunt:

1. Automatică
2. Chimie
3. Energetică
4. Ingineria Chimică
5. Inginerie Civilă
6. Inginerie Electrică
7. Inginerie Electronică şi Telecomunicaţii
8. Inginerie Industrială
9. Inginerie Mecanică
10. Ştiinţa Calculatoarelor
11. Ştiinţa şi Ingineria Materialelor
12. Ingineria sistemelor
13. Inginerie energetică
14. Calculatoare şi tehnologia informaţiei
15. Ingineria materialelor
16. Inginerie şi Management
17. Arhitectură
18. Inginerie civilă și instalații

Universitatea Politehnica din Timişoara a iniţiat seriile de mai sus în scopul diseminării expertizei, cunoştinţelor şi rezultatelor cercetărilor întreprinse în cadrul şcolii doctorale a universităţii. Seriile conţin, potrivit H.B.Ex.S Nr. 14 / 14.07.2006, tezele de doctorat susţinute în universitate începând cu 1 octombrie 2006.

România, 300159 Timişoara, Bd. Republicii 9,
Tel./fax 0256 403823
e-mail: editura@edipol.upt.ro

Foreword

This thesis was developed during my activity (2014 – 2018) within the Department of Steel Structures and Structural Mechanics (CMMC), and the Centre of Excellence in the Mechanics of Materials and Safety of Structures (CEMSIG), from the "Politehnica" University of Timișoara.

The main topic of this thesis is the pre-qualification of a set of buckling restrained braces (BRBs), which are used for seismic protection of building framed structures. The pre-qualification eliminates the necessity of project-based experimental validation for future projects. Therefore, this thesis aims to clear the way for a rapid adoption of BRBs into the current design practice in Romania by developing pre-qualified technical solutions and by transferring the "know-how" on the design of BRBs to the industry.

This thesis can be used as a reference for developing new BRB technical solutions, which involves both numerical and experimental testing procedures. The numerical models developed in this thesis might be very useful for both beginner and advanced users of the finite element method-based software packages.

Timişoara, november 2018 Ciprian-Ionuț Zub

I would like to thank the distinguished scientific referees – **Assoc.Prof. Atsushi Sato**, from Nagoya Institute of Technology, Nagoya, Japan; **Prof. Radu Sorin Văcăreanu**, from the Technical University of Civil Engineering, Bucharest, Romania; **Prof. Chiorean Cosmin-Gruia**, from the Technical University of Cluj-Napoca, Cluj-Napoca, Romania – for honouring the invitation to review this thesis.

My deepest gratitude goes to the scientific coordinator of this thesis, **Acad.Prof. Dan Dubină**. His scientific vision, guidance and support on this thesis is deeply acknowledged. Also, I would like to thank him for involving me in research projects (IMSER, STEELEARTH, EQUALJOINTS), which gave me the opportunity to meet and work with remarkable personalities in the field.

My sincere thanks go to **Assoc.Prof. Aurel Stratan**, director of the IMSER project, for his great support, assistance and for sharing his knowledge and experience throughout my research activity. Many thanks are given to the advising committee, including **Prof. Aurel Stratan**, **Prof. Florea Dinu** and **Prof. Adrian Ciutina**, for their guidance. Also, I want to express my gratitude to **Assoc. Prof. Adrian Dogariu** for his technical advice in performing numerical simulations.

Special thanks are given to **Assist.Prof. Ionel Mărginean** for his entire support. Also, I am profoundly grateful for the support of the research team and colleagues from CMMC department and CEMSIG research centre.

The most important, I am grateful to my parents, **Aurelia-Maria** and **Ioan**, for their great support and help throughout my PhD stage.

Zub, Ciprian-Ionuț

Seismic protection of building framed structures with Buckling Restrained Braces

(Protecția antiseismică a structurilor în cadre cu contravântuiri cu flambaj împiedecat)

Teze de doctorat ale UPT, Seria 5, Nr. 143, Editura Politehnica, 2018, 207 pagini, 144 figuri, 28 tabele.

ISSN: 1842-581X

ISBN: 978-606-35-0239-2

Cuvinte cheie: steel structure, buckling restrained brace, experimental program, numerical simulations, pre-qualification, cyclic material model

Rezumat,

This thesis mainly addresses to the seismic protection of building framed structures located in earthquake prone areas by using pre-qualified buckling restrained braces. Numerical and experimental procedures were used to develop, test and qualify BRB technical solutions.

The complex numerical models developed for the steel material and the qualified BRBs could be used for the development and pre-qualification through numerical testing of new BRBs solutions.

Design recommendations are given as to transfer the "know-how" on BRBs to the industry.

Table of contents

List of figures

List of tables

Notations, abbreviations, acronyms

Notations

Chapter 2

N_p	axial strength of BRB
K_{eff}	axial stiffness of BRB
μ	ductility ratio
$\varepsilon_{u,BRB}$	ultimate strength of steel
$\varepsilon_{y,BRB}$	yield strength of steel
ε_c	axial core strain
θ_y	yield storey drift
θ	storey drift
F_b	base shear
F_{by}	yield base shear
L_p	length of the core plastic zone
L_n	node-to-node core length
f_y	yield strength of steel
f_u	ultimate strength of steel
ε_r	rupture strain of steel
ε_y	yield strain of steel
g_t	core to BRM gap on through thickness direction
g_w	core to BRM gap on through width direction
β	compression strength adjustment factors
C_{max}	maximum compression force developed by BRB
T_{max}	maximum tensile force developed by BRB

Chapter 3

g	ground acceleration
T_C	control period
$f_{y,n}$	nominal yield strength of steel
$f_{u,n}$	nominal ultimate strength of steel
γ_{ov}	material overstrength factor
ε_u	ultimate strain of steel
F	force
A_p	area of the cross-section of the plastic zone
L_{BRB}	length of the BRB core
L_{BRM}	length of the BRM
E	elastic modulus
E_s	elastic modulus of steel
E_c	elastic modulus of concrete
ν	Poisson’s coefficient
ρ	density of material
f_r	rupture strength of steel

C_k k^{th} plastic hardening modulus
γ_k rate of C_k
$Q_{infinity}$ maximum increase in size of the yield surface
b rate of $Q_{infinity}$
σ^0 initial yield stress at zero plastic strain
Δ_{by} displacement corresponding to the yielding of the core
Δ_{bm} displacement corresponding to the design story drift
N axial force
D axial displacement
$T_{max,T}$ maximum tension force under monotonic loading
$T_{max,Cyc}$ maximum tension force under cyclic loading
N_{cr} critical elastic axial load of the BRM

Chapter 4

L_p length of the core elastic zone
L_t length of the core transition zone
L_c length of the core connection zone
t_p thickness of plastic zone
h_p height of plastic zone
t_e thickness of elastic zone
h_e height of elastic zone
w_{stf} width of the stiffener
t_{stf} thickness of the stiffener
R_t radius of the core transition zone
L_s length of the stopper
h_s height of the stopper
R_s radius of the stopper
L_G length of the longitudinal gap
D_e exterior diameter of the steel tube
t thickness of the steel tube
L length of the steel tube
D_c deformation of the BRB core
D_{bb} displacement of the bottom core end with respect to the BRM
D_{bt} displacement of the top core end with respect to the BRM
D_{jb} displacement of the bottom core end with respect to the bottom gusset
D_{jt} displacement of the top core end with respect to the bottom gusset
L_0 original gauge length
A_0 cross-sectional area of the original gauge length
a_0 original thickness
b_0 original width
d_0 original diameter
L_u final gauge length after fracture
R_{eH} upper yield strength
R_m tensile strength
A percentage elongation after fracture
σ axial stress
ε axial strain
σ_{ts} maximum tensile stress value reached during the saturation cycle
σ_{tk} maximum stress value during the k^{th} cycle
$f_{c,cube}^{w}$ averaged compression strength of the specimens cured in water

$f^{a}_{c,cube}$ averaged compression strength of the specimens cured at normal conditions
ω strain hardening adjustment factor
R_t maximum deformation ratios in the top part of the core
R_b maximum deformation ratios in the bottom part of the core
D_t total BRB deformations

Chapter 5

$\sigma^0{}_1$ initial yield stress
$\sigma^0{}_s$ saturation yield stress
$\sigma^0{}_r$ rupture stress
ε_{sh} strain at the end of yield plateau
ε^{pl} plastic strain
ε^{-pl} cumulative plastic strain
$\sigma_{1,2,3}$ principal stresses
$\boldsymbol{\sigma}$ "true" (Cauchy) stress tensor
$\mathbf{D}^{\mathbf{el}}$ fourth-order elasticity tensor
$\boldsymbol{\varepsilon}^{\mathrm{el}}$ logarithmic strain tensor
F yield surface
σ^0 yield stress
$\boldsymbol{\alpha}$ backstress tensor
$\mathbf{S}$ deviatoric stress tensor
$\boldsymbol{\alpha}^{\mathbf{dev}}$ deviatoric part of the backstress tensor
$\dot{\varepsilon}^{-pl}$ equivalent plastic strain rate
σ_{nom} engineering or nominal stress
ε_{nom} engineering or nominal strain
R amount of isotropic hardening recorded until the saturated cycle
$\Delta\varepsilon$ strain range
$\sigma^c{}_j$ compressive yield stress
Ψ dilation angle
ϵ eccentricity
σ_{b0} initial equibiaxial compressive yield stress
σ_{c0} initial uniaxial compressive yield stress
K_c ratio of the second stress invariant on the tensile meridian to that on the compressive meridian
μ viscosity parameter
f_{cm} mean value of the compressive cylinder strength of concrete
f_{ck} characteristic compressive cylinder strength of concrete
f_{ctm} tensile strength of concrete
E_{cm} secant modulus of elasticity of concrete
k plasticity number
ε_c compressive strain in concrete

Chapter 6

$\varepsilon_{c,max}$ maximum core strain
$N_{p,req}$ required strength of BRB
α insertion angle of BRB
$d_r{}^{SLU}$ relative inter-storey displacements
L length of frame
H height of frame

δ_{Ed} axial deformation of the core
$f_{y,m}$ mean value of the experimentally determined yield strength of the steel
$\bar{\lambda}$ relative slenderness
$L_{g,cr}$ maximum length of the unconstrained plastic segment
A cross-sectional area of the zore
δ_{Rd} axial deformation that can be developed by the core
D_i Interior diameter of the steel tube
K_{eff} effective axial stiffness of the BRB

Chapter 7

T_B corner period
T_C corner period
T_D corner period
a_g peak ground acceleration
F_y BRB yield force
b slope of hardening
K stiffness
$\varepsilon_{p,max}$ maximum axial strain in the plastic zone
$\varepsilon_{p,d}$ design value of axial strain in the plastic zone

Abbreviations & Acronyms

ABRI	Architecture Buildings Research Institute
AISC	American Institute of Steel Construction
ANSI	American National Standards Institute
ASCE	American Society of Civil Engineers
ASTM	American Society for Testing and Materials
BRAD	Buckling-Restrained Axial Dampers
BRB	Buckling Restrained Brace
BRBF	Buckling Restrained Braced Frame
BRM	Buckling Restraining Mechanism
BSLJ	Building Standard Law of Japa
C3D6	6-node linear triangular prism
C3D8	8-node first order elements with full integration
C3D8I	8-node linear brick finite elements with incompatible modes
CBF	Concentrically Braced Frame
CEMSIG	Research Center for Mechanics of Materials and Structural Safety
CID	cumulative inelastic deformation
CMMC	Department of Steel Structures and Structural Mechanics
CSA	Canadian Standards Association
EQUALJOINTS	European pre-qualified steel joints
FEM	Finite Element Method
IMSER	Implementation into Romanian seismic resistant design practice of buckling restrained braces
ISO	isotropic hardening
KIN	kinematic hardening
MEN-UEFISCDI	Executive Agency for Higher Education, Research, Development and Innovative Funding
NBCC	National Building Code of Canada
NCREE	National Center for Research on Earthquake Engineering
NSEUSA	Nippon Steel & Sumikin Engineering USA
PEEQ	equivalent plastic strain
PWLAM	Waterproofing liquid applied membrane
RFCS	European Community's Research Fund for Coal and Steel
SHS	Square Hollow Section
SLS	Serviceability Limit State
SMRF	Special Moment Resisting Frame
UBB™	Unbonded Brace
ULS	Ultimate Limit State

REZUMAT

Proiectarea anti-seismică a clădirilor amplasate în zone seismice are o importanță critică în prevenirea de pierderi de vieți omenești si distrugeri de bunuri materiale. În ultimele decade au fost propuse câteva sisteme structurale anti-seismice pentru a reduce și a controla avarierea clădirilor în timpul unui cutremur. Acest tip de sisteme utilizează elemente disipative ("siguranțe" structurale) pentru protecția clădirii. Un exemplu de "siguranță" structurală o reprezintă contravântuirea cu flambaj împiedicat (BRB). În comparație cu contravântuirea convențională, BRB-urile au dovedit a avea caracteristici îmbunătățite: lipsa flambajului la compresiune, răspunsul ciclic stabil și cvasi-simetric, capacitatea de a disipa o cantitate mare de energie.

BRB-urile au un potențial ridicat în aplicații anti-seismice datorită performanței histeretice. Totuși, în România încă nu există aplicații ale BRB-urilor în proiecte reale, deși recomandări de proiectare pentru cadrele cu contravântuiri cu flambaj împiedicat (BRBF) au fost introduse în codul românesc de proiectare seismică începând cu data de 1 ianuarie 2014. Limitarea largii utilizări a BRB-urilor poate fi cauzată de faptul că BRB-urile comercializate sunt brevetate de producători, de nevoia de validare experimentală a BRB-ului, sau de lipsa experienței de proiectare a inginerilor practicieni a BRB-urilor sau a cadrelor BRBF.

De aceea, principalul obiectiv al tezei îl constituie *precalificarea experimentală* a unui set de contravântuiri BRB utilizate pentru clădiri tipice de înălțime mică și medie amplasate în România. Precalificare va elimina necesitatea validării experimentale pentru fiecare proiect. Programul experimental a fost conceput pentru a facilita implementarea rapidă a BRB-urilor în practica de proiectare din România prin dezvoltarea de soluții tehnice precalificate și prin transferul de "know-how" despre proiectarea BRB-urilor către industrie.

Precalificarea BRB-urilor prin *experimentare numerică*, utilizând procedura propusă în teză, a necesitat dezvoltarea unui model numeric avansat, în măsura să simuleze comportarea miezului de oțel activ din contravântuire in domeniul post-elastic în regim ciclic. Sunt foarte puține informații în literatura de specialitate cu privire la această problemă, iar cele care sunt disponibile sunt prezentate succint, cu rezultate, în general, nerelevante. Construirea si validarea acestui model este una din realizările importante ale tezei.

Această teză este structurată pe opt capitole și prezintă programul de precalificare a BRB-urilor, program ce include atât încercări experimentale cât și simulări numerice pre/post-încercări, și un studiu de caz al aplicării BRB-urilor pe o structură în cadre metalice. În continuare se prezintă o descriere succintă pe capitole a tezei.

Capitolul 1: Introducere

În primul capitol se prezintă motivația, obiectivele și cadrul în care s-a realizat teza. Motivația acestei teze constă în necesitatea de a soluționa problemele legate de utilizarea BRB-urilor în România. Obiectivul principal constă în precalificarea unui set de contravântuiri BRB în vederea facilitării implementării rapide a acestora în practica curentă de proiectare. Cadrul principal in care s-a dezvoltat teza îl constituie un proiectul național de cercetare, intitulat "Implementarea în practica de proiectare anti-seismică din România a contravântuirilor cu flambaj împiedicat", acronim IMSER.

Capitolul 2: BRB – stadiul cunoașterii în domeniu

Capitolul doi prezintă stadiul cunoașterii în domeniu al BRB-urilor, accentul fiind pus pe principul de funcționare, istoria dezvoltării, aplicabilitate, avantaje și dezavantaje. Performanța diverselor sisteme de contravântuiri (BRBF vs. CBF) sunt comparate din punctul de vedere al reducerii costului. Evaluarea critică a soluțiilor tehnice de BRB existente permite identificarea detaliilor tehnice optime a fi utilizate în vederea dezvoltării de noi soluții BRB. De asemenea sunt prezentate coduri existente de proiectare a BRB-urilor, dar și nevoile de cercetare și dezvoltare ulterioară.

Capitolul 3: Dezvoltarea soluțiilor tehnice

Capitolul trei prezintă dezvoltarea soluțiilor de contravântuiri BRB, atât "convenționale" cât și "uscate". Pentru precalificare au fost propuse două valori ale rezistenței BRB-urilor, 300 kN și 700 kN. Au fost utilizate atât pre-testări numerice cât și pre-testări experimentale în vederea definirii soluțiilor conceptuale BRB. Patru tipologii BRB au fost propuse, două "convenționale" și două "uscate". Au fost propuse îmbinări cu șuruburi pentru BRB-uri, utilizându-se un detaliu de îmbinare special ce permite îmbunătățirea performanței ciclice a BRB-urilor.

Capitolul 4: Încercări experimentale pentru precalificarea BRB-urilor

Programul experimental ce include încercări de precalificare pe BRB-uri și încercări de material pe componente de bază sunt prezentate în capitolul patru. 14 contravântuiri BRB la scala reală au fost încercate ciclic. Detalierea specimenelor a avut în vedere investigarea influenței unor parametrii asupra performanței ciclice a BRB-urilor. Pe baza criteriilor de performanță, soluțiile BRB precalificate au fost selectate, iar pentru acestea au fost propuse recomandări de proiectare.

Capitolul 5: Simulări numerice post-test

Capitolul cinci prezintă rezultatele a două seturi de simulări care au fost efectuate în vederea evaluării: (1) acurateței diverselor modele de material în reproducerea comportării oțelului sub încărcări monotone și ciclice: (2) influenței unor parametrii (care nu au putut fi evaluați/măsurați în timpul încercărilor experimentale) asupra răspunsului ciclic al BRB-urilor.

Capitolul 6: Recomandări de proiectare

Pe baza rezultatelor experimentale și numerice obținute pe BRB-uri, recomandările de proiectare se prezintă numai pentru soluția precalificată. De asemenea, se precizează și limitele de aplicare a procedurii de proiectare îi vederea asigurării unui grad ridicat de încredere pentru proiectarea unor noi contravântuiri BRB.

Capitolul 7: Proiectare bazată pe criterii de performanță a cadrelor BRBF

Capitolul șapte prezintă un studiu de optimizare a geometriei miezului BRB-ului. Pentru studiul de caz s-a considerat o structură metalică in cadre contravântuită cu BRB-uri având diferite geometrii pentru miez. Este evaluată influența nivelului de deformație specifică din miez asupra performanței seismice a structurii și sunt elaborate recomandări de proiectare suplimentare pentru BRB-uri. De asemenea, este evaluată influența tipului de reazem ale bazei stâlpilor asupra răspunsului seismic al structurii și sunt elaborate soluții de îmbunătățire a răspunsului.

Capitolul 8: Concluzii

O sinteză a concluziilor din teză, precum și contribuțiile autorului și valorificarea cercetării sunt prezentate în capitolul opt. Direcții viitoare de cercetare sunt stabilite în vederea continuării studiilor dezvoltate in teza de doctorat.

SUMMARY

The seismic protection of building structures located in earthquake-prone areas is of a critical importance in preventing human losses and material damages in case of an earthquake. During the last decades, several earthquake-resistant structural systems were proposed to reduce and control the damage of buildings during a seismic event. Such systems use dissipative elements (structural "fuses") to protect the structure. An example of such fuse is the buckling restrained brace (BRB). In comparison to the conventional braces, the BRBs proved to have enhanced features: no buckling in compression, stable and quasi-symmetric cyclic response, capacity to dissipate a large amount of energy.

BRBs have a great potential for seismic applications due to their hysteretic performance. However, in Romania there are no project applications yet, even though design provisions for buckling restrained braced frames (BRBFs) were introduced in the national seismic design code starting with January 1st, 2014. It might be the proprietary character of the commercialized BRB solutions or the experimental qualification required by the design code that limits their wide adoption. The lack of experience of structural engineers in designing BRBs/BRBFs is also considered to limit the large applicability of BRBs.

Therefore, the main objective of this thesis is to pre-qualify a set of BRBs for typical low-rise and mid-rise steel framed buildings located in Romania. The pre-qualification will eliminate the necessity of project-based experimental validation for future projects. The research program was intended to clear the way for a rapid adoption of the BRBs into the design practice by developing pre-qualified technical solutions and by transferring the "know-how" on the design of BRBs to the industry.

The pre-qualification of BRBs through numerical testing, using the procedure proposed in this thesis, required the development of a complex numerical model, able to simulate the behaviour of the active steel core of the BRB in the post-elastic domain under cyclic loading regime. There is few information in the technical literature regarding this subject, and the available ones are briefly presented, with results, in general, not relevant. Therefore, the development and validation of this numerical model represents an important achievement of this thesis.

This thesis is structured on eight chapters and presents the pre-qualification program of BRBs, which included both experimental tests and pre/post-tests numerical simulations, and a study case application of BRBs on a steel framed building. Detailed description per chapter are presented below.

Chapter 1: Introduction

The first chapter presents the motivation, the objectives and the research framework of the thesis. The need to overcome the problems related to the application of BRBs motivates this thesis. The main objective is to pre-qualify set of BRBs as to clear the way for a rapid adoption of the BRBs into the design practice. The main research framework of the thesis is a National research project, entitled: "Implementation into Romanian seismic resistant design practice of buckling restrained braces", acronym IMSER.

Chapter 2: BRB – state of knowledge

The second chapter presents the state of knowledge on BRBs with the emphasis on the principle of work, history of development, applicability, advantages and disadvantages. The performance of different bracing systems are compared (BRBF vs. CBF) from the point of view of cost savings. Critical evaluation of existing BRB technical solutions will reveal the optimal technical details to be used for the development of the new BRB solutions. Existing design regulations are also presented and needs for further research and development are set.

Chapter 3: Development of technical solutions

Chapter three presents the development of both "conventional" and "dry" BRBs solutions. Two values of resistance, 300 kN and 700 kN, are proposed for pre-qualification. Both numerical and experimental pre-tests are used as to obtain the conceptual BRB solutions. Four typologies are proposed, two "conventional" and two "dry". Bolted connections are proposed for the BRBs and special detail is used to enhance their cyclic performance.

Chapter 4: Experimental tests for pre-qualification of BRBs

The experimental program including the pre-qualification tests on BRBs and the tests on component materials are presented in chapter four. 14 full-scale BRBs are cyclically tested, and different detailing was used for the specimens as to investigate the influence of a series of parameters on the cyclic performance of the BRBs. Based on the performance criteria, the pre-qualified BRB solutions are selected, and design recommendations are given.

Chapter 5: Post-test numerical simulations

Chapter five presents the results of two sets of simulations that were performed as to assess: (1) the accuracy of different material models in reproducing the behaviour of the steel material under monotonic and cyclic loading; (2) the influence of several parameters (that could not be observed/measured during experimental tests) on the cyclic response of BRBs.

Chapter 6: Design recommendations

Based on the experimental and numerical results obtained on BRBs, design recommendations are given for the pre-qualified solution. Applicability limits of the design procedure are also given to provide the new BRBs with a high level of reliability.

Chapter 7: Performance-based design of BRBF

Chapter seven presents an optimization study of the core geometry. A study case steel framed building equipped with BRBs of different geometries is considered for this investigation. The influence of the strain level in the core on the seismic performance of the building is assessed and additional design recommendations for BRBs are given. The influence of different column-base supports on the seismic response of the building is assessed and solutions are proposed to improve the response.

Chapter 8: Conclusions

A synthesis of the conclusions of the thesis, as well as the contributions of the author and valorisation of research are presented in chapter eight. Further research directions are set as to provide a continuity of the studies developed within the thesis.

1 INTRODUCTION

1.1 Motivation

The seismic design of building structures located in earthquake-prone countries (e.g. Japan, Romania) is of a critical importance. During the last decades, several earthquake-resistant structural systems were developed, aiming at reducing and controlling the damage of a structure during a severe seismic event. Such systems make use of structural fuse elements to dissipate the seismic energy, thus protecting the structure. Frames equipped with buckling restrained braces (BRB) are an example of earthquake-resistant structural system.

Since the first project application of buckling restrained braced frames (BRBF) in Japan in 1989 [1], BRBs have been extensively studied, used and implemented into design codes in countries like Japan, USA, Taiwan, Canada, among others. In Europe, the seismic design code EN 1998-1 [3] does not have regulations regarding the use of BRBF system yet (2018). Instead, the European norm EN 15129 [4] have requirements regarding testing and manufacturing of BRBs.

Starting with January 2014, Romania is only country in Europe that regulated the use of BRBs through the national seismic design code P100-1/2013 [5]. For project applications, the code [5] requires experimental qualification of BRBs either project-specific or based on existing experimental evidence.

Even though the buckling restrained braces proved to be anti-seismic devices suitable for seismic protection of structures (buildings, bridges, TV towers, etc.), a wide adoption of BRBs is precluded by their proprietary character (most BRBs are patented), by the design codes that require experimental qualification, and by the lack of design experience in countries were BRBs are not so popular (as the case of Romania).

The need to overcome these problems motivates this thesis. Therefore, the aim of this thesis is to provide a reliable BRB solution, which is then pre-qualified by (mainly) experimental and (complementary) numerical testing in order to be used for typical low-rise and mid-rise buildings located in Romania. The pre-qualification of a set of BRBs will facilitate the use of such devices, by sharing the "know-how" (design recommendations) with the structural engineers and the BRB manufacturers.

As computer science and numerical methods developed considerably during the last years, the use of an advanced numerical model for BRB represents a powerful and useful tool in view of numerically testing since is faster and considerably cheaper. Calibrated based on experimental results at component and element level, the numerical results obtained with the BRB model have a high level of reliability. Therefore, numerical testing could substitute experimental testing to some extent.

So far, different modelling techniques involving the Finite Element Method (FEM) were developed by researchers depending on the software used. To the author's knowledge, there are few comprehensive studies with both experimental and numerical tests at both component (materials) and BRB level to assure numerical results with a high level of reliability. Therefore, the thesis also aims to solve the problems of numerical FEM modelling of BRB at component (materials), element (BRB) and structure (BRBF) level. This powerful numerical tool can be used to extend

the existing BRB database, to pre-test new BRB prototypes, and to perform optimization of the BRB solutions by performing nonlinear time history analyses on structures equipped with BRBs.

1.2 Objectives

The thesis has two main objectives and several derived secondary objectives, as presented below:

- To pre-qualify a set of BRBs using experimental testing procedures:
  - To develop prototypes for two BRB typologies: "conventional" (steel core and mixed steel-concrete buckling restraining mechanism) and "dry" (steel core and steel buckling restraining mechanism).
  - To assess the performance of BRBs based on several criteria: cyclic response, adjustability, technology, economic.
  - To propose qualified BRB solutions and design recommendations for structural engineers and BRB manufacturers.
- To extend the database of pre-qualified BRBs using numerical testing procedures:
  - To develop a calibration procedure of the input parameters for steel material model under monotonic and cyclic loading conditions using either monotonic or cyclic experimental tests results.
  - To develop and calibrate three-dimensional numerical finite element models for the tested BRBs based on experimental data.
  - To investigate in detail the tested BRBs.
  - To validate the design methodology of BRB components.
  - To perform parametric studies aiming at extending the BRB database.
  - To develop a two-dimensional numerical model for a reference buckling restrained braced frame.
  - To provide additional design rules for BRB/BRBF by performing optimization studies using nonlinear time history analyses on BRBFs.

1.3 Research framework

The research program of this thesis was mainly developed within the frame of a National research project, entitled: "Implementation into Romanian seismic resistant design practice of buckling restrained braces", acronym IMSER, contract no. 99/2014 [6], funded from MEN-UEFISCDI grant Partnerships in priority areas PN II (code project: PN-II-PT-PCCA-2013-4-2091). The project involved three partners with experience in the construction industry: Politehnica University of Timisoara - as research organisation; SC Popp & Asociatii SRL – as designer; SC Hydromatic Sistem SRL – as BRB manufacturer.

The research program of IMSER project consisted in:

- Identification of two capacities of BRBs, representative for low-rise and mid-rise steel framed buildings in Romania.
- Conceptual development of two types of BRBs, "conventional" and "dry".
- Numerical pretesting of the final BRB concepts (FEM, Abaqus).
- Experimental testing of base materials (steel and concrete).
- Experimental testing of 14 BRBs.
- Evaluation of experimental data.
- Numerical post-testing of BRB models: calibration of models and parametric studies.

- Qualification of BRBs based on their performance: cyclic response, adjustability, technology, economic.
- Elaboration of design guidelines (book) for both BRB elements and steel frames equipped with BRBs.
- Dissemination of research results to practising engineers through public presentations.

Knowledge and experience were achieved by the author on performing experimental uniaxial cyclic and monotonic tests on steel coupons within the frame of an international research project, entitled: "European pre-qualified steel joints", acronym EQUALJOINTS, grant agreement no RFSR-CT-2013-00021 [7], which received funding from received funding from the European Community's Research Fund for Coal and Steel (RFCS). Using the experimental cyclic results, a procedure for the calibration of input parameters for ductile metal plasticity to be used in FEM simulation was derived [8]. The knowledge achieved by the author on experimental testing and numerical modelling of mild carbon steel material was further used in IMSER project to design the material testing program, which was the basis on further developments on modelling the cyclic and monotonic response of steel material within Abaqus FEM software.

2 BRB – STATE OF KNOWLEDGE

2.1 Concept, principle of work and main features

Buckling restrained brace (BRB) is a state-of-the-art structural element [9] invented and developed for construction field as an enhanced version of conventional steel brace. BRB was invented to solve the problem of global buckling of conventional brace during compression loading.

The simplest *conceptual BRB design* (Fig. 2.1) consists of a steel plate (hereinafter called core), wrapped with an unbonding material, and introduced into a concrete-filled steel tube (hereinafter called buckling restraining mechanism, BRM).

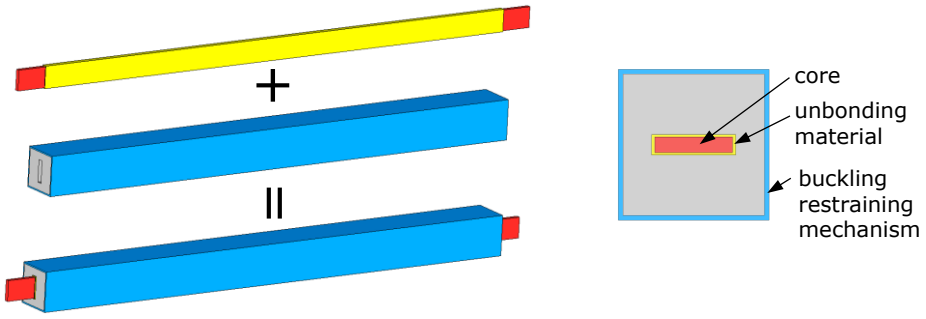

a) b)

Fig. 2.1. The simplest conceptual BRB design: a) perspective view, b) cross-section

The *principle of work* of a BRB in comparison to the principle of a conventional brace is schematically presented in Fig. 2.2. As the conventional brace buckles under compression forces due to its slenderness (Fig. 2.2.a), resulting in a compression strength reduction with respect to the tensile strength. In the case of the BRB, the transversal displacements of the core are restrained by the BRM, thus, no global buckling occurs. Instead local buckling phenomenon occurs as the core achieve higher buckling modes under compression forces. Decoupling the axial load transfer from the core to the BRM by providing un unbonding interface allows the BRB to develop a symmetric and stable hysteretic cyclic response under compression and tension forces beyond elastic limit. The area inside the hysteretic loops represents the energy dissipated through plastic deformations of the base material – steel (the concept of steel yielding). As schematized in Fig. 2.2.b, BRBs can dissipate a large amount of seismic energy (induced into a building during an earthquake) through plastic deformation of the core member in comparison to the conventional brace [10]. Therefore, BRBs are considered hysteretic dissipative elements.

Real BRB applications (or tests) require the brace to be connected to the framed structure by using either bolted, pinned or welded connections. Therefore, the core can no longer be a plate of a constant cross-section, since concentrations of plastic deformations might take place in the net area or welded gussets causing brittle failure. To avoid this failure mode, a typical BRB has a variable cross-section core that can be divided in several distinct zones: plastic zone, transition zone, elastic zone,

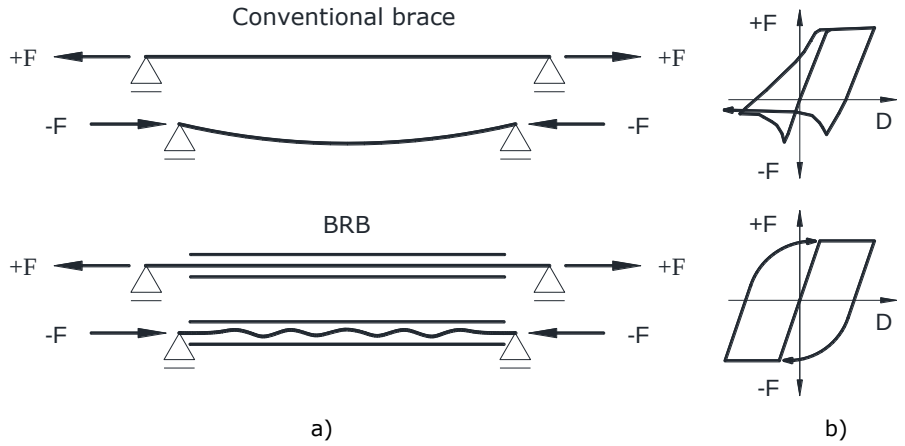

Fig. 2.2. Principle of work of BRB vs. conventional brace: a) deformation, b) axial response

connection zone (Fig. 2.3). All the plastic deformations are intended to take place in the (reduced) plastic zone, while all the other (enlarged) zones remain in the elastic domain. A stopper is usually provided in the midspan of the plastic segment for two reasons: to prevent sliding of the BRM relative to the core, and to uniformize the distribution of plastic deformations in the core plastic zone. Enlarged cross-sections are provided for the elastic and connection zones, while a variable cross-section is provided for the transition zone. A smooth transition will minimize stress concentrations and reduce the risk of a brittle failure mode of the core. The elastic zones must assure stability of the unrestrained part of the core (outside the BRM), allowing it to slide relative to the BRM but with limited rotations, so that BRB behaves mainly axially. Depending on the connection detail used to insert the BRB in the structure, the connection zone will adapt its configuration such that to assure a simple and straight flow of the external forces between the BRB (core) and the connecting gussets. Throughout the years, some other core configurations were also proposed, as it will be later discussed.

The unbonding interface wrapping the core is of a crucial importance for the cyclic performance of a BRB. It can be either a material layer or a small gap, depending on the BRB typology. Besides its main role of decoupling the axial load transfer, the unbonding interface allows the core to transversally deform under compression forces (Poisson's phenomenon). If using a material layer, its toughness (deformability) must allow the core to develop buckling waves while compression loading.

The global stability of the BRB is mainly assured by the buckling restraining mechanism, BRM. Depending on its conceptual configuration, the BRM can be "conventional" (the BRM is a concrete-filled steel tube) or "dry" (the BRM does not include concrete, e.g. a steel assembly) [11]. The "dry" BRM was developed as an

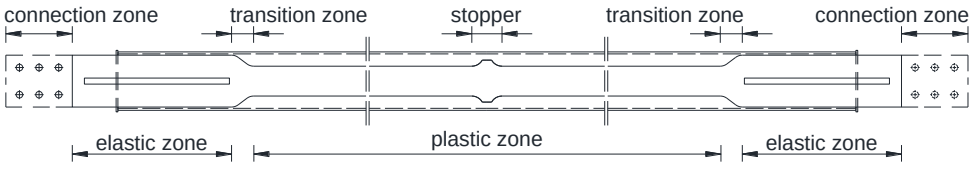

Fig. 2.3. Specific zones of the core of a typical BRB

alternative to the " conventional" solution in order to reduce the weight of BRB [12], to reduce the technological time (and cost) for pouring and curing the concrete [10], to allow for visual inspection after an earthquake [13], and to allow for the possibility of "in-situ" demounting and replacing the core damaged after an earthquake [14].

BRBs with variable cross-section core have longitudinal gaps provided in the extension of the transition zone to allow for free movement under compression cycles. In the case of "conventional" BRBs polystyrene foam is used, while for "dry" BRBs a gap. A perspective view of a model representing a tested "conventional" BRB solution is presented in Fig. 2.4.a and its axial cyclic response in Fig. 2.4.b [11].

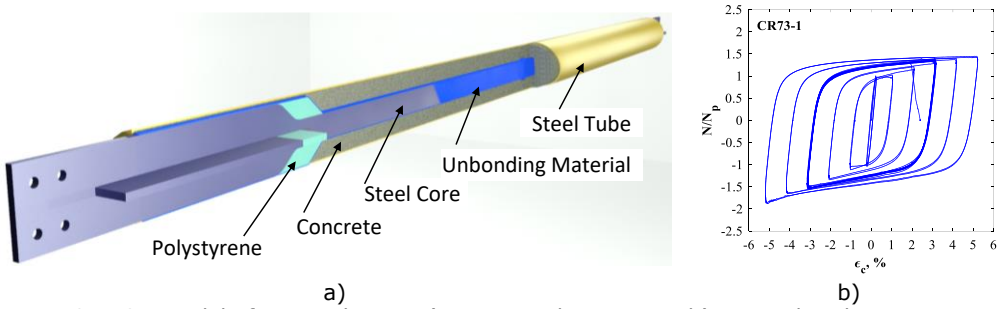

Fig. 2.4. 3D model of a tested BRB: a) conceptual geometry, b) uniaxial cyclic response

BRBs have several *main features* that distinguish them from other structural elements, as presented below:

- BRB allows for fine adjustments of its axial strength (N_p), axial stiffness (K_{eff}), and ductility ($\mu = \varepsilon_{u,BRB}/\varepsilon_{y,BRB}$; $\varepsilon_{u,BRB}$ – BRB ultimate axial strain, $\varepsilon_{y,BRB}$ – BRB yield axial strain) by choosing different steel grade and determining the appropriate geometry of core. Furthermore, from Fig. 2.4.b it can be observed that the axial cyclic response is stable even at large axial core strains, $\varepsilon_c = \pm 5\%$. These features make the BRB a suitable and feasible solution for seismic protection of building structures located in earthquake prone areas (i.e. Romania). This is why the Romanian National Seismic Design Code, P100-1/2013 (2014) [5], defines the buckling restrained braces (BRB) as dissipative elements designed to develop large plastic deformations during the design seismic action.
- The European norm that regulates the general design rules, material characteristics, manufacturing and testing requirements of anti-seismic devices, EN 15129 (2010) [4], defines the BRBs as hysteretic displacement dependent devices. The energy dissipation is activated by the sway of the building during a seismic event. The BRB might have a linear elastic response, thus no dissipation, for inter-storey drifts corresponding to Serviceability Limit State, (SLS), while for inter-storey drifts corresponding to Ultimate Limit State (ULS) the BRB will have a nonlinear plastic response, thus dissipating the kinetic energy induced int the building structure by earthquake. It needs to be noticed that the efficiency of the BRB device is dependent on the lateral displacement capacity of the structure.
- BRBs are treated as passive dissipative systems by the Building Standard Law of Japan, BSLJ-2000 [15]. No additional external energy is required for a BRB to start dissipating seismic energy, the sway of the building "activates" the BRB.

2.2 History of development

The initial development of buckling restrained braces was based on the idea of restraining the global buckling of steel elements. This concept was first studied in Japan in 1971 by Yoshino et al. [2], who tried to restrain the global buckling of steel braces. In India, in 1982 Sridhara and Ramaswamy [16] tried to restrain the global buckling of steel columns, "sleeved compression member". While in Japan the concept was further used to create hysteretic dampers (BRBs) for seismic protection [1], in India the concept was used to obtain compression members of minimum weight [17].

In Japan, the BRBs were developed under two conceptual forms [18]:

- steel core restrained by reinforced concrete (RC) panels;
- steel core restrained by a tube.

As described in [2], the *first experimental tests* on BRBs with RC panels used as buckling restraining mechanism were performed by Yoshino et al. in 1971. Two specimens ("shear wall with braces") were used to perform a comparative study under cyclic loading conditions. The specimens consisted of flat steel plates disposed in X configuration and encased in RC panels (Fig. 2.5.a). For the first specimen a debonding material ("internal clearance" [19]) was provided around the steel plates, while for the second no clearance was provided. As it can be observed in Fig. 2.5.b, the unbonding interface was critical in achieving larger capacities of deformation (ductility) and energy dissipation, in comparison to the specimen that was not provided with unbonding interface (Fig. 2.5.c). This type of BRBs was also studied by Wakabayashi et al. who performed in 1973 *pioneering tests* on BRBs having the steel core provided with unbonding material and restrained by precast reinforced concrete panels. They performed 11 pull-out tests, 21 compression tests, 14 subassemblage tests and 2 system tests (2 storey 2 bay frame) [18]. Stable hysteretic loops were obtained up to 2.5 % storey drift (Fig. 2.6) [1]. This concept of BRB having steel plates encased in reinforced concrete panels was further studied and developed by other researchers: Takahashi et al. 1979, 1980, 1982; Inoue et al. 1992, 1993, 2001. An analytical formulation for this type of BRB was proposed by Inoue et al. in 1992 [19].

According to [1], attempts to improve the compression behaviour of steel braces of H-shaped cross-section by encasing the brace in reinforced concrete were performed by Takeda et al. in 1972. Even though an improvement in performance was obtained, since no unbonding material was provided to reduce the axial force transmitted to the BRM, the buckling restraining mechanism cracked and globally buckled. Kimura et al. are considered the first researchers who tested in 1976 BRBs

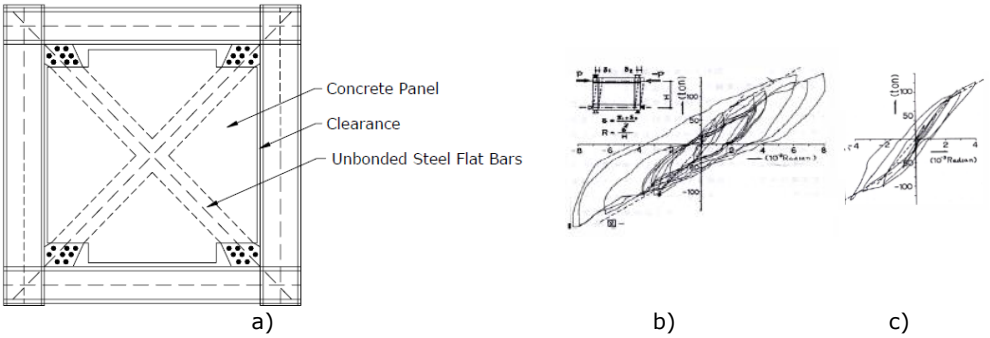

a) b) c)

Fig. 2.5. First tests on BRBs by Yoshino et al.: a) specimen, cyclic response b) with and c) without unbonding interface [19]

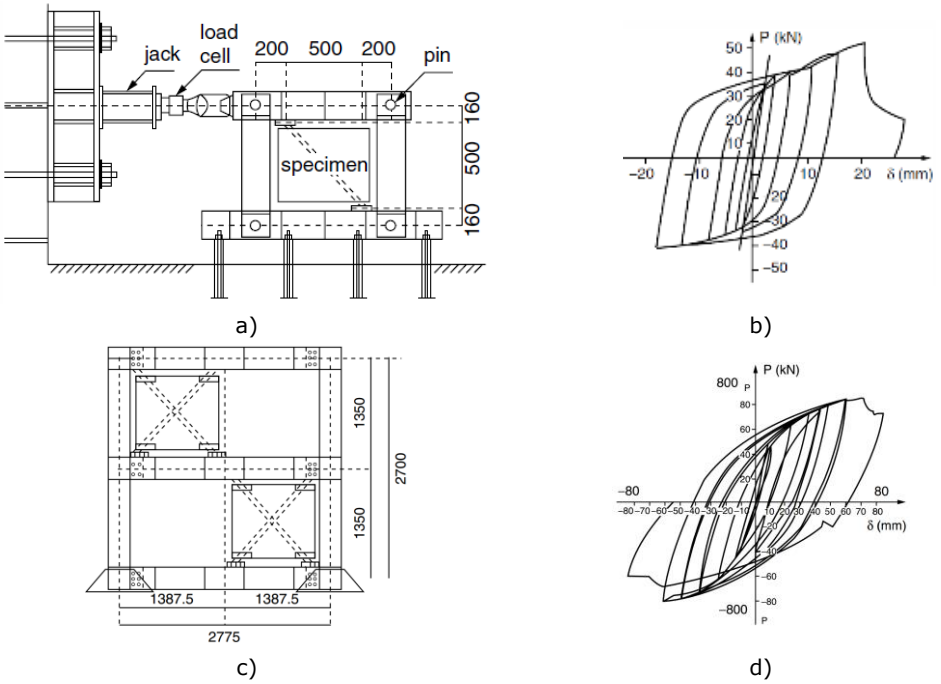

Fig. 2.6. Pioneering tests on BRBs by Wakabayashi et al.: a) subassemblage test setup and b) hysteretic response; c) system test setup and d) hysteretic response [18]

consisting of a steel core restrained by a mortar-filled square steel tube. Since no unbonding material was provided, limited cyclic performance was recorded as the mortar undergone permanent transversal deformations under compression loading due to Poisson's effect. Thus, the core experienced local buckling. In 1979, Mochizuki et al. presented the experimental results on BRBs consisting of an "unbonded" steel core (plate) restrained by a reinforced concrete tube. Using as unbonding interface a "shock-absorbing material", the axial force transfer was successfully decoupled. Limited cyclic performance was obtained due to core buckling in the unrestrained zones (outside the tube), causing cracks and damage to the buckling restraining mechanism. It was professor Wada and his collaborators from Nippon Steel Corporation (Saeki et al.) who combined the previous conceptual BRB designs to obtain "*the first practical buckling-restrained brace*" (called "Unbonded Brace, UBB™") [1], see Fig. 2.7. The refined BRB concept consisted of a variable cross-section steel core wrapped with unbonding material and restrained by a mortar-filled rectangular steel tube (Fig. 2.7.a). In 1987, they performed subassemblage full scale tests (Fig. 2.7.b) on five BRB specimens with similar core cross-section, but with steel tubes of different sizes to evaluate the design methodology proposed for the buckling restraining mechanism [20]. Even though two specimens experienced global buckling, the remaining specimens had a stable and quasi-symmetric hysteretic response, see Fig. 2.7.c, thus validating the BRB concept and the design methodology used.

Following the breakthrough by professor Wada and his team, many researchers continued to study the buckling restrained braces and new conceptual design were proposed and experimentally tested. Even though some researchers continued to study BRBs consisting of steel core restrained by concrete panels (Inoue et al. 1992, 1993, 2001 [19]), most researchers focused on developing new concepts

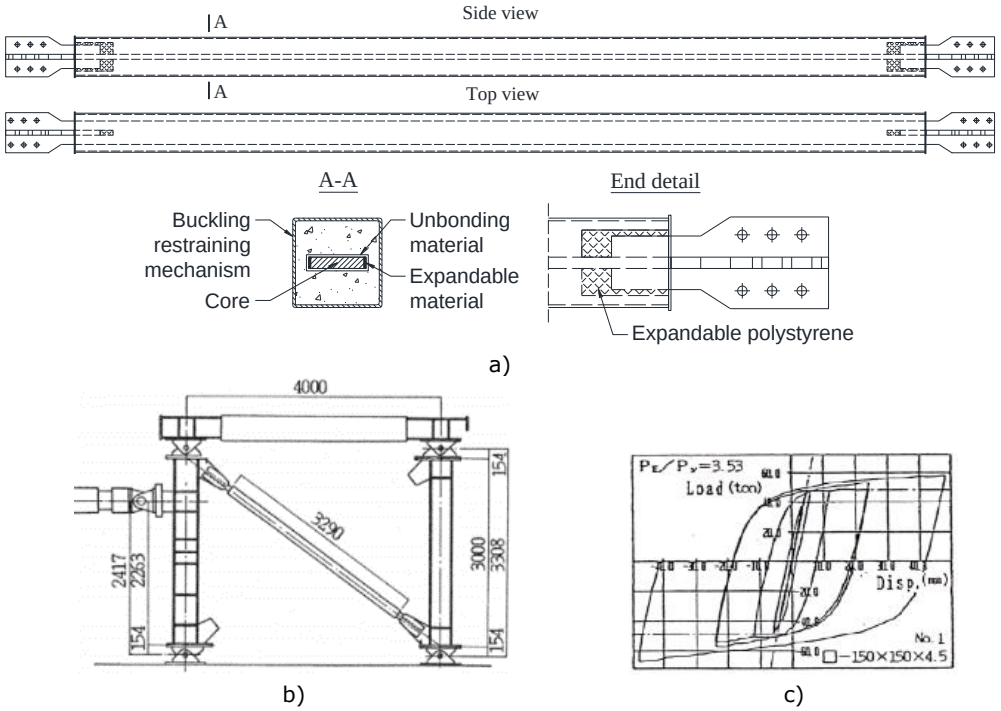

Fig. 2.7. First tests on Unbonded Braces by Wada et al.: a) typical specimen details, b) subassemblage test setup, c) successful hysteretic response (adapted from [20])

for BRBs consisting of an unbonded steel core restrained by a tube. Different cross-sections (flat, round, cruciform, H, O) and steel materials (low-yield, normal, high-strength steel) were proposed for the core. A major interest was also given to the design of the buckling restraining mechanism, BRM. Therefore, steel bar reinforced concrete BRMs (Nagao et al. 1988, 1992, 1990; Horie et al. 1993), see Fig. 2.8.a, or steel fiber-reinforced concrete BRMs (Horie et al. 1993) consisted an alternative to mortar-filled steel tubes [19], see Fig. 2.8.b. To eliminate the technological time for pouring and curing the concrete, all-steel BRMs were proposed and tested by several researchers: (first tests by) Tada et al. in 1993 [19] (Fig. 2.9), Suzuki et al. in 1994 [2], Kamya et al. in 1995 [2], Shimizu et al. in 1997 [2], Lin and Tsai in 2003 [21] (Fig. 2.10), among the others. Successful results were also obtained using a glulam casing to restrain the global buckling of the steel core, as reported by Blomgren et al. in [22], see Fig. 2.11.

To overcome the problem of BRBs of having remanen deformations after incursions in the plastic domain, during the last years a new conceptual design has been developed that uses composite tendons to re-center the BRB to its initial position. Fig. 2.12 presents the specimen and the hysteretic response of such type of BRB tested by Zhou et al. [23].

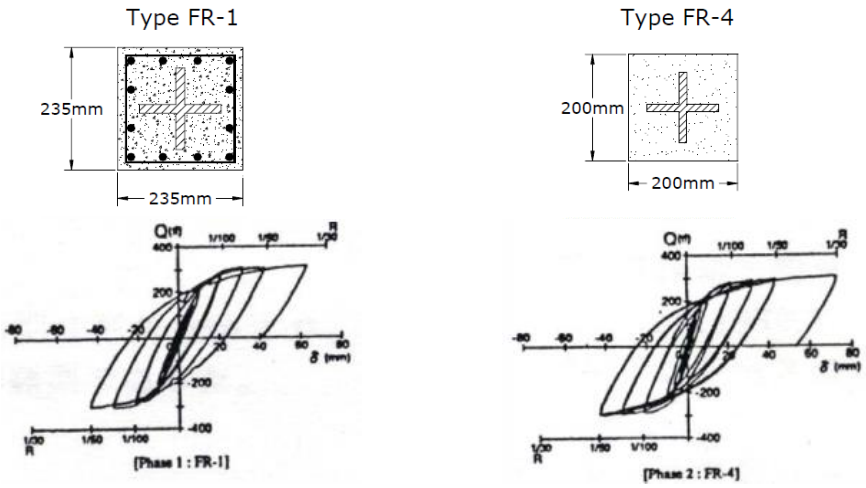

a) b)

Fig. 2.8. BRBs tested by Horie et al.: a) steel bar reinforced concrete BRM, b) steel fiber-reinforced concrete BRM [19]

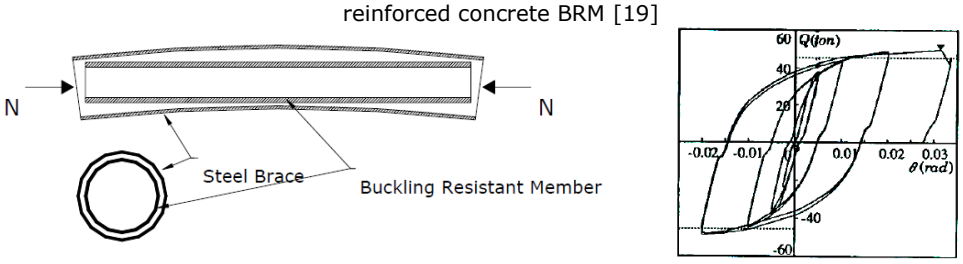

a) b)

Fig. 2.9. BRB tested by Tada et al.: a) tube-in-tube specimen, b) cyclic response [19]

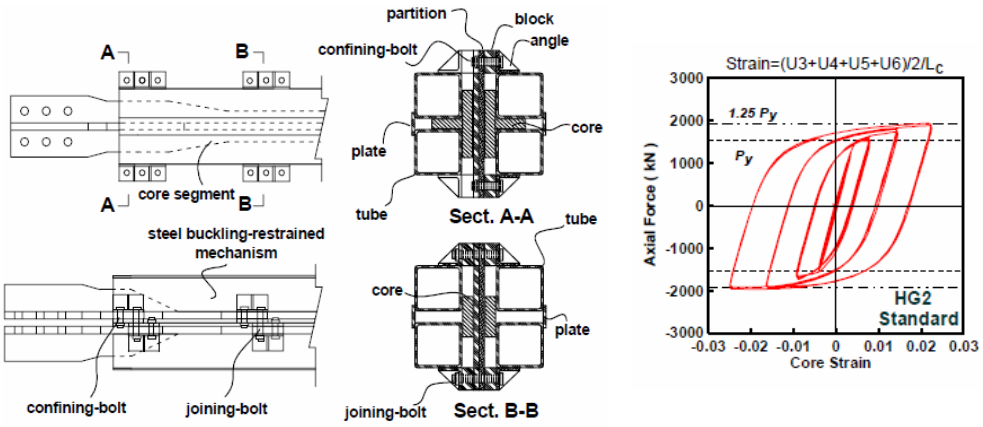

a) b)

Fig. 2.10. BRB tested by Tsai et al.: a) detachable specimen, b) cyclic response [21]

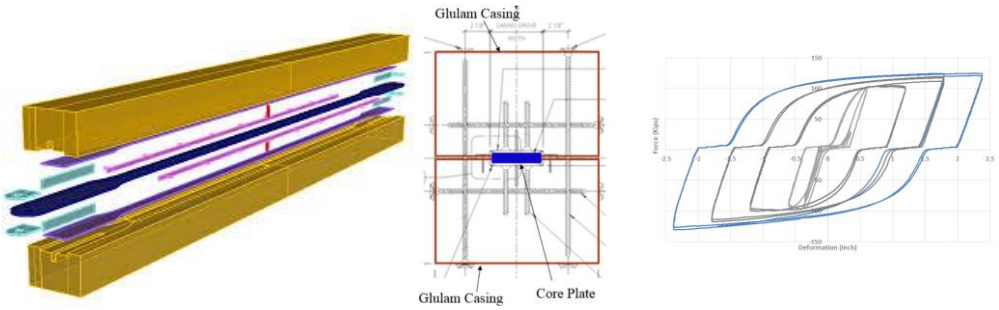

a) b)

Fig. 2.11. BRB tested by Blomgren et al.: a) specimen details, b) cyclic response [22]

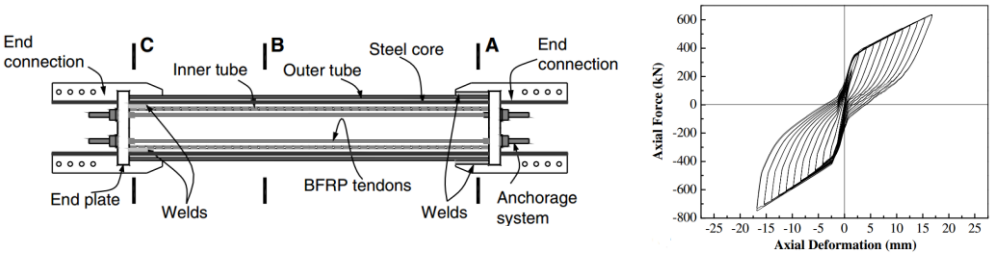

Fig. 2.12. BRB tested by Zhou et al.: a) specimen details, b) cyclic response [23]

Due to their hysteretic properties (see 2.1), the use of BRBs rapidly increased and many countries imported the technology and perform their own tests. The timeline of BRB development, project implementation and first codifications is presented below:

- Invention of BRB concept: Japan, 1971 [2];
  - Invention of UBB™: early 1980's [24];
  - Testing of UBB™: mid 1987;
  - Implementation of UBB™: February 1988;
  - Codification: 1996 [1].
- Technology transfer to USA: 1998 [24];
  - Testing: Spring 1999;
  - Implementation: January 2000;
  - Codification: 2005.
- Technology transfer to Canada: late 1990's [25];
  - Testing: late 1990's;
  - Implementation: 1999;
  - Codification: 2010.
- Technology transfer to Taiwan: 2001 [26];
  - Testing: early 2000's;
  - Implementation: 2002 [21];
  - Codification: 2005.
- Technology transfer to Korea: 2004 [27];
  - Testing: 2009 [28].
- Technology transfer to Europe: 2005;
  - Testing: Italy, 2005 [29]; Romania, 2010 [30] and 2017 [11]; Hungary, 2011 [31];
  - Implementation: Italy, 2005 [32]; Bulgaria, 2011 [33].

  - Codification: only in Romania, January 1st, 2014.
- Technology transfer to China: 2008 [34];
  - Testing: late 2000's;
  - Implementation: 2008.
- Technology transfer to Iran: 2008 [35];
  - Testing: late 2000's.
- Technology transfer to Turkey: 2009 [36];
  - Testing: late 2000's [36], 2010's [37], [38];
  - Implementation: 2011 [39].
- Technology transfer to New Zealand: 1991 [40];
  - Testing: early 2010's;
  - Implementation: 2011 [41].
- Technology transfer to Chile: 2015 [42];
  - Testing: late 2010;
  - Implementation: 2015 [43].

2.3 Structural systems using BRBs

Buckling restrained braces might be used as dampers in "Damage Tolerant Structures", or as lateral resisting system in buckling restrained braced framed structures.

Starting with 1992, BRBs were used in Japan as "damage fuses" (dampers) in what was called "Damage Tolerant Structure", a concept proposed by Wada et al. [44]. The concept is schematically presented in Fig. 2.13. It consists of a main gravity resisting structure (e.g. a steel moment resisting frame) which can remain in the elastic domain during an earthquake, and dampers (e.g. BRBs) which dissipates the seismic energy by incursions in the plastic domain. After a severe earthquake, the "damaged fuses" can be replaced and the main frame can restore to its initial position ("Easy Repairable Structure") [44].

In the case of the buckling restrained braced frame system (BRBF), the resistance against lateral forces is given by the BRB system (Fig. 2.14). Since the beams and the base of the columns have pinned connections, there is no additional contribution to the base shear (F_b) – storey drift (θ) response of the BRBF from the gravity resisting system. The BRBs will undergo plastic deformations at a level of lateral forces beyond the yield base shear, F_{by}. Therefore, large remanent storey drifts might be recorded for a ductility ratio μ ($\mu = \theta_y/\theta$, θ_y is the yield storey drift), as reported by Fahnestock et al. in [45]. This aspect might be a drawback for large applicability of the BRBF system. To reduce the remanent storey drifts, the use of a dual system was proposed by Kiggins and Uang [46]. The dual system consists in using a Special Moment Resisting Frame (SMRF), in addition to the BRBF system, as to provide a restoring force mechanism.

2.4 Advantages and disadvantages

BRBs have several advantages which makes them feasible solutions for both new and retrofit projects, as listed below:

- BRBs have the same yield strength in both tension and compression [10].
- During cyclic loading, the maximum compression force is slightly larger than the maximum tension force [1].
- The stable cyclic response of BRB allows for large energy dissipation [10].

- BRBs allow for flexible design since strength, stiffness and ductility can be adjusted to fit the requirements [18].
- Different available BRB-to-gusset connections allow for easy installation (see section 2.6.4).
- The demands on the beams, columns, gussets and foundations of a new/existing framed structure is reduced if using BRBs as bracing system [47], [48].
- BRBs allow for a more economic design of the lateral resisting system. According to [47], the BRBFs are more economical with almost 34% for a six-storey structure than the concentrically braced frames, CBFs (Fig. 2.15). Also, the cost savings are proportional to the height of the building.
- The repair costs are lower if using the "Damage Tolerant" concept, in comparison to conventional design (Fig. 2.17) [49].
- After an earthquake, the BRBs can be visually inspected [50] and, if damaged, replaced [29].
- Using BRBs as retrofitting technique allows for the reversibility of the intervention since their installation (on the existing gussets [9]) does not require significant interference with the existing structure.

The wide adoption of BRBs is precluded by several disadvantages, which are listed below:

- Most BRBs are proprietary [18] and more expensive than conventional braces [48].
- The yield strength of the steel used for the plastic zone of the core must be experimentally determined as it might considerably vary.
- Project-specific experimental tests on BRBs are required by the design codes for qualification [4], [5].
- BRBF structures may have large residual storey drifts under strong earthquakes [45].
- To start dissipating seismic energy, BRBs requires a certain storey drift to be attained.
- For retrofit projects, BRBs may introduce additional local stresses in the existing elements (e.g. nodes, beams); therefore, complementary techniques (e.g. FRP wrapping) may be required to locally increase the strength and ductility of the existing elements [30].
- Recorders of the cumulative/maximum deformation should be used for post-earthquake inspection in order to detect the level of damage of BRBs (Fig. 2.18) [1].
- Erection tolerances for BRBFs are smaller than those for CBFs [18].

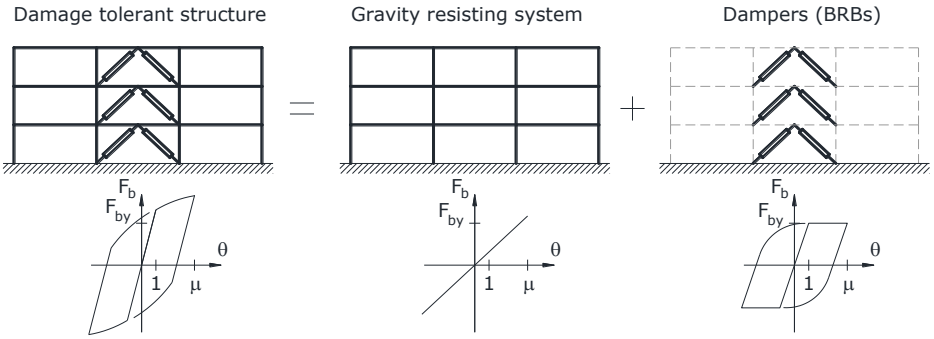

Fig. 2.13. Working concept of "Damage Tolerant Structure" (adapted from [44])

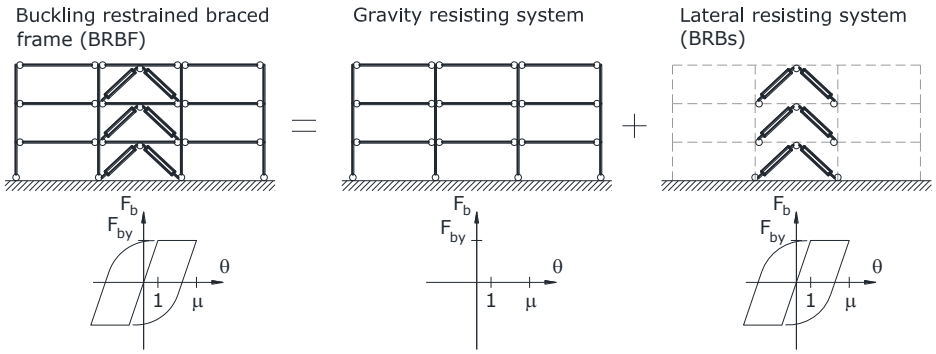

Fig. 2.14. Working concept of BRBF

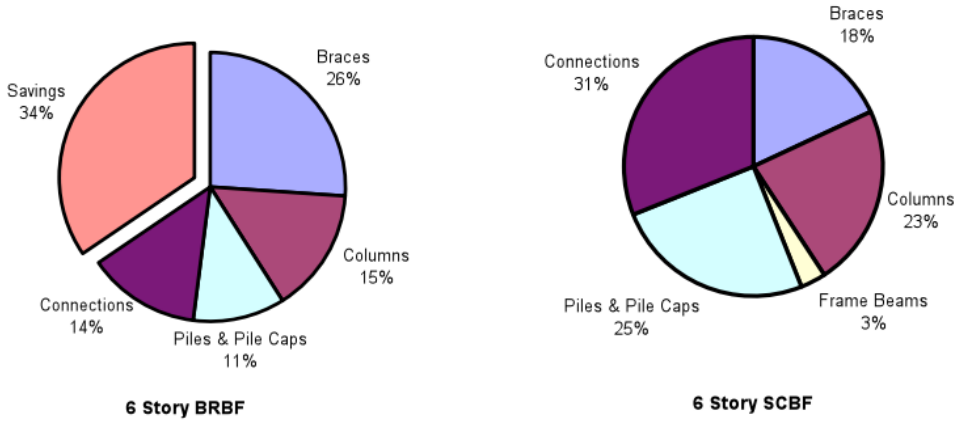

Fig. 2.15. Relative cost of lateral resisting systems: a) BRBF vs. b) CBF [47]

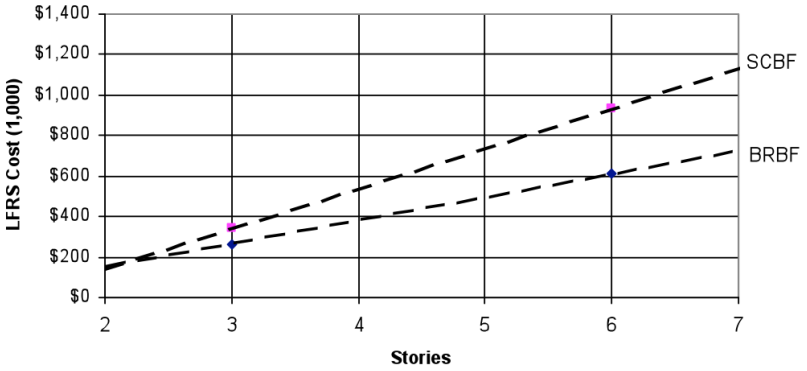

Fig. 2.16. Cost of the lateral resisting system relative to the storey height [47]

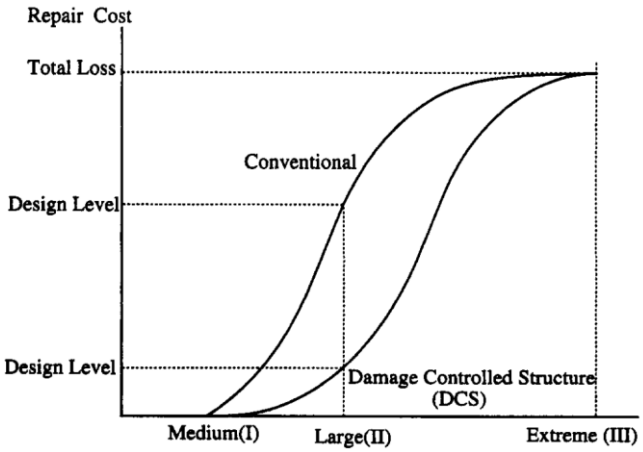

Fig. 2.17. Repair cost-earthquake intensity relations for conventional and "Damage Tolerant" designs [49]

a)

b)

Fig. 2.18. Meters for measuring a) the cumulative and b) the maximum deformation [1]

2.5 Examples of applications

In 1989, BRBs were used for the first time worldwide for a project application: the construction of the Nippon Steel Headquarter no. 2, Tokyo, Japan (Fig. 2.19) [1]. Many project applications soon followed under the concept of "Damage Tolerant Structure". An example of such structure is the Triton Square Project, located in Tokyo, Japan, built in 1992 (Fig. 2.20) [1].

Buckling restrained braces were embraced by many designers and used worldwide for seismic protection of building structures located in earthquake-prone areas. As detailed in [1], the first international application of UBB™ was in 1998 for the project UC Davis Plant and Environmental Science Facility (Davis, California, USA). After the transfer of "know-how" to the international market, the applications of BRBs increased substantially as new BRB concepts started to be developed, tested and produced in series by local and international manufacturers.

In Europe, the first BRB application was in Italy [32] in 2005 for the construction of the Faculty of Engineering of Ancona (Fig. 2.22). For the seismic protection of the precast reinforced concrete and steel framed building 86 buckling-restrained axial dampers (BRAD) were used. BRAD devices were provided by the local firm Fip Industriale S.p.A. [52]. After this project, many BRAD applications followed.

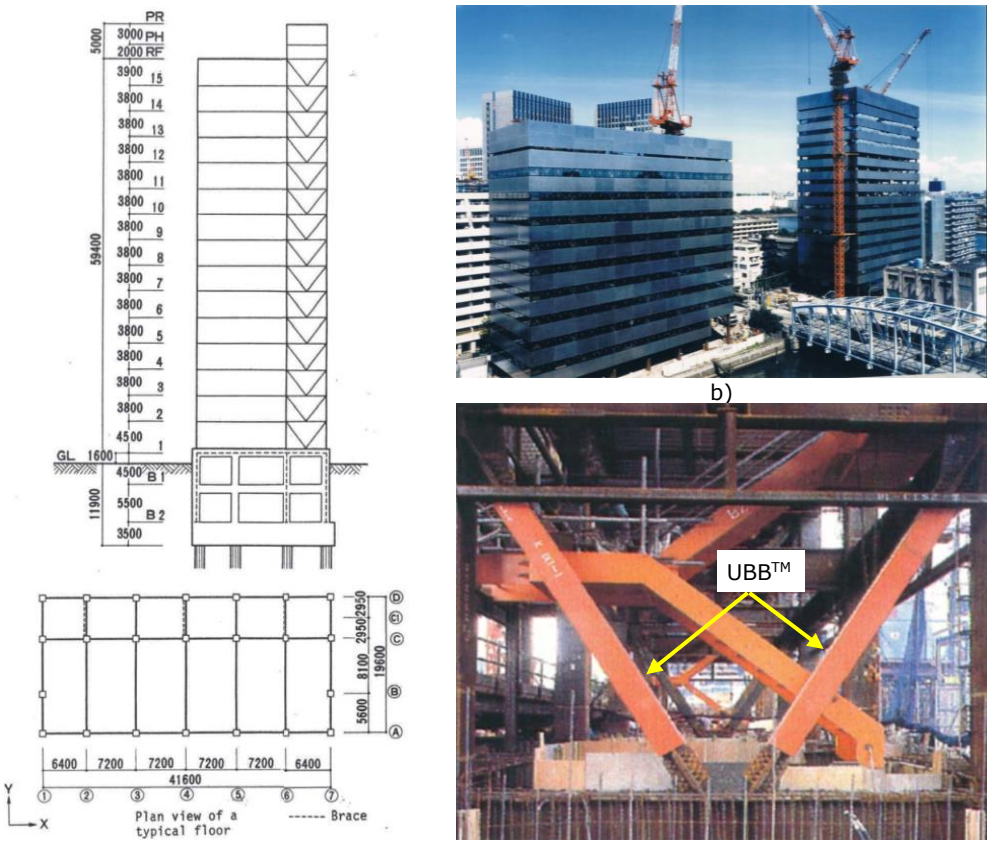

Fig. 2.19. First BRB (UBB™) application: Nippon Steel Headquarter No. 2, Tokyo, Japan, 1989: a) elevation and plan views [51], b) perspective view, c) BRB layout [1]

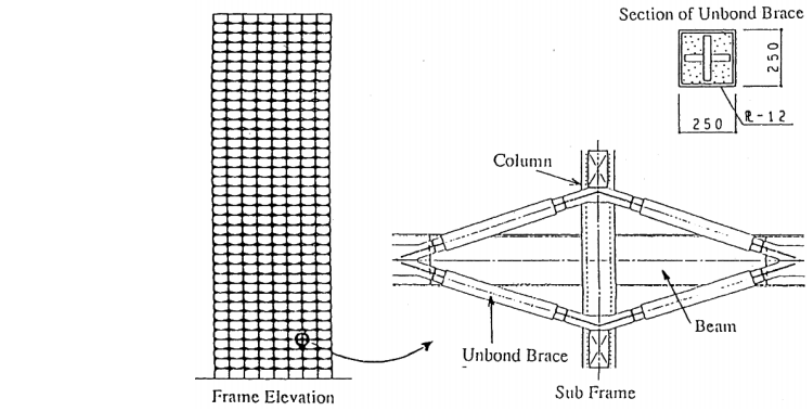

a)

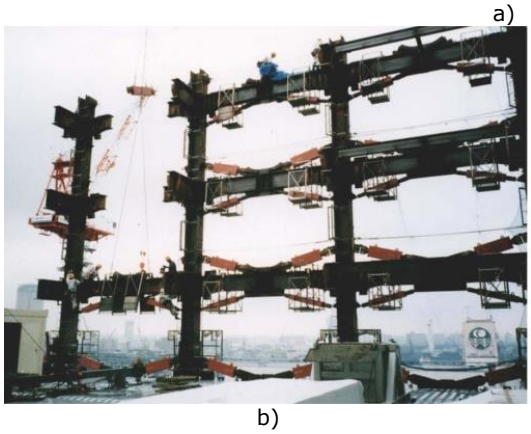

b)

c)

Fig. 2.20. The use of BRBs for "Damage Tolerant Structure" - Triton Square Project, Tokyo, Japan, 1992: a) frame elevation and structural details, b) construction stage and c) final stage perspective views [1]

Fig. 2.21. The first international BRB application - UC Davis Plant and Environmental Science Facility, Davis, California, USA, 1998

Due to their adjustability of strength, stiffness and ductility the BRBs have been used worldwide for both new and retrofit projects that involved either steel or concrete buildings [1]. BRBs proved to be feasible solutions for low-rise, mid-rise and high-rise residential buildings as the main lateral resisting system or to add additional damping or stiffness to the structure – outrigger systems. Also, BRBs found applicability in large projects, such as airports, stadiums, parking structures, medical and industrial facilities, even bridges or dam structures. Fig. 2.23 presents few representative projects that used BRBs for: new high-rise steel framed building (Fig. 2.23.a), outrigger system (Fig. 2.23.b), retrofit of reinforced concrete (RC) framed building (Fig. 2.23.c), retrofit of a communication steel tower (Fig. 2.23.d).

Fig. 2.22. First BRB application in Europe (Faculty of Engineering, Ancona, Italy, 2005) [52]

a)

b)

Fig. 2.23. BRB applications: a) Nagoya Lucent Tower [53], b) Washington Mutual Tower [33], c) Webb Tower [54], d) communication tower [55]

c)

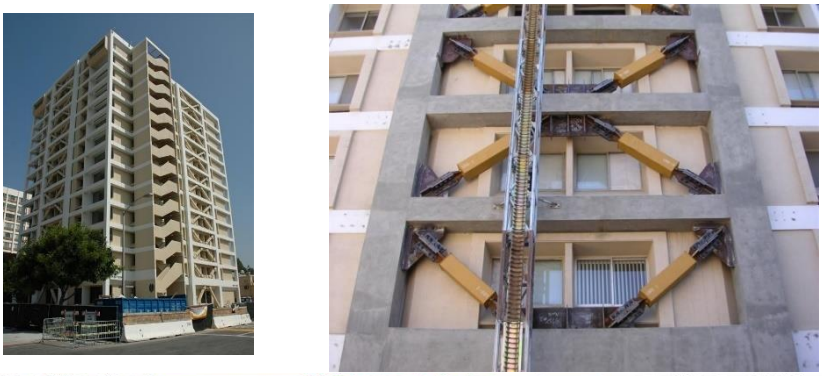

d)

Fig. 2.23 (continued)

2.6 Existing technical solutions

During the last 30 years, a wide range of technical solutions for the BRBs have been developed, tested and produced in series by either international (CoreBrace [56], Unbonded Brace [57]) or local suppliers (FIP Industriale [52], ROAD [58], SBC [59], among others). The BRB solutions existing on the market can be classified in two main typologies if considering as criterium the conceptual configuration of the buckling restraining mechanism, BRM:

- "conventional" BRBs – classical solution: the steel core is wrapped with a layer of unbonding material and then introduced into the BRM which consists of a concrete (mortar) filled steel tube [1];
- "dry" BRBs – alternative solution: the steel core is wrapped with a layer of unbonding material or a small gap and then introduced into the BRM which does not include concrete (e.g. a steel assembly [21], glulam casing [22]).

Other criteria can be also used to classify the existing BRB solutions:

- Plastic to node-to-node length ratio of the core, L_p/L_n:
  - Normal length BRBs – the ratio is between L_p/L_n = 0.5 – 0.8 [60];
  - Reduced length BRBs – the ratio is between L_p/L_n = 0.2 – 0.4 [61].
- Number of cores:
  - Single-core BRBs – the brace is equipped with only one core [10][61];
  - Multi-core BRBs – the brace is equipped with multiple cores, thus resulting a redundant system [21], [33].
- Number of core materials:

- Regular BRB - the core is made of a single material [10];
- Hybrid BRB – the core is made of plates of different materials (e.g. low-yield and high-strength steel) [62], [63].

- Type of core material:
  - Steel-core BRBs – the core is made of either low-yield [26], mild [29], high strength steels [62] or combination of the two [62], [63];
  - Aluminium-core BRBs – the core is made of aluminium alloy [64].
- Type of BRB-to-gusset connections [56], [57]:
  - Bolted connected BRBs – BRB is connected to the gusset using bolts and splices.
  - Pinned connected BRBs – BRB is connected to the gusset using a pin.
  - Welded connected BRBs – BRB is connected to the gusset using field welds.

From this classification it can be noticed that the differences between the exiting technical solutions relate to the configuration of the core (longitudinal and cross-sectional shape, material), of the buckling restraining mechanism (with or without infill concrete), of the unbonding material (a layer or gap) and of the BRB-to-gusset connection. A critical evaluation of the existing technical BRB solutions is presented below in order to identify the optimal configurations at component level.

2.6.1 Core

Several technical solutions have been used for the core of the BRB. The geometry of the cross-section can be of a compact shape (rectangular, circular, square, see Fig. 2.24.a-c), or can be a welded (Fig. 2.24.d-g) or as-rolled profile (Fig. 2.24.h-j). However, the compact cross-sections showed a more stable cyclic behaviour and a higher low-cycle fatigue resistance in comparison to the other sections. This enhance performance is caused by the absence of local buckling of the core walls and the absence of the residual stresses due to welding or forming process [65]. In Fig. 2.25.a is presented an example of local buckling of the walls of a four-angles welded cross-section core (Fig. 2.24.e), while in Fig. 2.25.b is presented the affected (pinched) hysteretic response of the BRB.

The longitudinal profile of the core is typically of a bone shape with a reduced cross-section in the mid-zone and enlarged cross-section at the ends [33], see Fig. 2.26.a. However, other longitudinal profiles were also proposed by different researchers. Black et al. [66] used a bone-shape longitudinal profile with cruciform cross-section (Fig. 2.26.b), while Tsai et al. [67] used a core with two distinct plastic segments (multi-curve), see Fig. 2.26.c. Cores of longitudinal profiles with constant width (flat-bars and plates) and stiffeners welded at the ends were used by Eryasar [36] (Fig. 2.26.d). Similarly, Oda and Usami [68] used hot-rolled H profiles and stiffeners to fabricate the core. Lately, Piedrafita et al. [69] (Fig. 2.26.e) used perforations of square shape to reduce the area of a constant cross-section plate in order to constrain the development of plastic deformations in a limited zone.

Fig. 2.24. Typical core cross-sections

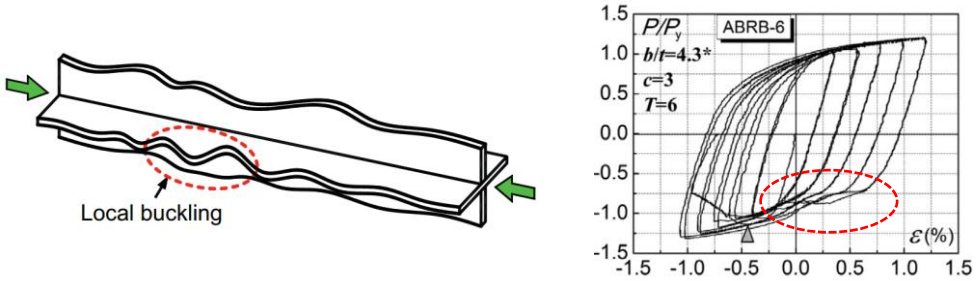

a) b)

Fig. 2.25. Local buckling of the walls of a composed core: a) schematic representation, b) affected hysteretic response [65]

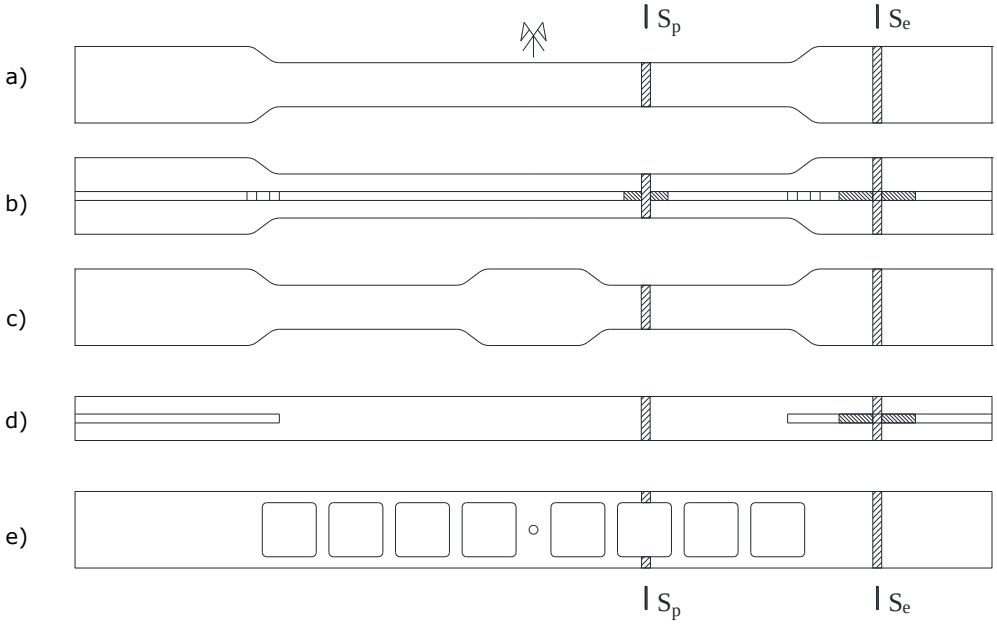

Fig. 2.26. Longitudinal core profiles: a) bone-shape (typical) [33], b) cruciform [66], c) multi-curve [67], d) constant width [36], e) perforated [69]

There are several advantages and disadvantages between these types of longitudinal core profiles which relate to the possibility of adjusting the capacity (geometry) of the core depending on the tested yield strength of the material, the difficulty of fabrication technology, the cost of production, and the low-cycle fatigue resistance of the BRB. From the point of view of adjustability, the longitudinal profiles with variable cross-section are the optimal solutions since fine adjustment can be made. From the technological point of view, the longitudinal core profiles consisting of a constant width plate/bar and stiffeners are the simplest and fastest solutions to be manufactured since no cutting or milling is required to crate the bone-shape. Also, the cost of producing such type of longitudinal profiles (constant width) is significantly lower, since the expensive process of cutting/milling is reduced/missing, and the welding process of stiffeners is much cheaper. The detailing of the core has a big influence on the low-cycle fatigue resistance of the BRB. Section variations might

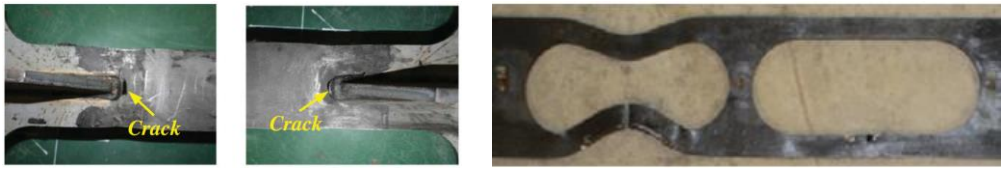

Fig. 2.27. Undesired brittle failure modes: a) cracks in base material at the stiffener base [71], b) excessive local buckling [69]

cause stress concentrations [70] which can lead to brittle failure modes, see Fig. 2.27. Therefore, the longitudinal core profiles with smooth transitions from reduced to enlarged cross-sections are the solutions with the lowest risk of a brittle failure mode.

For most of the existing technical BRB solutions, structural steels (low-yield [26], mild [29], high-strength steels [62] or combination of low-yield and high-strength [62], [63]) are used as the base material for the core due to their ductile plastic behaviour. Aluminium alloys were proposed as alternative materials due to their reduced weight. However, limited experimental results on aluminium-core BRBs are available in the technical literature [64], [80], [81], [82]. Within this thesis only structural steels are considered.

Table 2.1 summarizes different types of structural steels used for core. It can be noticed that the yield strength, f_y, varies within the range of 86-802 N/mm^2. The ultimate strength, f_u, might be roughly of one up to three time the yield strength. In most cases, ductile steels are used with the rupture strain, ε_r, of at least 15 times the yield strain, $\varepsilon_y = f_y/E$ (E is the elastic modulus of steel).

Most applications are using BRBs with the material yield strength within the range of 200-400 N/mm^2. However, according to Chen [83] and Ma et al. [84], the BRBs with the core made of steels with low yield strength (LYS100, Q100) are feasible solutions for bracing reinforced concrete structures (retrofit or new projects) due to the mechanical property of the base material of yielding at small strains (ε_y = 0.0005 for Q100, ε_y = 0.002 for LYS). This allows the BRB to start dissipating energy at small storey drifts. According to Sugisawa et al. [62] the (hybrid) BRBs using both low yield and high strength streel are feasible solutions for both seismic protection and vibration control. As concluded by Atlayan in [63], using hybrid BRBs caused a reduction of the residual displacements with 30-40 %.

Table 2.1 Different types of structural steels used for core

Researcher	Steel type	f_y, N/mm^2	f_u, N/mm^2	f_u/f_y, -	ε_r, mm/mm
Chen [83]	LYS100	86*	253*	2.94	0.57*
Ma et al. [84]	Q100	90	247	2.74	0.60
Razavi et al. [61]	ST37	235	340-470	1.45-2.0	0.24
Iwata et al. [75]	SN400B	262*	432	1.65	0.32*
Dunai et al. [31]	S235	280*	448*	1.60	0.35
Watanabe et al. [20]	SM490	282*	490-610	1.74-2.16	0.21
Mazzolani et al. [14]	S275	319*	410-560	1.29-1.76	0.23
Wu et al. [85]	CNS SN490B	344*	490-610	1.42-1.77	0.21
Tsai et al. [67]	A572	350	450	1.29	0.21
Atlayan [63]	HPS-70W	503	585-760	1.16-1.51	0.19
Atlayan [63]	HPS-100W	745	760-895	1.02-1.20	0.18
Sugisawa et al. [62]	WT780	802**	860**	1.07	0.10**

* test values.
** mechanical properties from [86].

2.6.2 Unbonding interface

As the unbonding interface is of a critical importance in allowing the BRB to develop symmetric hysteretic behaviour, details regarding its composition are not given by the international suppliers. Therefore, for most on the market BRBs the unbonding interface is proprietary. However, some researchers shared their technical solutions used for the unbonding interface. Table 2.2 summarizes the relevant solutions adopted for both "conventional" and "dry" BRBs typologies. In most of the cases different thicknesses of the unboding material were used for the through-thickness, g_t, and the through-width, g_w, direction with respect to the core cross-section.

While for "conventional" BRBs the unbonding interface is a layer of material (Fig. 2.28.a), in the case of "dry" BRBs the interface can be either a material layer or a gap (Fig. 2.28.b). Tremblay et al. [10] suggested the use of a material layer for "dry" BRBs to reduce the friction forces transmitted to the BRM. Also, Chen et al. [91] concluded that in the case of "dry" BRBs that were provided with unbonding material (not only a gap) lower compression strength adjustment factors, β, were obtained in comparison with "dry" BRBs that had only a gap (space) as unbonding interface. The β factor is defined as the ratio between the maximum compression for, C_{max}, divided by the maximum tension force, T_{max}, developed during cyclic loading.

Table 2.2 Relevant technical solutions for the unbonding interface

BRB type	Researcher	Unbonding interface	g_w mm	g_t mm	β
"conv."	Watanabe et al. [20]	forming of polystyrol (fp) & vinyl/mastic tape (tp)	3 (tp)	1 (fp)	1.18
	Suzuki et al. [2]	silicone paint	-	-	-
	Tremblay et al. [10]	dow ethafoam (de) & polyethylene film (pf)	3 (de)	0.8 (pf)	1.30
	Iwata et al. [75]	fp & tp	3 (tp)	1 (fp)	1.17
	Lai and Tsai [73]	silicone rubber (best out of 10 material configurations)	2	2	1.18
	Tsai et al. [88]	self-adhesive chloroprene rubber (best of 4 materials)	2	2	1.13
	Midorikawa et al. [89]	butyl rubber	1	1	-
"dry"	Tremblay et al. [10]	gap (g)	0.3	0.3	-
	Iwata et al. [75]	gap	1	1	-
	Iwata et al. [75]	fp & tp	3 (tp)	1 (fp)	-
	Eryasar [36]	pf & gap +/- grease	1 (g)	0.2 (pf)	1.05-1.22
	Wu et al. [85]	gap	2	1	1.18
	Wu et al. [90]	butyl rubber	2	1	1.07
	Chen et al. [91]	butyl rubber	1	1	1.07
	Chen et al. [91]	gap	1	1	1.27

Among the presented studies in Table 2.2, industrial applications followed the research performed by Lai and Tsai [73]. In a later study, Tsai et al. [88] reduced the overall construction cost of the unbonding interface with almost 50%. They selected the self-adhesive chloroprene rubber (CR) as the optimal solution from the point of view of construction cost-BRB cyclic performance. The other tested materials were: high-density styrofoam sheet (HR), rubber sheet (R), silicone rubber sheet (SR), see Fig. 2.28.a.

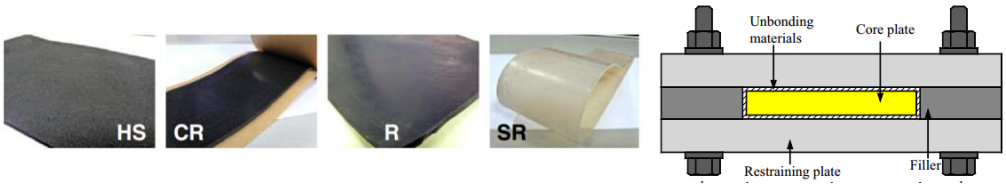

Fig. 2.28. Technical solutions for unbonding interface: a) material layer [88], b) gap [91]

2.6.3 Buckling restraining mechanism

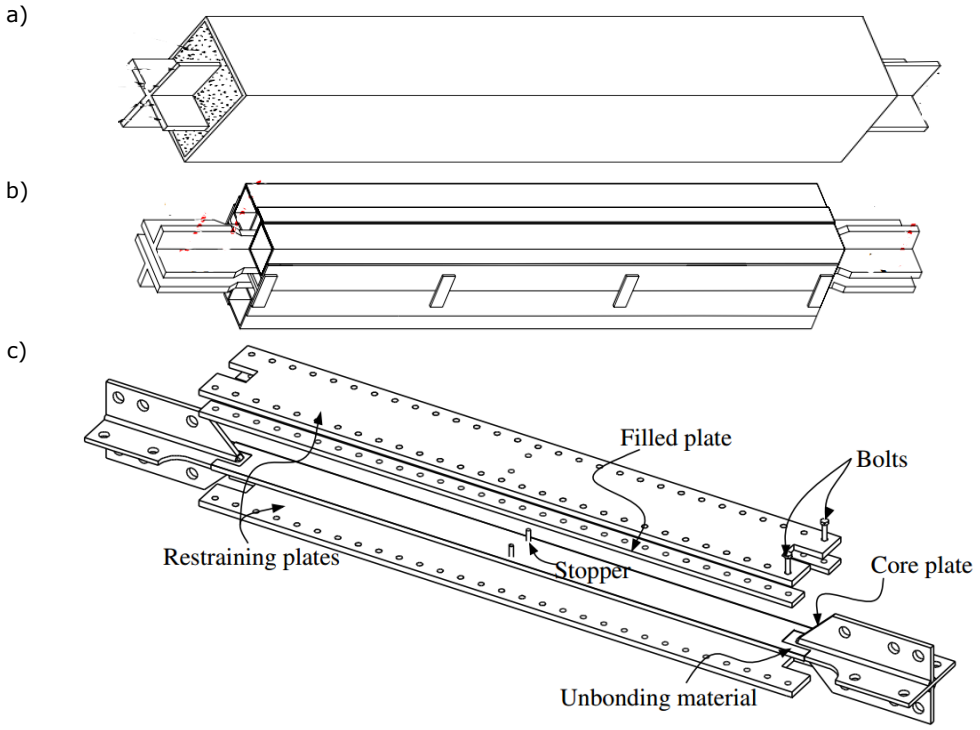

Fig. 2.29. BRM geometries of a) "conventional" BRB (typical) [66], b) welded [73] and c) bolted "dry" BRB [74]

The geometry of the buckling restraining mechanism, BRM, depends on the longitudinal profile and the cross-section of the core. For "conventional" BRBs, the typical configuration consists of a concrete filled rectangular, square or circular tube.

The rectangular BRMs may be suspected to local bulging, as shown in [1]. Also, better fire-resistance of circular cross-section BRBs was numerically shown by Talebi et al. [72] with respect to the rectangular cross-section. For "dry" BRBs there is no typical configuration. However, welded or bolted (detachable) steel assemblies were proposed. The welded BRMs are sensitive to initial imperfections caused by the welding process and requires additional technological processes for assembling and welding the components. In the case of bolted BRMs, the assembling welds are reduced/eliminated, reduced tolerance holes and high strength bolts are required. A more complicated design is required for bolted BRMs to assure successful results.

Fig. 2.29 schematically presents longitudinal profiles of BRMs used for "conventional" BRBs (typical configuration) [66], welded [73] and bolted [74] "dry" BRBs. Fig. 2.30 presents the mid-span cross-section of different BRM types.

2.6.4 BRB

The geometry of the BRB is rather simple as it consists of only three components: core, unbonding material and buckling restraining mechanism. Up to date, a wide range of cross-sections have been proposed by researchers for both the "conventional" (Fig. 2.30.a-b) and "dry" BRBs (Fig. 2.30.c-d) by varying one of its components. According to [1], the best performance among all available BRBs is obtained using the "conventional" solution consisting of either a rectangular or cruciform steel core encased by a mortar-filled circular of rectangular steel tube. Fig. 2.31 presents the cyclic performance of four BRBs with different cross-sections, which were commercially available on the Japanese market in the early 2000's [75]. Furthermore, it was experimentally demonstrated by Nakamura et al. [76] that the BRBs with rectangular core cross-sections can develop greater cumulative inelastic deformations prior fracture in comparison to BRBs of cruciform core cross-section.

In the initial phase of the development of BRBs, single core cross-sections were proposed for relative low capacities (Fig. 2.30.a). As the BRBs started to be used for high-rise buildings, cross-sections with up to four cores were used for large capacities (Fig. 2.30.b) [33]. The BRBs with cross-section equipped with multiple cores are considered redundant systems [33]. As shown by Lai and Tsai [73], this type of (double core) BRBs have a good low-cycle fatigue behavior.

The overall geometry of the BRB varies between the manufacturers and most of the time is protected by a patent. Various BRB-to-gusset connection details are available which allows for flexible connection design. In the following paragraphs several BRB solutions available on the current market are presented, with the emphasis on their unique features. It needs to be noticed that the unbonding material is proprietary in most of the cases and no details are given.

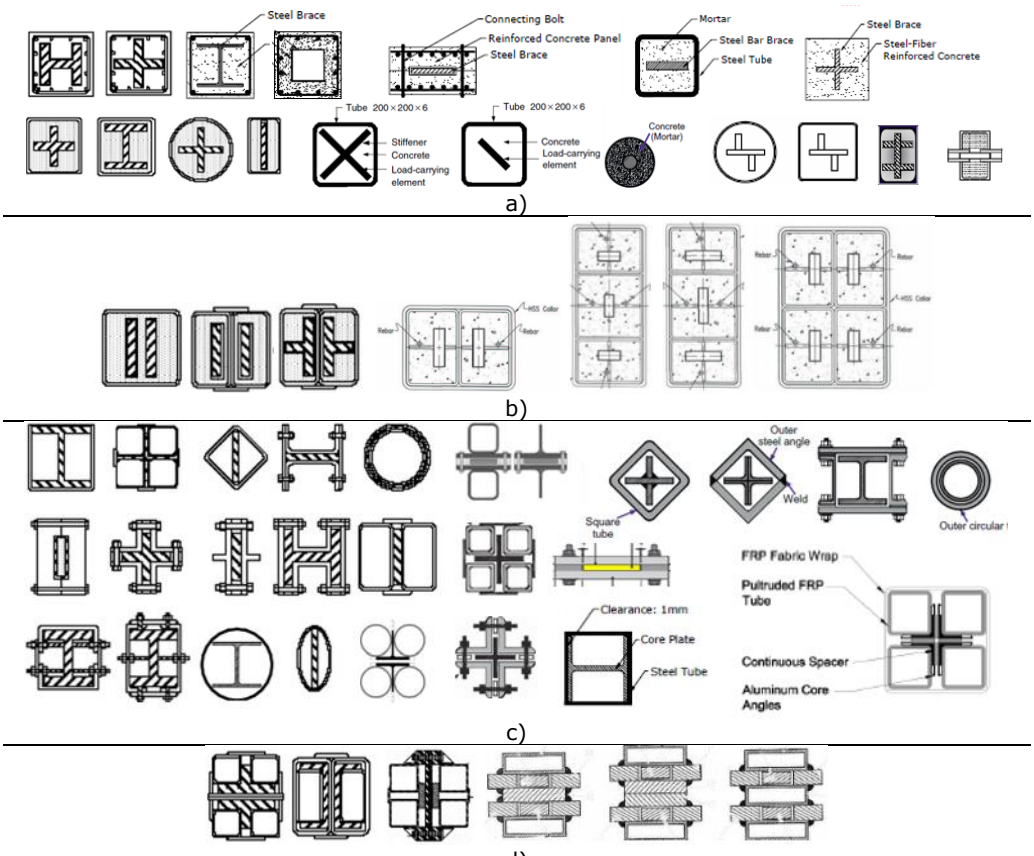

Fig. 2.30. BRB cross-sections: "conventional" a) single and b) multi-core, "dry" c) single and d) multi-core [1] - [74]

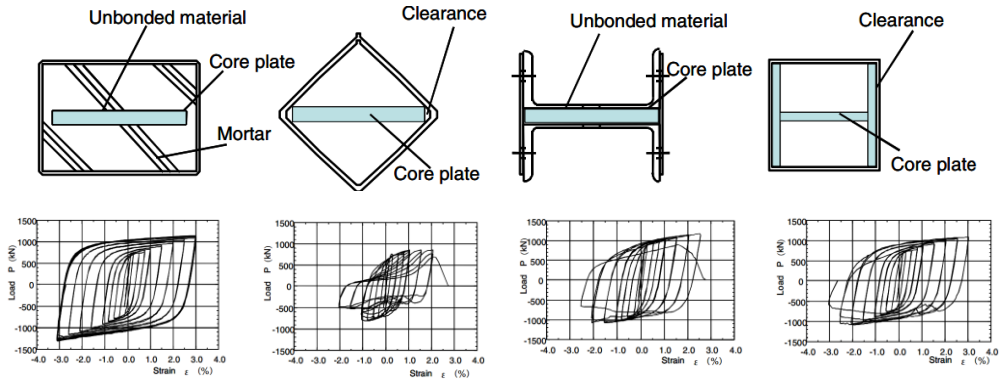

Fig. 2.31. Cyclic performance of BRBs with different cross-sections [75]

Nippon Steel & Sumikin Engineering, NSEUSA, [57], [77], the first BRB supplier, uses cores of variable rectangular or cruciform cross sections plates along the length (Fig. 2.32.a). In the case of rectangular cores, end stiffeners are welded at the ends, perpendicular on the core for the stability of the connection zone. The BRM can be either circular or rectangular mortar-filled steel tube. Plate (Fig. 2.32.b) or tube-welded (Fig. 2.32.c), bolted (Fig. 2.32.d) and pinned (Fig. 2.32.e) connections are available. According to [57] "it is the most rigorously reviewed and approved BRB system".

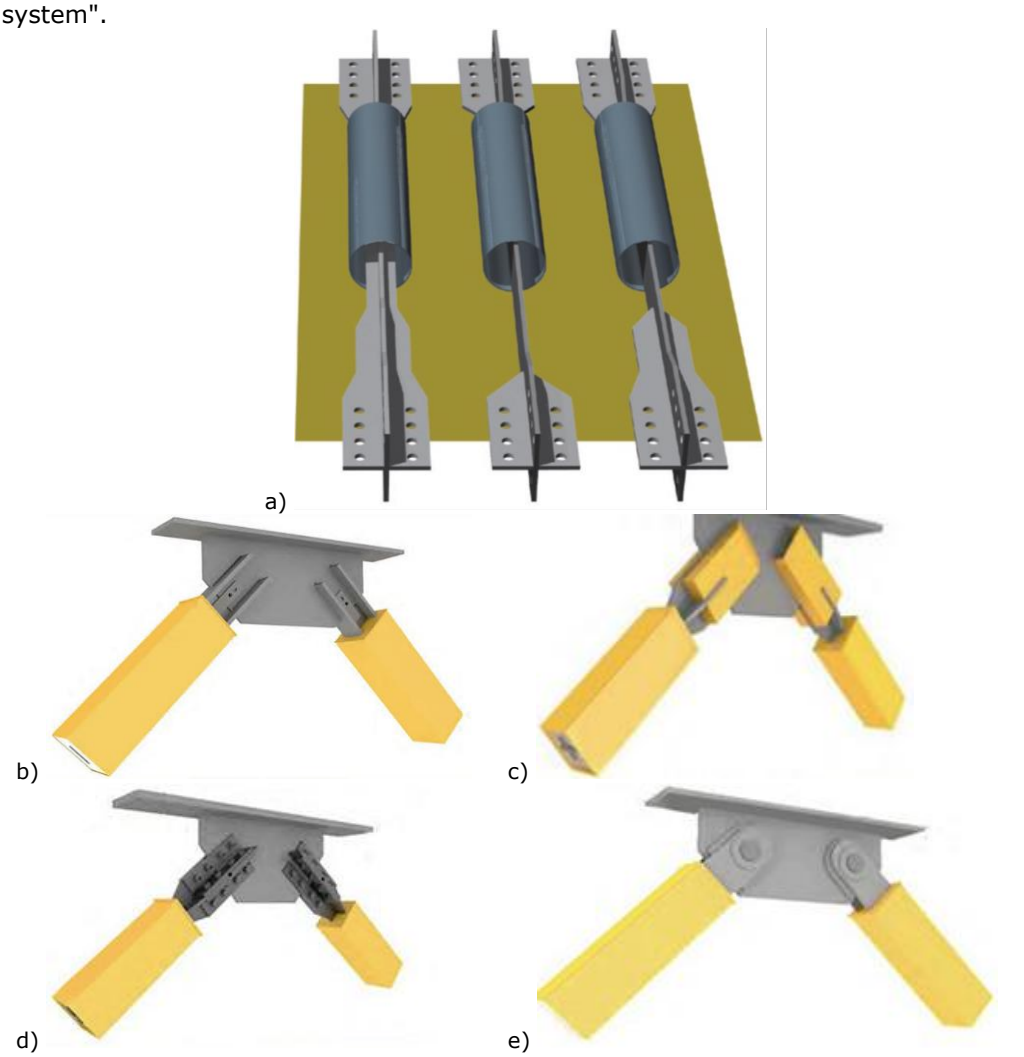

Fig. 2.32. NSEUSA BRBs (Unbonded Braces): a) typologies, b) - e) connections details [77]

Star Seismic LLC [78] (a CoreBrace LLC company starting with February 5th, 2016) uses for the core rectangular steel plates of variable cross-section with radiused cut-outs to allow for a smooth transition between plastic and elastic zones ((Fig. 2.33.a-b)). The BRM consists of a rectangular or circular concrete-filled steel tube and end collars for the stability of the connection zone (Fig. 2.33.c). The collars are also used to connect the cores of the redundant system for equal deformation. Using two

T-shape plates, the length of the bolted connection and the number of bolts is reduced by half. Welded or pinned connections are also available (Fig. 2.33.d).

Fig. 2.33. Star Seismic (a CoreBrace company) BRBs: a) – c) typologies, d) connections details [78]

CoreBrace LLC [56] uses steel cores of variable rectangular or cruciform cross-sections with stiffeners and connecting plates welded at the ends (Fig. 2.34.a-c). The transition from the plastic to elastic zone is done using inclined cut-outs (no radius). Concrete-filled steel tubes are used for the BRMs. Classical (bolted) splice, welded and pinned connections are available (Fig. 2.34.d). To reduce the number of bolts, lug connections were proposed.

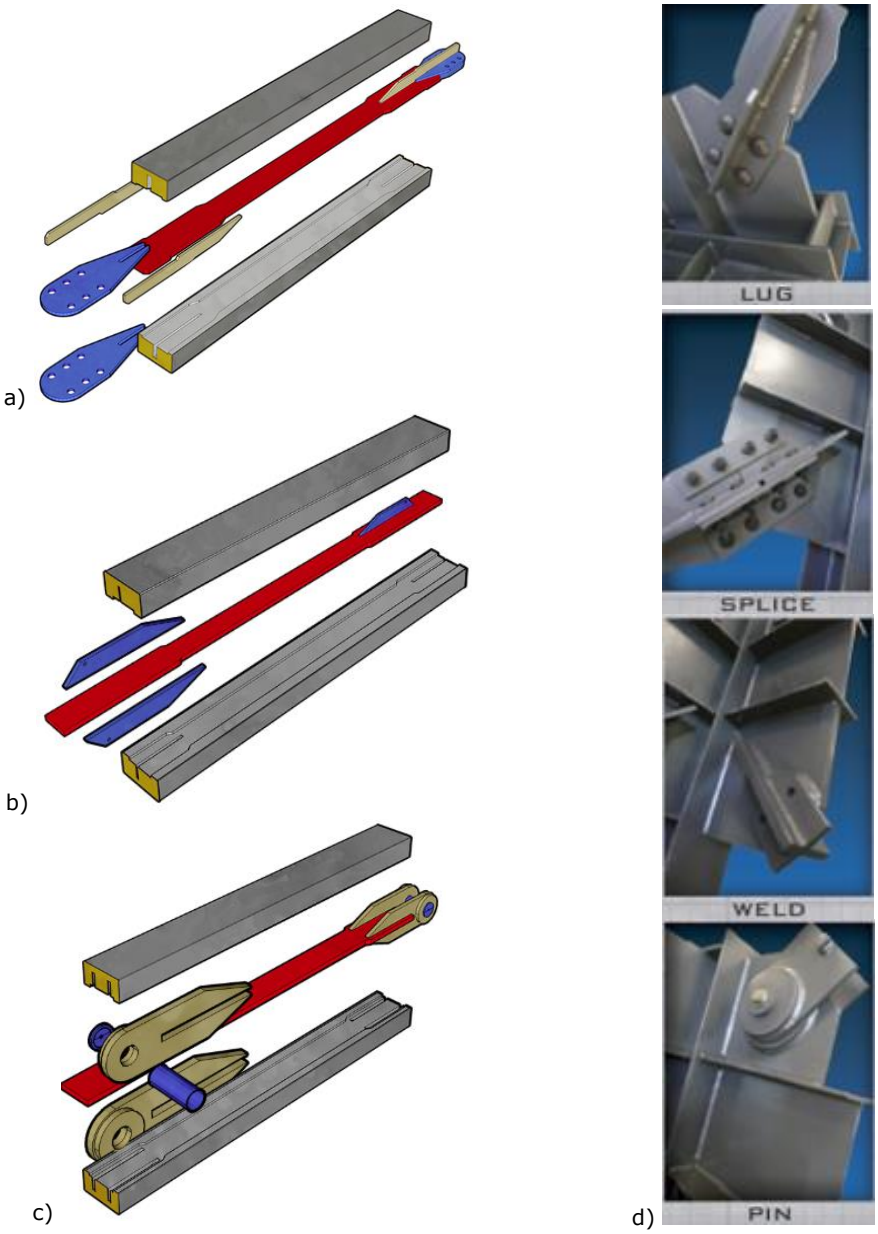

Fig. 2.34. CoreBrace BRBs: a) - c) typologies, d) connections details [56]

Both "conventional" and "dry" (all steel) BRBs were developed at the National Center for Research on Earthquake Engineering, NCREE, in Taiwan by Tsai et al. [21]. Two technical solutions were developed for "conventional" BRBs using either rectangular or cruciform cross-sections: double cored, DC-BRB (Fig. 2.35.a), and welded end-slot buckling restrained brace, WES-BRB (Fig. 2.35.b). "Dry" BRBs were developed using either welded (Fig. 2.35.c) or bolted steel assemblies (Fig. 2.35.d). Inspectable BRBs were also developed using bolted BRM to allow for visual inspection

of the core (Fig. 2.35.e) [50]. Bolted or welded BRB-to-gusset connections can be used (Fig. 2.35.f-g). Special detailing allows for shorter (lap) connection length.

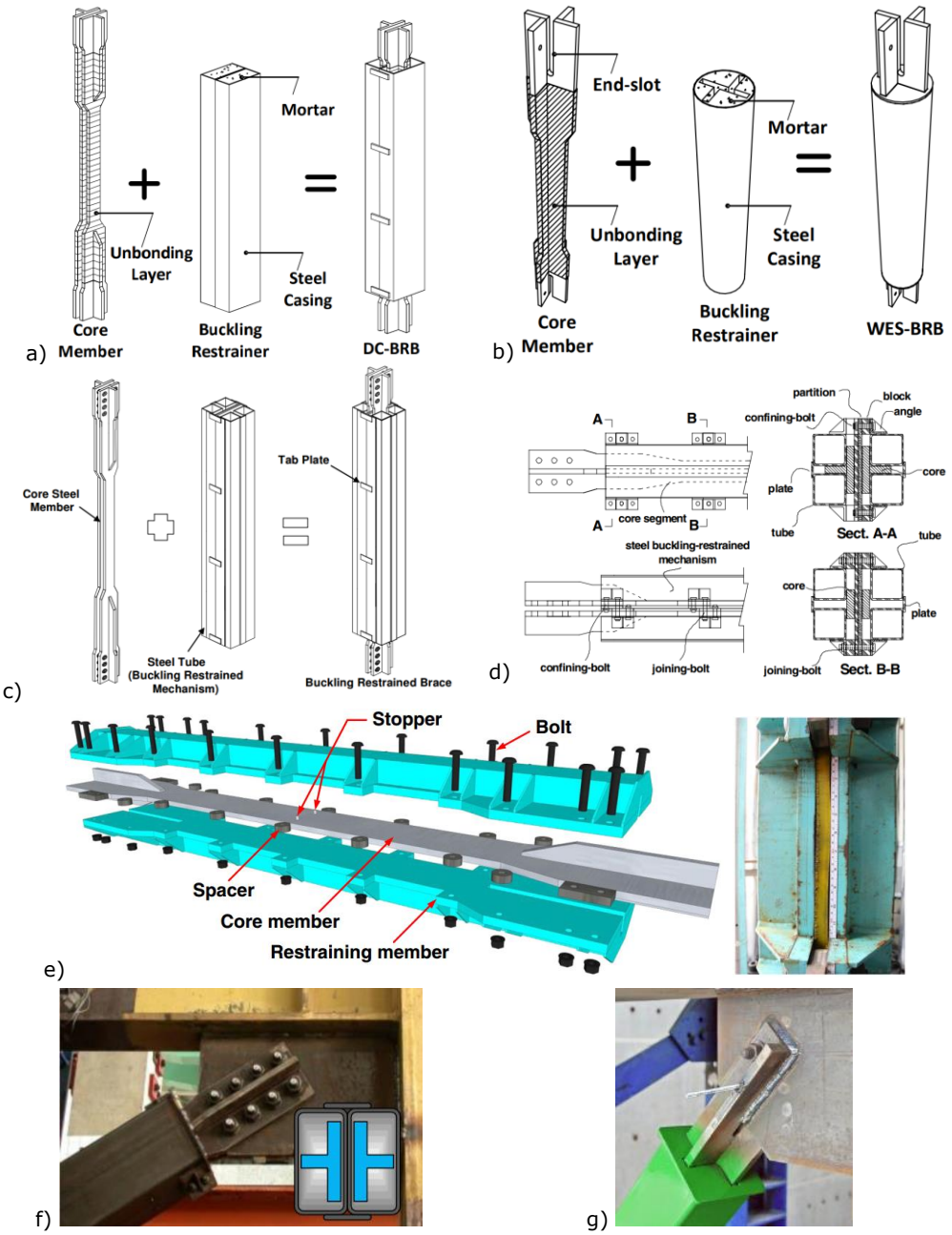

Fig. 2.35. NCREE BRBs: a) - b) "conventional" and c) – e) "dry" typologies, f) – g) connections details [21], [50]

There are several advantages and disadvantages regarding the BRB-to-gusset connections presented above (Fig. 2.33, Fig. 2.34, Fig. 2.35). Bolted connections are the most used due to the oversized holes which allow for larger tolerances for on-site erection. The redundancy of the connection is given by the multiple bolts, which allow for a more uniform distribution of stresses in the gusset plate in comparison to pin connection. Multiple bolts require larger gussets, thus shorter core plastic length. As in the case of welded and lug connections, bending moments are transmitted to the brace due to the frame effect (opening and closing of the beam-to-column angle). Reduced connection length can be obtained if using welded, pinned or modified bolted (lap connection with T-shape connection plates) connections. Pinned connections eliminate the end moments but require small erection tolerances [79]. Using pinned or bolted connections, a pinched hysteretic behavior is obtained due to connection slippage. This problem can be solved if using welded connections, which requires on-site welding and verification.

2.7 Existing design regulations

Up to date, several countries have included regulations for BRBs or BRBFs in their design codes. The currently used norms are listed below:

- Japan: BSLJ - 2000, "Building Standard Law of Japan" [15].
- SUA:
  - ANSI/AISC 341-16, "Seismic Provisions for Structural Steel Buildings" [92].
  - ASCE/SEI 41-17, "Seismic Evaluation and Retrofit of Existing Buildings" [93].
- Taiwan: ABRI 2005, "Recommended Provisions for Building Seismic Regulations" [94].
- Canada:
  - CSA S16-14, "Design of Steel Structures" [95].
  - NBCC 2015, "National Building Code of Canada 2015" [96].
- Europe:
  - EN 15129, "Anti-seismic devices" [4].
  - Romania: P100-1/2013, "Code for seismic design – Part I – Design prescriptions for buildings" [5].

In Europe, the seismic design code EN 1998-1 [3] does not have design regulations regarding the use of BRBF system yet (2018); they will be introduced within the next revision of the core [3]. Instead, the European norm EN 15129 [4] have requirements regarding testing and manufacturing of BRBs. In this context, Romania is the only country in Europe that regulated the use of BRBF system starting with January 1st, 2014. The provisions from P100-1/2013 [5] are similar to those from ANSI/AISC 341-10 [100] (the previous version of ANSI/AISC 341-16 [92]).

According to [25], design regulations for BRBF system will be included also in Chile and in New Zealand in the next revision of their building codes [98], [99].

The design method of the frames equipped with BRBs is based on the "Performance Based Design" concept [44]. There are two approaches regarding the consideration of the BRBs in the structural design:

- BRBs (BRBF) are the main lateral resisting system, as regulated by AISC 341-16 [92], P100-1/2013 [5].
- BRBs are secondary dissipative systems, as regulated by BSLJ – 2005 [15].

2.8 Needs for further research and development

In the context of existing design provisions for BRBFs in Romania, the proprietary character of commercialized BRB solutions limits their wide adoption. The experimental qualification required by the design code P100-1/2013 [5] and the lack of design experience of structural engineers also limits their large applicability.

Therefore, research and development of new BRB solutions is carried out within this thesis in the frame of "IMSER" grant [6] aiming at providing open-source pre-qualified BRB solutions as to facilitate their wide adoption. Unique BRB technical solutions ("conventional" and "dry") are intended to be developed as not to conflict with the copyright law. This involves comprehensive studies involving both numerical and experimental tests as to assure BRB solutions with a high level of reliability.

The research and development of the pre-qualified BRB solutions and the assessment of their seismic performance are organized in a research program, as to assure their accomplishment. The research program of the thesis is closely related to the one of the "IMSER" grant [6]. The state of art provided a comprehensive background on the experimental tests and the existing BRB technical solutions in order to provide the basis for the development of new conceptual designs. It needs to be mentioned that limited past research on BRBs is available in Romania, as only two PhD theses focused on experimental [30] and numerical [101] investigations. Based on the critical evaluation of existing BRB technical solutions, new conceptual designs will be proposed for "conventional" and "dry" BRBs. Numerical and experimental pre-testing will allow for optimization of the proposed solutions. The final solutions will be fabricated and then tested using a cyclic loading protocol. Uniaxial tests on base materials (steel and concrete) will allow for calibration of the input parameters of material models, which are used in numerical simulations on BRBs. Assessment using both experimental and numerical results will allow to define the design recommendations for BRBs. Performance based design on two-dimensional models of steel framed buildings equipped with BRBs of similar capacity and stiffness but different levels of the axial strain in the plastic zone will allow for optimization of the core geometry as to properly fit the demands. Nonlinear static and dynamic analyses will be carried out on case study frames, and additional design criteria for BRBFs will be proposed.

It can be concluded that this research program is required as to clear the way for a rapid adoption of the BRBs into the design practice by developing pre-qualified technical solutions and by transferring the "know-how" on the design of BRBs to the industry.

2.9 Concluding remarks

Since the initial development of the buckling restrained braces (BRBs) in Japan in the mid 1980's, many conceptual designs were proposed, and successful hysteretic results were obtained. In most cases, their use is protected by a patent.

The cost savings provided by the buckling retrained braced frames (BRBF) make this system to be a more feasible solution for seismic protection of buildings in comparison to conventional braced frames (CBF).

BRBs have been intensively used for the last 30 years in earthquake-prone countries, like Japan, USA, Taiwan, New Zealand, among others. Up to date, limited applications are recorded in Europe, and no applications in Romania.

The critical evaluation of existing technical solutions revealed that the cores of compact cross-sections showed a more stable cyclic behaviour and a higher low-

cycle fatigue resistance in comparison to the other sections. Longitudinal core profiles of bone-shape allow for fine adjustment of the BRB capacity, while using a hot-rolled compact-shape steel profile with stiffeners welded at the ends allow for faster and less expensive production-cost of the core. The longitudinal core profiles with smooth transitions from reduced to enlarged cross-sections are the solutions with the lowest risk of a brittle failure mode. The failure mode of the BRB caused by buckling of elastic core zone outside the BRM can be avoided by welding stiffeners perpendicular to the core. Self-adhesive (rubber) tape significantly reduces the overall construction cost of the unbonding interface (almost 50%). Concrete-filled steel tubes (used for "conventional" BRBs) are the most used solutions for the buckling restraining mechanism. Steel assemblies (used for "dry" BRBs) represent an alternative solution, with reduced weight and technological time, in-situ visual post-earthquake inspection, and damaged-core replacement. BRBs with bolted connections are feasible solutions for seismic applications due to the redundancy of the connection and easy installation.

Several countries introduced regulations for BRBs/BRBFs in their design codes. The European norm EN 1998-1 [3] does not currently have design regulations regarding the use of BRBFs. Romania is the only country in Europe that regulated the use of BRBF system starting with January 1st, 2014. Even though seismic design provisions for BRBF are available in P100-1/2013 [5], there are no project applications in Romania yet. This might be caused by: the proprietary character of BRBs, the project-based experimental validation required by P100-1/2013 [5], the lack of experience of the practicing structural engineers in designing the BRBs/BRBFs.

It is this thesis aim to develop, in the framework of the "IMSER" grant [6], a set of pre-qualified BRBs to be used for low-rise and mid-rise framed buildings located in Romania. The pre-qualification will eliminate the necessity of project-based experimental validation for future projects. Both "conventional" and "dry" BRBs are intended to be developed.

Comprehensive (further) research and development is required to assure the new BRB solutions with a high level of reliability.

3 DEVELOPMENT OF TECHNICAL SOLUTIONS

3.1 Selection of capacities

Within the frame of the IMSER grant [6], multi-storey steel framed structures with three and six storey height were considered representative for typical low-rise and mid-rise buildings located in Romania [102] (Fig. 3.1).

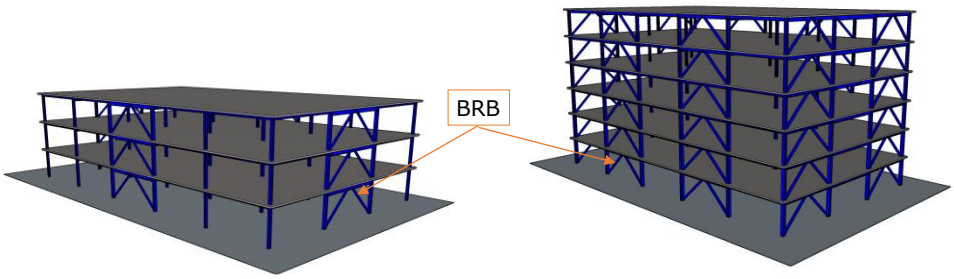

a) b)

Fig. 3.1. Three-dimensional models of the a) low-rise and b) mid-rise BRBF structures [102]

Eight archetype steel BRBFs were designed according to P100-1/2013 [5], both in standard and dual configuration. Buildings had three and six storeys of 3.5 m, and 3x5 bays of 7.5 m. Two sites were considered: Timisoara, with corresponding design peak ground acceleration of 0.2*g* (and a control period T_C = 0.7 s), and Bucharest with 0.3*g* (and a control period T_C = 1.6 s). Design forces in BRBs in the seismic load combination were 150 kN to 840 kN. Considering the ANSI/AISC 341-10 [100] (in use at the time of design of BRBF structures) requirement that the yield strength of tested BRBs be in the range 0.5 to 1.2 times the nominal capacity of the prototype, two values of resistance of prototype BRBs were selected: 300 kN and 700 kN [11].

3.2 Conceptual solutions

As most BRBs are protected by a patent, the adoption of their unique configuration conflicts with the copyright law. Therefore, the aim of this thesis (in the frame of IMSER grant [6]) is to develop new technical solutions for both "conventional" and "dry" BRBs.

Based on the conclusions from the section 2.9, three conceptual BRB solutions were proposed, two "conventional" (*type A* and *type B*) and one "dry" (*type C*), as shown in Fig. 3.2. The differences between the proposed BRB solutions relate to the shape of the core cross-section (rectangular or square) and to the conceptual solution adopted for the BRM (concrete-filled steel tube or steel assembly).

Mild carbon steel material (S355) was proposed for all the cores. A rectangular compact-shape cross-section was proposed for the plastic zone of the BRBs of *type A* and *type C*, since most BRB applications use this shape of cross-section. A circular compact-shape cross-section was proposed as an alternative solution for BRBs of *type*

B with the intention to reduce the friction forces between the core and the BRM (by providing a more compact distribution of core material), and to improve low-cycle fatigue resistance of the core by eliminating the corners that a polygonal cross-section has (thus reducing stress concentrations). A smooth transition zone is desired as to reduce the stress concentrations when changing the cross-section shape of the core (from reduced to enlarged), and the risk of a brittle failure mode of the core. As the detail for the transition zone is of critical importance, numerical investigations validated by experimental tests were performed and are presented in section 3.4. A cruciform cross-section is proposed for the elastic zone of the core to provide stability. Therefore, for all BRB typologies the solution of welding stiffeners, perpendicular on the width, at both ends of the core was adopted.

For all BRB typologies an unbonding interface was provided all-around the core to allow for free expansion of the core under compression loading (Poisson's effect). For BRBs of *type A* and *type B* an acrylic self-adhesive tape was proposed to provide the required gap for core expansion. For BRBs of *type C* a waterproofing liquid applied membrane (PWLAM) was proposed since the size of the core-to-BRM gap is not given by the thickness of the unbonding layer, but by the height of the fillers. The PWLAM membrane can be applied using a paint roller which significantly reduces the application time but requires time for drying. Also, PWLAM membrane is considerably cheaper.

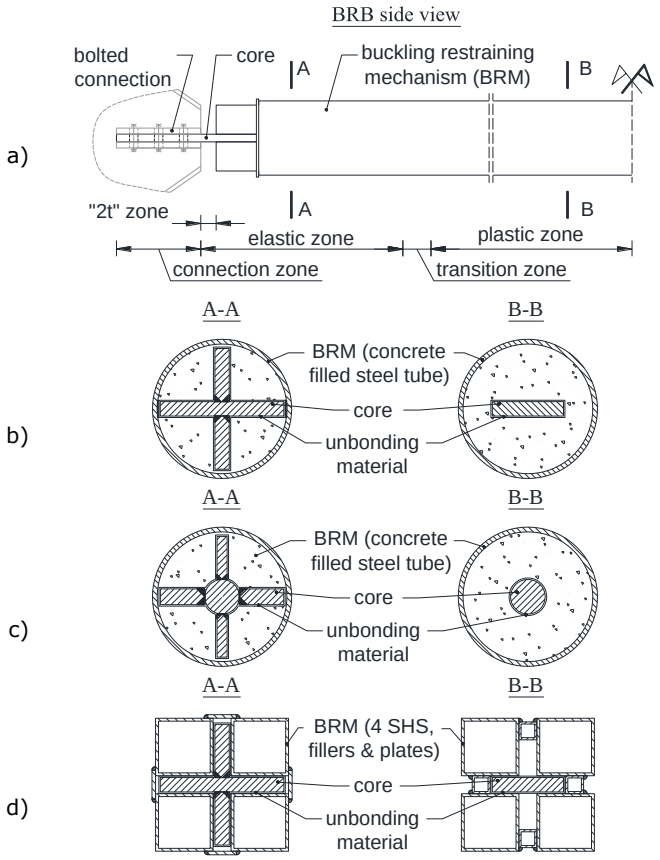

Fig. 3.2. Conceptual BRB solutions: a) general configuration, b) type A, c) type B, d) type C

The buckling restraining mechanism proposed for BRBs of *type A* and *type B* consisted of a concrete filled steel tube; it uses a relatively simple technology but requires concrete pouring and casting, which are time consuming. Centering of the core it required prior concrete pouring to avoid initial geometrical imperfections of the core. Initial imperfections of the core are reduced if using a steel assembly, as in the case of BRBs of *type C*. Therefore, four steel profiles of square hollow section (SHS), fillers and plates were used to form a welded steel-only BRM. The main advantage of this solution is that it eliminates the technological time for concrete pouring and casting. On the other side, it requires significant more welding for assembling the components.

3.3 Connection

BRB-to-gusset bolted connections were proposed due to the fact that this type of connection is feasible for seismic applications due to its redundancy and easy on-field application. Most available bolted connections used by the BRB suppliers are rigid connections; thus, bending moments are transmitted to the BRB ends due to the frame effect (opening and closing of the beam-to-column angle). To limit the end moments, a "2*t*" zone with no stiffeners was proposed based on a similar detail recommended by AISC 341-10 [100] in the case of conventional brace-to-gusset connection for out-of-plane buckling (Fig. 3.3). Limiting the end moments to the plastic moment of the cross-section of the "2*t*" zone significantly reduces the rotation demands on the BRB ends. As shown in [1], these rotation demands might cause the BRM or the elastic zone of the core to yield, thus increasing the risk of a failure mode by global buckling of the BRB. In a parallel study Dehghani [103] used a similar BRB-to-gusset connection detail and successful results in limiting the flexural demands were reported. For the proposed conceptual BRB solutions, the length of the unstiffened "2*t*" zone is twice the thickness *t* of the core in this zone (Fig. 3.2.a). Slotted gussets with welded plates were proposed to reduce the length of connection zone and, consequently, to reduce the strain levels in the plastic zone of the core. Numerical investigations were performed on the upper gusset-connection assembly in order to validate the proposed technical solution (Fig. 3.4.a). The final connection details are schematically presented in Fig. 3.4.b.

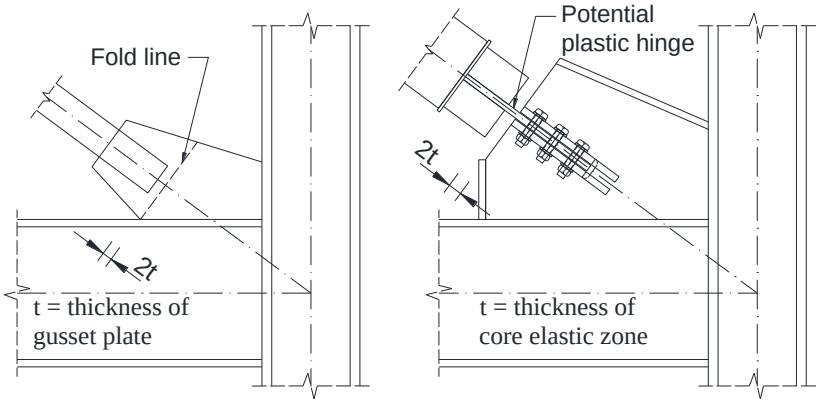

Fig. 3.3. Brace-to-gusset connection details: a) AISC requirement [100], b) proposal [6]

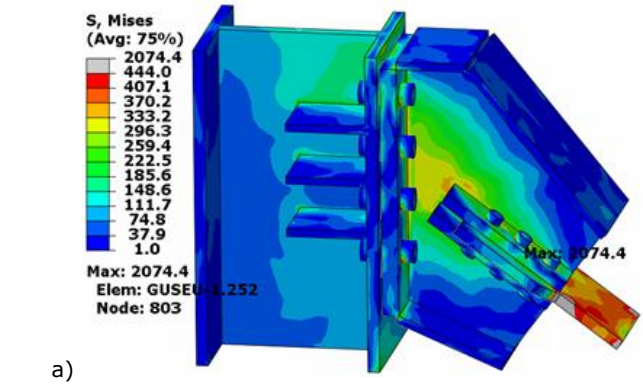

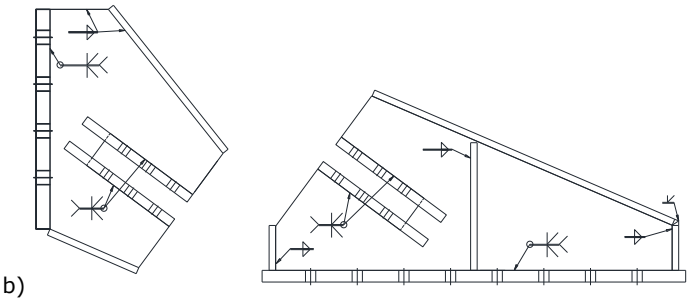

Fig. 3.4. Gusset-connection assembly: a) FEM simulation, b) details [6]

3.4 Transition zone

The transition zone is of critical importance in assuring a stress flow without (significant) concentrations when changing from the reduced to the enlarged cross-section zones of the core. Several causes might lead to stress concentrations in the transition zone: sudden change in the axial stiffness which attracts larger axial forces, manufacturing defects (cuts/copes), residual stresses caused by the technological process (plate cutting, welding of components). The stress concentrations cause localization of plastic deformations, which may decrease the low-cycle fatigue resistance of the BRB and increase the risk of a brittle failure mode by premature core fracture. Therefore, the detailing of the transition zone for the proposed technical BRB solutions was numerically investigated and validated by experimental results.

To obtain the bone-shape longitudinal variation for the proposed core cross-sections (rectangular and circular), two technological solutions were analysed [70]:

- by machine cutting from a steel plate, applicable to BRBs of *type A* and *type C*.
- by using a rectangular or round hot-rolled profile with stiffeners welded at the ends, applicable to BRBs of *type A*, *type B* and *type C*.

In the first step of the investigation, numerical analyses were performed in Abaqus finite elements software [104] on three-dimensional models using a simplified geometry of the core, see presented in Fig. 3.5.a-d. The residual stresses caused by the technological processes were not modelled in Abaqus, and therefore only the influence of the geometrical configuration of the core with respect to the stress concentration phenomenon was analysed. Several concepts were investigated to evaluate the susceptibility to brittle fracture of the transition zone and of the plastic

zone close to it. In a simplified way, the assessment was done in terms of maximum stresses and equivalent plastic strains. The following conceptual solutions for the transition zone were analysed [70]:

- *concept 1*: steel core obtained by machine cutting of a steel plate, using fillet radius to reduce the stress concentrations (Fig. 3.5.a).
- *concept 2*: steel core obtained by welding four stiffeners at the ends of a rectangular steel profile (Fig. 3.5.b).
- *concept 3*: steel core obtained by welding four stiffeners at the ends of a round steel profile (Fig. 3.5.c).
- *concept 4*: similar to *concept 3*, except that the four stiffeners were substituted by a circular "stiffener" (Fig. 3.5.d).

All the parts of the transition zone concepts were considered as being made of a S355 steel. In Abaqus, an isotropic hardening material model was used to define the plastic behaviour. True stress-strain relation was introduced in Abaqus, based on the following engineering properties: the nominal yield and ultimate strength were considered $f_{y,n}$ = 355 N/mm^2 and $f_{u,n}$ = 510 N/mm^2, respectively; the material overstrength factor was considered γ_{ov} = 1.25; the expected yield and ultimate strength were determined as $f_y = \gamma_{ov} \cdot f_{y,n}$ = 444 N/mm^2 and $f_u = \gamma_{ov} \cdot f_{u,n}$ = 638 N/mm^2, respectively; the strain corresponding to ultimate stress was set to ε_u = 0.015 [70].

The numerical analyses were performed using the "Dynamic Implicit" procedure available in Abaqus. Quasi-static force-controlled analyses were performed on all the finite element models. The force, F, was applied at the free-end of the model, increasing monotonically up to the value of 95% of the tensile resistance of the cross-section of the core ($0.95 \cdot f_u \cdot A_p$, where A_p is the area of the cross-section of the plastic zone). A fine mesh was adopted for the transition zone (mesh size 2 mm). 8-node linear brick finite elements with incompatible modes, C3D8I, and 6-node linear triangular prism, C3D6, finite elements were used for the discretization. The boundary conditions used are presented in Fig. 3.5.e: for the enlarged end section a fix support

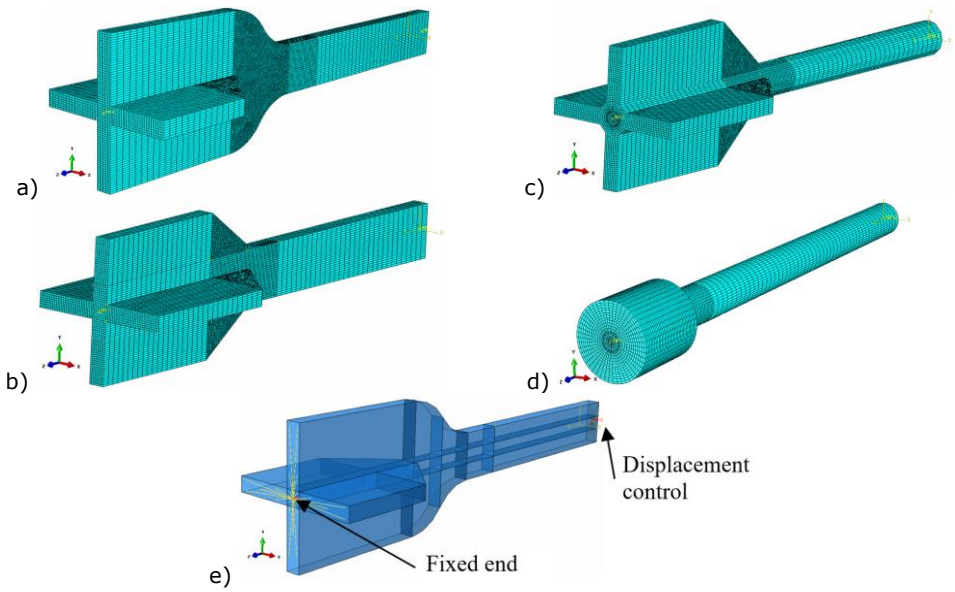

Fig. 3.5. Discretization of investigated transition zones: a) *concept 1*, b) *concept 2*, c) *concept 3*, d) *concept 4*; e) Common boundary conditions

was assigned, for the reduced end section a roller support was assigned to allow the free movement of the core in the longitudinal direction [70].

Fig. 3.6 shows the distribution of the von Misses stresses (σ_M) and the equivalent plastic strains (*PEEQ*) in the four models, while Table 3.1 summarizes the peak *PEEQ* values in the transition zone and in the plastic zone of the core. Sensitivity of the model to brittle fracture was associated with large values of *PEEQ* [70].

It can be observed that in the case of *concept 1* there is a gradual transition of stresses from the reduced to the enlarged cross-section, *PEEQ* in the core being the smallest among the four models (9.24 %). Due to the fact that the stiffeners are positioned in the elastic zone and the transition zone is smooth, there is no susceptibility to brittle failure.

For the *concept 2*, stress concentrations can be observed in the core at the base of the stiffeners, which correspond to *PEEQ* values of 20.5 %, more than twice the value recorded for *concept 1*. On the other hand, in the transition zone the *PEEQ* values are slightly smaller than the ones in the case of *concept 1* (7.82 %).

In the case of *concept 3*, stress concentrations in the core occur in a similar manner to *concept 2*, but the *PEEQ* values are significantly smaller (13.49 %). Smaller demands are also noticed in the transition zone of this model (4.73 %).

In the case of *concept 4,* the stress concentrations in the core are slightly reduced with respect to *concept 3* (*PEEQ* = 11.06 %), while in the transition zone the *PEEQ* values are almost the same (4.28 %). This solution is however rather theoretical, as it has difficulties in being adopted as a transition zone for the core.

Concept 1 clearly represents the best solution in terms of minimising the risk of brittle fracture in the core, close to the transition zone. *Concepts 2* (stiffeners welded to slender plates) is to be avoided as it is susceptible to brittle failure. *Concept 3* provides reasonable alternative to *concept 1* when it is desired to optimize the costs by reducing the machining and using instead stiffeners welded to a compact as-rolled core.

Based on these numerical results it was found that *concept 1* and *concept 3* are the optimal solutions for the transition zone. To validate their performance under cyclic loading, experimental tests were performed on reduced length specimens, as presented in Fig. 3.7. Two specimens were designed using *concept 1* as detail for the transition zone, see Fig. 3.7.a. The specimens were manufactured using different technologies for obtaining the core: laser cutting or milling. This parametric study aimed at assessing the influence of the manufacturing process of the core on the cyclic performance of the BRBs (reduced-length specimens): thermal (laser cutting) versus mechanical process (milling). Almost similar cyclic responses were obtained for the two specimens, with a slightly higher resistance for the specimen that used laser cutting technology. Both specimens had a ductile failure mode without premature initiation of cracks.

To validate *concept 3* as the detail for the transition zone two reduced-length specimens were designed, as presented in Fig. 3.7.b. Each specimen was assembled using welds of different strength: normal-strength weld (NS-weld) and high-strength weld (HS-weld). Almost similar cyclic responses were obtained, with the specimen assembled using high-strength welds having a slightly larger plastic resistance. Both specimens had a ductile failure mode even though premature initiation of cracks was noticed at the base of the welds, close to the plastic zone. Based on the successful experimental results obtained, further enhancement of the technical solution of *concept 3* was proposed: the core to be made of a square profile with the welded stiffeners positioned on the corners as to eliminate the milling of stiffeners. It was assumed that similar results would be obtained.

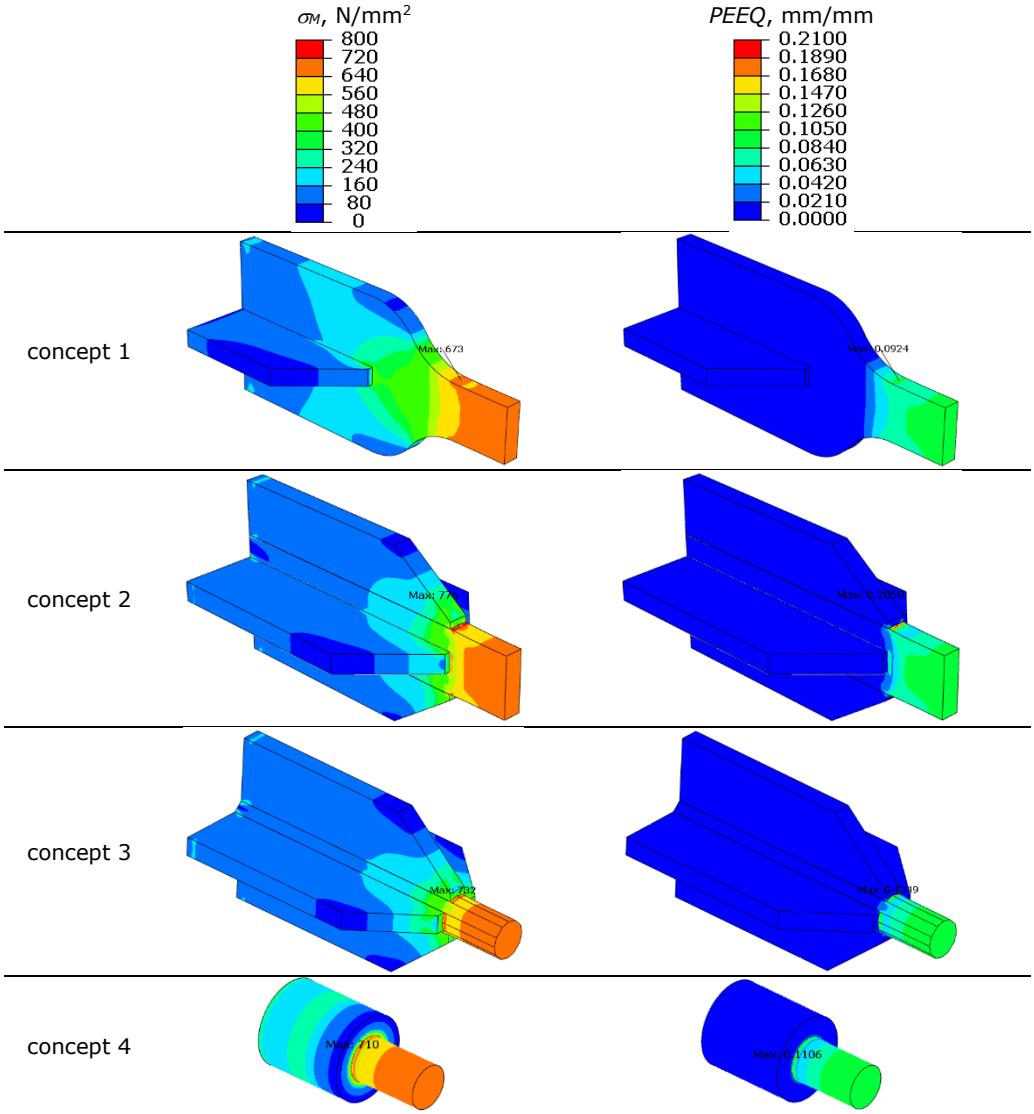

Fig. 3.6. FEM results of different transition zone concepts

Table 3.1 Evaluation of the performance of different transition zone concepts

Concept	Concept description	PEEQ in the transition zone [%]	PEEQ in the core [%]
1	machined plate & 2 stiffeners	9.24	9.24
2	rectangular profile & 4 stiffeners	7.82	20.50
3	round profile & 4 stiffeners	4.73	13.49
4	round profile & 1 CHS stiffener	4.28	11.06

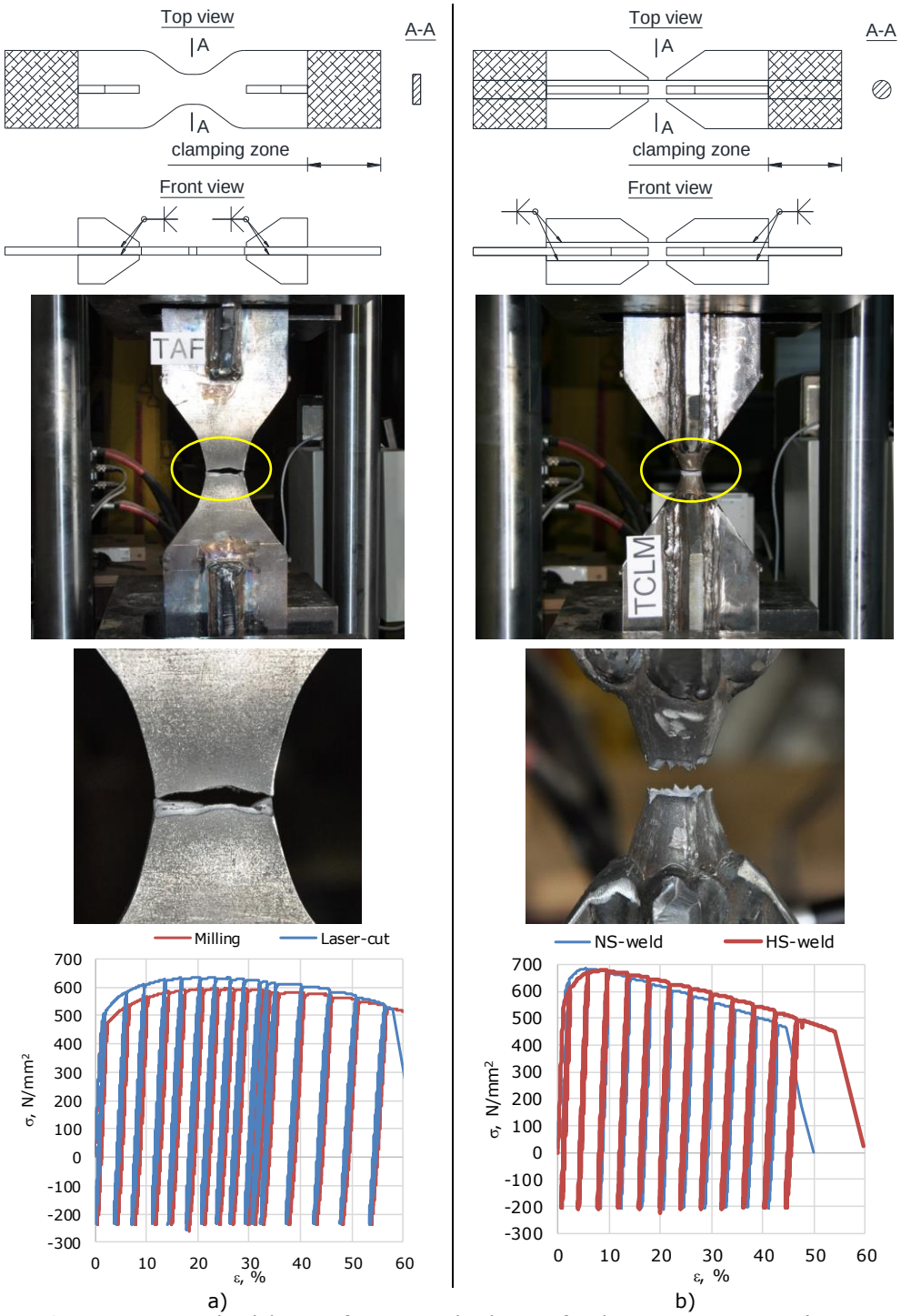

Fig. 3.7. Experimental validation of conceptual solutions for the transition zone: a) *concept 1*, b) *concept 3*

3.5 Pre-test numerical simulations on BRBs

3.5.1 Solutions investigated

Using the numerical and experimental results obtained from the investigation of the transition zone (see section 3.4), the conceptual BRB solutions proposed for the pre-test numerical simulations in view of evaluation of their cyclic performance are presented in Fig. 3.8. To provide a reference for the development of different core geometries, the length of the core (L_{BRB}) was kept fixed for all BRB solutions, while the length of the BRM, L_{BRM}, varied among the models. The investigated BRB solutions are briefly described below:

- *Type A* – "conventional" BRB, consisting of a rectangular steel core wrapped with acrylic self-adhesive tape (on the length L_{BRM}) and introduced into a concrete-filled circular steel tube (Fig. 3.8.a). The core is obtained by milling of a steel plate and the smoothness of the transition zone is assured by using fillet radius. Two stiffeners (positioned at the end of the transition zone) are welded perpendicular to the width of the core for stability of the elastic zone. Gaps (polystyrene foam) are provided in extension of the transition zones and stiffeners to allow for free movement of the core under compression loading.
- *Type B* – "conventional" BRB, with a similar BRM as in the case of BRBs of *type A*, but with the core obtained by welding core-extension plates at each end of a square hot-rolled steel profile (Fig. 3.8.b). The smoothness of the transition zone is assured by chamfered cuts in the core-extension plates. Two chamfered

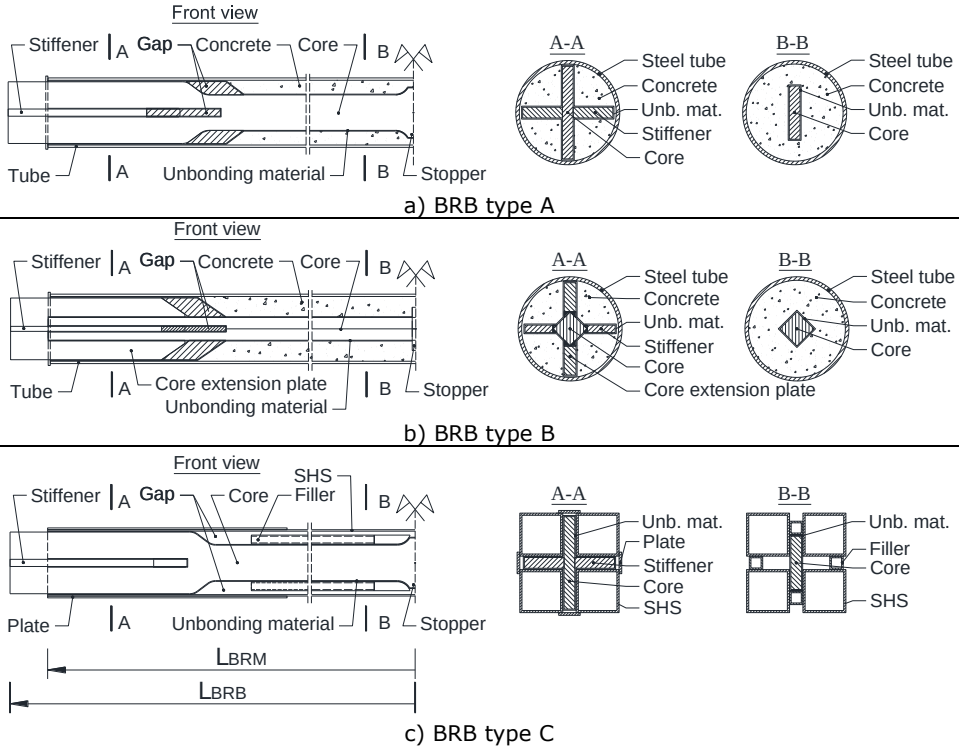

a) BRB type A

b) BRB type B

c) BRB type C

Fig. 3.8. BRB solutions used in pre-test numerical simulations: front views, cross-sections

stiffeners (positioned at the beginning of the transition zone) are welded perpendicular to the width of the core-extension plate for stability of the elastic zone. Acrylic self-adhesive tape and gaps (polystyrene foam) are also provided, similar to BRB *type A*.

- *Type C* – "dry" BRB, consisting of a steel core of similar configuration as in the case of BRB of *type A*, and steel assembly acting as BRM (Fig. 3.8.c). PWLAM membrane is applied on the core, on the length L_{BRM}. The height of the fillers assures the required core-to-BRM gap. Gaps (air) are provided in extension of the transition zones and stiffeners.

3.5.2 Calibration of FEM model

The pre-evaluation of the proposed BRB solutions involved finite element numerical simulations, performed in Abaqus computer program [104]. The numerical FEM model adopted was calibrated against experimental data available in [31]. The calibration had the purpose of providing information on specific input parameters (vertical and horizontal core to concrete gap, contact law definition, value of the friction coefficient) that are necessary for modelling the BRBs. Using the BRB's geometry from [31], a finite element model was constructed, see Fig. 3.9.a [105].

All the components (steel core, infilled concrete, steel casing) were directly modelled using 3D finite elements, except for the unbonding layer which was modelled using a small gap (through thickness direction, 1 mm; through width direction 0.2 mm) and a contact law (normal behaviour set as "hard" contact, tangential behaviour set to "penalty" with the friction coefficient set to 0.1). Due to the complex nonlinearity and type of loading (cyclic) the Dynamic Explicit solver was used. To reduce the dynamic effects, a mass scaling factor equal to 0.0001 and a time of 79 s were used, assuring the quasi-static application of the load.

To predict a proper spatial stress state, all the components were modelled with three-dimensional deformable solid elements. The discretization was performed using C3D8I finite elements. This type of finite element was used in order to prevent shear locking and hourglass effects that can appear when using first order finite elements (e.g. 8-node first order elements with full (C3D8), of reduced (C3D8R) integration) loaded in bending. Partitions were done to allow for a structural discretization of the parts.

Several material models were used for the BRB components. The buckling restraining mechanism (concrete filled steel tube) was modelled using elastic material

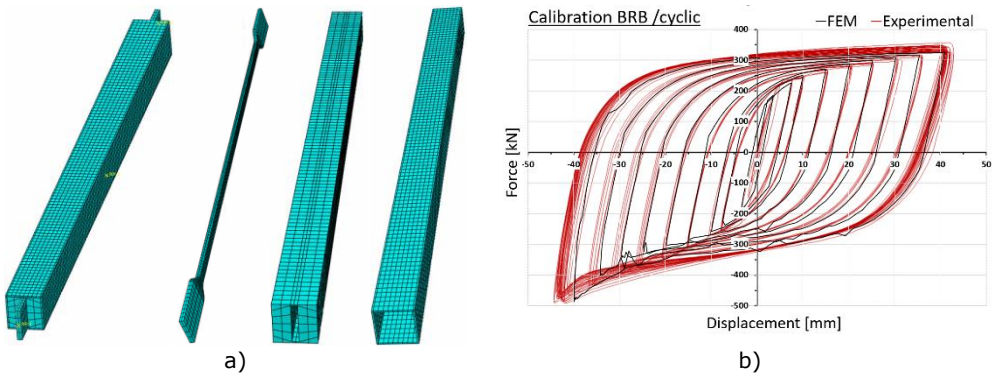

a) b)

Fig. 3.9. Calibration of BRB model used for pre-test simulations: a) numerical model, b) calibrated cyclic response

models. Therefore, the elastic moduli (E), the Poisson's coefficients (ν), and the density of materials (ρ) were needed. The following values were used to define the concrete behaviour: E_c = 21000 N/mm^2, ν = 0,18, ρ =2.5 E- 9 tonne/mm^3; while the steel behaviour was defined by: E_s = 210000 N/mm^2, ν =0.3, ρ = 7.85E-9 tonne/mm^3. The material associated with the dissipative core was chosen with respect to the type of loading that was applied: monotonic or cyclic. For the case of monotonic loading, isotropic hardening plastic model [104] was used, based on Hubert von Mises yield criterion (f_y = 282 N/mm^2, f_u = 510 N/mm^2, f_r = 490 N/mm^2, where f_y, f_u, f_r are the engineering values of the yield, ultimate and rupture stress, respectively). In the case of cyclic loading, the combined isotropic-kinematic hardening plasticity model [104] was used, which consists of a nonlinear kinematic and a nonlinear isotropic component. The nonlinear kinematic component was defined using five backstresses, each backstress being defined by two parameters, the plastic hardening modulus, C_k, and its corresponding decreasing rate, γ_k. The following kinematic parameters were used: C_1 = 25000 N/mm^2, γ_1 = 500, C_2 = 21000 N/mm^2, γ_2 = 375, C_3 = 5950 N/mm^2, γ_3 = 120, C_4 =935 N/mm^2, γ_4 = 25, C_5 = 300 N/mm^2, γ_5 = 0. The nonlinear isotropic component was defined by two parameters, the maximum increase in size of the yield surface, $Q_{infinity}$= 60 N/mm^2, and its corresponding rate of hardening, b = 4.

A general contact of type "all with self" was defined using a friction coefficient equal to 0.1 to account for the friction forces that may take place between the exterior surface of the core and the interior surface of the concrete. A "tie" constraint was defined between the exterior surface of the concrete and the interior surface of the steel casing. Fixed boundary conditions were defined at the ends of the steel core. The load was applied as a displacement controlled, using the "smooth step" method.

After performing the analyses, a good correlation between the experimental and the numerical results was observed. The numerical model was able to capture all the main characteristics of the tested BRB: initial elastic stiffness, yield stress and displacement, strain hardening, the energy dissipated. The comparison between experimental and numerical results is presented in Fig. 3.9.b [105].

3.5.3 "Conventional" BRBs

3.5.3.1 Finite element model

The pre-test numerical simulations on BRBs were performed using some of the information obtained from the calibration tests (friction coefficient 0.1, gap 1 mm, finite element type C3D8I, contact laws, material definition approaches). Different types of solvers were preliminarily used in order to establish the proper one to be used for the entire pre-testing program. Static General, Dynamic Implicit (quasi-static) and Dynamic Explicit were initially used. Due to the complex nonlinearity (material, geometry, contact laws) the first two solvers took a large amount of computational time. Therefore, the Dynamic Explicit solver was used with similar results as in the case of implicit solvers. To validate the results, the output energies were compared assuring that a quasi-static analysis is being performed: artificial strain energy and kinetic energy were kept to a minimum (less than 1%) when comparing to internal energy and external work. It must be mentioned that mass scaling was used, with a target increment of 5E-5 [105].

The finite element model used to simulate the "conventional" BRBs of *type A* and *type B* consists of three parts (steel core, concrete, steel tube with end-caps), gaps (transversal and longitudinal) and interactions between parts. The core was modelled using C3D8I finite element type, with a size of 10 mm for the plastic zone and 20 mm for the elastic zone. Several C3D6 elements were used for the transition

zones to facilitate the mesh propagation. The unbonding interface was modelled using a core–to–concrete gap and a contact law. The concrete part was modelled using C3D8R elements due to its less significant contribution to the global behaviour of the BRB. The tube including the end-caps were modelled using shell elements, S4R, with five integration points per thickness. Gaps are placed in the extension of the transition zones and stiffeners to allow for free movement of the core in compression. The assembly, the independent discretized constitutive parts and the longitudinal gaps are presented in Fig. 3.10.a-e [105].

The interactions are very important when modelling BRBs. Therefore, a general contact was defined with the contact domain consisting of two selected surface pairs that were assigned different contact properties, as follows: the core–to–concrete interaction was defined as having the tangential behaviour defined as "penalty" with a friction coefficient of 0.1 and the normal behaviour set to "hard" contact; the concrete–to-steel casing interaction had the same properties except the friction coefficient which was set to 0.4 to account for the partial composite behaviour. A coupling constraint was defined at each end of the core by connecting a reference point to a surface using the "continuum distributing" coupling type, allowing for free transversal deformation of the selected surface [105].

To include initial geometrical imperfections into the numerical model, a previous buckling analysis was performed. The two contact pairs were redefined as "tie" constraints as to obtain a deformed shape of all the BRB components (core and BRM). The first buckling mode was scaled to the length of the BRM divided by 1000, $L_{BRM}/1000$ = 3.7 mm, and then used as "Imperfection" for the main model [105].

The BRB model was considered pinned at both ends. The load was applied in displacement control, as shown in Fig. 3.10.f.

Both simple (linear elastic) and complex (linear elastic and nonlinear plastic) material models were used for the BRB components, depending on their influence on the response of the BRB. For the concrete part, just the elastic behaviour definition was assigned, using the following parameters: E_c = 29108 N/mm^2, ν = 0.2, ρ = 2.5E - 9 tonnes/mm^3. Plastic behaviour was also used within preliminary analyses, but no difference in the BRB response was noticed, just an increased in computational time (and convergence problems), therefore only the elastic definition was further used.

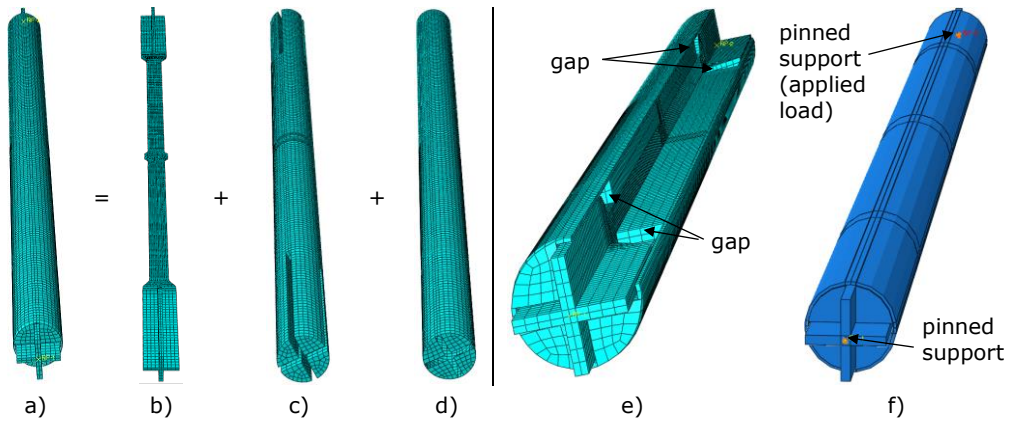

Fig. 3.10. Finite element model of "conventional" BRB: a) assembly, b) core, c) concrete, d) tube, e) longitudinal gaps, f) boundary conditions

The steel tube and the core were modelled using the same material model, with both elastic and plastic components. The plasticity was simulated using the combined isotropic-kinematic hardening model. It consists of a linear/nonlinear kinematic component and a multilinear (tabular data)/nonlinear (exponential law) isotropic component. A very good prediction of the steel behaviour can be obtained with this model for both monotonic and cyclic analyses. Due to the fact that in [31] the steel material (S235 JR) used to manufacture the core was different than the one (S355) proposed for the technical BRB solutions, another reference was used for the calibration of the material parameters [106]. The calibration procedure described in [104] was used. The input parameters for the kinematic hardening component were determined using the "Stabilized" data type option. Yield stress–plastic strain data pairs were introduced, and five backstresses were requested for better prediction. Small adjustments of the input parameters (generated by Abaqus) were necessary for finer prediction of the kinematic behaviour. For the isotropic behaviour, a multilinear isotropic softening (up to the end of plateau) followed by isotropic hardening was obtained following the calibration methodology from [104]. The use of softening was necessary to obtain the yield plateau. The calibrated tensile monotonic and cyclic stress-strain responses are presented in Fig. 3.11.a-b.

For the evaluation of the proposed technical BRB solutions, the calibrated parameters defining the initial size and the evolution of the yield surface were scaled up as to provide an initial yield stress at zero plastic strain (σ^0) of 444 N/mm^2. The input curve of the isotropic behaviour is presented in Fig. 3.12. The following parameters were used to define the kinematic hardening component: σ^0 = 444 N/mm^2, C_1 = 18518 N/mm^2, γ_1 = 954, C_2 = 13855 N/mm^2, γ_2 = 184, C_3 = 966.2 N/mm^2, γ_3 = 15, C_4 =480 N/mm^2, γ_4 = 4, C_5 = 200 N/mm^2, γ_5 = 0.1.

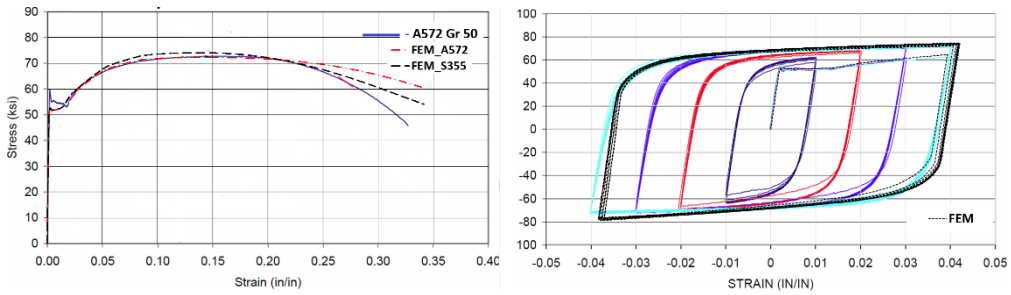

a) b)

Fig. 3.11. Calibration of material model for a) monotonic and b) cyclic loading

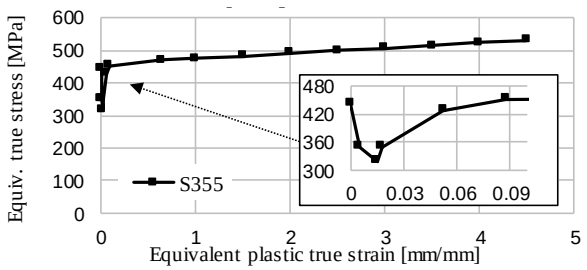

Fig. 3.12. Input curve of the isotropic component used in pre-tests simulations

3.5.3.2 Finite element analyses

In the first phase of the pre-testing program, numerical simulations were performed on four BRB models to determine the cyclic loading protocol that fulfils both requirements within AISC 341-10 [100] regarding to prequalification of BRBs. The requirements are expressed as minimum values of the design story drift (greater than 1%) and the cumulative inelastic deformation capacity (CID, greater than 200 time the yield displacement). The four models used for this investigation were corresponding to the BRB of *type A* (rectangular core) and were similar except for the amplitudes of the loading protocol function. The AISC 341-10 [100] cyclic loading protocol that was used is presented in Fig. 3.13. The criterion for determining the amplitudes was expressed as the maximum value for the axial strain developed by the plastic zone of the core. Based on this criterion and considering the notations from Fig. 3.13, Δ_{by} represents the displacement corresponding to the yielding of the core (Δ_{by} obtained from a monotonic tensile analysis on BRB), while Δ_{bm} represents the displacement corresponding to the design story drift (in this case considered as a function of core strain, $\Delta_{bm} = \varepsilon_c \cdot L_p$, where ε_c is the strain level in the plastic zone of the core, and L_p is the length of the plastic zone of the core). Four protocols corresponding to 3.5%, 3.0%, 2.75%, 2.5% demand core strain were used. Only the last two protocols were completed by the BRB models without premature failure. The protocol corresponding to 2.75% core strain was declared as the upper limit of allowed demand to be used with the following experimental tests. The results are summarized in Table 3.2. The cyclic response expressed as axial force (N) – displacement (D) is presented in Fig. 3.14 [105].

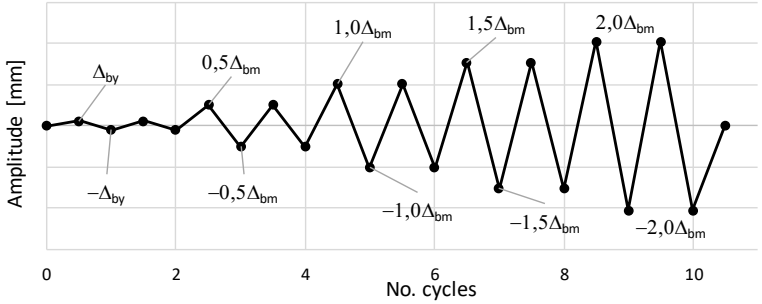

Fig. 3.13. Loading protocol used for pre-test numerical simulations on BRBs

Table 3.2 Cyclic performance BRB models at different levels of axial core strain

Model	CID	CID/Δ_{by}	Status
LP.eps.2.50%	2224	344	completed
LP.eps.2.75%	2467	381	completed
LP.eps.3.00%	2710	419	fractured
LP.eps.3.50%	3196	494	fractured

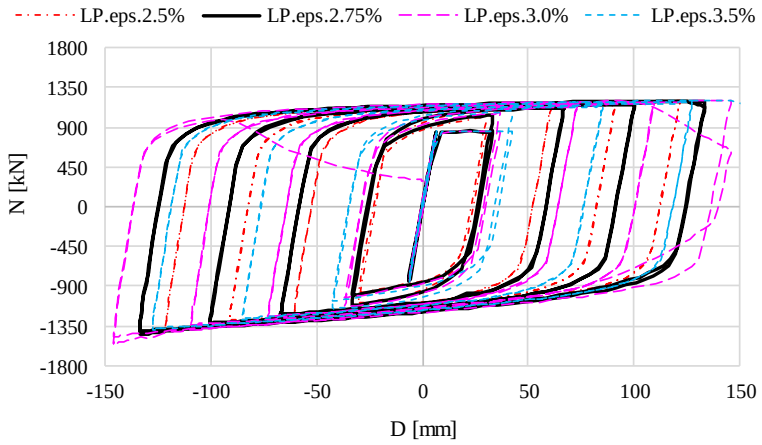

Fig. 3.14. Cyclic response of BRB models at different levels of axial core strain

To investigate the uniaxial response and assess the performance of the BRB models under monotonic and cyclic loading, a parametric study was performed on three similar models corresponding to the BRB of *type A*. The uniaxial response for monotonic tension/compression and cyclic loading is presented in Fig. 3.15. Several aspects can be noticed as follows. The yield force was about 878 kN corresponding to a displacement of (Δ_{by} =) 6.47 mm. A 2.2% difference was noticed between the maximum tension force when monotonically loaded, $T_{max,T}$ = 1176 kN, and the maximum tension force for cyclic loading, $T_{max,Cyc}$ = 1202 kN. Due to the cyclic loading effect (accumulated plastic deformations), the failure of the specimens took place at different displacement ranges, i.e. for the monotonic case, the BRB was able to develop a displacement range of 310.06 mm before failure, but when cyclically loaded, just 272.6 mm were achieved (from $-\Delta_{bm}$ to $+\Delta_{bm}$). The difference is about 13.7%, with respect to the monotonic case [105].

The influence of the shape of the cross-section of the core in the plastic zone, rectangular vs. square, was numerically investigated by running cyclic analyses and assessing the cyclic performance of two BRB models in terms of compression strength

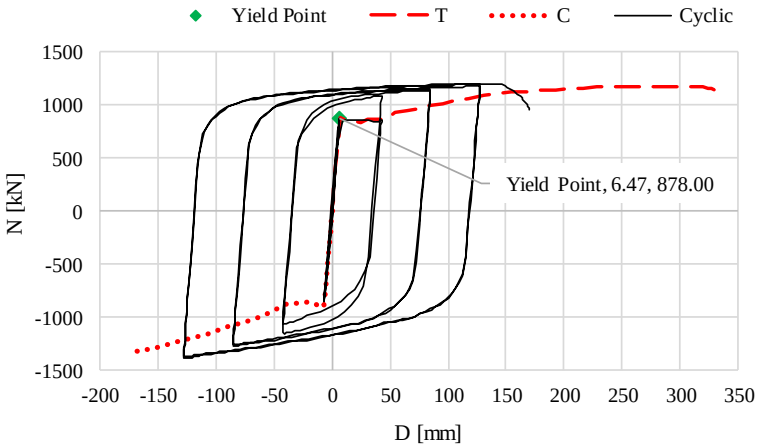

Fig. 3.15. Uniaxial response of BRB models to monotonic and cyclic loadings

adjustment factor (β) and equivalent (cumulative) plastic strain (*PEEQ*). The model with square-core performed slightly better in terms of β factor, with β = 1.13 compared to the rectangular-core model with β = 1.16. The plastic zone of square-core model is slightly larger than the one of the rectangular-core model, this allowing to undergo slightly larger amplitudes successfully (the amplitudes of the loading protocol are a function of L_p, Δ_{bm} = 3.5%·L_p). Also, the square-core model proved to possess a slightly larger ductility capacity, as can be noticed from Fig. 3.16. The difference between the two models was more visible when analyzing the maximum *PEEQ* values (Fig. 3.17): for the rectangular-core model the value of $PEEQ_{max}$ = 1.723 was 30% higher than in the case of square-core model ($PEEQ_{max}$ = 1.334). This aspect would lead to a lower low cycle fatigue resistance for the rectangular-core model in comparison with the square-core model. For both models, the failure mode was a ductile one by rupture of the core in tension, near the stopper [70]. Based on these comparative results it can be concluded that the proposed core shapes for the plastic zone of the core proved to be reliable technical solutions for the BRBs.

A parameter of critical importance in assuring a quasi-symmetric cyclic response of the BRB is the thickness of the unbonding material. Therefore, the value of the core–to–BRM gap sizes for the through-thickness direction (g_t) and the through-

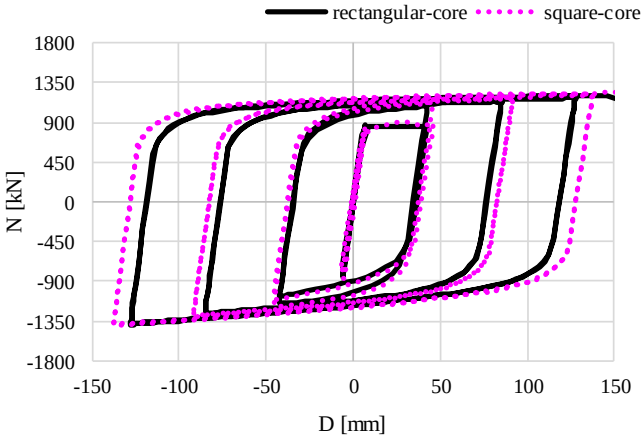

Fig. 3.16. The influence of core shape

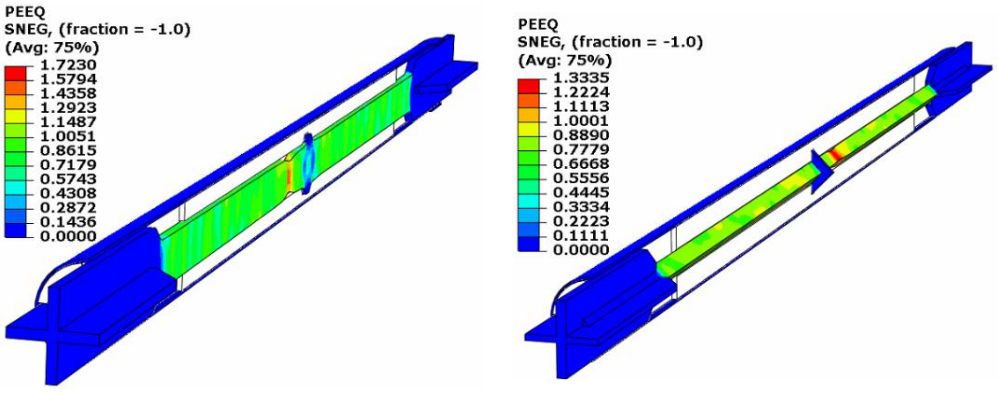

a) b)

Fig. 3.17. Distribution of *PEEQ*: a) rectangular-core model, b) square-core models

width direction (g_w) was studied in view of optimization. A friction coefficient of 0.1 was used for the core-to-concrete interaction. The influence of the gap layout was analysed on rectangular-core models with respect to the β factor. The lowest β value (1.16) was obtained for the g_t = 1 mm and g_w = 2 mm (model g.1&2). For the models heaving a uniform gap of 1 mm (g.1) and 2 mm (g.2), values of β = 1.43 and β = 1.38, respectively were obtained. According to P100-1/2013 [5] and AISC 341-10 [100] regulations, the value of β should be greater than 1 and less than 1.3. Therefore, only the model g.1&2 fulfilled the code requirements (Fig. 3.18). It must be mentioned that to a FEM gap equal to 1 mm / 2 mm corresponded a real gap of 2 mm / 3 mm, respectively. Based on those observations, the BRBs equipped with rectangular cores were designed with different values for the gaps (greater value for g_w). BRBs with square cores were provided with a uniform gap of 2 mm [70].

The optimization of the unbonding interface involved also numerical studies on the value of the friction coefficient assigned to the core-to-BRM interaction. Considering the previous BRB model with the optimal gap configuration (rectangular-core with g_t = 1 mm and g_w = 2 mm), a parametric study was performed by using

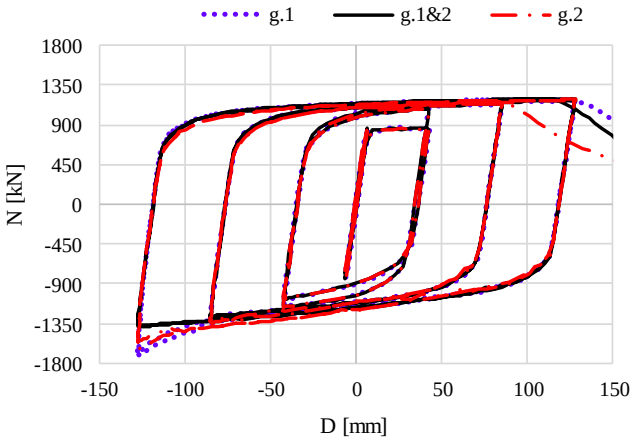

Fig. 3.18. Influence of core-to-BRM gap size

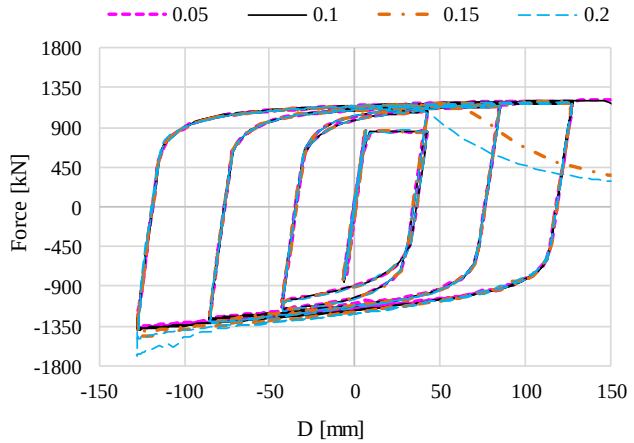

Fig. 3.19. Influence of friction coefficient value

different values for the friction coefficient: 0.05, 0.1, 0.15, 0.2. Based on the cyclic response of the models presented in Fig. 3.19 it was concluded that the value of the friction coefficient has a large influence on the behavior of the BRB. The value of the β factor increased considerably when using higher value for the fiction coefficient. As expected, the lowest value for β = 1.13 was obtained for the case of 0.05 friction, and the highest value, β = 1.41, for the case of 0.2 friction. The model with the friction coefficient equal to 0.2 cannot be qualified according to P100-1/2013 [5] and AISC 341-10 [100] since β factor is larger than the upper qualification limit (1.3). There was also noticed that the higher the friction, the less accumulated plastic deformation capacity [105].

A parametric study was performed to evaluate the required strength of the buckling restraining mechanism (BRM) as to assure a stable global response of the BRB. According to Watanabe et al. [20] the BRM should be designed for a value of the ratio between the nominal resistance of the core (N_p) and the critical elastic axial load of the buckling-restraining mechanism (N_{cr}) equal to N_{cr}/N_p = 1.5. However, in practice design ratios of N_{cr}/N_p = 3 were used by Black et al. [66]. Therefore, for this investigation two BRB models having BRMs of different strength were used. Both models were BRBs of *type A*. For the first model the BRM was designed for N_{cr}/N_p = 1.5, while for the second model a ratios of N_{cr}/N_p = 3 was used. The numerical analyses revealed that the critical elastic axial load of BRM had a small influence from the β factor point of view; a small difference (2.58 %) was noticed when comparing the results from the model with N_{cr}/N_p = 3 (β = 1.16) with the results from the model with N_{cr}/N_p = 1.5 (β = 1.19), see Fig. 3.20. The global behavior of the BRB was also investigated with respect to maximum lateral deformation of the BRM under maximum compression force. Even though for model with N_{cr}/N_p = 1.5 a lateral deformation of 23.73 mm of the BRM was recorded (at the mid-length), compared to 8.71 mm of the model with N_{cr}/N_p = 3, both steel tubes remained in the elastic domain (Fig. 3.21). Also, both models had a ductile failure mode by rupture of the core in tension [70]. Based on these results, a ratio of N_{cr}/N_p = 3 was recommended to be used for the development of the other BRB solutions.

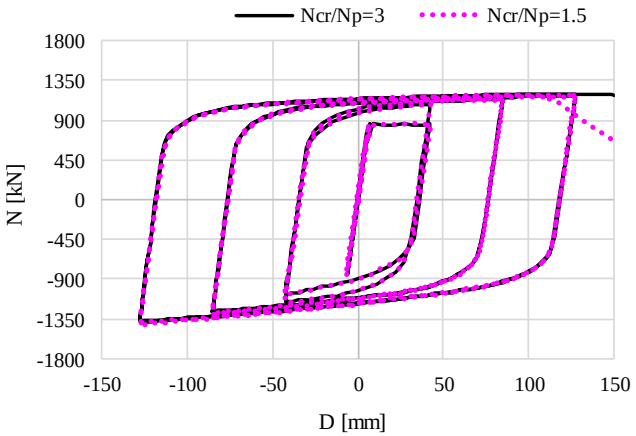

Fig. 3.20. Cyclic response of BRB models having the BRMs of different strength

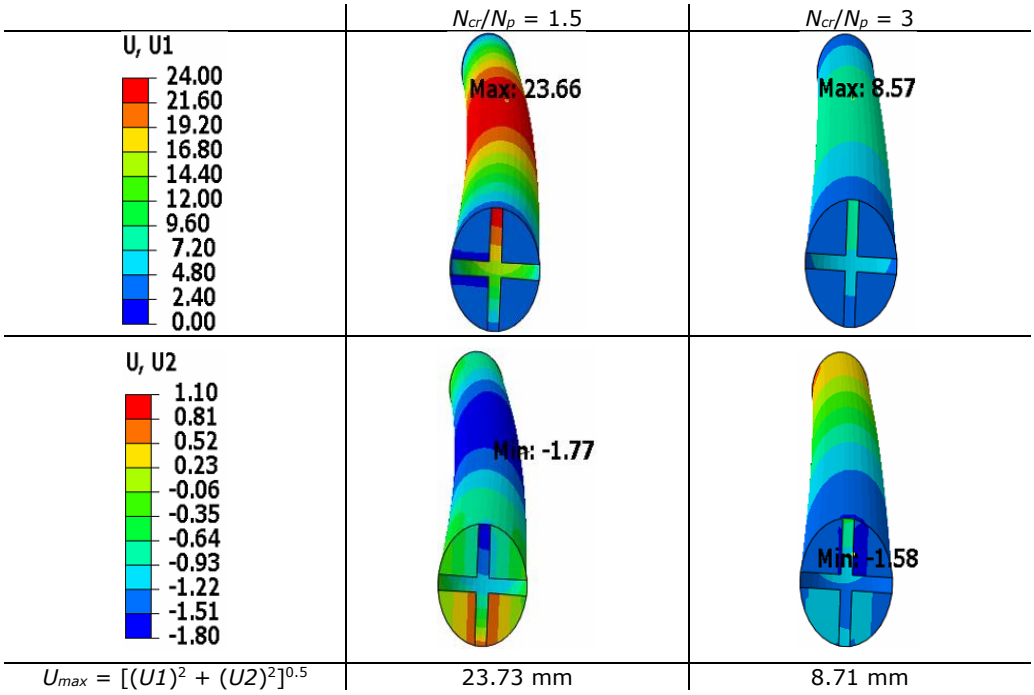

Fig. 3.21. Maximum mid-span deformation of BRMs of different strength

3.5.4 "Dry" BRBs

3.5.4.1 Finite element model

"Dry" BRBs were modelled similarly to "conventional" ones. Parts with thin walls (tubes) were modelled using S4R shell elements, and C3D8I elements were used to model parts made of thick plates (core, stiffeners), see Fig. 3.22.a-c. Longitudinal gaps for free movement of the core in compression and pinned supports were also similarly provided (Fig. 3.22.e-f). "Tie" constraints between edge-pairs were used to simulate the welds. The demand was to provide a lighter BRM, made of steel parts only, robust enough to withstand global buckling [70].

3.5.4.2 Finite element analyses

Cyclic analyses were performed using displacement control loading procedure.

Even though the initial solution of the BRM made of four SHS welded together globally fulfilled the requirements, locally, instead, it did not perform well up to the maximum compression capacity of the BRB due to local damage of the thin walls of the SHS profiles. The same phenomenon was notices for both capacity cases, 700 kN and 300 kN (Fig. 3.23.a and Fig. 3.23.b) [70].

Strengthening of the BRM was performed for each BRB capacity. The performance of the strengthened BRMs was evaluated by analyzing the cyclic response of the BRB and by evaluating the stress and deformation state of the BRM. Several solutions were analyzed, and the optimal configurations are presented below.

In the case of the 700 kN BRB, additional steel plates were placed on the sides of the core, with stiffened slotted ends. "Tie" constraints simulated the fillet welds used to assemble the additional components. The new BRM configuration proved to

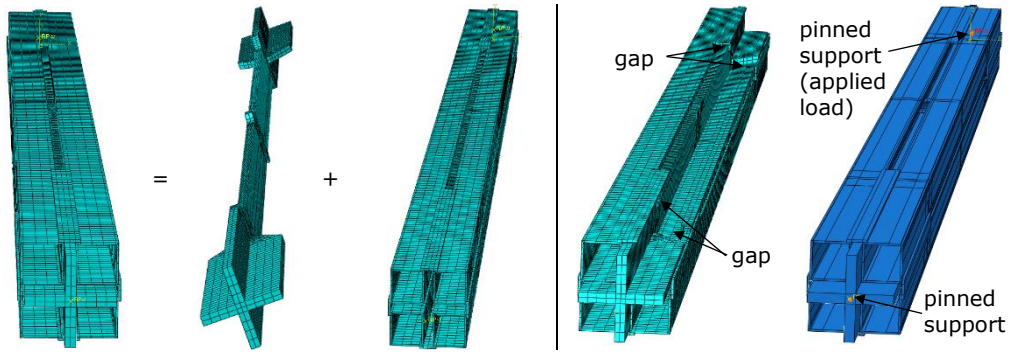

Fig. 3.22. Finite element model of "dry" BRB: a) assembly, b) core, c) BRM, d) longitudinal gaps, e) boundary conditions

be stable and a factor β = 1.26 was obtained (Fig. 3.23.a). Also, the energy dissipation capacity was considerably improved, since the local buckling of the BRM was restrained by the additional steel plates. However, compared to the "conventional" BRBs of 700 kN, it could be observed that the former dissipated less energy, was less stable and had a smaller ductility (Fig. 3.16 vs. Fig. 3.23.a).

In the case of the 300 kN BRB, the tubes were filled with concrete. "Tie" constraints were defined between the interior surface of the SHS profile and the exterior surface of the infilled-concrete. The new BRM configuration proved to be stable and a factor β = 1.25 was obtained (Fig. 3.23.b). Also, the energy dissipation capacity was considerably improved, since the local buckling of the BRM was restrained by the infill concrete. This BRM solution can be prefabricated, since filling the SHS profiles with concrete can be done prior assembling the BRM.

Based on the numerical simulations on "dry" BRBs, two solutions derived from the initial concept of *type C*, that used four SHS profiles, fillers and plates to form a welded steel-only assembly acting as BRM. Therefore, the derived conceptual solution for the 700 kN BRB (Fig. 3.24.a) will be further referred as BRB of *type C*, since is a steel-only technical solution (4 SHS, thick and thin plates, fillers). The derived conceptual solution for the 300 kN BRB (4 concrete filled SHS, plates, fillers), see Fig. 3.24.b, is still a "dry" solution as the concrete does not come in contact with the core and it will be further referred as BRB of *type D*.

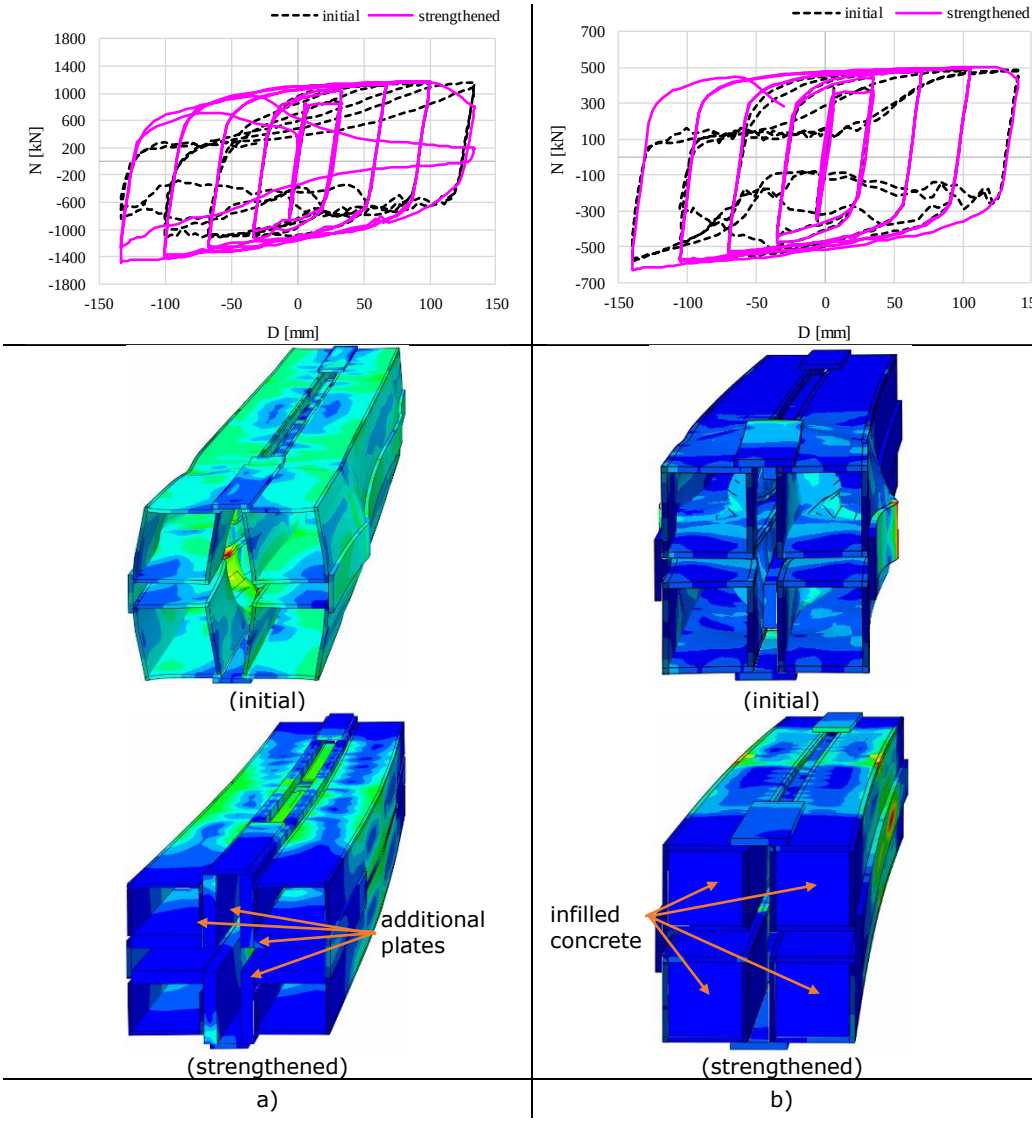

Fig. 3.23. FEM results of "dry" BRBs: a) 700 kN, b) 300 kN

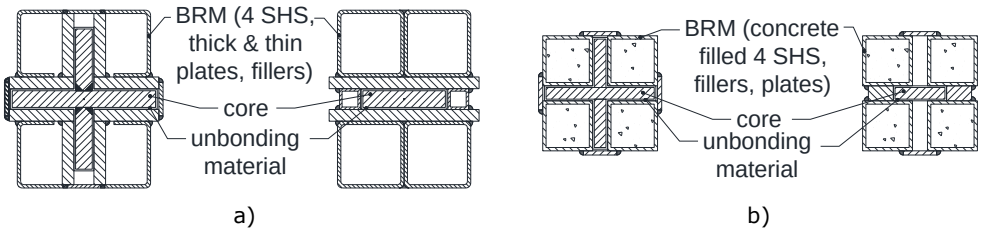

Fig. 3.24. Conceptual BRB solutions ("dry"): a) type C, b) type D

3.6 Concluding remarks

For the development of the prequalified BRBs two values of resistance were selected, 300 kN and 700 kN.

In the initial phase of development of BRBs, three conceptual solutions were proposed: (1) *type A* – "conventional" BRB with rectangular core; (2) *type B* – "conventional" BRB with square core; (3) *type C* – "dry" BRB with rectangular core.

A special detail was proposed for the BRB-to-gusset bolted connection to limit the bending moments transmitted to the ends of the BRB due to the frame effect. The technical solution adopted was validated based on numerical FEM results.

Four conceptual solutions were analysed for the transition zone detail. Both numerical and experimental tests were performed and the solutions with the lowest risk of a brittle failure mode were proposed to be used for core manufacturing. *Concept 1* (milling of a steel plate and fillet radiuses) was proposed for the core of BRBs of *type A* and *type C*. *Concept 3* (chamfered core-extension plates welded to a square hot-rolled profile) was proposed to be used for the core of BRBs of *type B*.

Pre-test numerical simulations were performed on both "conventional" and "dry" BRBs. A numerical three-dimensional model was developed in Abaqus finite element software and validated against experimental data. The calibrated parameters and the modelling technique were further used to develop FEM models for the proposed conceptual BRB solutions. Parametric studies aimed at investigating the influence of several parameters on the performance of the BRB models: the demand of the loading protocol, type of loading, core shape, core-to-BRM gap and friction, strength of BRM. The numerical results obtained were used the basis for the conceptual development of the technical solutions for both "conventional" and "dry" BRBs.

Based on the numerical simulations on "dry" BRBs, two solutions derived from the initial concept (*type C*). The BRB solution using a steel-only assembly as buckling restraining mechanism will be further referred as solution of *type C*, while the other BRB solution using concrete filled SHS profiles will be further referred as solution of *type D.*

4 EXPERIMENTAL TESTS FOR PRE-QUALIFICATION OF BRBS

4.1 Experimental program

The experimental program for the prequalification of a set of BRBs [108] consisted in cyclic tests on BRB-column subassamblage and uniaxial tensile/compression tests on base materials, steel and concrete. The mechanical properties obtained from the material tests were used for the design of the BRB specimens. Cyclic material tests were also performed on steel coupons extracted from the core of a BRB in order to obtain the input parameters used for finite element simulations.

Four BRB typologies resulted from the development of the technical solutions: two "conventional" typologies, *type A* (Fig. 4.1.a) and *type B* (Fig. 4.1.b), and two "dry" typologies, *type C* (Fig. 4.1.c) and *type D* (Fig. 4.1.d).

For the BRBs of *type A, C* and *D* the core is milled from a steel plate and fillet radiuses assure a smooth transition from the plastic (L_p) to the elastic (L_e) zone. The elastic cross-section section consists of the enlarged core segment (of height h_e, thickness t_e, and length L_e) and the two stiffeners (of width w_{stf}, thickness t_{stf}, and length L_{stf}). The main role of the elastic zone is to allow sliding of the core ends with respect to the buckling restraining mechanism, without excessive rotation, so that the BRB behaves essentially axially. Stiffeners are missing over a short length ($2t_e$) of the elastic zone to limit the bending moment transmitted to the BRB ends due to the frame effect to the value of the plastic moment of the cross-section in the "$2t_e$" zone [108].

The core of the BRB of *type B* is fabricated from compact hot-rolled square steel profile, while the elastic zone is obtained by welding core extension plates and stiffeners to each end of the core. The gradual increase of the cross-sectional area of the core from the plastic (reduced) to the elastic (enlarged) zone is assured by chamfering the core extension plates and stiffeners [108].

The transition zone (of length L_t and radius R_t, see Fig. 4.1.e) is an intermediate segment between the plastic and elastic zones and needs a careful design and fabrication to prevent stress concentrations and brittle failure modes. The plastic zone (of height h_p, thickness t_p, and length L_p) is split into two segments due to the presence of the stopper (of length L_s, height h_s and ,depending on the case, radius R_s, see Fig. 4.1.e), which prevents free sliding of the BRM with respect to the core under cyclic loading [108].

A gap (polystyrene foam) of length L_G = 70 mm is provided in the extension of the transition zone and stiffeners to allow for free movement under compression cycles. Core-to-BRM gaps in the through-thickness (g_t) and the through-width (g_w) directions were provided for all BRB specimens [108].

For all typologies bolted BRB-to-gusset connections (of length L_c) are provided at both ends.

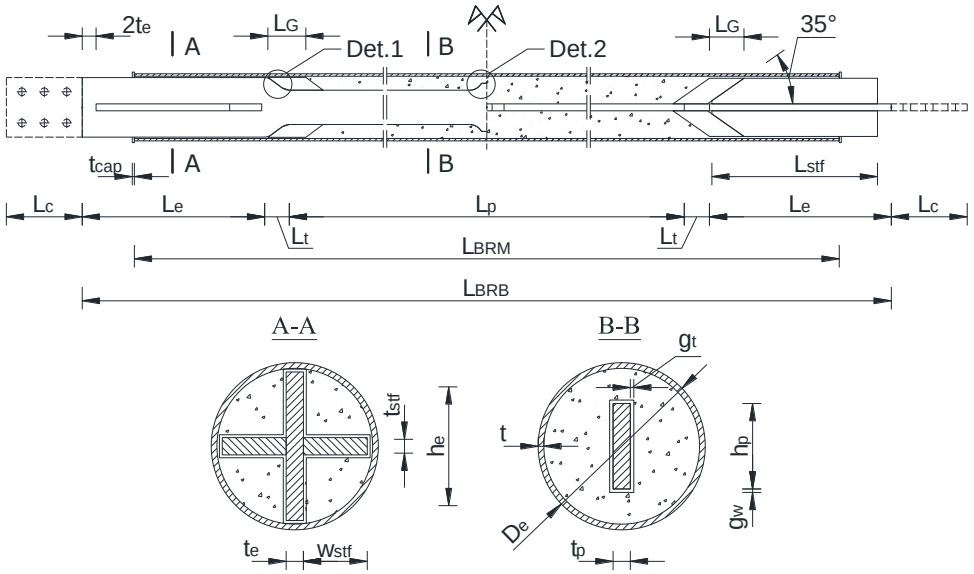

a) BRB type A: CR33, CR71, CR73

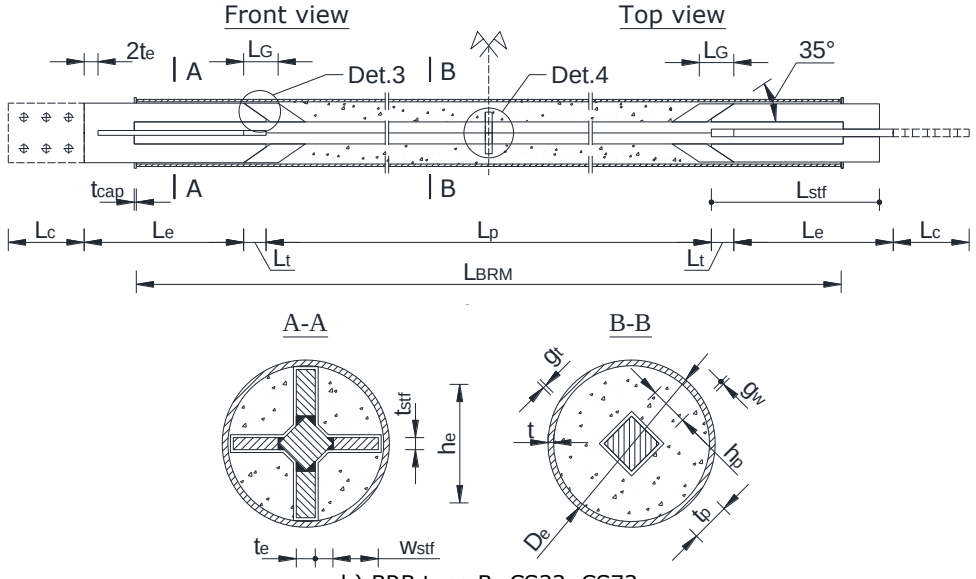

b) BRB type B: CS33, CS73

Fig. 4.1. The conceptual geometry of the tested BRBs

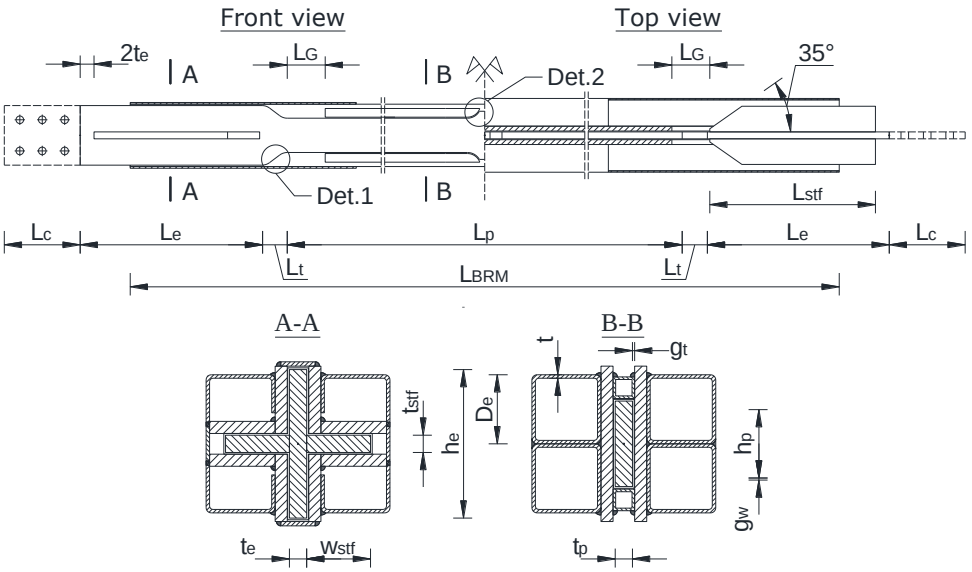

c) BRB type C: D73

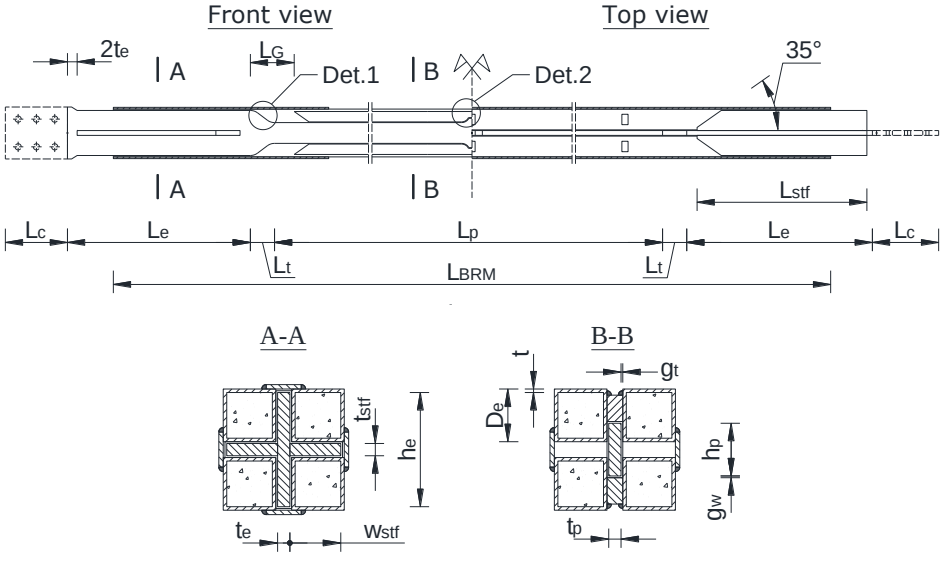

d) BRB type D: D33

Fig. 4.1. The conceptual geometry of the tested BRBs (continued)

For the BRBs of *type A* and *type B*, the buckling restraining mechanism (BRM) is a concrete-filled circular steel tube with exterior diameter D_e and wall thickness t, while the unbonding material is a self-adhesive acrylic tape. For the BRB of *type C* the BRM is a steel-only assembly consisting of fours SHS profiles of width D_e and wall thickness t, additional plates of 15 mm thickness with stiffened slotted ends, fillers (SHS 25x4xL mm, where L is the length) and plates (5x40xL mm). For the BRB of *type D* the BRM is a mixed steel-concrete solution consisting of fours concrete filled

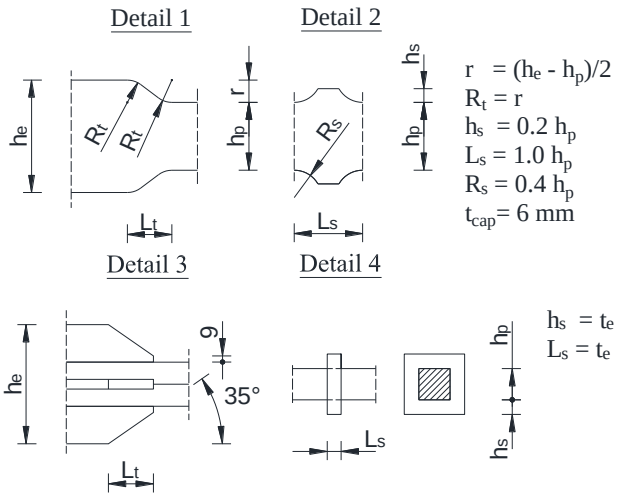

e) common details

Fig. 4.1. The conceptual geometry of the tested BRBs (continued)

SHS profiles of width D_e and wall thickness t, fillers (plate 16(18)x30xL mm) and plates (5x40xL mm). Different lengths, L_{BRM}, resulted due to different geometrical configurations of the core. The steel tubes were infilled with concrete obtained from ready-mix cement mortar and 4-8 mm aggregates. The length between the gussets L_{BRB} was the same for all specimens. The measured geometrical characteristics of the BRBs specimens are presented in Table 4.1 [108].

There are several advantages and disadvantages among the proposed typologies, as expressed below:

- BRBs of *type A*, *C* and *D* have the advantage of easy adjustment of the resistance, based on the tested yield strength of the steel plate used to fabricate the core. BRBs of *type B* have less freedom in adjusting the capacity, which depends on the available size of the profiles.
- In the case of BRBs of *type A,* because the core is very slender, it is sensitive to bow imperfections, and, therefore, careful alignment of the core relative to the BRM must be done prior to poring/casting of concrete. Less sensitive to bow imperfections are the cores of BRBs of *type B* since the shape is more compact. However, this solution requires a careful alignment of the core-extension plates and stiffeners on the opposite ends of the core. For BRBs of *type C* and *D* easy alignment of the core is facilitated by the welded assemblies.
- Among all typologies, the simplest technology of fabrication is required for the BRBs of type B, since the costly and time-consuming milling operation is avoided. BRBs of *type C* have the advantage of eliminating the technological time related to concrete casting and curing, but significantly more welding is required for assembling the BRM. Compared to *type C*, less welding is needed in the case of BRBs of *type D* but filling of the tubes with concrete is required.
- A better control of the thickness of the unbonding interface can be assured in the case of the "conventional" BRB typologies in comparison to "dry" ones, since deformations of the BRM might appear during its welding.

Table 4.1 Geometry of BRB specimens (measured dimensions, mm)

Type	ID	Plastic zone				Tr. z.	Elastic zone					BRM			BRB
		t_p	h_p	L_p	L_s	L_t	t_e	h_e	L_e	t_{stf}	L_{stf}	D_e	t	L_{BRM}	L_{BRB}
A	CR33-1	14.39	60.29	2532	60	90	14.39	150	609	13.8	565	168.33	3.71	3652	3930
	CR33-2	14.38	60.33	2532	60	90	14.38	150	609	13.8	565	168.47	3.74	3652	
	CR71-1	20.35	99.12	2478	100	65	20.35	164	661	20.1	609	177.97	3.97	3628	
	CR71-2	20.22	99.25	2478	100	65	20.22	164	661	20.1	609	178.07	4.04	3628	
	CR73-1	19.95	99.09	2462	100	73	19.95	172	661	20.1	614	193.8	5.99	3628	
	CR73-2	20.33	99.08	2462	100	73	20.33	172	661	20.1	614	193.87	6.01	3628	
B	CS33-1	30.11	30.22	2778	14	65	15.32	150	576	7.6	546	168.9	3.71	3648	
	CS33-2	30.16	30.28	2778	14	65	15.11	150	576	7.6	546	168.77	3.79	3648	
	CS73-1	44.80	44.75	2638	20	65	22.02	172	646	13.9	606	193.65	6.00	3628	
	CS73-2	44.82	44.73	2638	20	65	22.01	172	646	13.9	606	193.77	5.96	3628	
C	D73-1	19.88	98.94	2462	100	73	19.88	172	661	20.3	614	80.0	4.0	3640	
	D73-2	19.76	99.11	2462	100	73	19.76	172	661	20.2	614	80.0	4.0	3640	
D	D33-1	14.33	60.29	2572	60	90	14.33	130	579	13.8	551	60.0	3.0	3664	
	D33-2	14.30	60.26	2572	60	90	14.30	130	579	13.9	551	60.0	3.0	3664	

The experimental program is summarized in Table 4.2, and consists of 14 BRB specimens. Two identical specimens were fabricated for each distinct solution in case of *typologies A* and *B*. For *typologies C* and *D* also two specimens were fabricated, but they were slightly different, to allow investigation of some parameters, as described below [11].

The objective of the testing program was to pre-qualify two BRB capacities: 300 kN and 700 kN. All specimens were fabricated using S355 material in the core. The nominal size of the core of BRBs of *type A, type C* and *type D* was 14x60 mm for the 300 kN specimens, and 20x99 mm for the 700 kN specimens. In the case of the *type B* specimens, the core was fabricated from squares of 30x30 mm and 45x45 mm, for 300 kN and 700 kN capacities, respectively.

Early studies on BRBs suggested that the bucking-restraining mechanism be designed by assuring a minimum ratio of the critical elastic force of the BRM to the nominal resistance of the core N_{cr}/N_p = 1.5 [20]. However, some studies [107] suggested that N_{cr}/N_p = 3 are necessary in order to obtain cumulative inelastic deformations in excess of 200 times the yield deformation, as per requirements of ANSI/AISC 341-10 [100]. Two specimens (CR71-1 and CR71-2) were designed for N_{cr}/N_p = 1.5, while all the others for N_{cr}/N_p = 3.

To evaluate the influence of the starting direction of the loading protocol on the cyclic performance of the BRBs, where duplicate specimens existed, the first specimen was loaded starting the protocol in tension (*T*) and the second specimen was loaded starting the protocol in compression (*C*).

To evaluate the influence of the unbonding interface, two different materials were used: acrylic self-adhesive tape and a polyurethane, waterproofing liquid applied membrane (PWLAM). The application of the latter solution is much more time-efficient, and considerably cheaper, but requires more time for drying. On the other hand, due to small thickness (0.3 … 0.4 mm per one application), it is feasible only for *typologies C* and *D*, where the gap is assured by fillers, and not directly by the unbonding material. The acrylic self-adhesive tape was used for specimens of *type A* and *B*. The polyurethane membrane was used in the case of specimens of *type D*. The membrane was applied on both the core and the interior of the BRM. The two specimens of *type C* were fabricated using different unbonding materials, to study its influence on the performance of the BRB (see Table 4.2).

In order to take into account the Poisson effect, the thickness of the unbonding layer was adjusted depending on the core shape and BRB capacity. Therefore, a uniform 2 mm acrylic tape was applied on the cores of the BRBs of *type B* (square cross-section) and of the 300 kN *type A* (rectangular cross-section). A nonuniform thickness configuration (2 mm for the through thickness direction, g_t, and 3 mm for the through width, g_w, direction) was adopted in the case of the 700 kN BRBs of *type A* (rectangular cross-section). For the 700 kN BRBs of *type C*, g_t = 2.5 mm and g_w = 3 mm were used. In the case of specimens of 300 kN of *type D*, the gap size was used as a parameter in order to assess its influence on the BRB performance. Consequently, g_t = 1 mm and g_w = 2 mm was adopted for specimen D33-1; and a uniform gap of 2 mm for the D33-2 specimen.

The BRB specimens are identified using the following notation: e.g. CR71-2, first letter is the type of BRB – "conventional" (C) or "dry" (D), second letter (only for *typologies A* and *B*) is rectangular (R) or square (S) core cross-section, first number is nominal resistance – 300 kN (3) or 700 kN (7), the second number is the ratio N_{cr}/N_p = 1.5 (1) / 3 (3), the last number represents the first (1) or the second (2) specimen.

Table 4.2 Experimental program for BRBs

Type	ID	A_p, mm^2	N_p, kN	N_{cr}, kN	N_{cr}/N_p	L.P.	Unbonding material	Gaps, mm	
								g_t	g_w
A	CR33-1	867.6	345.1	873	2.53	T	acrylic tape	2	2
	CR33-2	867.5	345.1	881	2.55	C	acrylic tape	2	2
	CR71-1	2017.1	724.3	1103	1.52	T	acrylic tape	2	3
	CR71-2	2006.8	720.7	1123	1.56	C	acrylic tape	2	3
	CR73-1	1976.8	709.5	2093	2.95	T	acrylic tape	2	3
	CR73-2	2014.3	722.9	2102	2.91	C	acrylic tape	2	3
B	CS33-1	909.9	331.3	882	2.66	T	acrylic tape	2	2
	CS33-2	913.2	332.5	897	2.70	C	acrylic tape	2	2
	CS73-1	2004.8	565.0	2091	3.70	T	acrylic tape	2	2
	CS73-2	2004.8	565.0	2083	3.69	C	acrylic tape	2	2
C	D73-1	1966.9	705.9	3734	5.29	T	PWLAM	2.5	3
	D73-2	1958.4	702.9	3734	5.31	T	acrylic tape	2.5	3
D	D33-1	864.0	344.7	1192	3.46	T	PWLAM	1	2
	D33-2	861.7	343.8	1192	3.47	T	PWLAM	2	2

A_p – area of the plastic zone of the core computed using mean values of the measured dimensions.
N_p – plastic resistance of the core computed using A_p and the mean yield strength of the steel of the core, R_{eH} (Table 4.3).

4.2 Experimental setup and instrumentation

A general view of the testing facility used for the prequalification of the BRBs is presented in Fig. 4.2. It includes a strong floor, a reaction wall, a reaction girder, out-of-plane system, an actuator (for 300 kN BRBs)/ two actuators (for 700 kN BRBs), a pinned base column, BRB, cameras, control unit. The experimental setup presented in Fig. 4.3 is based on the P100-1/2013 [5] and ANSI/AISC 341-10 [100] recommendations regarding the testing procedure for the BRBs. It consists of a BRB-column sub-assemblage, loaded by a horizontal force at the column tip in displacement control. This loading set-up reproduces the frame effect, which induces bending moments on the BRB ends due to lateral drifts, as required by ANSI/AISC 341-10 [100]. Out of plane displacements were restrained at the top of the column.

The ANSI/AISC 341-10 [100] loading protocol was used (Fig. 4.4), up to the attainment of a deformation in the BRB corresponding to twice the design inter-storey drift ($2\Delta_{bm}$). It consists of 2 cycles at each of the following amplitudes: Δ_{by}, $0.5\Delta_{bm}$, $1.0\Delta_{bm}$, $1.5\Delta_{bm}$, $2.0\Delta_{bm}$, where Δ_{by} is the yield deformation of the BRB. The condition of attaining a minimum cumulative inelastic deformation (CID) of 200 times the yield deformation was guaranteed by this loading sequence. In a second step, the loading was continued with 2 cycles at $2.5\Delta_{bm}$, followed by cycles at $1.5\Delta_{bm}$ until failure was attained. The design inter-storey drift at the ultimate limit state in the seismic design combination was 2% of the storey height, or 70 mm, and was determined according to P100-1/2013 [5]. The corresponding BRB deformation was 51 mm [108].

The instrumentation consisted in two sets of transducers: global transducers –used to monitor the displacements of the experimental stand, local transducers – used to monitor the deformations of the BRB and the BRB-to-gusset connections. The following displacements were monitored by the global transducers: the slippage of

the reaction girder (*DHG*), the lower gusset (*DHB*) and the column base (*DHBC*); the uplift of the lower gusset (*DVB*) and column base (*DVBC*); the displacements/rotations of the tip of the column (*DHT1*, *DHT2*).

Deformation of the BRB core (D_c) was obtained as the average of four displacement transducers (*DC1…DC4*) and was used as the control displacement:

$$D_c = (DC1 + DC2 + DC3 + DC4)/4 \quad (4.1)$$

Displacement of the bottom core end with respect to the BRM (D_{bb}) was measured with transducers *DB1* and *DB2*. Similarly, displacement of the top core end with respect to the BRM (D_{bt}) was measured with transducers *DB3* and *DB4*:

$$D_{bb} = (DB1 + DB2)/2 \quad (4.2)$$

$$D_{bt} = (DB3 + DB4)/2 \quad (4.3)$$

Transducers *DJ1…DJ4* were used to monitor connection deformations. Displacement of the bottom core end with respect to the bottom gusset (*Djb*) was measured with transducers *DJ1* and *DJ2*. Similarly, displacement of the top core end with respect to the top gusset (*Djt*) was measured with transducers *DJ3* and *DJ4* [108]:

$$D_{jb} = (DJ1 + DJ2)/2 \quad (4.4)$$

$$D_{jt} = (DJ3 + DJ4)/2 \quad (4.5)$$

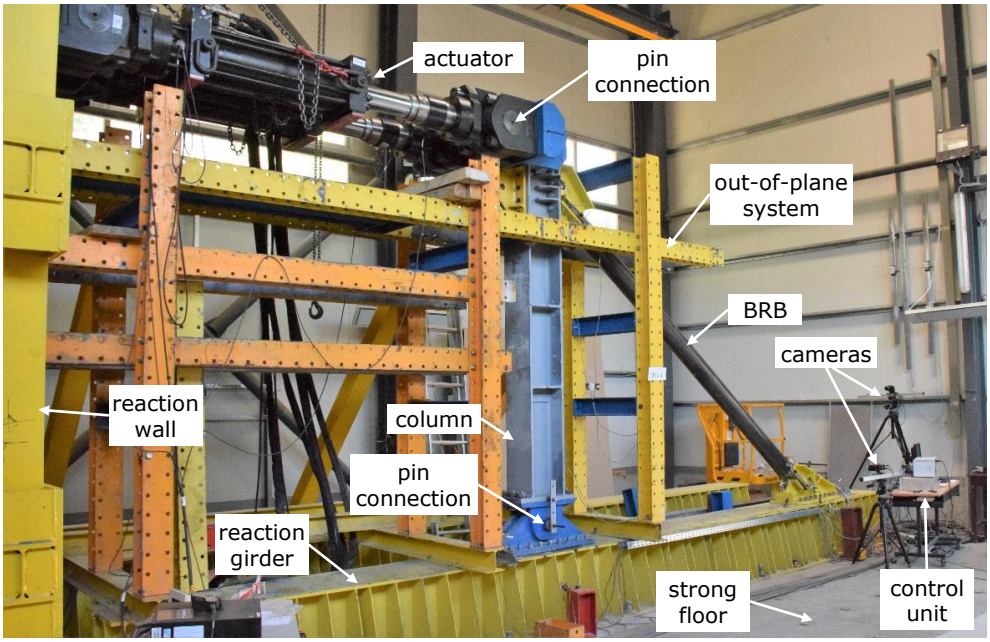

Fig. 4.2. General view of the testing facility

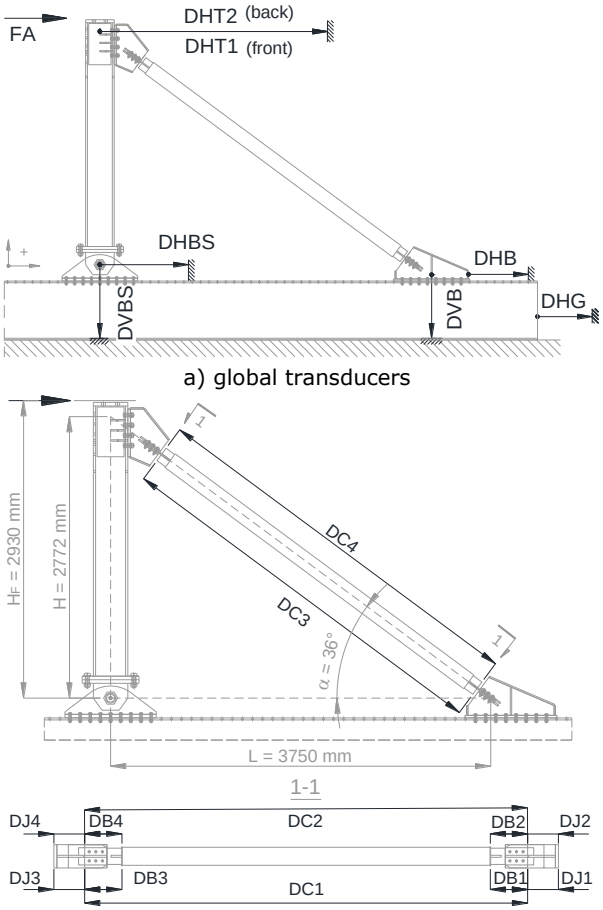

Fig. 4.3. Experimental test setup and instrumentation

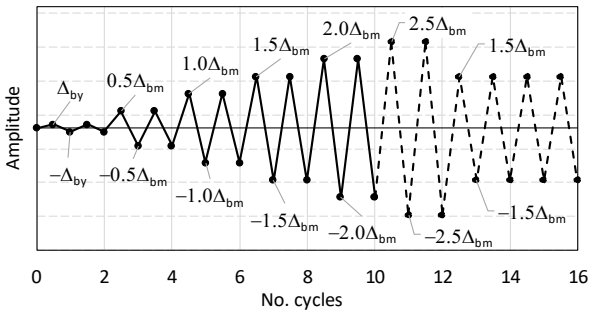

Fig. 4.4. Loading protocol used for the experimental qualification of BRBs

4.3 Tests on component materials

4.3.1 Tensile tests on steel material

Uniaxial tensile tests were performed at CEMSIG laboratory [109] to determine the mechanical properties of steel used to manufacture the core of the BRBs. The coupon specimens were designed with proportional geometry, according to SR EN ISO 6892-1:2016 [110] (Fig. 4.5.a). Three coupons were extracted parallel with the rolling direction from each of the plates/squares used to fabricate the cores. Therefore, material *C14* corresponds to the core of the BRBs specimens CR33 and D33, material *C20* to CR71, CR73 and D73, material *C30* to CS33, and material C45 to CS73.

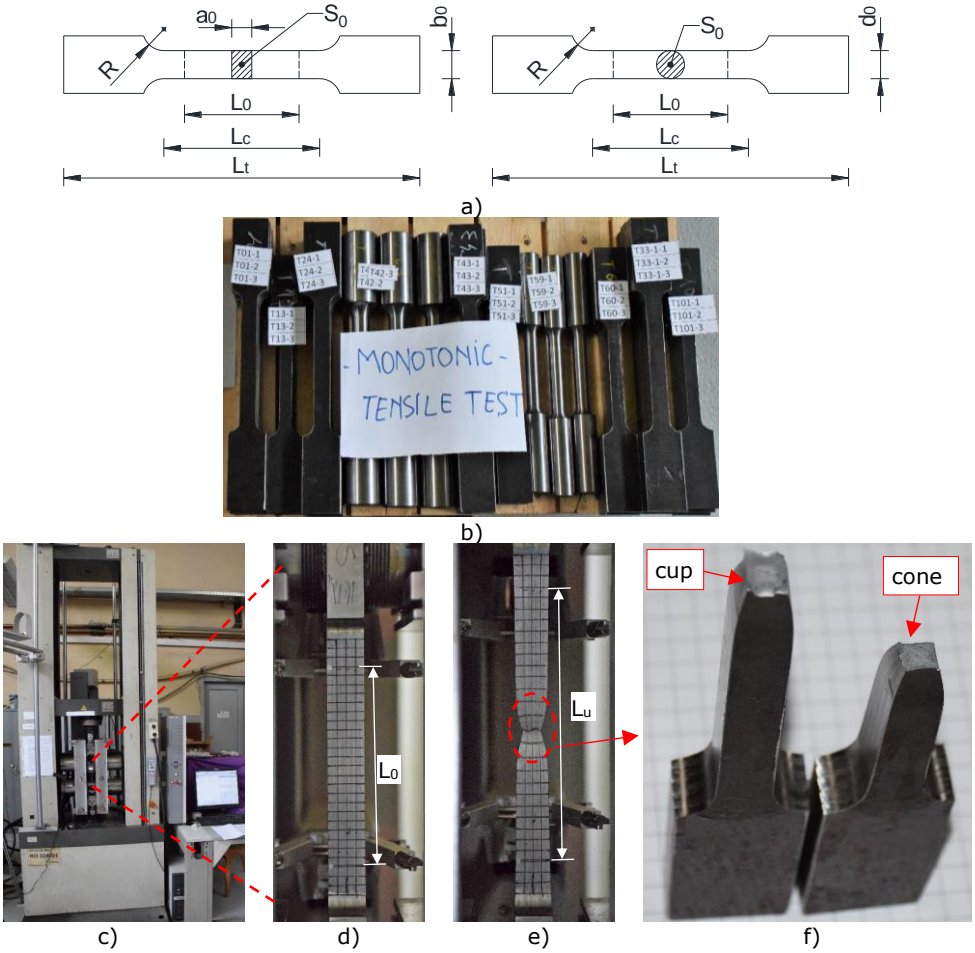

Fig. 4.5. Tensile tests on steel material: a) proportional geometry, b) coupon specimens, c) testing machine, d) initial and e) deformed shape, f) cup-and-cone fracture mode

The coupons were machined as to obtain specimens of variable cross-section along the total length L_t and with a reduced-area zone of length L_c. The cross-sectional area S_0 of the original gauge length L_0 was of either rectangular ($S_0 = a_0 \cdot b_0$, where a_0

and b_0 are the original thickness and width of the L_0 zone, respectively) or round ($S_0 = \pi \cdot (d_0)^2/4$, where d_0 is the original diameter of the L_0 zone) shape (Fig. 4.5.b), depending on the core shape (round shape coupons for square shape cores).

A Universal Testing Machine with a maximum capacity of 250 kN was used to apply the mechanical load in displacement control, see Fig. 4.5.c. As it can be observed from Fig. 4.5.d-e, the coupons can undergo large plastic deformations, $L_u >> L_0$, where L_u is the final gauge length after fracture, thus a ductile plastic behavior. Also, in case of all coupons a (ductile) cup-and-cone failure mode was obtained, see Fig. 4.5.f.

The mean values of the mechanical characteristics obtained are summarized in Table 4.3: upper yield strength (R_{eH}), tensile strength (R_m), percentage elongation after fracture (A), over-strength factor of the material (γ_{ov}), defined as the ratio between the measured and nominal values of upper yield strength. All the tensile tests results comply with the product standard except for the *C45* material [108].

The characteristic engineering stress-strain (σ-ε) curves obtained under monotonic tensile loading are shown in Fig. 4.6.a-d.

Table 4.3 Mechanical properties of steel components (strength in N/mm^2)

Mate-rial	Product standard			Quality certificate			Tensile test				
	R_{eH}	R_m	A, %	R_{eH}	R_m	A, %	R_{eH}	$R_{p0.2}$	R_m	A, %	γ_{ov}, -
C14	355	470-630	22	N/A	N/A	N/A	398	395	513	36	1.12
C20	345	470-630	22	358	508	33	359	349	510	35	1.04
C30	345	470-630	22	384	600	25	364	354	525	31	1.06
C45	335	470-630	21	353	498	30	282	278	442	35	0.84

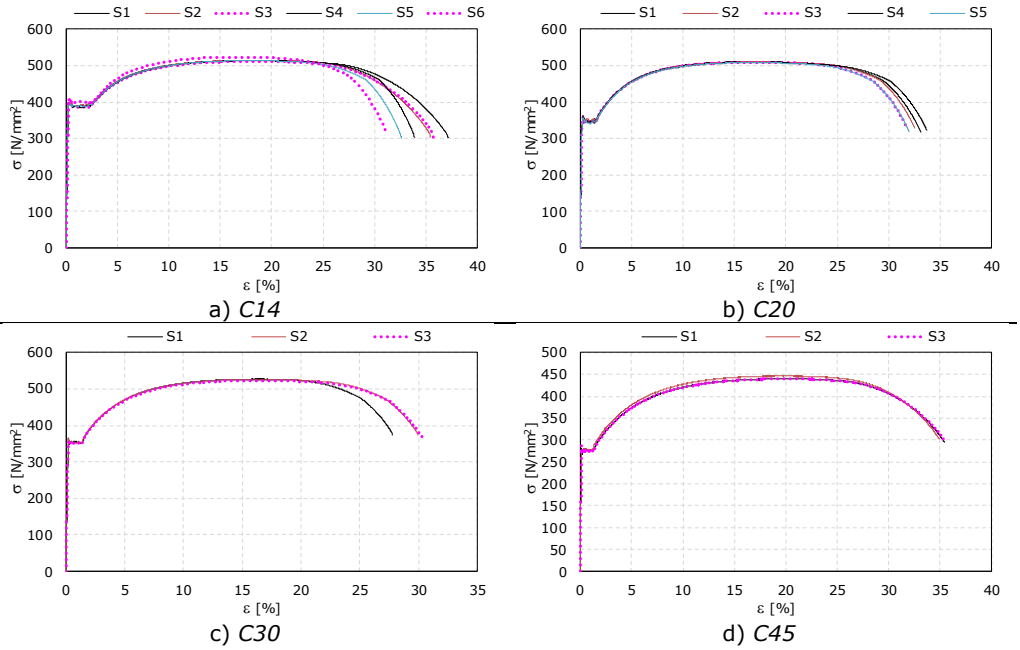

a) *C14* b) *C20*

c) *C30* d) *C45*

Fig. 4.6. Characteristic stress-strain curves from monotonic tensile tests

4.3.2 Cyclic tests on steel material

Five tests for assessment of cyclic response of steel were performed on short coupons extracted from the material used in fabrication of the core of the CS33 BRBs. The specimens of round cross-section were designed according to ASTM E606/E606M 12 [111] specifications. The coupons were turned to the dimeter d_0 of 14 mm and the initial gauge length ($L_0 = d_0$), see Fig. 4.7.a.

The testing program for assessing the cyclic response of steel is summarized in Table 4.4. Specimen *C30-m* was tested monotonically to provide data related to the yield strength, the strain at the end of the plateau, ultimate strength and its corresponding strain. The other specimens were tested cyclically at constant strains of 1.4% (*C30-1.4%*), 3.0% (*C30-3.0%*) and 5.0% (*C30-5.0%*), respectively. The last specimen, *C30-var*, was tested cyclically at variable strain amplitudes of ±1%, ±3%, ±5%, ±7%, and continued with cycles at ±5% until failure occurred. All coupons fractured in the midzone of the reduced-section zone (Fig. 4.7.b). The typical failure mode (without necking) and the fracture surface (half flat, half inclined – due to load eccentricity) are presented in Fig. 4.7.c and Fig. 4.7.d, respectively. Specimen *C30 - m* showed necking prior fracture, as shown in Fig. 4.7.e [108].

The characteristic stress-strain (σ-ε) curves obtained under cyclic loading are shown in Fig. 4.8.a-d.

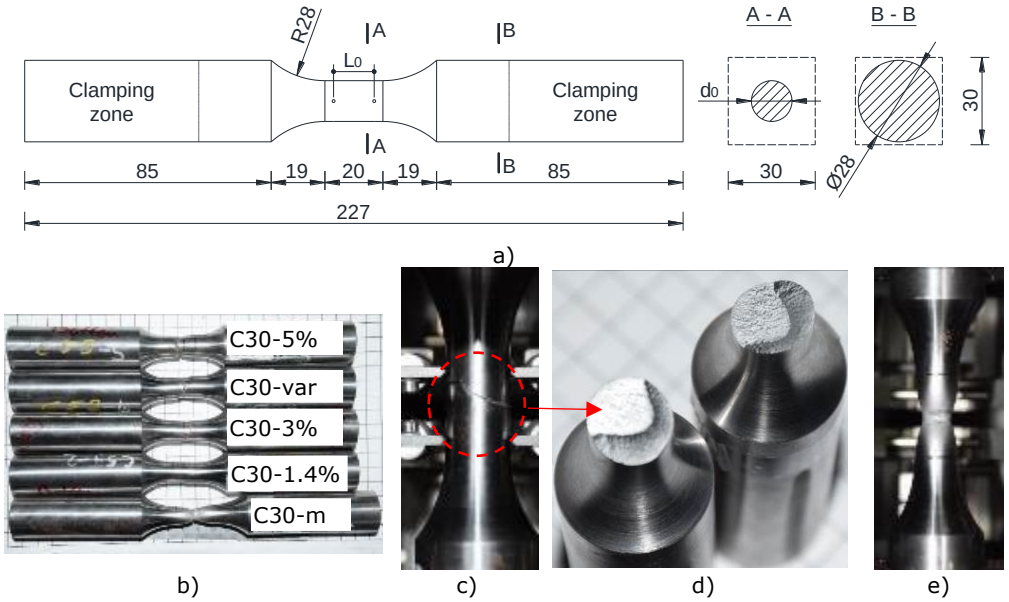

Fig. 4.7. Cyclic tests on steel material: a) typical geometry, b) tested coupon specimens, c) typical failure mode, d) fracture surface, e) failure mode of *C30-m* specimen

Table 4.4 Testing program for assessing the cyclic response of steel

ID	d_0 [mm]	L_0 [mm]	Loading type
C30-m	13.90	15	monotonic
C30-1.4%	13.90	14	cyclic LCF 1.4%
C30-3.0%	13.91	14	cyclic LCF 3.0%
C30-5.0%	13.91	14	cyclic LCF 5.0%
C30-var	13.90	14	cyclic variable

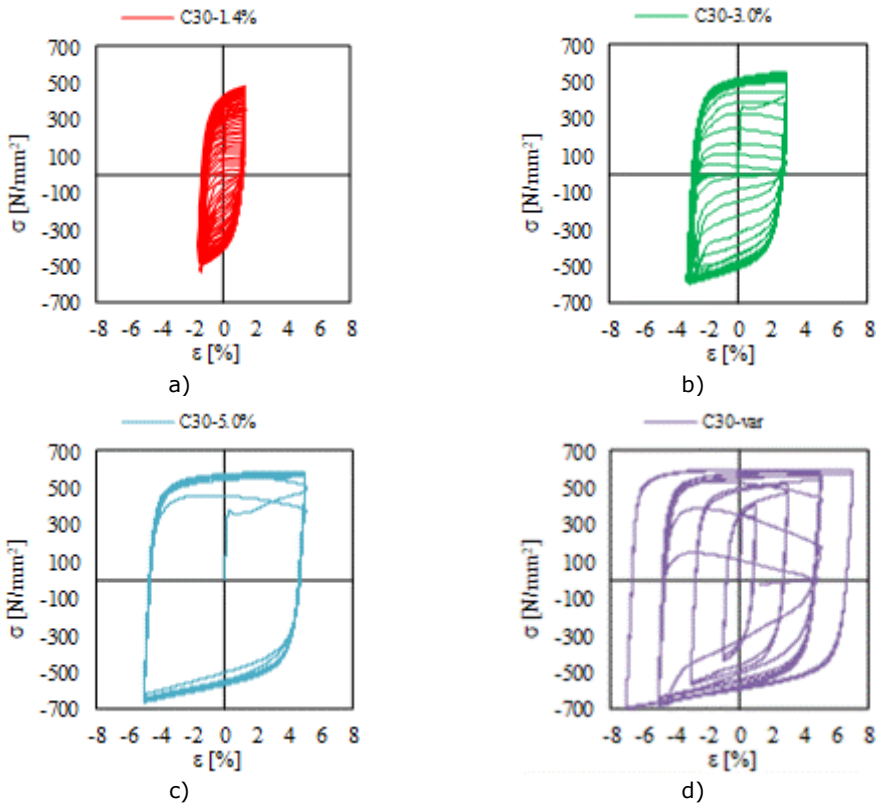

Fig. 4.8. Characteristic stress-strain curves from cyclic tensile tests

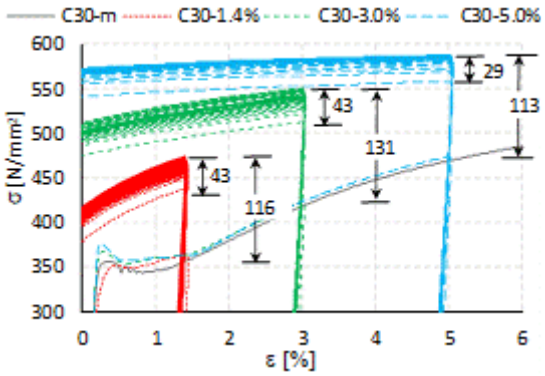

Fig. 4.9. Dependency of the cyclic hardening on the strain range

In Fig. 4.9, the results from the three cyclic tests (*C30-1.4%*, *C30-3.0%*, *C30 - 5.0%*) show that the amount of cyclic hardening differs as a function of strain range, $\Delta\varepsilon$. The amount of cyclic hardening was computed as the difference between the maximum tensile stress value reached during the saturation cycle, σ_{ts}, and the maximum stress value during the second cycle, σ_{t2}. The first cycle was not considered for the computation due to the presence of the yield plateau which reduces the amount of kinematic hardening for the first loading phase (in tension). It can be

observed that in the case of *C30-1.4%* and *C30-3.0%* the amount of cyclic hardening is 43 N/mm^2 and it decreases to 29 N/mm^2 in the case of *C30-5.0%*.

Fig. 4.10 presents the results from the monotonic test (*C30-m*) in comparison to the cyclic results (limited cycles) to observe the influence of cyclic loading with respect to strain hardening. An increase in the axial stress is noticed due to the cyclic hardening phenomenon. Also, the yield plateau disappears under cyclic loading, being present only in the first incursion in the plastic domain of the mild carbon steel S355 material.

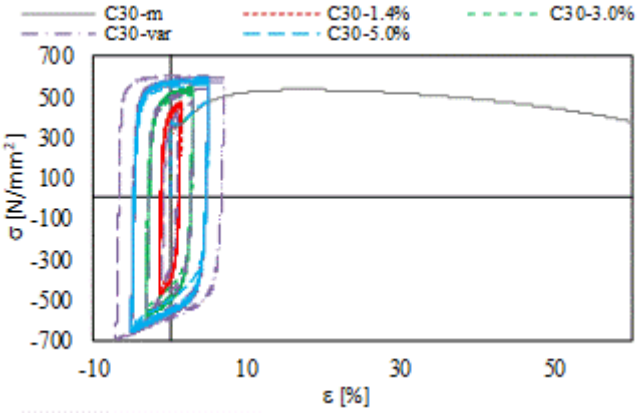

Fig. 4.10. Monotonic vs. cyclic characteristic stress-strain curves

4.3.3 Compression tests on concrete material

To evaluate the uniaxial compression strength of the concrete (a ready-mix cement mortar and 4-8 mm aggregates) used in BRBs, six 150x150x150 mm cube specimens were tested (Fig. 4.11.a). Three specimens were cured in water to assure the standard conditions for testing, while the other three specimens were cured in room conditions (similar to the ones that the BRBs are usually exposed to).

The tests on the concrete specimens were performed at the same time with the tests on BRBs, at 96 days from poring. The cubes were positioned on the testing machine such that the direction of loading (*Z*) to be perpendicular on the direction of concrete poring (*Y*), see Fig. 4.11.b and Fig. 4.11.d. The initial cracks were parallel to the loading direction (*Z*), see Fig. 4.11.e. Under increasing load, an hourglass-shaped failure mode was obtained (Fig. 4.11.c), due to the presence of the friction between the specimen and the steel plates of the testing machine. The failure was ductile, as no explosion occurred.

The experimental results of compression tests on concrete cubes are summarized in Table 4.5. Slightly larger (7%) averaged compression strength was recorded for the specimens cured in water ($f_{c,cube}^{w}$ = 50.5 N/mm^2) with respect to the ones in room conditions ($f_{c,cube}^{a}$ = 47.3 N/mm^2).

Fig. 4.12 presents the characteristic stress-strain (σ-ε) curves obtained from the compression tests on concrete cubes. It needs to be mentioned that the values of strain were not properly measured with the two transducers, since the top steel plate of the press machine had significant displacement/rotations prior the contact with the specimen. Thus, these graphs have rather a qualitative than quantitative meaning, proving the ductile failure mode of the specimens.

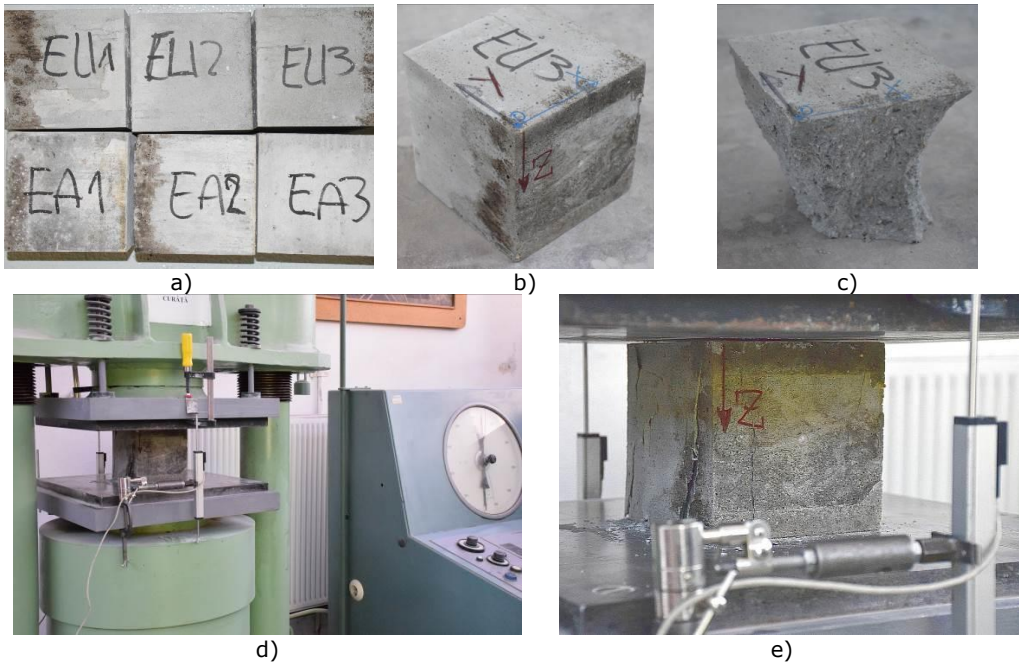

Fig. 4.11. Compression tests on concrete material: a) cubic specimens, b) perspective view of a specimen b) before and c) after test, d) testing machine, e) crack initiation

Table 4.5 Experimental results of compression tests on concrete cubes

Specimen ID	L_x, mm	L_y, mm	L_z, mm	A_c, mm^2	F_{max}, x10^3 N	f_c, N/mm^2	Curing cond.	Age, days
EU1	149.8	149.5	149.5	22395	N/A	N/A	air	92
EU2	149.5	151.9	149.9	22709	1073	47.2	air	96
EU3	149.7	151.3	149.7	22650	1071	47.3	air	96
EA1	150.4	151.4	150.1	22771	1136	49.9	water	96
EA2	149.9	152.3	150.0	22830	1112	48.7	water	96
EA3	150.4	150.5	149.8	22635	1197	52.9	water	96

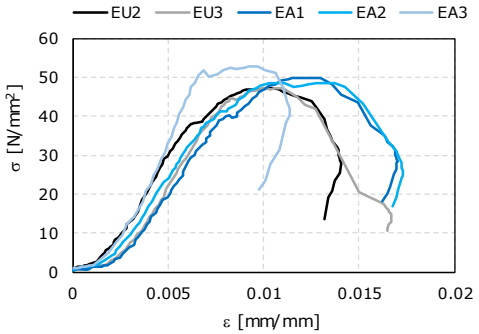

Fig. 4.12. Characteristic stress-strain curves of concrete cubes under compression load

4.4 Tests on BRBs

4.4.1 Cyclic response

The cyclic response of the tested BRBs in terms of normalized axial force (N/N_p) and core axial strain ($\varepsilon_c = D_c/L_p$) is presented in Fig. 4.13, Fig. 4.14, Fig. 4.15 and Fig. 4.16. In almost all cases, the response is stable and quasi-symmetric during the prequalification loading protocol [11].

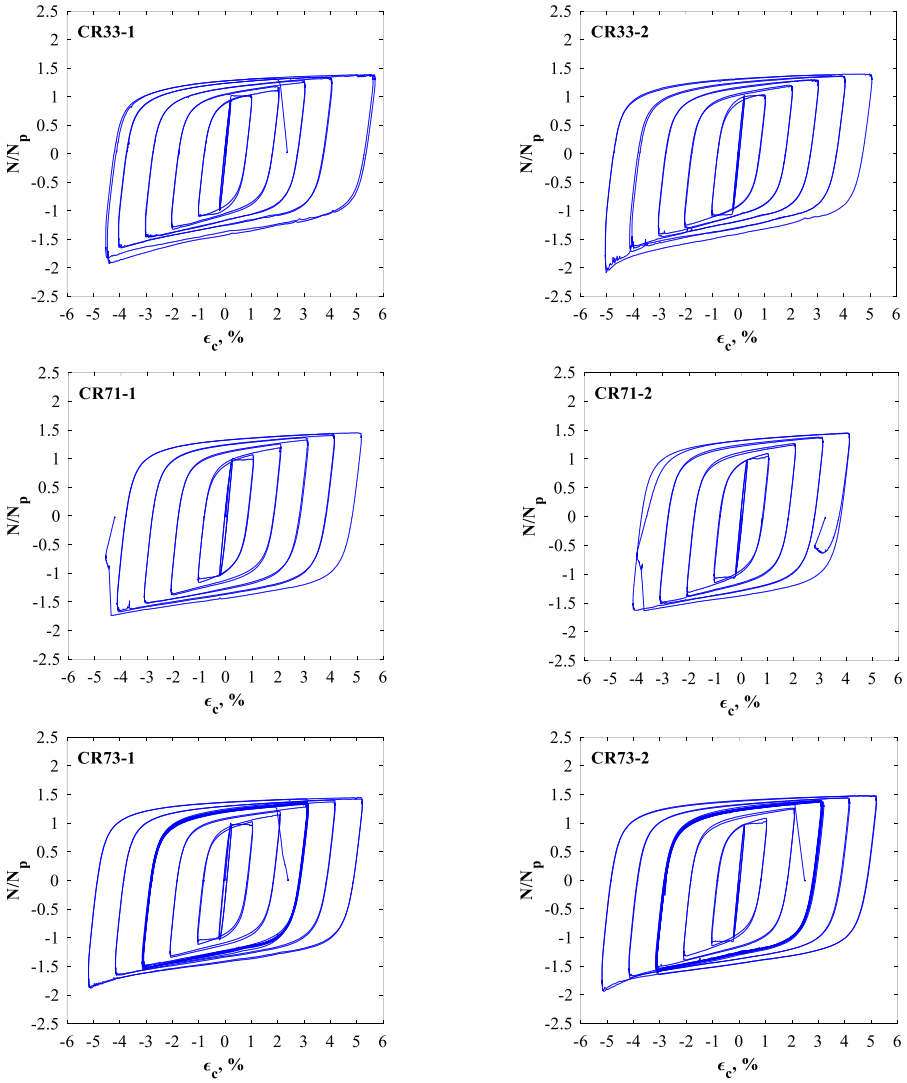

Fig. 4.13. Cyclic behaviour of BRBs type A

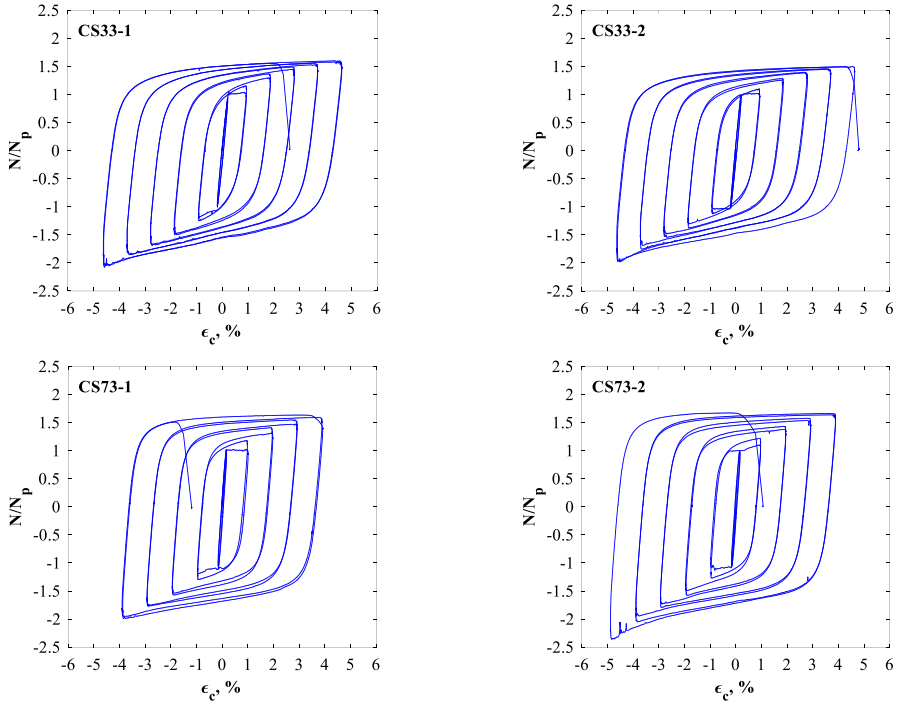

Fig. 4.14. Cyclic behaviour of BRBs type B

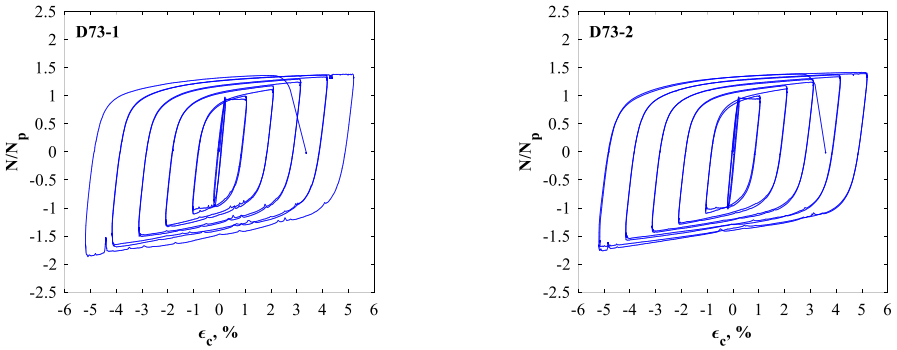

Fig. 4.15. Cyclic behaviour of BRBs type C

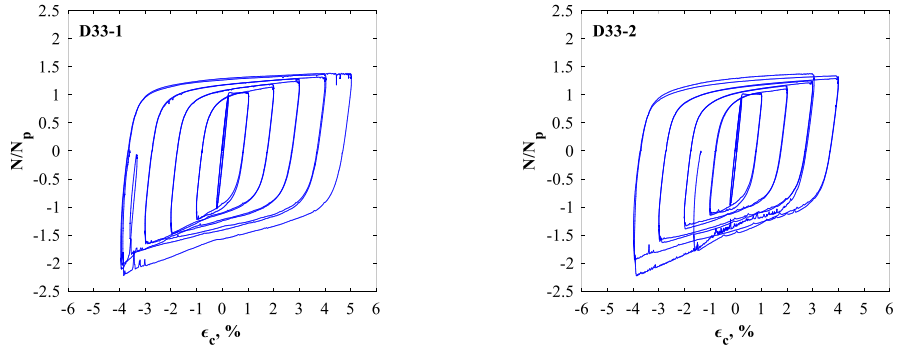

Fig. 4.16. Cyclic behaviour of BRBs type D

4.4.2 Performance parameters

Performance parameters of the tested BRBs are summarized in Table 4.6. Only 10 out of 14 BRBs could sustain the entire prequalification loading protocol (10 cycles up to $2\Delta_{bm}$). All BRB specimens except *D33-1* and *D33-2* developed a cumulative inelastic deformation (*CID*) greater than 200 times the yield deformation, Δ_{by}. The compression strength adjustment factor β is defined as (Fig. 4.17) [108]:

$$\beta = C_{max}/T_{max} \tag{4.6}$$

where C_{max} is the maximum compression force and T_{max} is the maximum tensile force.

The strain hardening adjustment factor ω is defined as:

$$\omega = T_{max}/N_p \tag{4.7}$$

where N_p is the yield force.

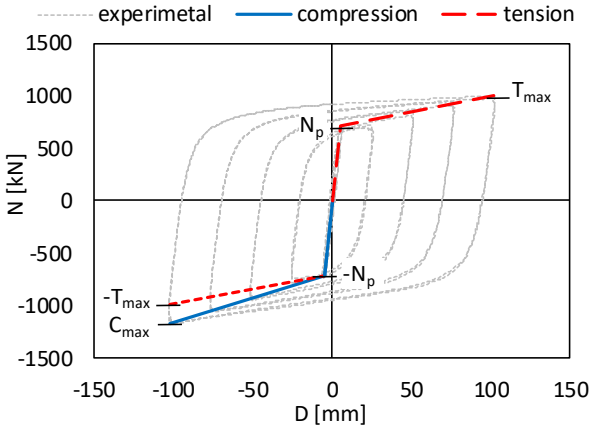

Fig. 4.17. Forces characterising the response of a BRB

During the prequalification loading protocol, for all BRB specimens except *D33-1* and *D33-2*, the β factor is in the range 1.12-1.24, less than the maximum allowed value, 1.3 (P100-1/2013 [5] and ANSI/AISC 341-10 [100]). Unqualified values for β factor were obtained in the case of *D33-1* and *D33-2* (1.55 and 1.66, respectively). The ω factor ranged between 1.34 and 1.66. In Table 4.6 the $\omega\beta$ product is presented.

The starting direction of the loading protocol (tension/compression) did not seem to influence notably the response of the specimens. Individual observations per BRB typology are given below [11].

The four specimens of *type A* (BRBs with milled rectangular core, Fig. 4.13) designed for $N_{cr}/N_p \geq 3$ (*CR73* and *CR33*) had a stable cyclic response during the qualification part of the protocol, fulfilling the P100-1/2013 [5] and ANSI/AISC 341 - 10 [100] qualification criteria. The cumulative inelastic deformation, *CID*, exceeded 330 times the yield Δ_{by}. The response was stable also during the extended protocol, but the maximum β value increased from 1.23 to 1.49. This is attributed to unsymmetrical deformations of the core at large amplitudes (see sub-chapter 4.4.3).

The *CR73* specimens (with the resistance of 700 kN) sustained a very large number of cycles (25), as well as *CID* of 1250 times Δ_{by}. Ultimate strains of 4.5-5.2% were attained. The failure took place by fracture of the core in tension (Fig. 4.18).

Table 4.6 Summary of performance parameters

Type	ID	Qualification protocol				Extended protocol				Cycles to failure
		ω	$\omega\beta$	ε_c,%	CID/Δ_{by}	ω	$\omega\beta$	ε_c,%	CID/Δ_{by}	
A	CR33-1	1.35	1.65	4.05	334.4	1.39	1.92	4.53	509.6	12.0
	CR33-2	1.37	1.66	4.04	334.4	1.40	2.09	5.06	465.8	11.5
	CR71-1	1.43	1.65	4.14	354.8	1.45	1.74	4.59	401.2	10.5
	CR71-2	1.45	1.63	4.13	281.5	-	-	-	-	9.0
	CR73-1	1.40	1.64	4.16	358.8	1.45	1.88	5.19	1256.3	25.0
	CR73-2	1.44	1.70	4.17	358.8	1.48	1.94	5.20	1283.7	25.5
B	CS33-1	1.56	1.85	3.69	348.5	1.60	2.08	4.62	530.7	12.0
	CS33-2	1.46	1.76	3.70	348.5	1.50	1.98	4.64	507.9	11.75
	CS73-1	1.64	1.99	3.90	435.3	-	-	-	-	9.75
	CS73-2	1.66	2.05	3.88	458.9	1.67	2.36	3.88	518.3	10.5
C	D73-1	1.37	1.70	4.17	358.8	1.39	1.35	5.20	452.5	11
	D73-2	1.37	1.58	4.16	358.8	1.42	1.24	5.19	546.2	12
D	D33-1	1.36	2.11	2.98	165.2	-	-	-	-	7.5
	D33-2	1.34	2.22	2.98	91	-	-	-	-	6.5

One of the specimens designed for N_{cr}/N_p = 1.5 (*CR71*), fulfilled the qualification protocol but buckled in the first compression cycle of $2.5\Delta_{bm}$ (Fig. 4.19). The second one failed to complete the qualification protocol, buckling in the cycles of $2.0\Delta_{bm}$. Nevertheless, both specimens achieved *CIDs* larger than $200\Delta_{by}$.

The four specimens of *type B* (BRBs with square as-rolled core, Fig. 4.14) had a stable cyclic response, with β values ranging from 1.19 to 1.23 and *CIDs* of 349- 459 times Δ_{by} during the qualification protocol. However, one of the specimens (*CS73- 1*) failed to complete the last cycle, and consequently the qualification criteria. This is attributed to the large misalignment of the core extension plates. It is also noted that the measured yield strength of the *CS73* specimens did not respect the specified steel grade. During the extended part of the protocol, ultimate strains of 3.88-4.64 % were attained (smaller than for *type A* specimens due to longer core plastic zone). The failure took place by fracture of the core in tension.

The specimens of *type C* ("dry" BRBs of 700 kN, with milled core, Fig. 4.15) had a stable cyclic response and *CIDs* of 359 times Δ_{by} during the qualification protocol. The β value was smaller for the specimen *D73-2*, with the core wrapped with acrylic tape, and which was the smallest (1.15) of all tested specimens. The specimen with polyurethane membrane had slightly worse performance in terms of β value (1.24). During the extended part of the protocol, ultimate strains of 5.19-5.20% were attained. Failure took place by fracture of the core in tension.

The specimens of *type D* ("dry" BRBs of 300 kN, with milled core and concrete-filled SHS, Fig. 4.16.) had an unsatisfactory performance. Out-of-plane buckling of the elastic zone (Fig. 4.20) occurred in the compression cycles of $1.5\Delta_{bm}$. It is to be mentioned that the width of the elastic zone was smaller for the *type D* specimens (*D33*) – 130 mm, in comparison with the corresponding *type A* specimens (*CR33*) – 150 mm, because of BRM size. The *CIDs* of 91-165 times Δ_{by} during the qualification protocol were recorded (less than the minimum of 200 times Δ_{by}). The β values were

very large, 1.55-1.66, with the largest value corresponding to larger transversal gap (*D33- 2*). Ultimate strains of 2.98 % were attained.

a) front view b) side view c) lower connection view

Fig. 4.18. Typical failure mode of BRBs designed for N_{cr}/N_p = 3.0

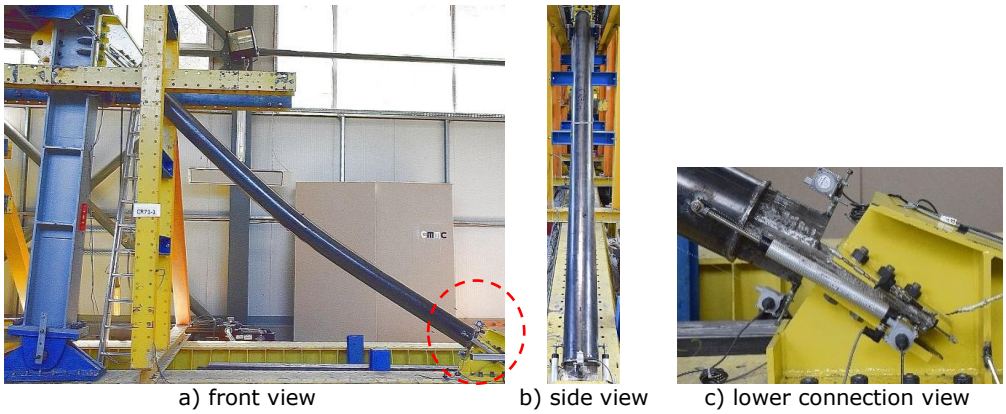

a) front view b) side view c) lower connection view

Fig. 4.19. Typical failure mode of BRBs designed for N_{cr}/N_p = 1.5

a) front view b) side view c) upper connection view

Fig. 4.20. Particular failure mode of BRBs of *type D*

4.4.3 Sizing of longitudinal gap

Since the "conventional" BRBs showed a better cyclic performance in comparison to "dry" BRBs, the investigations within this sub-chapter will refer only to the former ones.

Visual examination of the tested BRBs was performed after uncovering the core and removing the acrylic tape. Fig. 4.21 presents two representative specimens (*CR73-2*, *CS73-2*) per BRB typology, which failed by core fracture during tensile loading. Analysing the core-to-concrete interface, in the case of *CR743-2* specimen, see Fig. 4.21.a, eight distinguished friction zones (dark spots) per half plastic zone length can be observed. In the case of specimen *CS73-2*, see Fig. 4.21.b, the friction zones per plastic zone length cannot be clearly distinguished, due to a stockier ross-section. In both cases, significant core-to-concrete interaction is observed near the transition zones. No damage to the concrete infill was observed for both specimens [108].

a) BRB *type A*: specimen CR73-2

b) BRB *type B*: specimen CS73-2

Fig. 4.21. Uncovered BRBs after tests

Fig. 4.22 presents the positions where the core fractured for the specimens which have the BRM designed for N_{cr}/N_p = 3.0. It needs to be noticed that welding of BRBs *type B* did not affect their cyclic performance since no fracture took place in or near the welding. It can be observed that all cores, except for the core of specimen *CR73- 2*, fractured in the top part of the plastic zone, with respect to the position of

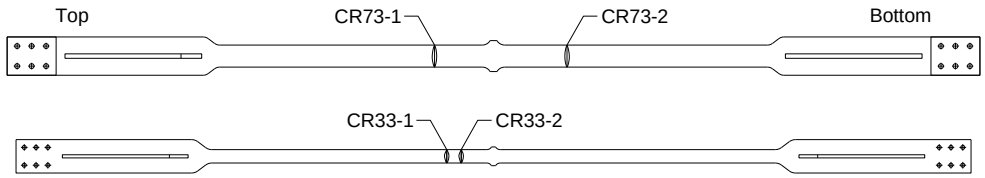

a) BRBs *type A*: specimens CR33, CR73

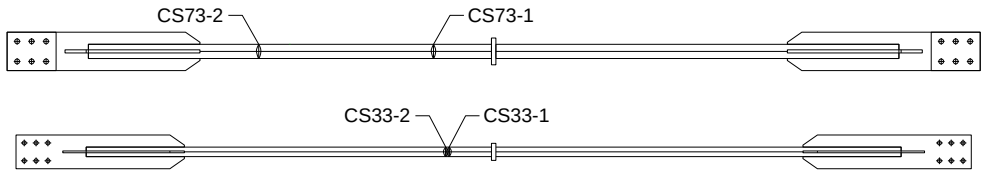

b) BRBs *type B*: specimens CS33, CS73

Fig. 4.22. Failure position for "conventional" BRBs designed for N_{cr}/N_p = 3.0

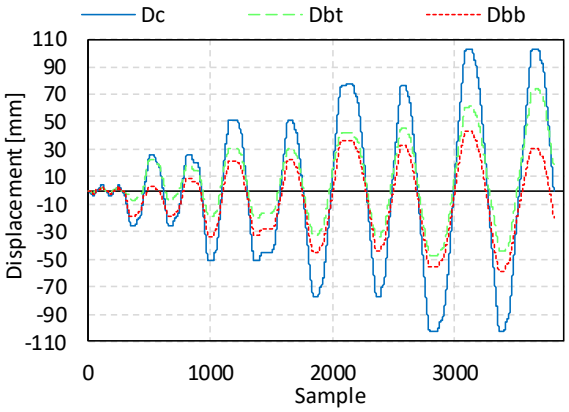

Fig. 4.23. Evolution of displacements D_{bb}, D_{bt} and D_c for the *CS73-2* specimen

the BRB in the experimental setup. Except for the specimen *CS73-2* whose fracture position is rather close to the transition zone, in the case of all the other specimens the fracture position is close to the stopper. The failure positions from Fig. 4.22 suggest that the top part of the core plastic zone experienced larger deformations during the tensile phases of the cyclic loading than the bottom part, causing the fracture to take place in the top segment of the core of almost all BRBs. This aspect is confirmed by analyzing the time-history of the displacements between the tube and the ends of the core (D_{bb} and D_{bt}), in comparison to the core deformation (D_c), see Fig. 4.23. It can be observed that during the tensile phase the top segment of the core undergoes larger deformations than the bottom part, while during compression phase the bottom segment is undergoing larger deformations [108].

The non-symmetrical deformations in the top and bottom segments of the core affects the design of the longitudinal gap that allows the free movement of the core under compression cycles. To quantify this effect, maximum deformation ratios in the top (R_t) and bottom (R_b) parts of the core were determined for the 2.0Δ_{bm} cycles [108]:

$$R_t = D_{bt}/D_c \tag{4.8}$$

$$R_b = D_{bb}/D_c \quad (4.9)$$

Maximum deformation ratios R_t and R_b are summarized in Table 4.7. Ideally, for a symmetrical response, both rations would be equal to 0.5. For all except one specimen, the deformation ratios in the top segment of the core are larger in tension (R_t = 0.52-0.72), while in the bottom part of the core the deformation ratios are larger in compression (R_b = 0.53-0.60). The longitudinal gap L_G (see Fig. 4.1) depends on the deformation in compression. Therefore, based on the present experimental tests, it is proposed that for design of a BRB the longitudinal gap L_G is determined as [108]:

$$L_G \geq 0.7\delta_{Ed} \quad (4.10)$$

where δ_{Ed} is the design deformation of the core.

Table 4.7 Maximum deformation ratios R_t and R_b

BRB ID	R_t		R_b	
	Tension	Compression	Tension	Compression
CR33-1	0.59	0.43	0.46	0.60
CR33-2	0.62	0.41	0.41	0.60
CR73-1	0.59	0.46	0.42	0.55
CR73-2	0.47	0.53	0.54	0.48
CS33-1	0.52	0.49	0.51	0.54
CS33-2	0.56	0.48	0.47	0.53
CS73-1	0.72	0.46	0.43	0.59
CS73-2	0.72	0.46	0.42	0.58

If the longitudinal gap is designed assuming symmetrical response of the top and bottom core segments, the gap is insufficient, which results in the transition segment of the core coming longitudinally into contact with the concrete infill at one of the core ends. This leads to an increase in the compression force adjustment factor β, as occurred for some specimens (e.g. *CR33-2*, see Fig. 4.13) at the $2.5\Delta_{bm}$ cycles [108].

4.4.4 Connection response

A typical response of the bolted BRB-to-gusset connection is shown in Fig. 4.24.a, where a pronounced pinching effect can be observed, due to the fact that the connection is not slip-resistant. Total deformation in a connection is the sum of slipping and bearing deformations of bolt in bolt holes. It can be observed that the connection deformation is roughly the same over the entire loading history, being governed by the slip [108].

The influence of the bolted BRB-to-gusset connection on the shape of the hysteretic loops of the BRB is presented in Fig. 4.24.b, where core (D_c) and total (D_t) BRB deformations are shown. The latter is determined as:

$$D_t = D_c + D_{jt} + D_{jb} \quad (4.11)$$

The connection has a large contribution to the total deformations during small-amplitudes cycles. However, at large cycles, the effect of the connection is rather small. Consequently, bolted connections may affect the performance of the structure at the Serviceability Limit State (*SLS*) but would have a limited effect at the Ultimate Limit State (*ULS*). Therefore, it is recommended that slip-resistant bolted connections are used if serviceability criteria are critical [108].

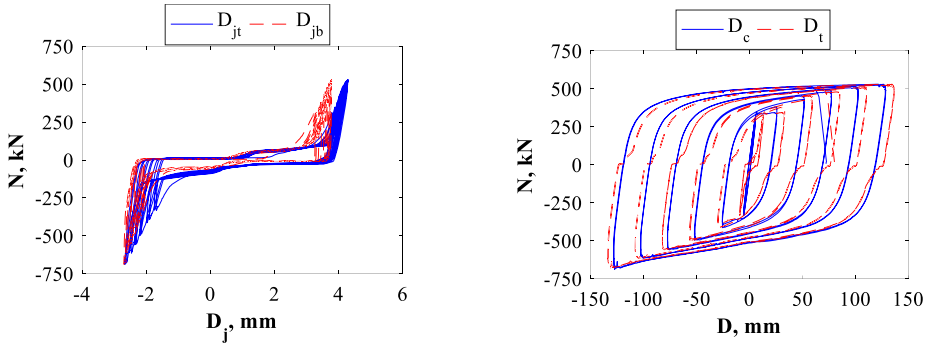

a) b)

Fig. 4.24. Bolted connection of specimen *CS33-1*: a) deformations, b) influence on the cyclic response of BRB

4.4.5 Design parameters for qualified BRBs

To choose the optimal prequalified BRB solution, in addition to the performance parameters, two additional criteria were considered, see Table 4.8 [108].

The first additional criterium refers to the possibility of adjusting the axial resistance of the BRB based on the tested yield strength of the steel plate or profile used to fabricate the core. BRBs of *type A, C* and *D* have the advantage of easy adjustment of the resistance since the core is obtained by milling of a steel plate. BRBs of *type B* have less freedom in adjusting the resistance since the core is fabricated from a compact hot-rolled square steel profile, thus the resistance depends on the available size of the profiles [108].

The second additional criterium, technology, refers to the following aspects: difficulty of the manufacturing process of the BRB, and sensitivity of the core to initial imperfections caused by the technological process (e.g. misalignment of the component parts). Based on technical-economical evaluation [6], the "dry" BRB solutions were found to be more difficult to fabricate and more expensive in comparison to "conventional" solutions due to the large amount of welding. Also, the welding process reduced the control of the size of the core-to-BRM gap, as the parts forming the buckling restraining mechanism (BRM) tend to deform during the welding. On the other side, for the *type A* and *type B* BRBs, since the BRM is similar for both typologies, the fabrication of the core of BRB *type B* is much simpler, as the costly and time-consuming milling operation needed to manufacture the core of BRB *type A* is avoided. Also, because the core of BRB *type B* has a compact shape, it is less sensitive to bow imperfections in comparison with core of BRB *type A*. It was experimentally found that large misalignment of the core extension plates of BRBs *type B* caused premature failure, therefore careful alignment of the extension plates (and also stiffeners) on the opposite ends of the core is required.

Based on the above-mentioned criteria (performance, adjustability and technology) it was concluded that the optimal BRB solution is the *type A* (BRB with milled rectangular cross-section core, having the BRM designed for $N_{cr}/N_p \geq 3.0$). The recommended values of strength adjustment factors for design of such BRBs are $\omega = 1.45$ and $\beta = 1.17$, while the ultimate core strain $\varepsilon_c = \pm 4\%$. The strength range of the qualified BRBs is 150-840 kN [108].

Table 4.8 Selection of qualified BRBs

Type	ID	Selection criteria			Recommended
		Cyclic performance	Adjustability of N_p	Technology	
A	CR33-1	yes	yes	yes	yes
	CR33-2	yes	yes	yes	
	CR71-1	yes	yes	yes	no
	CR71-2	no	yes	yes	
	CR73-1	yes	yes	yes	yes
	CR73-2	yes	yes	yes	
B	CS33-1	yes	no	no	no
	CS33-2	yes	no	no	
	CS73-1	yes	no	no	no
	CS73-2	yes	no	no	
C	D73-1	yes	yes	no	no
	D73-2	yes	yes	no	
D	D33-1	no	yes	no	no
	D33-2	no	yes	no	

4.5 Concluding remarks

The experimental program included both prequalification tests on BRBs and tests on components materials (tensile and cyclic tests on steel material, and compression tests on concrete material).

A set of 14 full-scale BRBs were tested using the ANSI/AISC 341-10 [100] loading protocol in view of prequalification for typical low-rise and mid-rise buildings. Four different technical solutions were investigated. Most of the specimens performed well, with stable hysteretic response, and ultimate core strains larger than 4%. Unsatisfactory performance was observed for specimens with lower strength of the buckling-restraining mechanism (N_{cr}/N_p = 1.5), with insufficient strength of the elastic zone (*D33* specimens), or misalignments due to fabrication process (*CS73-1* specimen). Though more expensive and time-consuming to apply, the acrylic self-adhesive tape led to superior performance in comparison with the polyurethane membrane.

Based on the performance from the point of view of response, technology and adjustability, the "conventional" solution with milled core encased in concrete-filled tube was recommended as the qualified BRB for the strength range 150-840 kN. The recommended values of strength adjustment factors for design of such BRBs are ω = 1.45 and β = 1.17, while the ultimate core strain ε_c = ± 4%.

Gravity loading leads to unsymmetrical deformations in the two plastic segments of the core. Therefore, it is recommended that the length of each longitudinal gap is at least 70 % of the design deformation of the core.

Non-slip-resistant bolted BRB-to-gusset connections may affect the performance of the structure at the Serviceability Limit State but would have a limited effect at the Ultimate Limit State. If serviceability criteria are critical, slip-resistant bolted connections are recommended.

5 POST-TEST NUMERICAL SIMULATIONS

5.1 Modelling the behaviour of steel

5.1.1 Introduction

Modelling the cyclic response of structural steel plays an important role in the design and performance assessment of steel structures. During a seismic event, the structural steel elements (e.g. Buckling Restrained Braces, shear links/panels) are undergoing cyclic deformations. Therefore, a material model able to properly simulate the cyclic behaviour of structural steel must be experimentally validated. The calibrated material model can be further used to simulate the structural elements for cyclic numerical analyses [112].

The main objective of this chapter is to provide a modelling technique of the cyclic response of structural steel for FEM analyses using Abaqus "built-in" material models. Specific guidelines are given regarding the calibration of material parameters based on experimental data, since the case study is the mild carbon steel with yield plateau (S355) used to fabricate the core of the BRBs [112].

5.1.2 Cyclic response of steel

Up to date, several mathematical models were developed to simulate metal plasticity [104]. Only the kinematic hardening models are appropriate to simulate the structural steels under cyclic loading conditions [104] due to the presence of the Bauschinger effect. This effect can be experimentally observed when performing uniaxial cyclic coupon tests under symmetric strain control. As presented in Fig. 5.1.a-b, the Bauschinger effect consists in decreasing the yield strength, σ^0, when the direction of strain is changed. When simulating structural mild carbon steels, using only the kinematic hardening model is not sufficient to properly simulate the cyclic plastic behaviour, due to several specific aspects [112].

The first aspect is the presence of cyclic hardening and/or softening phenomenon (Fig. 5.2.a-b) during cyclic experiments. In the current study, the structural mild carbon steels S355 exhibits initial cyclic hardening (yield stress, σ^0_1, increases to a stable limit, σ^0_s), followed by cyclic softening (saturated yield stress, σ^0_s, decreases to the rupture limit, σ^0_r) [112].

The second aspect is the presence of the yield plateau which appears after the first yield in tension as a cause of Luders bands propagation [113] (Fig. 5.3.a). This phenomenon can be idealized as a non-hardening region with the lower bound defined by the yield strain, ε_y, and the upper bound defined by the onset of strain hardening, ε_{sh} (Fig. 5.3.b). As experimentally observed, the yield plateau disappears when the direction of strain is changed, thus suggesting that the yield plateau is not depending on the plastic strain, ε^{pl}, but rather on the cumulative plastic strain, $\varepsilon^{\sim pl}$ ($\varepsilon^{\sim pl}$ is a summation of the plastic strain components during j cycles, $\varepsilon^{\sim p} = \Sigma^n_{j=1} \varepsilon^{\sim pl}_j$; ε^p is obtained by deducting the elastic strain from the total strain, $\varepsilon^{pl} = \varepsilon - \varepsilon^{el}$) [112].

Considering the above presented phenomena, modelling the cyclic plasticity of steels with yield plateau is difficult due to the complex behaviour [112].

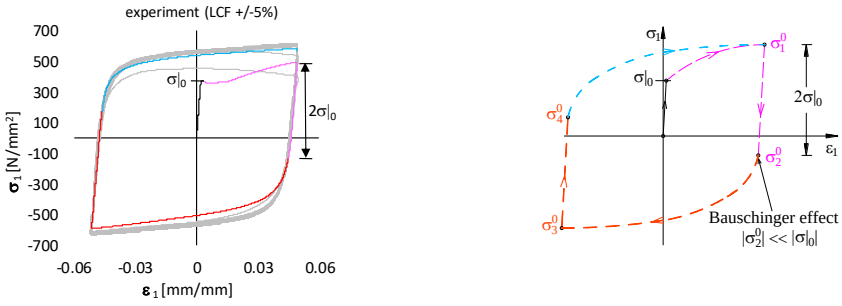

a) b)

Fig. 5.1. Bauschinger effect: a) experiment b), schematic

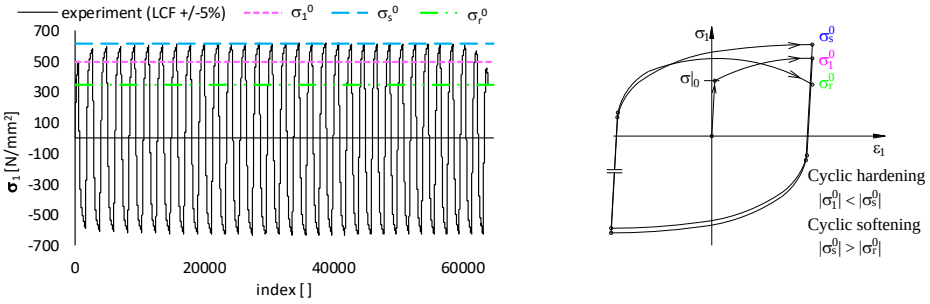

a) b)

Fig. 5.2. Cyclic hardening and softening phenomenon: a) experiment, b), schematic

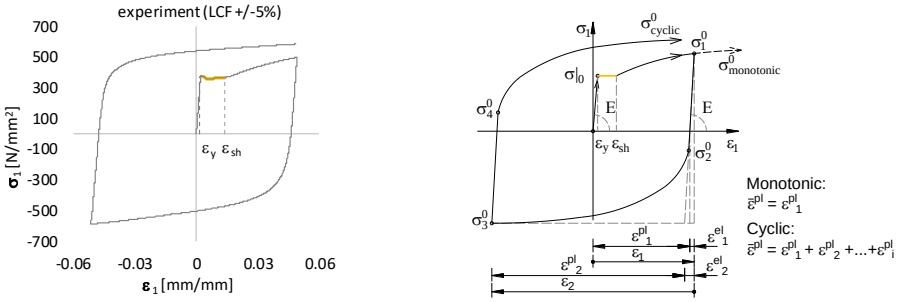

a) b)

Fig. 5.3. Yield plateau phenomenon: a) experiment, b), schematic

5.1.3 Built-in material models

Metal plasticity can be modelled using several approaches implemented in Abaqus 6.14 [104]. The plastic hardening behaviour can be defined using one of the available options: isotropic, kinematic, Johnson-Cook, user, combined. The first two models are relatively simple with respect to the other from the perspective of the calibration process of the input parameters. Johnson-Cook and user material will not be discussed within this paper. The combined option is a complex material model that requires a good understanding of plastic hardening to calibrate the material parameters. The three models will be further discussed [112].

The isotropic hardening model assumes the von Misses yield surface to having a fixed center, while the yield surface can increase (hardening) or decrease

(softening) in shape. This model is suitable for FEM analyses where the direction of the principal stresses (σ_1, σ_2, σ_3) does not change significantly. The input parameters, yield stress-plastic strain data pairs, can be easily obtained from a uniaxial tensile test. As can be observed in Fig. 5.4.a, a good prediction for the monotonic uniaxial tensile test can be obtained with this material model. When applying cyclic loading, the prediction is inaccurate Fig. 5.4.b [112].

The kinematic model assumes the yield surface having a fixed surface, while moving with a certain slope (constant rate of strain hardening) through the stress space. Since only one hardening slope can be provided, this model will lead to coarse predictions of the monotonic and cyclic behaviour of steel (Fig. 5.4) [112].

To capture the main features of mild carbon steel (Bauschinger effect, cyclic hardening) the combined isotropic-kinematic hardening material represents a proper material model. It consists of a nonlinear kinematic hardening component (used to simulate the Bauschinger effect) and an isotropic component (used to simulate the cyclic hardening) which can be linear, multilinear, or nonlinear, depending on the input type. The calibration of the input parameters requires uniaxial cyclic test data and the procedure is described in [104]. As can be observed in Fig. 5.4.a-b, acceptable predictions can be obtained for both monotonic and cyclic loading. It needs to be mentioned that the combined model has several limitations. The most important one is the fact that the material is history dependent and it will be further discussed [112].

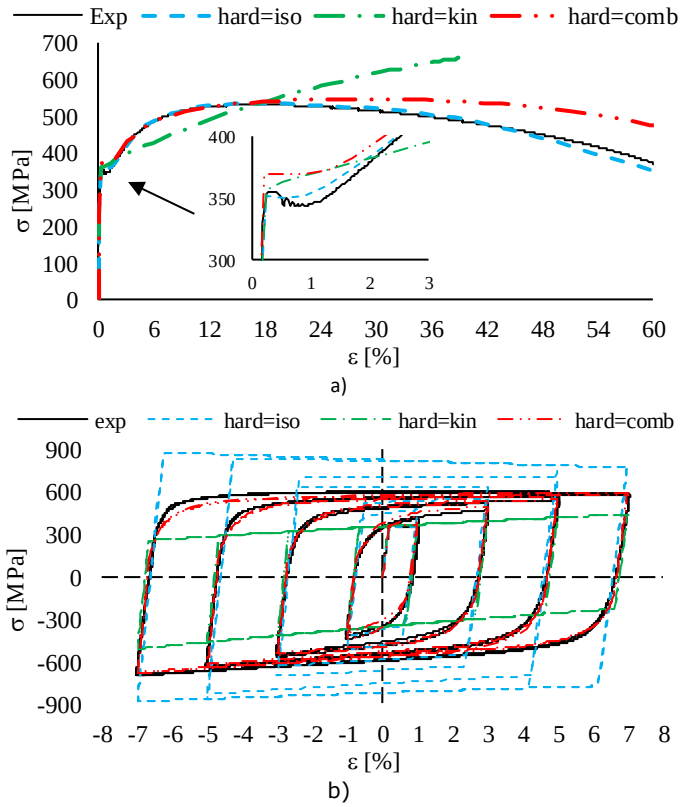

Fig. 5.4. Stress-strain response of several numerical models under a) monotonic and b) cyclic loading

5.1.4 Combined hardening model

The behaviour of the material model used in this study to simulate the behaviour of steel consists of a linear elastic and a nonlinear plastic component. The elastic behaviour is defined using the isotropic elasticity formulation [104]. Therefore, only the elastic modulus, E, and the Poisson ratio, ν, are required to describe the elastic behaviour based on the generalized Hook's law. The "true" (Cauchy) stress tensor, $\boldsymbol{\sigma}$, is defined as a linear function between the fourth-order elasticity tensor, $\mathbf{D}^{\mathbf{el}}$, and the logarithmic strain tensor, $\boldsymbol{\varepsilon}^{el}$, $\boldsymbol{\sigma} = \mathbf{D}^{\mathbf{el}}\,\boldsymbol{\varepsilon}^{\mathbf{el}}$. The plastic behaviour is defined using the pressure-independent plasticity theory [104]. The following constitutive equations and hypotheses were considered to define the plasticity of structural steel [112]:

- Total strain tensor, $\boldsymbol{\varepsilon}$, decomposed into elastic, $\boldsymbol{\varepsilon}^{\mathbf{el}}$, and plastic, $\boldsymbol{\varepsilon}^{\mathbf{el}}$, parts ($\boldsymbol{\varepsilon} = \boldsymbol{\varepsilon}^{\mathbf{el}} + \boldsymbol{\varepsilon}^{\mathbf{pl}}$).
- Yield surface, $F = f(\boldsymbol{\sigma} - \boldsymbol{\alpha}) - \sigma^0 = 0$, defined as a function of equivalent stress, $f(\boldsymbol{\sigma} - \boldsymbol{\alpha})$, and yield stress, σ^0 ($\boldsymbol{\alpha}$ is the backstress tensor). For $F < 0$ an elastic stress state is obtained, while $F = 0$ yields a plastic stress state; $F > 0$ is not admissible.
- von Mises yield criterion, $f(\boldsymbol{\sigma} - \boldsymbol{\alpha}) = [3/2(\mathbf{S} - \boldsymbol{\alpha}^{\mathbf{dev}}):(\mathbf{S} - \boldsymbol{\alpha}^{\mathbf{dev}})]^{0.5}$, defined as a function of deviatoric stress tensor, $\mathbf{S}$, and deviatoric part of the backstress tensor, $\boldsymbol{\alpha}^{\mathbf{dev}}$.
- Associated plastic flow rule, $\dot{\varepsilon}^{pl} = \dot{\varepsilon}^{-pl}(dF/d\boldsymbol{\sigma})$, depending on the equivalent plastic strain rate, $\dot{\varepsilon}^{-pl} = [2/3(\dot{\varepsilon}^{pl} : \dot{\varepsilon}^{pl})]^{0.5}$.
- Nonlinear isotropic/kinematic hardening rule having the kinematic component defined as a function of nonlinear backstress, $\boldsymbol{\alpha} = \Sigma^5_{k=1}\ (\boldsymbol{\alpha}_\mathbf{k})$ (where $\boldsymbol{\alpha}'_\mathbf{k} = C_k(1/\sigma^0)(\boldsymbol{\sigma} - \boldsymbol{\alpha})\dot{\varepsilon}^{-pl} - \gamma_k\,\boldsymbol{\alpha}'_\mathbf{k}\,\dot{\varepsilon}^{-pl}$) and the isotropic component, $\sigma^0 = \sigma|^0 + (\sigma^0{}_i - \sigma|^0)$, defined in a tabular form as a function of equivalent stress - defining the yield surface size, $\sigma^0{}_j$ - and equivalent plastic strain, ε^{-pl}.

The combined isotropic/kinematic hardening model is schematically presented in Fig. 5.5 [112].

Due to the complex nonlinear behaviour of the structural steel under cyclic loading regime, a special attention was given to the hardening rule. The nonlinear kinematic component responsible for the translation of the yield surface in the stress space through the backstress $\boldsymbol{\alpha}$ is based on the additive decomposed model proposed by Lemaitre and Chaboche in 1990 [115]. Five decomposed backstresses, $\alpha_{k=1..5}$, were considered to properly capture the nonlinear kinematic behaviour, thus allowing for close predictions. Each backstress is characterized by a set of material parameters, C_k and γ_k, where C_k is the kinematic hardening modulus and γ_k is the decreasing rate of C_k with respect to increasing plastic deformation, ε^{pl}. For the first backstress, α_1,

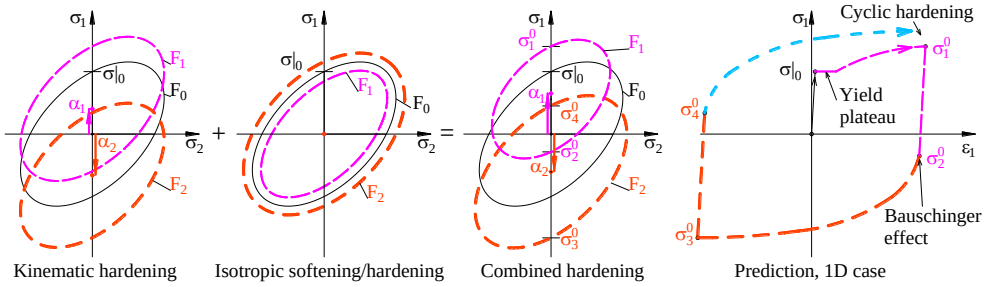

Fig. 5.5. Combined isotropic/kinematic hardening model

(corresponding to small plastic strains) large C_1 and γ_1 values are assigned to assure a smooth and quick transition from the elastic to the plastic behaviour. For the other backstresses, smaller values are assigned to C_k and γ_k since the slope of the stress-strain curve decreases. A linear backstress, α_5 (which corresponds to large plastic strains) is considered for $\gamma_5 = 0$ [112].

The isotropic hardening component is defined using a multilinear hardening model, which allows for different slopes of the hardening law. Therefore, the yield plateau can be simulated using a negative slope (softening), the cyclic hardening using a positive slope (hardening), while the failure using a negative slope (softening) [112].

5.1.5 Calibration procedure using cyclic tests

The calibration procedure refers to the determination of the parameters describing the elastic and plastic behaviour of the material model. The elasticity can be modelled using an elastic modulus of E_s = 210000 N/mm^2 and a Poisson's ratio of ν = 0.3. As regarding the definition of cyclic plasticity, the parameters describing the kinematic and isotropic hardening laws can be calibrated based on uniaxial cyclic tests under strain control loading regime. The procedure described in [104] was used for calibration and is presented below [112].

When performing experimental material tests, the measurements are usually expressed as the force (N) per unit undeformed cross-sectional area (A_0) of the specimen, called engineering or nominal stress ($\sigma_{nom} = N/A_0$), and the change in length (L) per unit undeformed monitored length (L_0), called engineering or nominal strain ($\varepsilon_{nom} = L/L_0$). When defining metal plasticity in Abaqus, true stress, $\sigma = \sigma_{nom}(1+\varepsilon_{nom})$, and logarithmic strain, $\varepsilon = ln(1+\varepsilon_{nom})$, relations must be used (Fig. 5.6.a) [112].

The kinematic hardening component is calibrated by using the "stabilized cycle" procedure defined in [104]. Abaqus automatically determines the material parameters C_k and γ_k describing the evolution of each of the five backstresses, $\alpha_{k=1..5}$, by using the "built-in" fitting subroutine. Data pairs (σ_i; ε_i^{pl}) from the stabilized cycle (corresponding to the saturated yield stress, σ^0_s) must be provided with the strain axis shifted to ε^0_p (Fig. 5.6.b). The plastic strain corresponding to σ_s is expressed as $\varepsilon_i^{pl} = \varepsilon_I - \sigma_i/E_s - \varepsilon^0_p$, thus ($\sigma_1$; 0.0). It is important to properly establish the onset of plastic hardening with respect to the Bauschinger effect: the first data pair (σ_1; ε_1^{pl}) corresponds to $2(\sigma_{|0} + R)$, where $R = \Sigma^s_{j=3}(R_j) = \Sigma^s_{j=3}(\sigma^t_j - \sigma^t_{j-1})$ is the amount of isotropic hardening recorded until the saturated cycle, $j = 1..s$. For the first and

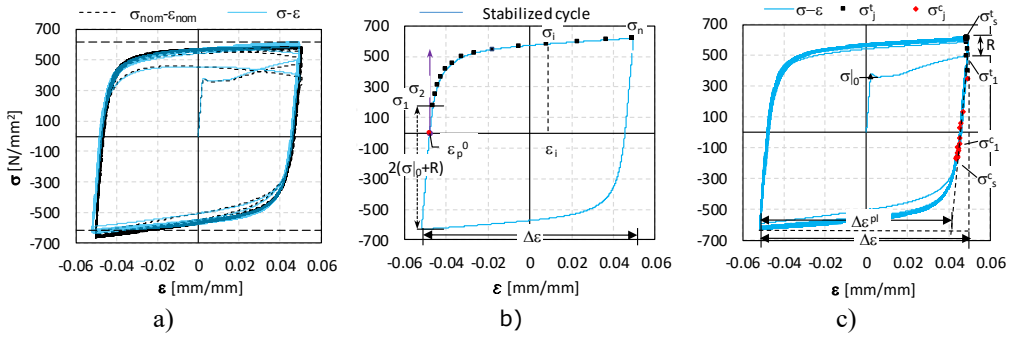

a) b) c)

Fig. 5.6. Stress-strain curves: a) engineering (nominal) vs. true, b) kinematic hardening, c) cyclic hardening

second cycle (j = 1, 2) the corresponding amount of cyclic hardening (R_j) is difficult to be determined due to the presence of the yield plateau. Therefore, the values for $R_{j=1,\,2}$ were determined based on trial and error. The evolution of R_j with respect to cycle number is presented in Fig. 5.7.a. The calibrated parameters defining the kinematic hardening component are presented in Table 5.1. The evolution of the backstress α with respect to plastic strain ε^{pl} is graphically presented in Fig. 5.7.b [112].

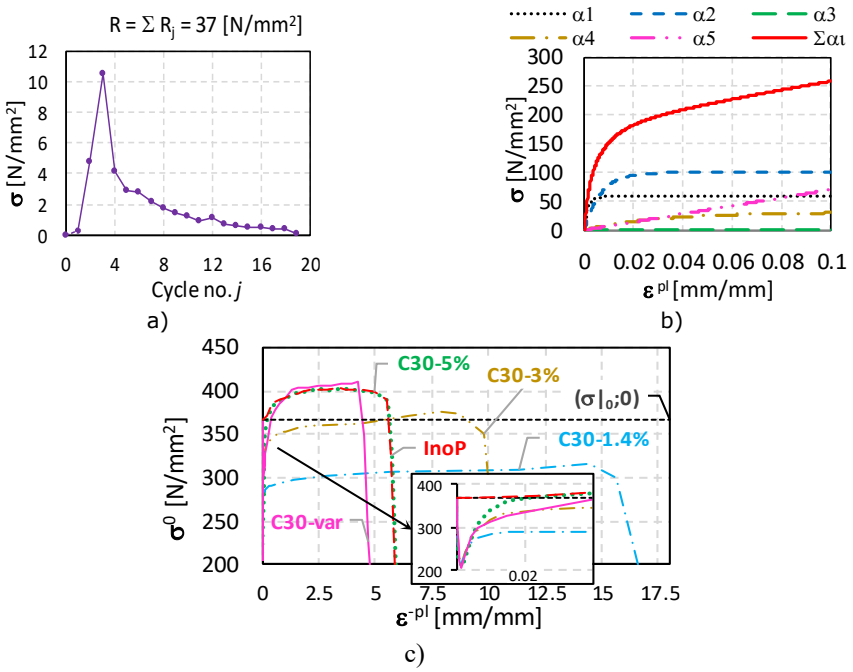

Fig. 5.7. Evolution of: a) R_i, b) α, c) σ^0

Table 5.1 Calibrated parameters defining kinematic hardening component

$\sigma\|_0$, $\frac{N}{mm^2}$	C_1, $\frac{N}{mm^2}$	γ_1, -	C_2, $\frac{N}{mm^2}$	γ_2, -	C_3, $\frac{N}{mm^2}$	γ_3, -	C_4, $\frac{N}{mm^2}$	γ_4, -	C_5, $\frac{N}{mm^2}$	γ_5, -
367.08	41513	697	15152	137.5	600	4.6	255	2.2	195	0

The isotropic hardening component is calibrated using the entire data from the symmetric strain-controlled experiment. Thus, the evolution of the size of the yield surface (σ^0) over the entire loading history can be determined. For the current cycle (j > 1), the strain range is $\Delta\varepsilon$ (Fig. 5.6.c), and the plastic strain range can be obtained by deducting the elastic part, $\Delta\varepsilon^{pl} = \Delta\varepsilon - 2\sigma^t_j/E_s$. Special consideration needs to be taken in the case of the first (tensile) cycle (j = 1), since the elastic strain range is $\Delta\varepsilon_1 = \Delta\varepsilon/2$ and the plastic strain range is $\Delta\varepsilon_1{}^{pl} = \Delta\varepsilon_1 - 2\sigma^t_1/E_s$. In Abaqus, the size of the yield surface at corresponding equivalent plastic strains must be defined by providing data pairs (σ^0_j; ε^{-pl}_j). The equivalent stress is obtained from the peak tensile stress (σ^t_j) by eliminating the kinematic component, $\sigma^0_j = \sigma^t_j - \alpha_j$, where $\alpha_j = (\sigma^t_j + \sigma^c_j)/2$, with σ^c_j the compressive yield stress corresponding to cycle j. The

corresponding equivalent plastic strain (ε^{-pl}_j) can be determined as a function of cycle number and plastic strain range, $\varepsilon^{-pl}_j = 0.5(4j - 3)\ \Delta\varepsilon^{pl}$. For the first cycle, $\varepsilon^{-pl}_1 = \varepsilon^{pl}_1$.

Due to the limitations of the isotropic hardening model [104], the calibration needed to be performed for each cyclic experiment, thus resulting different input (σ^0_j;ε^{-pl}_j) curves, as presented in Fig. 5.7.c (*C30-1.4%*, *C30-3.0%*, *C30-5.0%*, *C30-var*). It can be observed that the isotropic input is loading history dependent. In addition, two isotropic inputs were also obtained: ($\sigma|_0$; 0.0) – no isotropic hardening; *InoP* – isotropic hardening without initial yield plateau [112].

An application of this material model is presented in the following paragraphs.

One cubic finite element of type *C3D8I* (incompatible mode eight-node linear brick element) was used as FEM model for the material calibration process (Fig. 5.8.a). The reason for choosing a unitary cube is related to the strain ranges of the loading protocols which are smaller than the value of the strain corresponding to the ultimate stress (ε^u_{nom} = 17.24 %), and therefore no necking appears. Thus, material failure mode is caused by low-cycle fatigue [112].

No transversal deformations were limited (U_x = U_z = free, where U_i is translational degree of freedom corresponding to axis *i*) to allow for the Poisson effect. The loading protocol is applied at the top (U_y) as displacement control. By using this procedure, the required strain amplitudes can be easily simulated. Different combinations of kinematic (*KIN*) and isotropic (*ISO*) hardening were used to prove the necessity of using a multilinear isotropic hardening capable of simulating both the yield plateau and the cyclic hardening, as presented in Fig. 5.8.b-d. The Static-General Abaqus procedure with nonlinear effects of large deformations and displacements was used to run the cyclic analyses [112].

The predictions using the complex combined hardening model are presented in Fig. 5.9. As a general observation, the material model can reproduce the experimental results with a high level of accuracy, including bot cyclic behaviour and failure mode of the specimens [112].

Based on these numerical results, it was recommended to use the combined hardening material model for simulating the core of the BRBs.

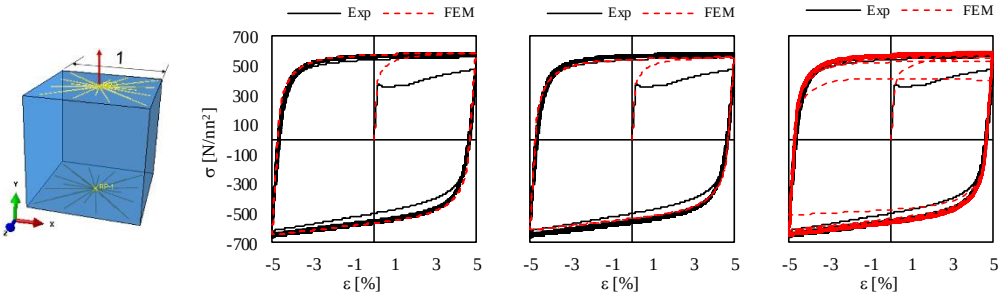

U_x=U_z=free, U_y=load control
a)

KIN = stabilized
ISO = no
b)

KIN = stabilized
ISO = ($\sigma|_0$; 0.0)
c)

KIN = stabilized
ISO = InoP (no-plateau)
d)

Fig. 5.8. a) FEM model, b) – d) unsatisfactory predictions using inappropriate isotropic input

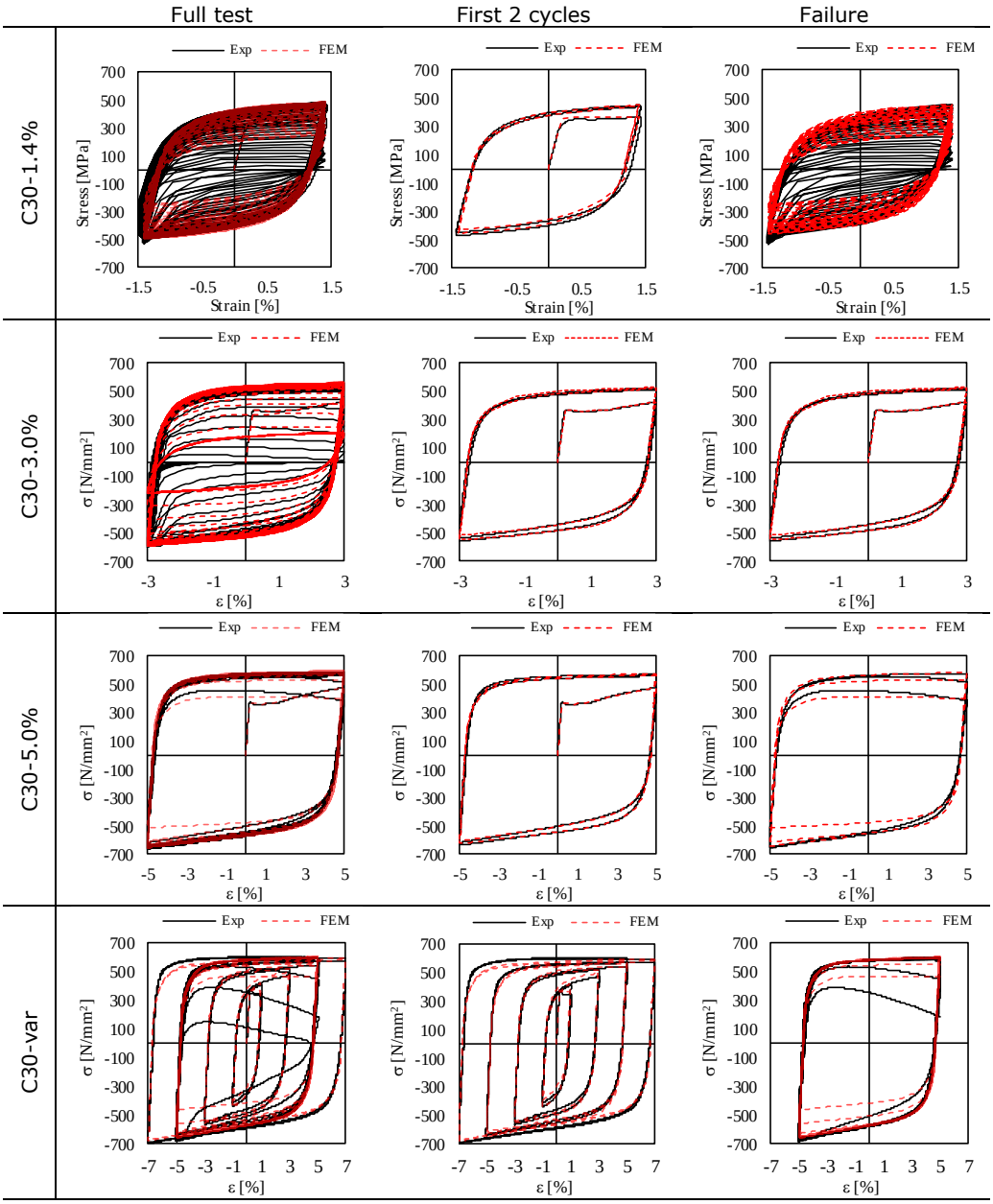

Fig. 5.9. FEM predictions using the combined hardening model

5.1.6 Calibration procedure using tensile tests

Calibration of the parameters of combined isotropic-kinematic hardening material model using cyclic test data requires good knowledge of the plasticity theory and the implementation of the model into Abaqus FEM software. On the other side, cyclic tests are more difficult to be performed and requires special equipments as to performed strain controled tests. Therefore, a simplified calibration procedure using only tensile test data is presented in this chapter using an analytic approach developed on the basis of the research performed by Hu et al. [150].

Hu et al. [150] developed a user material subroutine (UMAT) which can be used with implicit integration procedures (Abaqus/Standard). As in this thesis all the simulations were performed using the Abaqus/Explicit procedure due to high nonlinearities (material, geometrical, contacts), the UMAT proposed in [150] can not be used and, therefore, built-in material models available in Abaqus/Explicit had to be considered. The calibration procedure proposed in [150] had to be modified as to adjust to the requirements of the built-in models regarding input parameters.

It needs to be mentioned that the parameters calibrated with the proposed simplified calibration procedure can be used with both Abaqus/Standard and Abaqus/Explicit integration shemes.

Considering a monotonic tensile test as schematically presented in Fig. 5.10, the proposed calibration procedure uses as input the mechanical properties summarized in Table 5.2. The engineering stress (f) and strain (e) values obtained from the test must be transformed to true values (Cauchy stress σ and logarithmic strain ε) using the formulas:

$$\sigma = f(1 + e) \tag{5.1}$$

$$\varepsilon = \ln(1 + e) \tag{5.2}$$

As presented in Table 5.2, for simplification reasons and based on experimental observations, several assumptions were made regarding the rupture strength f_r (stress), yield strain e_y, strain corresponding to ultimate strength e_u. The other mechanical properties must be obtained from the uniaxial monotonic tensile test.

Within the proposed calibration procedure, the elastic modulus of steel is considered E_s = 210000 N/mm^2 and the Poisson's ratio ν = 0.3.

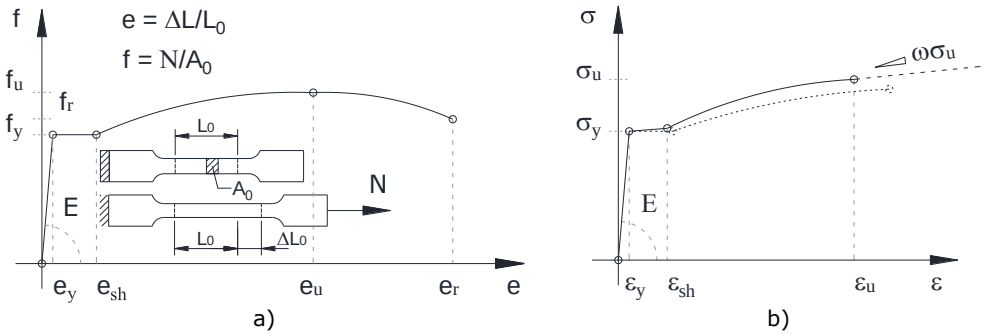

Fig. 5.10. Schematic representation of characteristic a) engineering stress-strain curve and b) true stress-strain curve under monotonic tensile loading

Table 5.2 Mechanical properties from tensile test used in the simplified calibration procedure

Mechanical property	Engineering value	True value
yield strength	$f_y = \text{input}$, N/mm^2	$\sigma_y = f_y(1+e_y)$
ultimate strength	$f_u = \text{input}$, N/mm^2	$\sigma_u = f_u(1+e_u)$
rupture strength	$f_r = 0.8 \cdot f_u$, N/mm^2	$\sigma_r = f_r(1+e_r)$
yield strain	$e_y = f_y/E$, mm/mm	$\varepsilon_y = ln(1+e_y)$
end of plateau strain	$e_{sh} = \text{input}$, mm/mm	$\varepsilon_{sh} = ln(1+e_{sh})$
ultimate strain	$e_u = 0.55 \cdot e_r$, mm/mm	$\varepsilon_u = ln(1+e_u)$
rupture strain	$e_r = \text{input}$, mm/mm	$\varepsilon_r = ln(1+e_r)$

Within the procedure described in [150] several assumptions are made, and additional simulations and calibrations of specific parameters are required. In this thesis, all the other derived parameters are determined based on the input data from Table 5.2, therefore no additional simulations or empirical assumptions are required.

In the cathegory of input (derived) parameters it can be also considered the weighted average factor *w* [150], which can be directly determined using the formula:

$$w = 1 - 0.1(1/e_r) \tag{5.3}$$

As presented in chapter 5.1.4, the combined hardening model consists of two components: a (main) kinematic hardening component which ca be linear or nonlinear, and an (optional) isotropic component which ca be linear, multilinear or nonlinear. Within this simplified calibration procedure, a nonlinear kinematic and a multilinear isotropic hardening component are considered.

The parameters defining the kinematic component of the combined hardening model can be simply defined using the formulas presented bellow:

$$\sigma|_0 = \sigma_y \tag{5.4}$$

$$C_1 = \frac{\sigma_u - f_y(1+e_{sh})}{2} \cdot \frac{\gamma_1}{3} \tag{5.5}$$

$$\gamma_1 = 10 \cdot \mathrm{w} \cdot \gamma_2 \tag{5.6}$$

$$C_2 = \frac{\sigma_u - f_y(1+e_{sh})}{2} \cdot \frac{\gamma_2}{3} \cdot 1.8 \tag{5.7}$$

$$\gamma_2 = \frac{\sigma_u - f_y(1+e_{sh})}{2} \cdot \frac{1}{5(\varepsilon_u - \varepsilon_{sh})} \tag{5.8}$$

$$C_3 = \left[\frac{\sigma_u - f_y(1+e_{sh})}{2} - C_4\left(\varepsilon_u - \frac{\sigma_u}{E} - \varepsilon_{sh}\right)\right] \cdot \gamma_2 \cdot 1.66 \tag{5.9}$$

$$\gamma_3 = \frac{e_{sh}}{e_y} \tag{5.10}$$

$$C_4 = \frac{\mathrm{w} \cdot \sigma_u}{1 - \mathrm{w} \cdot \sigma_u/E} \cdot 1.2 \tag{5.11}$$

$$\gamma_4 = 0.075 \cdot \gamma_3 \tag{5.12}$$

where: $\sigma|_0$ is the (true) yield stress at zero plastic strain, C_k are the kinematic hardening moduli and γ_k are and their corresponding decreasing rate with respect to increasing plastic deformation.

The kinematic parameters must be introduced in the following order in the "Parameters" "Data type" of combined model:

$$\mathrm{KIN} = \left[\sigma|_0,\ C_1,\ \gamma_1,\ C_2,\ \gamma_2,\ C_3,\ \gamma_3,\ C_4,\ \gamma_4\right] \tag{5.13}$$

The evolution of the isotropic component is more difficult to be determined due to: (1) specific features of the mild carbon steel under monotonic and cyclic loading, see chapter 5.1.2; (2) limitations of the Abaqus "built-in" cyclic (isotropic) hardening model – loading history dependent. To capture the main features of the mild carbon steel (yield plateau, Baushinger effect, cyclic hardening) the definition of the isotropic component must be of tabular data type, defined similarly as in chapter 5.1.5. The evolution of the size of the yield surface (σ^0) over the entire loading history can be specified directly by providing data pairs ($\sigma^0{}_j$; $\varepsilon^{pl}{}_j$).

The calibration of the input data pairs for the isotropic component can be performed considering a (fictional) tensile test with a large strain (e.g. $\Delta\varepsilon^{pl}$ = 2.0). The equivalent stresses, $\sigma^0{}_j$, corresponding to the equivalent plastic strains, $\varepsilon^{pl}{}_j$, can be obtained by using an incremental procedure (j = current increment):

$$\begin{aligned} \sigma_j^0 &= \sigma_{j-1}^0, && if\ \bar{\varepsilon}_j^{pl} = 0 \\ &= \sigma_{j-1}^0, + (R_j - R_{j-1}) && if\ \bar{\varepsilon}_j^{pl} > 0 \end{aligned} \qquad (5.14)$$

$$(\text{for } j = 1,\ \sigma_0^0 = \sigma|_0)$$

where, R_j is the amount of isotropic hardening at increment j,

The variation of R_j with respect to the equivalent plastic strain $\varepsilon^{pl}{}_j$ can be obtained using the superposition of several isotropic hardening rules (as in the case of the kinematic component) to properly capture the main features of the mild carbon steel under monotonic and cyclic loading:

$$R_j = R_j^{s1} + R_j^{s2} + R_j^{h1} + R_j^{h2} + R_j^{h3} \qquad (5.15)$$

$$(\text{for } j = 1,\ R_1 = 0)$$

where:

- R_j^{s1} – is the very-short-range nonlinear isotropic softening parameter in plateau region, activates immediately after yielding.
- R_j^{s2} – is the short-range nonlinear isotropic softening parameter in plateau region, activates on the entire plateau region.
- R_j^{h1} – is the short-range nonlinear isotropic hardening parameter in hardening region, activates up to ε_u.
- R_j^{h2} – is the additional short-range or long-range (depending on the case of fitting) nonlinear isotropic hardening parameter.
- R_j^{h3} – is the long-range linear isotropic hardening parameter. This hardening rule is used to provide the combined hardening model with isotropic hardening even at large values of equivalent (cumulative) plastic strain (e.g. ε^{pl} = 2.0).

For the isotropic softening rules ($R_j^{k\,=\,s1,\ s2}$), the following formulas are used to evaluate the amount of reduction of the yield surface at each increment j:

$$\begin{aligned} R_j^k &= Q^k + (R_{j-1}^k - Q^k) \cdot \exp[-b^k \left(\bar{\varepsilon}_j^{pl} - \bar{\varepsilon}_{j-1}^{pl}\right)], && if\ \bar{\varepsilon}_j^{pl} \le \varepsilon_{sh} \\ &= Q^k [1 - \exp(-b^k \cdot \varepsilon_{sh})], && if\ \bar{\varepsilon}_j^{pl} > \varepsilon_{sh} \end{aligned} \qquad (5.16)$$

$$(\text{for } j = 1,\ R_j^k = 0)$$

For the nonlinear isotropic hardening rules ($R_j^{k\,=h1,\ h2}$), the following formulas are used to evaluate the amount of increase of the yield surface at each increment j:

$$\begin{aligned} R_j^k &= 0, && if\ \bar{\varepsilon}_j^{pl} \le \varepsilon_{sh} \\ &= Q^k + (R_{j-1}^k - Q^k) \cdot \exp[-b^k \left(\bar{\varepsilon}_j^{pl} - \bar{\varepsilon}_{j-1}^{pl}\right)], && if\ \bar{\varepsilon}_j^{pl} > \varepsilon_{sh} \end{aligned} \qquad (5.17)$$

$$(\text{for } j = 1,\ R_j^k = 0)$$

For the linear isotropic hardening rule ($R_j^{k\,=h3}$), the following formula is used to evaluate the amount of increase of the yield surface at each increment j:

$$\begin{aligned} R_j^k &= 0, && if\ \bar{\varepsilon}_j^{pl} \le \varepsilon_{sh} \\ &= R^0 \cdot \bar{\varepsilon}_j^{pl}, && if\ \bar{\varepsilon}_j^{pl} > \varepsilon_{sh} \end{aligned} \quad (5.18)$$

(for $j = 1,\ R_j^k = 0$)

The parameters used by the hardening/softening isotropic laws are defined below:

$$Q^{s1} = -\frac{Q^{h1}(\varepsilon_{sh} - \varepsilon_y)}{3 \cdot w \cdot \varepsilon_{sh}} \quad (5.19)$$

$$b^{s1} = 0.5 \cdot b^{s2} \quad (5.20)$$

$$Q^{s2} = -0.7 \cdot Q^{h1} \quad (5.21)$$

$$b^{s2} = \frac{Q^{h1}}{\varepsilon_u - \varepsilon_{sh}} \cdot \frac{1}{2.8} \quad (5.22)$$

$$Q^{h1} = \frac{\sigma_u - f_y(1 + e_{sh})}{2.2} \quad (5.23)$$

$$b^{h1} = \frac{b^{s2} \cdot \varepsilon_{sh}}{\varepsilon_u + \varepsilon_{sh}} \cdot 1.5 \quad (5.24)$$

$$Q^{h2} = \text{additional (user input)} \quad (5.25)$$

$$b^{h2} = \text{additional (user input or} = 2b^{h1}) \quad (5.26)$$

$$R^0 = Q^{h1}\frac{2}{3} \quad (5.27)$$

where Q^k, b^k, R^0 are material parameters and represents:

- Q^{s1} and b^{s1} – are the maximum decrease in size of the yield surface and its corresponding rate, respectively, at very small plastic strains ($\ll \varepsilon_{sh}$).
- Q^{s2} and b^{s2} – are the maximum decrease in size of the yield surface and its corresponding rate, respectively, at plastic strains smaller than ε_{sh}.
- Q^{h1} and b^{h1} – are the maximum increase in size of the yield surface and its corresponding rate, respectively, at plastic strains larger than ε_{sh} but smaller than ε_u (the range of equivalent plastic strain $\bar{\varepsilon}^{pl}$ is not strictly defined). Since the isotropic component is loading history dependent two values can be used for b^{h1} depending on the type of loading (calibration): for monotonic loading it is recommended that $b^{h1} = \ldots \cdot 1.5$, while for cyclic loading $b^{h1} = \ldots \cdot 1.0$.
- Q^{h2} and b^{h2} – have similar meanings as Q^{h1} and b^{h1} and they are additionally used in cases where using only Q^{h1} and b^{h1} the calibration is not properly achieved over the range $\varepsilon_{sh} < \bar{\varepsilon}^{pl} \le \varepsilon_u$.
- R^0 – is the slope of the equivalent stresses $\sigma^0{}_j$ on the hardening region.

The above presented calibration procedure was validated against experimental tests performed within the frame of IMSER [6] and EQUALJOINTS [7] research projects. Mild carbon steels with yield plateau (steel grade S355) were used for assessing the capability of the proposed analytical formulas in providing input parameters for the combined hardening material model that yield reliable numerical predictions. The mechanical properties obtained from the tensile tests are summarized in Table 5.3.

Fig. 5.11 presents the influence of considering or not the isotropic component of the combined hardening material model in predicting the monotonic and cyclic behaviour of mild carbon steel with yield plateau. It can be observed from Fig. 5.11.a that using only the kinematic component the material model can not predict the monotonic or the cyclic behaviour of steel that was experimentaly obtained (*test-1-S355*). For the monotonic case, it can only accurately predict the yield and the

Table 5.3 Mechanical properties from tensile tests of steels used for the validation of the simplified calibration procedure

	test-1-S355	*test-2-S355*	*test-3-S355*	*test-4-S355**	*test-5-S355**
f_y, N/mm^2	363	345	349	398	398
f_u, N/mm^2	525	522	534	509	509
f_r, N/mm^2	420	417	374	331	331
e_y, mm/mm	0.0017	0.0016	0.0017	0.0019	0.0019
e_{sh}, mm/mm	0.0140	0.0170	0.0150	0.0180	0.0180
e_u, mm/mm	0.1650	0.1746	0.1655	0.1634	0.1634
e_r, mm/mm	0.3000	0.3880	0.3246	0.3230	0.3230

* *test-4-S355* and *test-5-S355* characterizes the same material. Since two coupon specimens were cyclicaly tested, therefore, individual IDs were assigned to each specimen/cyclic test.

ultimate strength, while for the cyclic case of loading the model underestimates the stress level and the capacity of energy dissipation.

Using both isotropic and kinematic components of the combined model acceptable predictions can be obtained for both monotonic and cyclic cases (Fig. 5.11.b). For the monotonic tensile simulation, the prediction is accurate up to the ultimate strength. Beyond this point the model can not accurately predict the failure (necking region) due to the fact that the calibration of the input parameters was performed to properly predict the cyclic response. In the case of the cyclic test, close predictions are obtained at all strain ranges. If the monotonic case is the target for the calibration, then the parameters describing the isotropic component can be modified, as follows: $b^{h1} = \ldots \cdot 1.5$ and $R^0 = Q^{h1} \cdot x/3$, where x can take values from $x = 0.002 \div 0.2$.

In Fig. 5.12 are presented the stress-strain predictions for the other tensile and cyclic tests (experimental results from EQUALJOINT project [7]). Considering the same observations as in the case of the *test-1-S355*, in all cases an acceptable level of correlation is observed with respect to the experimental results.

Based on these results, it can be concluded that the simplified calibration procedure proposed by the author in this thesis can yield numerical predictions with an acceptable level of accuracy for both tensile and cyclic loading. The great advantage of this calibration procedure is that it uses only tensile tests results for the calibration of input parameters wich can be used for both monotonic and cyclic loading histories. To allow for developing a database with input parameters (to be used for FEM simulations) for different steel grades, the procedure should be also validated agains different steel grades (S235, S275) which exhibits yield plateau.

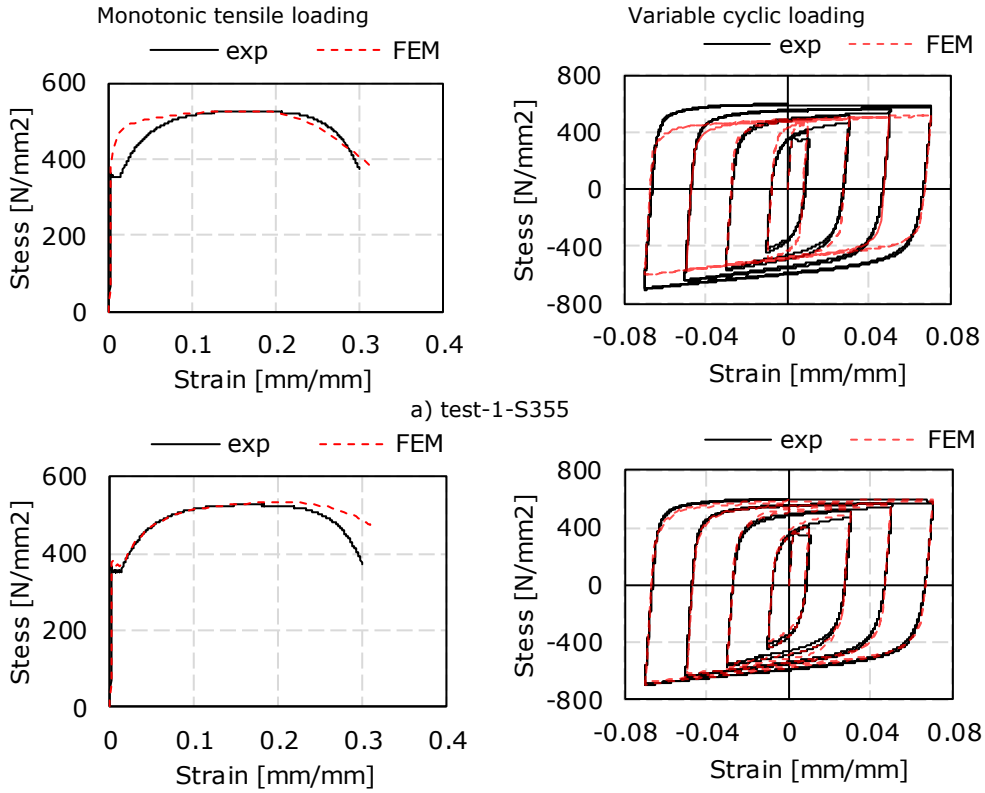

Fig. 5.11. FEM predictions using parameters calibrated with the simplified procedure: a) kinematic parameters only, b) kinematic and isotropic parameters

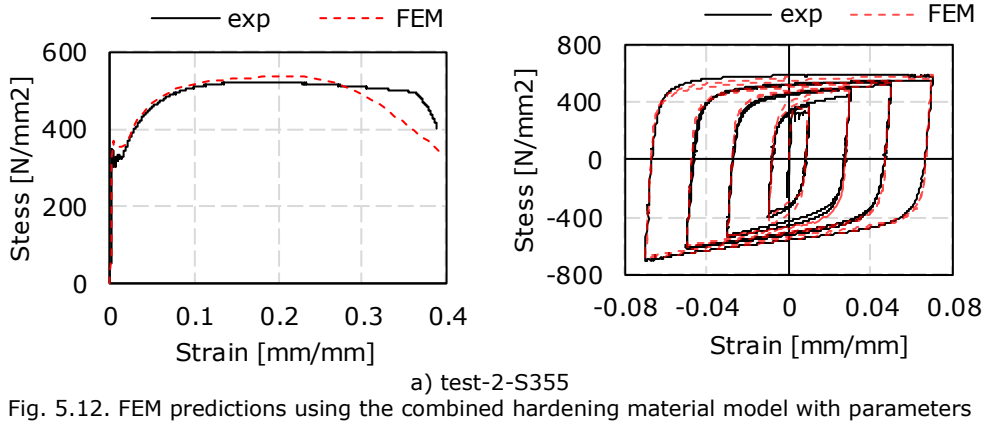

Fig. 5.12. FEM predictions using the combined hardening material model with parameters calibrated using the simplified procedure

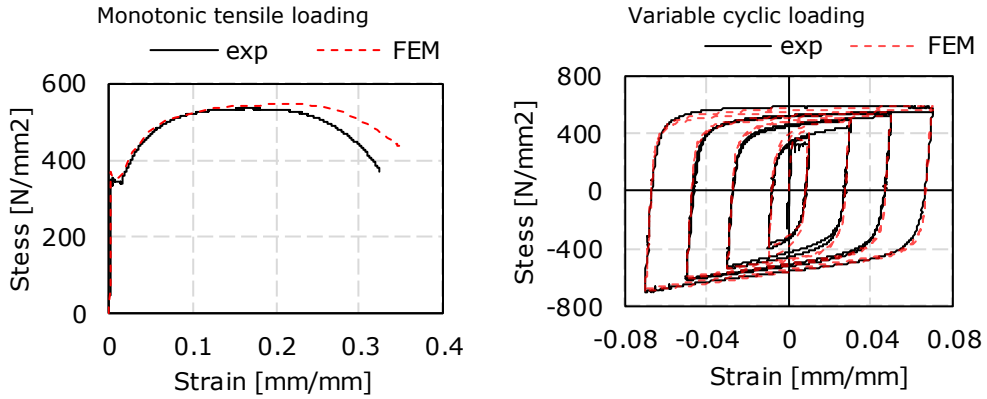

b) test-3-S355

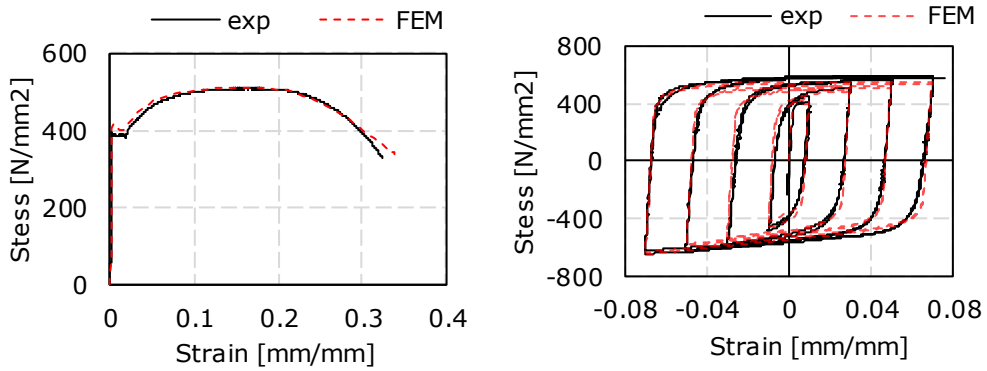

c) test-4-S355

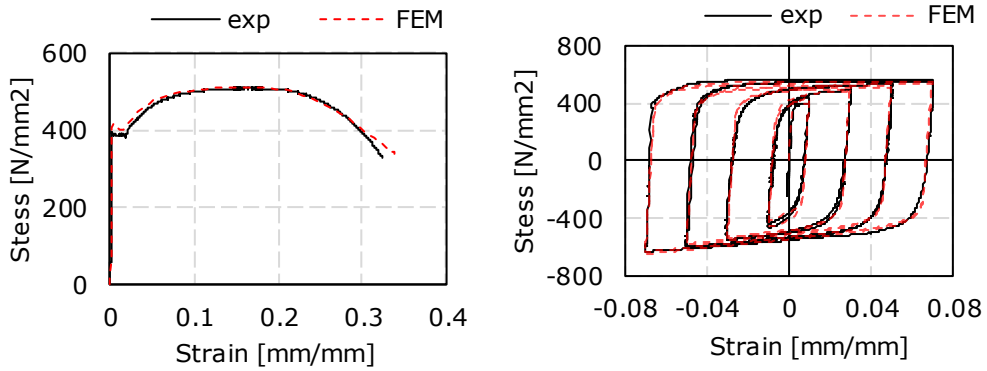

d) test 5: S355

Fig. 5.12. FEM predictions using the combined hardening material model with parameters calibrated using the simplified procedure (continued)

5.2 Finite element analysis of BRBs

5.2.1 Introduction

Though experimental tests are indispensable in development and validation of a new structural component [116], [117], numerical models are a powerful tool in understanding its response and development of improved solution [118]. The Finite Element Method (FEM) was used since early 1990's to evaluate the behaviour and to propose design recommendations for BRBs. In 1992 Inoue et al. [119] used the FEM method to create a two-dimensional model used for determining the size of the reinforced concrete panels depending on the width of the core (steel plate). In 1996, Saeki et al. [120] developed and calibrated against experimental results a three-dimensional nonlinear model for BRBs made up of a steel core encased in mortar-filled rectangular steel tube. The FEM model was further used by Saeki et al. [121] to perform parametric studies for assessing the position of the BRB in a steel frame. Simplified BRB models were used by Matsui et al. [122] to investigate the failure modes of the buckling restraining mechanism (BRM) due to local buckling. Korzekwa and Tremblay [118] calibrated a FEM model for all-steel BRBs (BRM is a steel assembly) and concluded that the model could be further used for optimizations of BRB components. Different solutions for the BRM were also investigated by Rahai et al. [123], Tinker [124], Rahai and Mortazavi [125], Yazdi et al. [126]. Influence of the plastic to total length ratios of the core on the energy dissipation capacity were investigated using FEM by Pandikkadavath and Sahoo [127]. FEM method was also used to investigated possible failure modes of the BRBs [128]. During the last decade, new conceptual designs of BRBs were developed based on numerical simulations: reduced length BRBs [129], ultra-lightweight BRBs [130]; inspectable BRBs [131]; self-centering BRBs [132], and others. As the FEM computer programs evolved in complexity, even coupled nonlinear thermal-stress analyses could be performed on three-dimensional BRB models with either circular [133] or rectangular cross-section [134]. [135]

Based on the above-mentioned studies, it can be concluded that, if using proper modelling hypotheses, the FEM analyses can be used as a reliable method to investigate parameters that could not be evaluated or observed during the experimental tests on BRBs [135].

Therefore, this chapter presents the development of a finite element model of a buckling restrained brace in Abaqus [104] software package and its validation with experimental results. Calibration at both component and BRB level is presented in detail. The numerical model is used to investigate in detail the tested BRBs, to validate the design methodology of the buckling restraining mechanism, to determine the appropriate class of concrete to be used for the infill material, to determine the influence of the steel grade of the core, and to assess the influence of the frame effect on the BRB cyclic behaviour [135].

5.2.2 Calibration of a finite element model

5.2.2.1 Model description

Throughout the years, FEM models of different levels of complexity were proposed for BRBs. Two-dimensional models were used by Eryasar [136] and Gena and Gelfi [137], while three-dimensional models were used by Budahazy and Dunai [138], and AlHamaydeh et al. [128], among others. To reduce computational time,

quarter models were preferred by several researchers, Saeki et al. [120], Mustapha [139], Montazerian and Mohammadreza [140]. To consider in plane bending of the core, half-length models were used by Korzekwa and Tremblay [118]. The predictions of full and quarter models under cyclic loading was investigated by AlHamaydeh et al. [128] and close matching was obtained [135].

Half or quarter models offer the advantage of reduced number of finite elements and, consequently, smaller computational time. However, these models are not appropriate when the response of the BRB is not symmetrical, as might be caused by gravity loading. Considering that one of the objectives of this study was assessment of the effect of gravity loading on the response of a BRB, a three-dimensional full model was used [135].

Finite element models were created for each BRB specimen of "conventional" type that was experimentally tested [108]. All BRB models have several common features: types of finite elements, type of material models, boundary conditions, geometrical nonlinearities, contact laws. The differences between the models relate to the geometry and material input. Fig. 5.13 presents a summary of FEM modelling per BRB typology [135].

A special interest was given to the discretization of the steel core since it is the only component supposed to undergo large plastic deformations under repeated cycles. Different finite elements were used by researchers to discretize the core: shell elements [122], [136], [123], first order brick elements [141], [142], or second order brick elements [118], [143]. In this study the core was modelled using incompatible mode eight-node linear brick elements, *C3D8I*, which are appropriate to model bending with contact interactions and avoid shear locking or hourglass modes [104]. Two finite elements per thickness were used (as recommended by Korzekwa and Tremblay [118]) and, for the plastic zone, an aspect ratio of approximatively 1:1 was considered, thus resulting cubic finite elements (FE). A finer mesh was assigned to the plastic zone (FE size approx. 10 mm), while a coarser mesh for the elastic zones (FE size approx. 20 mm) [135].

Several modelling approaches were used for the buckling restraining mechanism, BRM. A simplified shell or beam model was used by Matsui et al. [122] and Tinker [124], respectively. Other researchers explicitly modelled the concrete-infill with brick elements and the tube with shell elements [123], [144]. In this study, the components of the BRM were modelled explicitly and discretized using a coarse mesh. The concrete part was modelled using eight-node linear brick elements with reduced integration and hourglass control, *C3D8R*, with a global mesh size of 20 mm. The steel tube and the caps were modelled using a four-node doubly curved shell with reduced integration and hourglass control, *S4R*, due to their reduced thickness, with a global mesh size of 20 mm [135].

The unbonding material was not modelled explicitly due to its reduced thickness. Instead, a core-to-concrete gap and a contact law were used, as discussed in chapter 5.2.2.4. The polystyrene parts placed at the end of transition zones were modelled using a gap of length L_G = 70 mm [135].

A general contact was defined. The contact domain consists of two selected surface pairs having different contact properties, as follows. The core–to–concrete interaction was defined as having the tangential behaviour of "penalty" type with the friction coefficient set to 0.1 and the normal behaviour set to "hard" contact. The steel casing-to-concrete interaction had the same properties except the friction coefficient set to 0.4. In both cases, the metallic surfaces were considered "master" in the contact formulation to avoid excessive penetrations and numerical errors. Also, a coupling

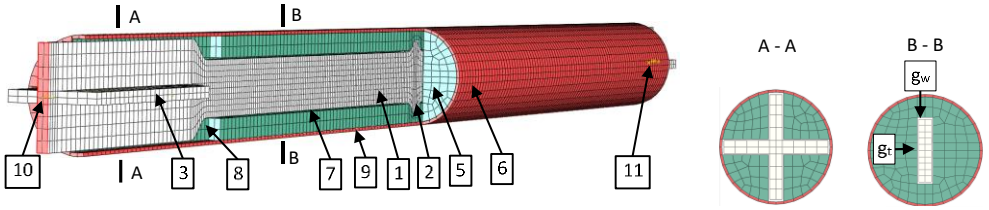

a) Buckling restrained brace of type A

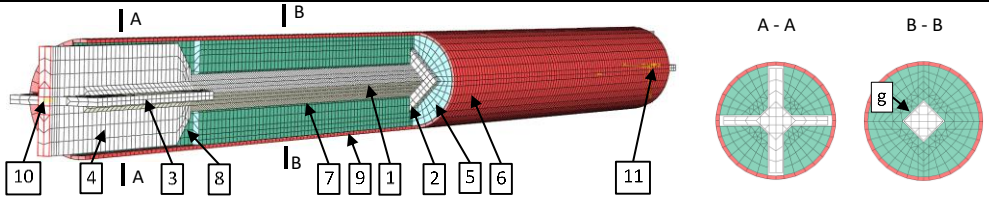

b) Buckling restrained brace of type B

- 1 - Core: mesh size 10 & 20 mm; *C3D8I*; steel – combined isotropic-kinematic hardening material.
- 2 - Stopper: mesh size 10 mm; *C3D8I*; steel – combined isotropic-kinematic hardening material.
- 3 - Stiffener: mesh size 20 mm; *C3D8I*; steel – combined isotropic-kinematic hardening material.
- 4 - Core extension plate: mesh size 20 mm; C3D8I; steel – combined isotropic-kinematic hardening material.
- 5 - Concrete: mesh size 20 mm; *C3D8R*; concrete – plastic (rectangular core BRBs) / elastic (square core BRBs) material model.
- 6 - Tube: mesh size 20 mm; S4R; steel – kinematic hardening material.
- 7 - Unbonding interface: gap + contact law (normal "hard"; tangential "Penalty", 0.1 friction coefficient). Core-to-concrete gap: through thickness/width direction, g_t / g_w; uniform gap, g.
- 8 - Gap for compression stroke, L_G = 70 mm.
- 9 - Contact law: concrete-to-tube composite effect (normal "hard"; tangential "Penalty", 0.4 friction coefficient).
- 10 - Fixed support-1: (U_x = U_y = U_z = UR_y = UR_z = UR_x = constrained).
- 11 - Fixed support-2: (U_x = UR_y = UR_z = constrained; U_z / U_y / UR_x = applied longitudinal / transversal / rotational cyclic loading).

Fig. 5.13. Finite element model

constraint was defined at each end of the core, by connecting a reference point to the end surface of the core using kinematic coupling [135].

5.2.2.2 Boundary conditions and loading

To the knowledge of the author, there are no numerical studies on BRBs that considers both the cyclic and the gravity loadings. Furthermore, if rigid (bolted or welded) BRB-to-gusset connections are used to insert the BRB in the (testing) frame, additional bending moments are transmitted to the BRB ends due to the frame effect (opening and closing of the beam-to-column angle). These additional moments were modelled by Saeki et al. [121] using an "obliquely loaded model", while Dusicka and Tinker [130] used load eccentricity applied each BRB end. As regarding the applied

cyclic loading, most researchers used the displacement control applied to either one end [130] or to the both ends of the BRB [91]. [135]

In this study the definition of the boundary conditions consisted in assigning fixed supports at the BRB ends (at the reference points) and applying the gravity and the cyclic load to assure similar conditions as in the experimental tests. The supports have the translational (U_i) and rotational (UR_i) degrees of freedom constrained with respect to axis i [135].

The gravity load was applied taking into account the position of the specimen in the experimental setup. Special consideration was given to modelling the cyclic load due to the fact that the BRBs were experimentally tested using the BRB-column sub-assemblage setup. This setup causes frame effects due to opening and closing of the angle α, Fig. 5.14.a, during the tension/compression phases. In the finite element model of the testing sub-assemblage, the column and the gusset-plate connections were not modelled, only the BRB in between the gussets. To simulate the frame effect due to rigid body rotation of the column, Fig. 5.14.a, transversal displacement U_y and rotations UR_x were applied at one of the BRB ends, in addition to the axial displacement U_z, Fig. 5.14.b. The axial displacement U_z was given by the axial deformation of the core of the experimental specimen. Displacement U_y and rotation UR_x were determined from displacement U_z assuming rigid-body displacements of the top BRB end [135].

As presented in chapter 4.2, the loading protocol used for experimental tests was based on ANSI/AISC 341-10 [100] provisions, but with additional cycles [135]. The same loading protocol was used for the calibration of the BRB models.

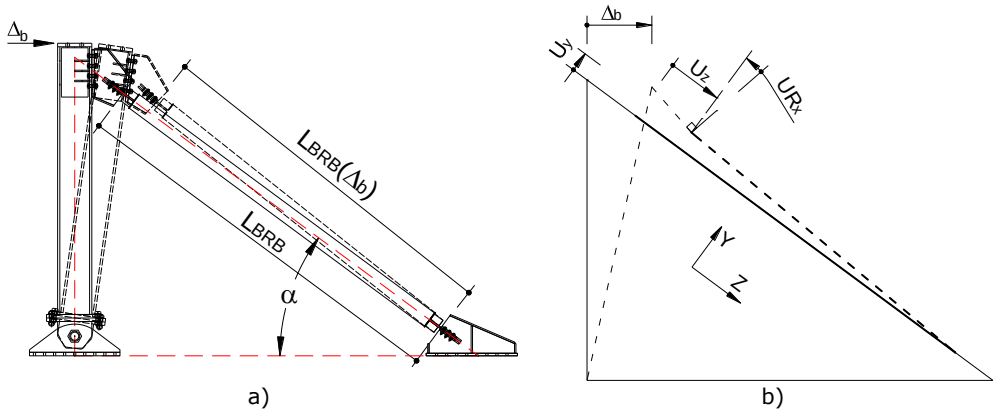

Fig. 5.14. Modelling of cyclic loading: a) rigid-body movement of the BRB-column assembly, b) corresponding components applied to the BRB model

5.2.2.3 *Analysis and validation*

Different Abaqus procedures can be used to solve the nonlinear equations. Static procedures incorporating also numerical techniques to improve the convergence rate were used by Hoveidae and Rafezy [142], Dehghani and Tremblay [145], Yazdi et al. [126]. Explicit formulation was used by Hadianfard et al. [146]. [135]

Due to the high nonlinearity of the full three-dimensional model, the FEM analyses were performed using the Dynamic Explicit solver. Three steps were defined: initial, gravity, cyclic. In the initial step, the model and the initial geometrical

imperfection (see chapter 5.2.2.6) are defined. In the second step, the gravity load is applied using a smooth step amplitude to avoid dynamic effects. In the third step, with the gravity load kept constant, the cyclic load is applied using a smooth step amplitude function to assure a quasi-static analysis. For the last two steps, nonlinear effects considering large deformations and displacements were considered [135].

Assessment of output energy balance must be performed to assure reliable FEM results [118]. The energy balance was monitored to check the analysis: kinetic energy was under 1% of the internal one, thus assuring a quasi-static analysis; artificial energy was also low, under 1% of the internal energy, thus validating the finite elements used (no shear locking of hourglass deformation modes of the elements). External work and internal energy had an almost similar path throughout the analysis, thus validating the results obtained [135].

5.2.2.4 Unbonding material

Due to the fact that the unbonding material has a relatively small thickness compared to the thickness of the core, in most cases it is not modelled explicitly. Instead, a gap and a contact law are used [123], [128], [138]. However, Eryasar [136] used planar shell elements with elastic mechanical properties to explicitly model the unbonding material. In this study the first approach was used [135].

The acrylic tape was modelled by using a gap and a contact law. The size of the gap was set equal to the nominal thickness of the unbonding layer. The definition of the contact law includes a normal "hard" and a tangential "penalty" behavior. For the tangential behavior different values of the friction coefficient (0.05, 0.1, 0.2, 0.3) were numerically tested on the BRB model corresponding to *CS33-1*. The BRB specimen *CS33-1* was chosen for this calibration since the material used to model the core was calibrated based on uniaxial cyclic test data and does not represent an unknown variable. Good agreement with the experimental results (*CS33-1*) was obtained by using a friction coefficient equal to 0.1 (similar valued use in [144]), see Fig. 5.15. Also, the higher the friction (0.2 or 0.3), the higher is the compression overstrength and less ductile is the BRB. Using less friction (0.05) leads to lower compression overstrength and no fracture occurs, contrary to the experimental results [135].

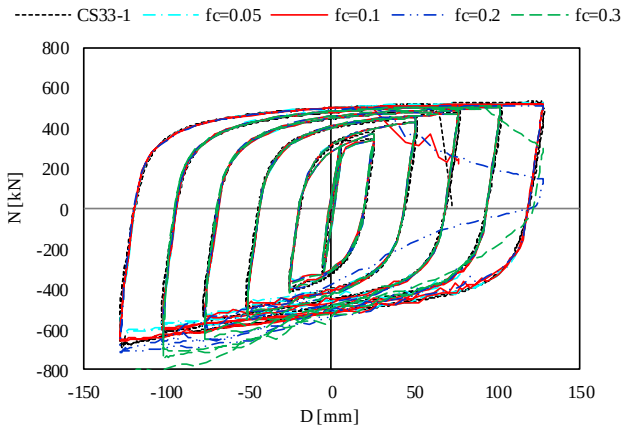

Fig. 5.15. Calibration of the value of the friction coefficient

5.2.2.5 *Material models*

Steel. Built-in material models are generally used to model both the elastic and plastic behavior of BRB steel components. The combined isotropic-kinematic hardening model is used by most researchers to model the steel core as it allows good representation of the Bauschinger and cyclic hardening phenomena [118], [91]. However, for closer predictions user material subroutines were developed and implemented in Abaqus and Ansys finite element computer programs by Piedrafita et al. [69] and Budahazy and Dunai [138], respectively. In this study Abaqus built-in models were used [135].

Two material models with different hardening laws were used for the steel parts of BRBs: kinematic and combined. Both models have the same definition of the elastic component (steel elastic modulus, E_s = 210000 N/mm^2 and Poisson's ratio ν = 0.3), but different definitions of the plastic component [135].

In the case of steel tubes, the plastic hardening behavior was defined using the kinematic option, since the tubes are not expected to experience cyclic plastic deformations. Thus, a simple bilinear model (elastic-plastic with strain hardening) was appropriate for FEM modelling of the tubes. Based on the data from the quality certificates, the kinematic material inputs expressed as true yield stress, σ^0, and true plastic strain, ε^{pl}, were obtained, and are presented in Table 5.4 [135].

A more complex material model, with combined isotropic-kinematic hardening, was used to model the steel core. The model consists of a nonlinear kinematic component and a multilinear isotropic (cyclic) hardening component. Based on the von Misses yield criterium and Chaboche plastic hardening model [147], the combined model can simulate the Bauschinger effect due to cyclic loading [104]. The multilinear definition of the cyclic hardening allows for the simulation of the yield plateau and the increase (or decrease) of the yield surface under repeated cycles at constant strain. Details regarding the calibration of the input parameters of the core material can be found in chapter 5.1.5 [135].

The combined model is loading-history dependent from the point of view of isotropic hardening definition. Therefore, calibration of the isotropic model must be performed using experimental results from a uniaxial coupon test having a loading history similar to the one used for testing the BRBs, with respect to the strain evolution recorded during BRB cyclic testing. Based on these observations, the calibration of the core material *C30* used for BRB FEM model *CS33* was focused on predicting the cyclic behavior under variable amplitude loading. The capability of the combined model to reproduce with a certain level of accuracy both the cyclic and monotonic behavior of mild carbon steel with respect to experimental data is presented in Fig. 5.16.a-b [135].

For the other BRB cores, where no cyclic material test data were available, the calibration of the material model was performed using a trial-and-error procedure using the force (N) – displacement (D) cyclic curve of the BRBs. Having as fixed parameter the yield stress and zero plastic strain, σ^0, the trial and error procedure

Table 5.4 Material inputs for steel tubes

CHS 168.3x4		CHS 177.8x4		CHS 193.7x6.3	
σ^0, N/mm^2	ε^{pl}, mm/mm	σ^0, N/mm^2	ε^{pl}, mm/mm	σ^0, N/mm^2	ε^{pl}, mm/mm
345.6	0.000	460.0	0.000	338.5	0.000
489.9	0.147	645.2	0.129	432.6	0.152

was focused on determining the appropriate values of the kinematic hardening moduli, C_k, and their corresponding decreasing rate, γ_k, with respect to increasing plastic deformation [135].

In Fig. 5.17 calibrated core material inputs are graphically presented for both kinematic, see Fig. 5.17.a, and isotropic component, see Fig. 5.17.b. The calibrated kinematic and isotropic hardening parameters are presented in a tabular form in Table 5.5 and Table 5.6, respectively [135].

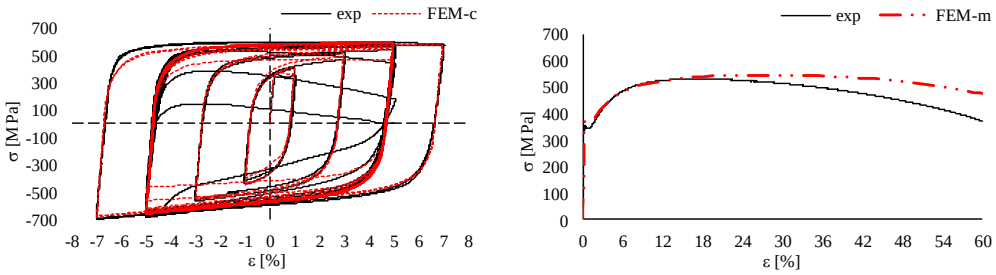

a) cyclic response b) monotonic response

Fig. 5.16. Calibrated FEM response of core material *C30* for specimens *CS33-1* and *CR33-2*

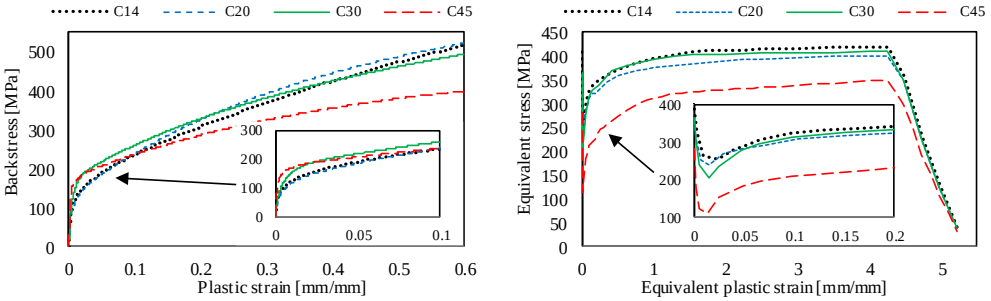

a) kinematic component b) isotropic component

Fig. 5.17. Calibrated inputs of core materials

Table 5.5 Calibrated parameters describing the kinematic hardening of the core material models (σ^0 and C_k in N/mm^2)

Mat.	σ^0	C_1	γ_1, -	C_2	γ_2, -	C_3	γ_3, -	C_4	γ_4, -	C_5	γ_5, -
C14	407.8	45000	850	12600	245	1900	35	630	1.3	210	1
C20	359.5	40000	900	10000	195	2000	67	950	3.5	350	1
C30	367.1	41513	697	15152	137.5	600	4.6	255	2.2	195	0
C45	282.1	95000	1300	40500	680	5000	120	500	2.5	200	2

Concrete. The concrete material model proved to have an important role when calibrating the specimens *CR71-1* and *CR71-2* that buckled during tests. Therefore, the performance of two approaches for modelling the concrete infill were assessed on the FEM model of the *CR71-1* specimen [135].

For modelling infill concrete, tests results on cubes cured in room conditions were used. The mean value of compressive cube strength of concrete is $f_{c,cube}$ = 47.3 N/mm^2. Using the provisions from EN 1992-1-1 [148] the other mechanical properties were determined and are summarized in Table 5.7. The mean value of the compressive cylinder strength of concrete was obtained as $f_{cm} = 0.8 f_{c,cube}$. The linear

Table 5.6 Calibrated parameters of the isotropic hardening for the core material models

C14	σ^0, N/mm^2	407.8	256.7	289.6	324.6	340.0	350.0	370.0
	ε^{-pl}, -	0.0	0.0237	0.0488	0.0962	0.166	0.250	0.500
	(continued)	395.3	412.3	419.5	356.6	38.2		
		1.000	2.00	4.256	4.476	5.226		
C20	σ^0, N/mm^2	359.5	239.2	284.0	312.0	320.0	333.0	358.0
	ε^{-pl}, -	0.0	0.0149	0.0488	0.1035	0.150	0.250	0.500
	(continued)	376.0	390.0	401.0	349.4	37.5		
		1.000	2.00	4.256	4.476	5.226		
C30	σ^0, N/mm^2	367.1	206.1	278.4	313.5	326.8	339.1	368.9
	ε^{-pl}, -	0.0	0.0139	0.0464	0.0966	0.150	0.235	0.424
	(continued)	393.4	404.6	410.2	348.7	37.4		
		0.990	2.00	4.256	4.476	5.226		
C45	σ^0, N/mm^2	282.1	112.0	185.0	211.7	220.5	245.0	274.0
	ε^{-pl}, -	0.0	0.0134	0.0488	0.0974	0.140	0.250	0.500
	(continued)	311.0	329.5	349.8	297.3	31.9		
		1.000	2.00	4.256	4.476	5.226		

elastic compressive limit was set to $0.4f_{cm}$. The mean value of axial tensile strength of concrete, f_{ctm}, was computed based on the characteristic compressive cylinder strength of concrete, f_{ck}, using the equivalent formula, $f_{ctm} = 0.3\ f_{ck}^{2/3}$, where $f_{ck} = f_{cm} - 8$ N/mm^2. The value of the secant modulus of elasticity of concrete was determined as $E_{cm} = 22[(f_{cm})/10]^{0.3}$, with f_{cm} in N/mm^2. The value of the compressive strain in concrete at the peak stress f_{cm} was computed as $\varepsilon_{c1} = 0.7f_{cm}^{0.31} \leq 2.8\ ^0/_{00}$. The plasticity number was determined as $k = 1.05E_{cm}|\ \varepsilon_{c1}|/f_{cm} = 1.96$ [135].

The first approach consists in modelling the concrete parts using an elastic material (similar in [141], [144]), see Fig. 5.18. Secant modulus of elasticity of concrete, E_{cm} = 32795 N/mm^2, and Poisson's ratio, ν = 0.2, define the isotropic elasticity [135].

The second modelling approach uses the Abaqus "built-in" Concrete Damaged Plasticity model, CDP (similar in [128], [125]). The following parameters define the concrete plasticity [104]: dilation angle, $\Psi = 36°$; eccentricity, $\epsilon = 0.1$; ratio of initial equibiaxial compressive yield stress to initial uniaxial compressive yield stress, $\sigma_{b0}/\sigma_{c0} = 1.16$; ratio of the second stress invariant on the tensile meridian to that on the compressive meridian, $K_c = 0.667$; viscosity parameter, $\mu = 0$. The constitutive stress-strain curves used to describe the compressive and tensile behavior of the CDP model are based on a simplified version of the EN 1992-1-1 [148] definition of the nonlinear behavior of the concrete material. As graphically presented in Fig. 5.18, the compressive behavior has the elastic limit set to $0.4f_{cm}$, while the plastic stress-strain relationship is parabolic up to the peak stress f_{cm} and constant afterwards. The tensile behavior is defined as elastic-perfectly plastic, with the elastic limit set to f_{ctm} [135].

Abaqus requires true stress-strain relationship to define the plastic behaviour of a material model. Therefore, yield stress and inelastic/cracking strain data pairs must be provided for compressive/tensile behaviour [104]. To obtain the material

Table 5.7 Mechanical properties of concrete infill

$f_{c,cube}$, N/mm^2	f_{cm}, N/mm^2	$0.4f_{cm}$, N/mm^2	f_{ck}, N/mm^2	f_{ctm}, N/mm^2	E_{cm}, N/mm^2	ε_{c1}, -
47.3	37.8	15.2	29.8	2.9	32795	0.00216

input, the engineering stress-strain data pairs (resulted following the provisions from EN 1992-1-1 [148]) were transformed into true stress and logarithmic strain using the following formulas: $\sigma = \sigma_{nom}(1 + \varepsilon_{nom})$, $\varepsilon = \ln(1 + \varepsilon_{nom})$. After deducting the elastic part, the compressive behaviour is expressed as yield stress and inelastic strain data pairs (σ^c_i; ε^{in}_i), with the first pair (i = 1) defined as (σ^c_1; 0), where $\sigma^c_i \approx 0.4f_{cm}(1 + 0.4f_{cm}/E_{cm})$ is the initial compressive yield stress. The tensile behaviour is defined by only one yield stress and cracking strain data pair (σ^t_1; 0), with $\sigma^t_1 = f_{ctm}(1 + f_{ctm}/E_{cm})$ [135].

As it can be observed in Fig. 5.19 the elastic concrete model overpredicts the cyclic response of the specimen *CR71-1* since no plastic deformations take place in the concrete part and, therefore, the material fully recovers when unloading. Instead, the CDP model leads to close FEM prediction with the cyclic response of specimen *CR71- 1*. Moreover, the BRB model is able to capture the failure mode by global buckling since irreversible plastic deformation can take place in the concrete part, reducing the stiffness [135].

Based on the above observations, the CDP model was considered appropriate to model CR71 specimens (*CR71-1*, *CR71-2*) since they experimentally buckled and, which led to plastic deformations in the concrete parts of the FEM model. The same concrete model was used in the case of the other BRB models of *type A* (*CR33-1 /-2*

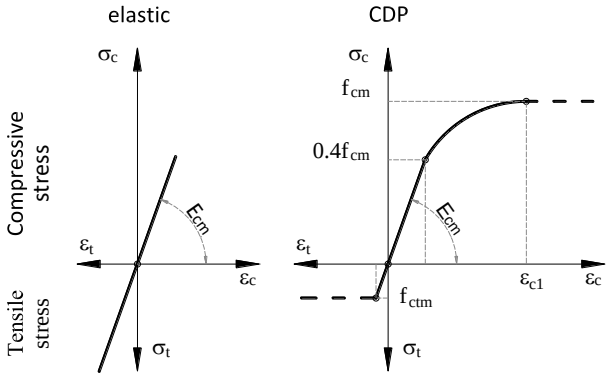

Fig. 5.18. Stress-strain relationships of concrete

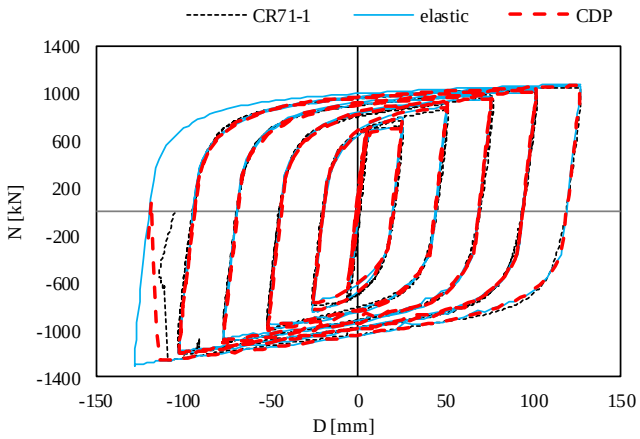

Fig. 5.19. BRB cyclic predictions using different concrete material models

and *CR73-1 /-2*) due to consistency reasons (the case of the *CR33* model) and due to the fact that the influence of concrete class is numerically investigated on the *CR73* model. As regarding the other BRBs that did not fail by global buckling, the response of the concrete parts is expected to be mostly elastic. Therefore, an elastic concrete model was used for finite element models of BRBs of *type B* (*CS33-1/-2*, *CS73-1/-2*), which proved to be efficient in reducing the numerical errors caused by excessive penetrations of the core into the concrete parts in the elastic zone [135].

5.2.2.6 Geometrical imperfections

The initial geometrical imperfections of BRBs can be classified as those due to the deviation from the rectilinear shape of the steel core (misalignment of the core components, core off-centring relative to steel tube) and those of the steel tube (bow imperfections and misalignment of connections). Core imperfections were not determined due to the difficulties in assuring reliable measurements: the core is very slender and has large initial deflections; after concrete casting, the position of the core relative to the tube cannot be determined precisely. Instead, tube imperfections were measured and a bow shape imperfection was obtained with a maximum amplitude of $e_{0,max} = L_{BRB}/14036 = 0.28$ mm, with respect to BRB length (L_{BRB}) [135].

According to EN 1993-1-1 [149], equivalent geometric imperfections must be used in structural analyses with values that reflect the possible effects of all types of imperfections (geometrical misalignments, loading eccentricities). Consequently, an initial equivalent geometrical bow imperfection (e_0) was introduced in the BRB model by using the first buckling mode, whose deformed shape was in the *YZ* plane of the gravity load (Fig. 5.20) [135].

Since it was not possible to measure all possible geometrical imperfections, an equivalent bow imperfection e_0 was determined by performing cyclic FEM analyses on *CR71* models and comparing the predictions with the experimental results. Different values for e_0 (0, $L_{BRB}/3000$, $L_{BRB}/2000$, $L_{BRB}/1000$, $L_{BRB}/750$, $L_{BRB}/500$) were

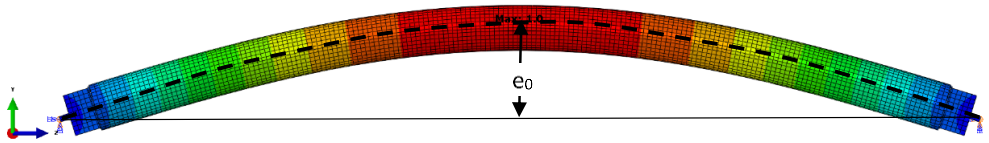

Fig. 5.20. Equivalent geometric bow imperfection

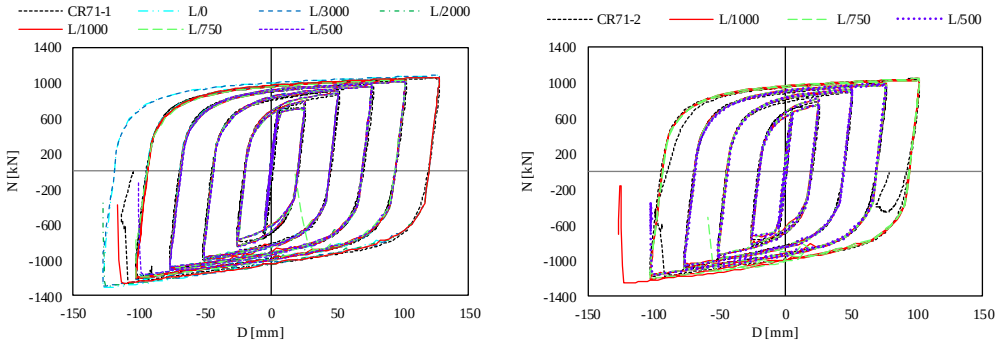

a) b)

Fig. 5.21. Effect of initial geometrical imperfections on BRB models *CR71*

considered. As it can be observed in Fig. 5.21.a, in the case of BRB model *CR71-1* close predictions are obtained using an initial bow imperfection of L_{BRB}/1000. In the case of BRB model *CR71-2*, see Fig. 5.21.b, an imperfection of L_{BRB}/750 leads to closer agreements with the experimental results. As an imperfection of L_{BRB}/750 caused premature buckling in the case of BRB model *CR71-1*, an initial equivalent bow imperfection of $e_0 = L_{BRB}$/1000 (similar in [142] and [144]) was applied for all other BRB models [135].

5.2.2.7 Model calibration

Using the above-mentioned FEM modelling hypotheses (material models, initial imperfections, contact laws), geometrically and materially nonlinear analyses including imperfections (GMNIA) were performed on FEM models of BRBs under cyclic loading. The predictions in terms of reaction force (N) and end displacement (D) are presented in Fig. 5.22 in comparison with experimental results. As a general remark, the BRB models reproduce the experimental hysteresis loops with a good level of accuracy. The failure of the core in tension due to excessive necking is captured for all models. Except for the models that failed by global buckling (*CR71-1* and *CR73- 2*), in the case of all the other BRB models the failure mode is by fracture of the core in the plastic zone during tensile loading. It is to be mentioned that the failure of the material due to low-cycle fatigue was not explicitly included in the material model [135].

For the *CR71* specimens (*CR71-1*, *CR71-2*), the model predictions are quite accurate. The FEM model was able to capture both the cyclic behaviour and the failure mode by global buckling of the BRBs [135].

In the case of *CR73* specimens, the predicted cyclic response has an acceptable level of accuracy, since between the two experimental responses (*CR73-1* and *CR73-2*) there were minor differences. For the first model, *CR73-1*, the failure occurred prematurely during the tensile phase of the 11th additional cycle at $1.5\Delta_{bm}$. Thus, the model was able to perform only 23.25 out of 25.0 cycles, as experimentally recorded. In the case of FEM model *CR73-2*, the failure occurred also prematurely during the tensile phase of the 9th additional cycle at $1.5\Delta_{bm}$. Thus, the model was able to perform only 21.5 out of 25.5 cycles, as experimentally recorded. In both cases, the FEM models developed larger compression hardening during the additional cycles at $1.5\Delta_{bm}$ due to material input [135].

Close predictions were also obtained for both *CR33* specimens (*CR33-1*, *CR33-2*). The FEM models were not able to fully capture the excessive hardening during compression cycles corresponding to $2.5\Delta_{bm}$. This might be caused by the material input used for the core, for which no experimental data was available for calibration [135].

From FEM results it was observed that the excessive hardening response at large deformations in compression is caused by increasing of the cross-sectional area of the core as a result of the Poisson effect. The increase took place mainly in the through-width direction of the plastic segment of the core, which is located near the transition zones. Therefore, the stress flow finds a new path, through the concrete part, leading to higher compression forces and un-symmetric cyclic response. Further investigations are required to properly determine the thickness of the unbonding material with respect to the Poisson effect under large strains [135].

In the case of *CS33* specimens, since cyclic material test data were available for calibration, the BRB models were able to predict with a very good level of accuracy both the cyclic response and the failure mode. As in the case of *CR73* specimens,

there are minor differences between the response of two experimental specimens (*CS33-1* and *CS33-2*) [135].

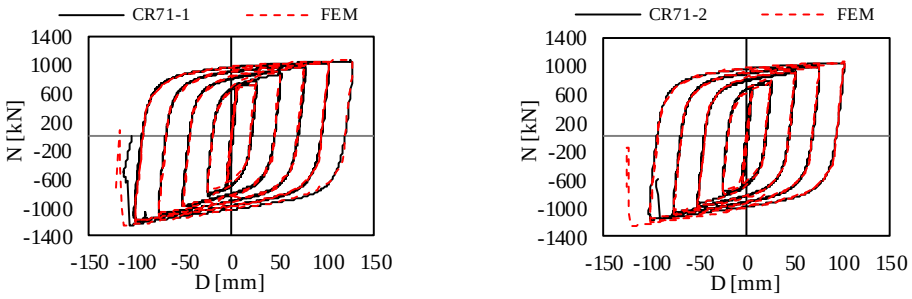

a) *CR71*

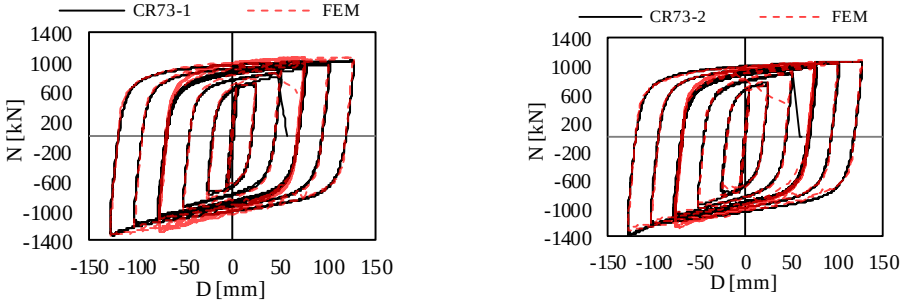

b) CR73

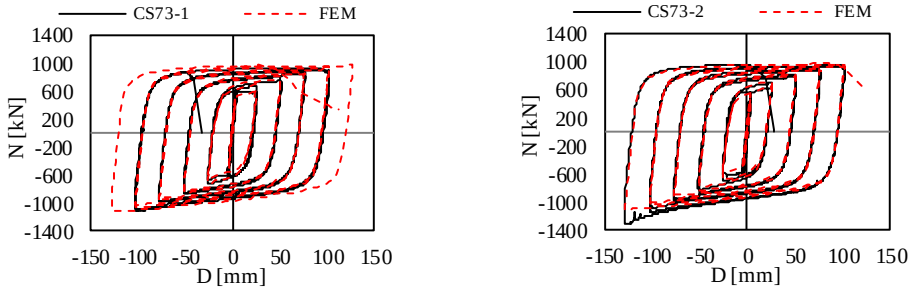

c) CS73

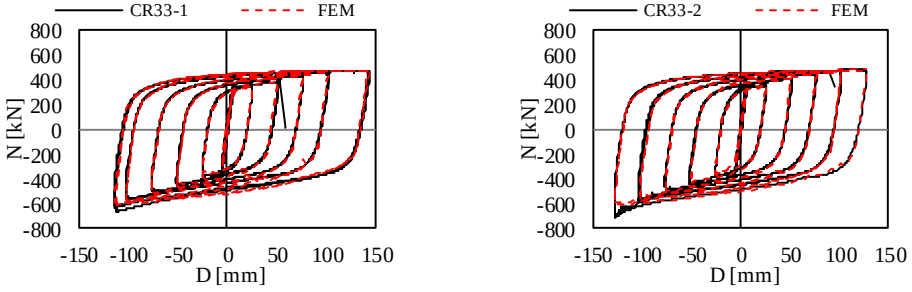

d) CR33

Fig. 5.22. Calibration of BRB models based on experimental results

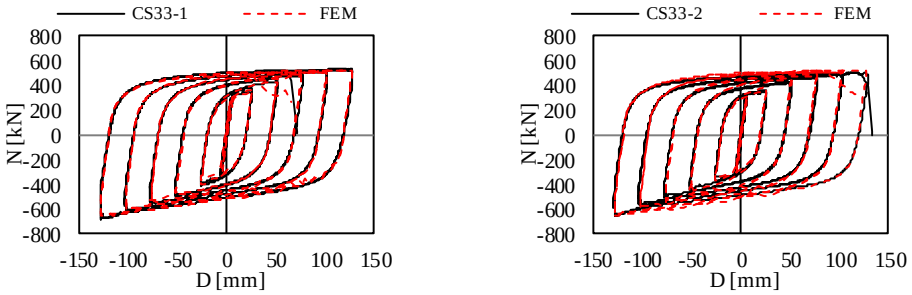

e) CS33

Fig. 5.22. Calibration of BRB models based on experimental results (continued)

Regarding *CS73* specimens, there are some differences between the experimentally obtained hysteresis loops due to the manufacturing imperfections (misalignment of the core components). When comparing the experimental and FEM results, it can be noticed that the cyclic performance of the specimen *CS73-1* was considerably reduced due to misalignments of the components. The FEM model *CS73- 1* was able to sustain an extra complete cycle at $2.5\Delta_{bm}$ prior fracture in tension. In the case of *CS73-2* specimen, excessive hardening response at the first compression cycle corresponding to $2.5\Delta_{bm}$ was recorded. The FEM BRB model is not able to capture this phenomenon and therefore is considered to be caused by manufacturing imperfections (misalignment of polystyrene parts). Also, close prediction of the fracture was obtained for *CS73-2* specimen. Based on the above observations, the numerical BRB models were able to capture the cyclic behaviour of the specimens *CS73-1* and *CS73-2* with an acceptable level of accuracy [135].

In Fig. 5.23.a-b are presented both the experimental and FEM deformed shape of the cores for two BRBs, *CR73-2* and *CS73-2*. It can be observed that fracture positions are relatively close to the stopper, as in the experimental cases. Also, the core of *CR73-2* model is more deformed about the minor axis of inertia, while the core of *CS73-2* is more uniformly deformed with respect to the principal axes of inertia [135].

In Fig. 5.24.a-b are presented the friction zones on the concrete infill in FEM model in comparison to the experimental specimens, *CR73-2* and *CS73-2*. A larger number of friction zones can be observed in the case of the *CR73-2* model since the cross-section is rectangular and has a small axis of inertia, while in the case of *CS73- 2* model the core has a compact square cross-section shape [135].

5.2.3 Parametric study

The numerical study aims at understanding some phenomena related to BRB cyclic behaviour and at extending the experimental database by performing parametric FEM analyses on the calibrated BRBs models. Therefore, the influence of the following parameters was numerically investigated: the strength of the buckling restraining mechanism, the class of the concrete infill, the steel grade of the core material, the effect of the gravity loading [135].

The cyclic analyses were performed using the loading protocol presented in Fig. 5.25. It is limited to the first 10 cycles as required by ANSI/AISC 341-10 [100], since the cumulative inelastic deformation, *CID*, for this loading history exceeds the minimum requirement of 200 times the yield deformation of the BRB, Δ_{by} [135].

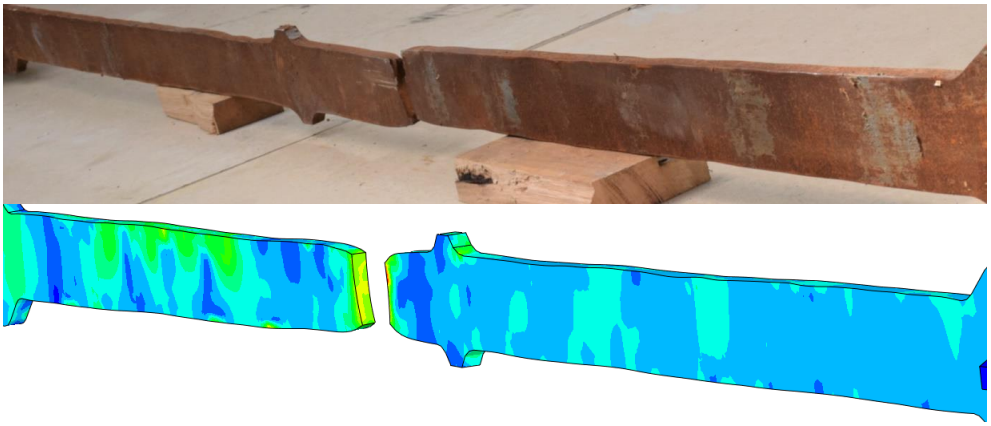

a) BRB *type A*: specimen *CR73-2*

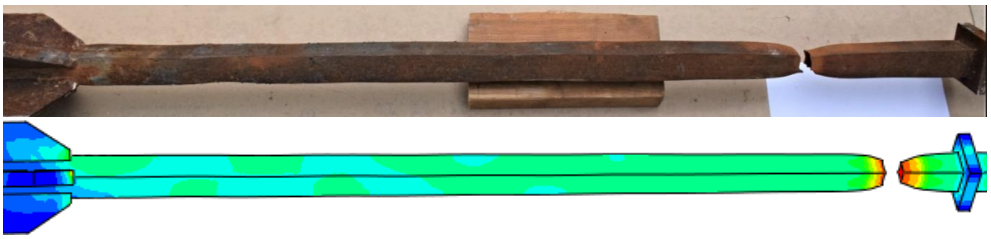

b) BRB *type B*: specimen *CS73-2*

Fig. 5.23. Deformed shape of BRB core: experimental vs. FEM

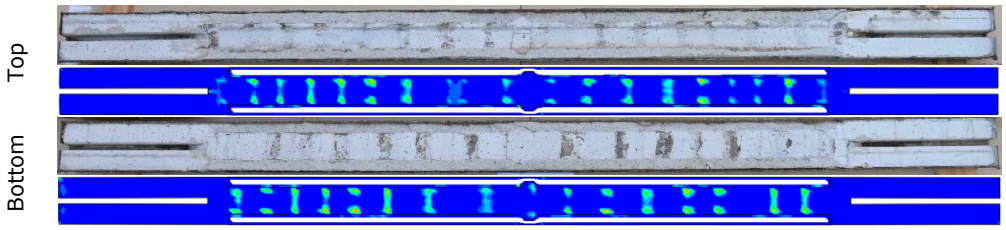

a) BRB *type A*: specimen *CR73-2*

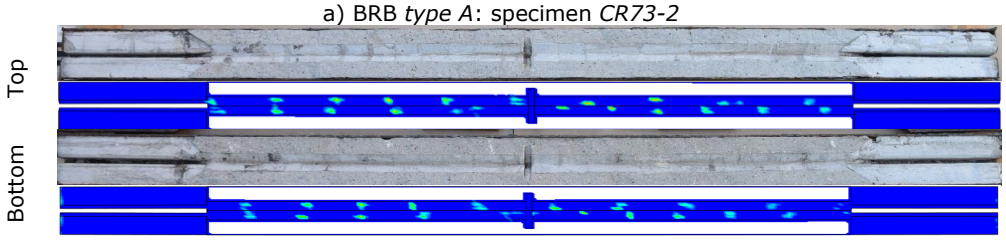

b) BRB *type B*: specimen *CS73-2*

Fig. 5.24. Friction zones on concrete infill: experimental vs. FEM

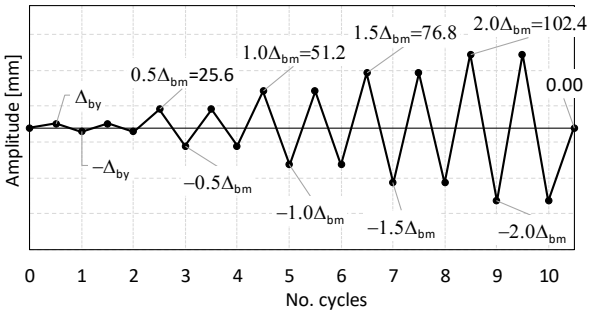

Fig. 5.25. Loading protocol used for parametric FEM analyses

5.2.3.1 BRM strength

Early studies on bucking-restrained braces suggested that global buckling of the BRB can be prevented if the elastic critical force N_{cr} of the bucking-restraining mechanism (BRM) is at least 1.5 times the nominal resistance of the core N_p [20]. However, some studies [107] suggested that $N_{cr}/N_p \geq 3$ is necessary to obtain cumulative inelastic deformations in excess of 200 times the yield deformation, as required by ANSI/AISC 341-10 [100]. [135]

Takeuchi and Wada [1] proposed the following expression for design of the buckling restraining mechanism [135]:

$$\frac{N_{cr}}{C_{max}} > 1 + \left(\frac{\pi^2 E_s}{2f_y} \cdot \frac{e_0}{L_{BRB}}\right) / \left(\frac{L_{BRB}}{D_e}\right) \tag{5.28}$$

where: C_{max} is the maximum compression force developed by the BRB; f_y is the yield strength of the steel tube; e_0 is the amplitude of the initial bow imperfection, taking into account geometrical imperfections of core, the brace, and of the connections (load eccentricity); D_e is the exterior diameter of the steel tube [135].

The initial bow imperfection used in equation (5.28) is difficult to be established. Moreover, equation (5.28) addresses monotonic compression case since there are no factors to take into account the strength degradation of BRM due to cyclic loading [135].

The influence of the strength of the BRM on the BRB performance was evaluated by assessing the response of five finite element models under monotonic and cyclic loading conditions. The numerical models are based on the calibrated model *CR71-1*. For each BRB model, the BRM was designed for different rations between the elastic critical load of the steel tube, N_{cr}, and the plastic resistance of the core, N_p. The following ratios were considered: N_{cr}/N_p = 1.50, 1.75, 2.0, 2.5, 2.79. The thickness of the steel tube, t, was offset to the exterior, thus the concrete section did not change from one model to the other [135].

The critical buckling load was computed based on Euler's formula:

$$N_{cr} = \pi^2 E_s I_s / L_{cr}^2 \tag{5.29}$$

where: E_s and I_s are the elastic modulus and the moment of inertia of the steel tube, respectively; L_{cr} = L_{BRB} = 3930 mm is the buckling length of the BRM, considered for this study equal to the length of the BRB [135].

To check the design equation (5.28), monotonic compression analyses were performed on the BRB models. FEM models of specimens *CR71-1* and *CR71-2* with different values of the initial geometrical imperfection (L_{BRB}/1000, L_{BRB}/500, L_{BRB}/450, L_{BRB}/250) were analysed. The value of the initial imperfection that resulted in best

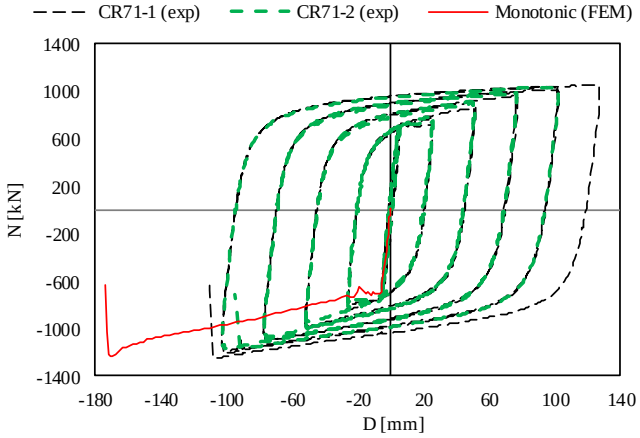

Fig. 5.26. Calibration of the equivalent imperfection of BRB model under monotonic compression loading

match with the experimental buckling load under cyclic loading was e_0/L_{BRB} = 1/450 (Fig. 5.26) [135].

Using the calibrated equivalent imperfection for monotonic loading ($e_0 = L_{BRB}/450$), monotonic compression analyses were performed on the other BRB models with varying ratios of N_{cr}/N_p. The maximum compression force developed by the brace prior to buckling represents the design axial resistance ($N_{Rd,f}$) of the BRM obtained using the FEM method [135].

Following the analytical approach from Takeuchi and Wada [1], the design resistance $N_{Rd,a}$ of the BRM can be obtained with equation (5.30), which is the ratio between the critical elastic force N_{cr} and the safety factor α defined by equation (5.31) [135]:

$$N_{Rd,a} = N_{cr}/\alpha \tag{5.30}$$

where,

$$\alpha = 1 + \left(\frac{\pi^2 E_s}{2f_y} \cdot \frac{e_0}{L_{BRB}}\right) / \left(\frac{L_{BRB}}{D_e}\right) \tag{5.31}$$

The analytical and the FEM results are summarized in Table 5.8. By analysing the ratio between the FEM and the analytical prediction of the design critical load ($N_{Rd,f}/N_{Rd,a}$), it can be noticed that the formula is less conservative for stronger BRM. This happens due to the fact that the influence of the concrete infill, imperfection and other modelling assumptions to the buckling resistance of the FEM model becomes less important with larger thickness of the steel tube, thus the steel tube becomes the main component responsible for the strength of the buckling restraining mechanism [135].

In the second phase, cyclic analyses were performed on the BRB models with BRMs of different strength. As presented in Fig. 5.27, the cyclic response is stable for all models during the entire loading protocol ($N_{Ed}/N_{Rd,f} \leq 1$). However, considering the maximum compression force C_{max} = 1219 kN developed by the models under cyclic loading as the design force $N_{Ed,BRM}$, from Table 5.8 it can be observed that only the models with $N_{cr}/N_p \geq 2.50$ are satisfying the design check $N_{Ed,BRM}/N_{Rd,a} \leq 1.0$ proposed in [1]. It means that the analytical design approach is conservative. Nevertheless, the mid-span deflection ($U_{y,mid}$) of the steel tube increases at a larger rate for small N_{cr}/N_p ratios. In the case of the model with N_{cr}/N_p = 1.50, $U_{y,mid}$ reached 37.63 mm, during

Table 5.8 Performance evaluation of BRB models with different $N_{cr,s}/N_{p,m}$ ratios

D_e x t, mm	N_{cr}, kN	N_{cr}/N_p, -	α, -	$N_{Rd,a}$, kN	$N_{Rd,f}$, (mon) kN	C_{max}, (cyc.) kN	$N_{Rd,f}/N_{Rd,a}$, -	$U_{y,mid}$, mm	$N_{Ed,BRM}/N_{Rd,a}$, -	$N_{Ed,BRM}/N_{Rd,f}$, -
177.77 x3.90	1081	1.50	1.227	881	1180	1208	1.34	37.6	1.384	1.033
179.01 x4.52	1266	1.75	1.229	1031	1427	1200	1.38	22.1	1.183	0.854
180.21 x5.12	1450	2.00	1.230	1178	1477	1199	1.25	15.9	1.034	0.825
182.51 x6.27	1811	2.50	1.233	1469	1746	1219	1.19	10.6	0.830	0.698
183.81 x6.92	2022	2.79	1.235	1637	1885	1216	1.15	9.1	0.745	0.646

the compression phase of the second cycle at $2.0\Delta_{bm}$. Moreover, the maximum compression force under cyclic loading for the model with N_{cr}/N_p = 1.5 amounts to 1208 kN, which is larger than the resistance under monotonic loading, $N_{Rd,f}$ = 1180 kN. For larger N_{cr}/N_p values this "anomaly" is not observed [135].

As presented in chapter 5.2.2.7, the calibrated FEM model (N_{cr}/N_p = 1.53) buckled during the first compression phase of the $2.5\Delta_{bm}$ cycle under a force C_{max} = 1260 kN, which is slightly larger than the maximum compression force recorded using the standard loading protocol from Fig. 5.25, with C_{max} = 1202 kN [135].

Fig. 5.28 presents the state of stress in the steel tube at peak compression during the second cycle at $2.0\Delta_{bm}$. It can be observed that in the case of BRB model with N_{cr}/N_p = 1.50 the maximum stress σ^{max}_{tube} = 462 N/mm^2 is beyond the true yield strength of the tube, σ^{0}_{tube} = 460 N/mm^2. For the other models, the maximum stress decreases as increasing the thickness of the tube [135].

Based on these facts, the model designed for N_{cr}/N_p = 1.50 is considered sensitive to global buckling. This fact is also confirmed by analysing the $N_{Ed,BRM}/N_{Rd,f}$ ratios from Table 5.8. In the case of BRB model with N_{cr}/N_p = 1.50, the ratio $N_{Ed,BRM}/N_{Rd,f}$ is equal to 1.033, while for all the other models subunit ratios are obtained [135].

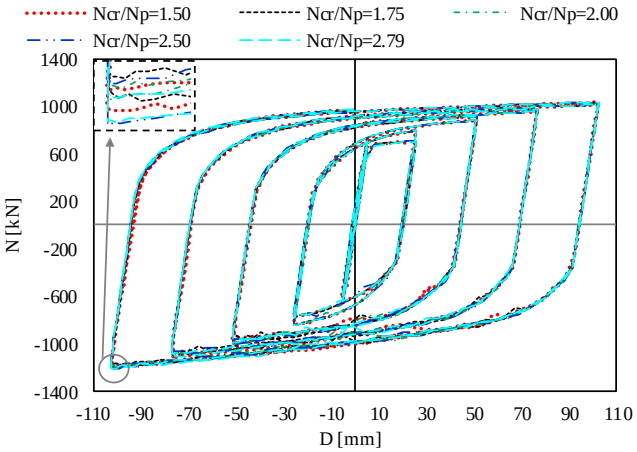

Fig. 5.27. Cyclic response of BRB models with BRMs of different strength

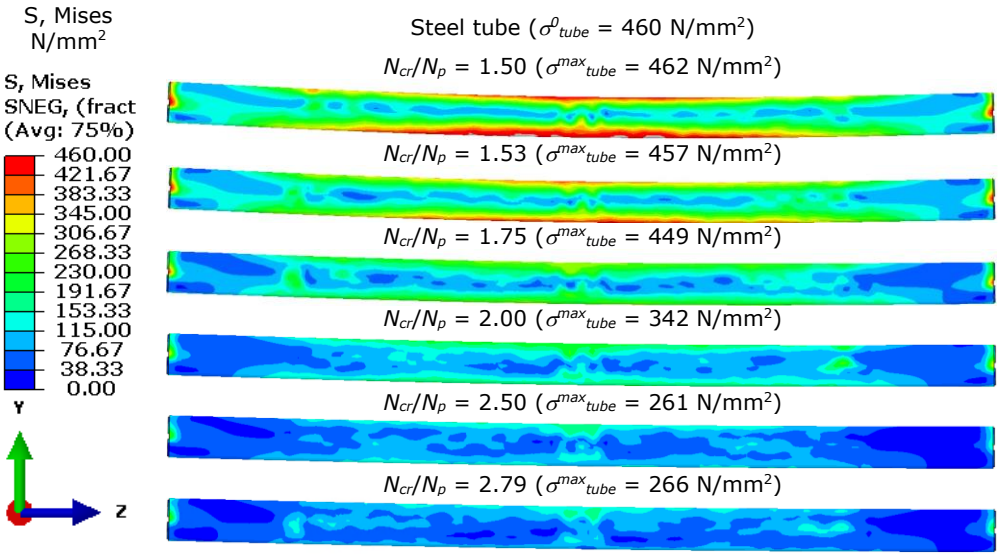

Fig. 5.28. State of stress in steel tube at peak compression during the second $2.0\Delta_{bm}$ cycle

It can be concluded that the analytical procedure proposed by Watanabe et al. [20], with a minimum ratio $N_{cr}/N_p > 1.5$, shows to be too simplistic and sometimes unconservative, since it does not take into account the maximum compression force, $C_{max} = \omega\beta \cdot N_p$, that could be developed by the BRB during cyclic loading. The analytical design procedure proposed by Takeuchi and Wada [1] takes into account C_{max} and also second order effects (α). It is found that their design formula is more conservative than the one proposed by Watanabe et al. [20], leading to N_{cr}/N_p ratios considerable larger than 1.5. Also, the design formula proposed by Takeuchi and Wada [1] is less conservative for stronger buckling restraining mechanisms. To pass the design check $N_{Ed,BRM}/N_{Rd,a} \leq 1.0$, a minimum ratio $N_{cr}/N_p > 2.5$ is needed to be used for the design of the BRM [135].

5.2.3.2 Concrete class

The influence of the class of concrete infill on the cyclic performance of BRB was investigated by assessing the response of four BRB models corresponding to *CR73-2*. The models are similar except for the concrete mechanical properties, which were modelled using the concrete damaged plasticity material (CDP), as described in section 5.2.2.5. In addition to the concrete class used for the calibrated BRB model, *C30/37*, the following concrete classes were chosen for this numerical study: low strength concrete *C12/15*, normal strength concrete *C20/25*, high strength concrete *C50/60*. The mechanical properties of the concrete material models used in these simulations are summarized in Table 5.9 [135].

The axial force (*N*) - displacement (*D*) responses are presented in Fig. 5.29. It can be observed that there are no significant differences in the *N-D* responses [135].

Table 5.10 presents the values of the plastic strain (*PE*) and cumulative plastic strain (*PEEQ*) in the concrete and the steel core obtained at the end of analysis. The table also gives the maximum values of the mid-span deflection of the steel tube

Table 5.9 Concrete material inputs

Class	f_{cm}, N/mm^2	$f_{cm}/f_{cm(exp)}$, -	E_{cm}, N/mm^2	υ, -	f_{ctm}, N/mm^2
C12/15	20	0.50	27088	0.2	1.6
C20/25	28	0.75	30303	0.2	2.2
C30/37(exp.)	37.8	1.00	33503	0.2	2.9
C50/60	58	1.50	38629	0.2	4.1

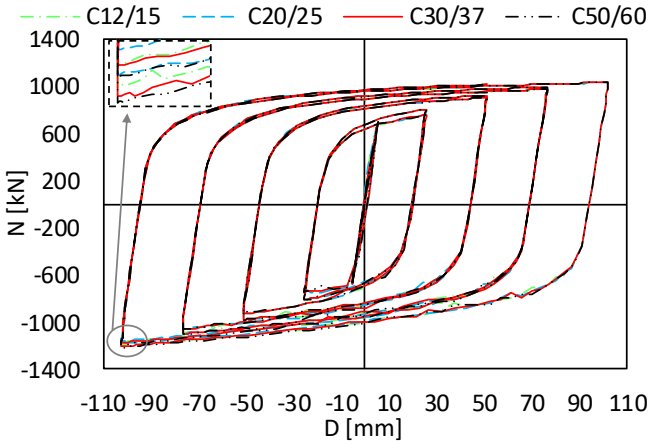

Fig. 5.29. Cyclic response of BRB models with the concrete infill of different classes

($U_{y,mid}$) in the vertical plane *YZ*, see Fig. 5.35.a, and the compression strength adjustment factor (β) [135].

In the case of all BRB models the maximum value of plastic deformation occurred in the mid-zone of the concrete part, near the stopper. In the case of the BRB model *C12/15*, concentrations of plastic deformations occurred also at the top end of the concrete part, where the load is applied. Based on the results from Table 5.10 it can be noticed that the concrete part undergoes larger plastic and cumulative plastic strains if its class is lower (*C12/15* and *C20/25*) in comparison to higher concrete classes (*C30/37* and *C50/60*), with a level of magnitude of almost twice [135].

The mid-span deflection ($U_{y,mid}$) of the steel tube has slightly larger values in the cases of lower concrete classes. On the other side, the *PE* and *PEEQ* values in the steel core are slightly increasing as the concrete class increases. This might be a consequence of increasing the elastic modulus of the concrete model, thus the concrete part is stiffer and less deformable, forcing the plastic deformations to develop in the core and not in the concrete part. The β factor is in the range of 1.13-1.16, with the lowest value recorded in the case of *C20/25* (β = 1.13) [135].

Table 5.10 Performance parameters of BRB models with different concrete classes

	Concrete		Steel core		Tube	BRB
Class	*PE*, mm/mm	*PEEQ*, mm/mm	*PE*, mm/mm	*PEEQ*, mm/mm	$U_{y,mid}$ mm	β, -
C12/15	0.0309	0.0239	0.058	1.323	9.00	1.14
C20/25	0.0283	0.0177	0.063	1.449	8.64	1.13
C30/37	0.0169	0.0105	0.071	1.516	7.98	1.15
C50/60	0.0139	0.0085	0.071	1.487	8.27	1.16

Based on the above numerical results, it can be concluded that the concrete class has little influence on the global performance of the BRB. However, to keep low levels of damage in concrete, it is prudent to use a concrete class of at least *C30/37* [135].

5.2.3.3 Steel properties

The dissipative component of a BRB is the steel core. Therefore, its properties are expected to have a major influence on the performance of the complete BRB. Four materials were considered such that to have a low (1.2) and a high (1.6) value of the tensile to yield strength ratio (f_u/f_y), and a small (0.22 mm/mm) and a larger (0.36 mm/mm) value of the rupture strain, ε_r. All materials have the same yield stress (f_y = 394 N/mm2), and the same strain at the onset of strain hardening, ε_{sh} = 0.015 mm/mm. The strain corresponding to the tensile strength, ε_u, was considered as 55 % of ε_r based on experimental observations, while the rupture strength was considered as 80 % of f_u. The mechanical properties are summarized in Table 5.11 [135].

Table 5.11 Mechanical properties of steel used for cores

Parameter	*mat-1*	*mat-2*	*mat-3*	*mat-4*
f_y, N/mm^2	394	394	394	394
f_u, N/mm^2	473	630	473	630
f_r, N/mm^2	378	504	378	504
f_u/f_y	1.20	1.60	1.20	1.60
ε_{sh}, -	0.015	0.015	0.015	0.015
ε_u, -	0.121	0.121	0.198	0.198
ε_r, -	0.220	0.220	0.360	0.360
$\varepsilon_u/\varepsilon_r$	0.55	0.55	0.55	0.55

Having the target properties set, the corresponding input material for Abaqus software was based on the calibration procedure described chapter 5.1.6.

The numerical stress-strain curves of the four materials under monotonic uniaxial tensile loading are presented in Fig. 5.30.a. They were obtained on numerical model of a standard specimen for tensile tests, with a proportional initial gauge length ($L_0 = 5.65\sqrt{A_0}$, where A_0 is the initial cross-sectional area), discretized using *C3D8I* finite elements [135].

The cyclic stress-strain response of steel presented in Fig. 5.30.b was obtained using a variable loading protocol with amplitudes that will generate similar strain levels as in the case of analyses on BRBs. A unit cube discretized with one finite element *C3D8I* was the numerical model for cyclic analyses since the strain range does not exceed ε_u and therefore no necking is expected to occur [135].

The four materials were assigned to the core of the BRB model corresponding to *CR33-1* specimen. Cyclic analyses were performed using the protocol from Fig. 5.25 and the axial force-displacement response of the four BRB models are presented in Fig. 5.31.a-b. It can be observed that only the BRB model having the material *mat- 4* assigned to the core could sustain the entire loading protocol (10 cycles) without premature necking or fracture. The other models failed prematurely due to lack of ductility or low tensile to yield strength ratio [135].

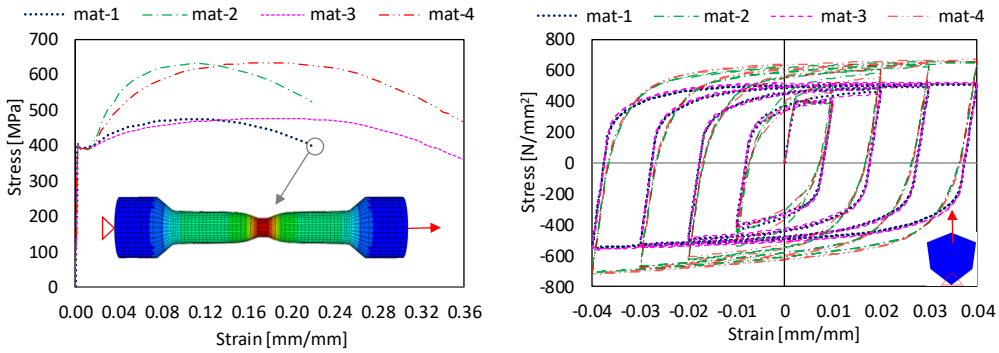

Fig. 5.30. Response of steel models under different loadings: a) monotonic, b) cyclic

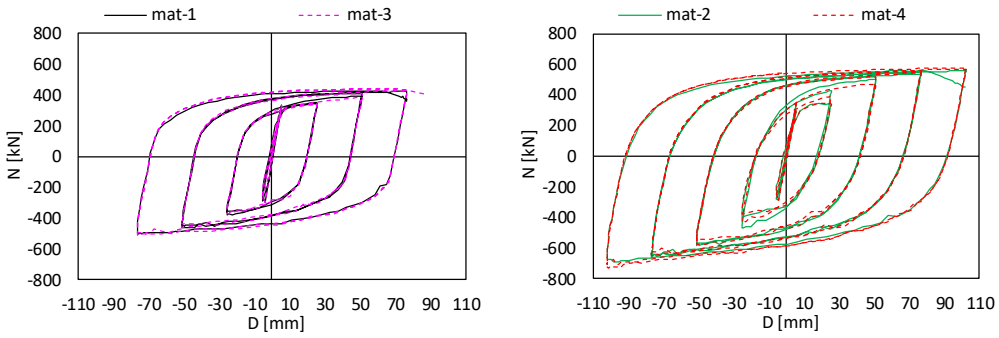

Fig. 5.31. Influence of plastic properties of steel on BRB response under cyclic loading: a) f_u/f_y = 1.2, b) f_u/f_y = 1.6

The cyclic response of the BRB models is also evaluated with respect to the performance parameters presented in Table 5.12. As expected, the value of the strain hardening adjustment factor (ω) is larger in the cases of BRB models having f_u/f_y = 1.6 (*mat-2* and *mat-4*), with a maximum value of ω = 1.54 for *mat-4* model. Also, the $\omega\beta$ factor is higher for BRB models *mat-2* and *mat-4*. This increase leads to higher values of the maximum compression force which is used to design the non-dissipative components of the BRB (elastic segments of the core, BRM, connections). Consequently, larger sections might be needed [135].

On the other hand, the compression strength adjustment factor β (Table 5.12) is affected to a very low extent by the material properties (tensile to yield strength ratio and ultimate strain) [135].

The cumulative inelastic deformation, *CID*, exceeded 200 times the yield deformation, Δ_{by}, only in the case of the models with f_u/f_y = 1.6 (*mat-2* and *mat-4*). Thus, the models *mat-1* and *mat-3* could not satisfy the ANSI/AISC 341-10 [100] requirement for qualification [135].

With respect to the energy dissipated by the BRB, E_{dis}, computed as the area inside the hysteretic loops prior to necking, major differences can be observed between the BRB models. The larger value of E_{dis} = 845 kNm was obtained in the case of BRB model *mat-4* which has the material defined by f_u/f_y = 1.6 and ε_r = 0.36 mm/mm. Using a steel material of similar tensile to yield strength ratio (f_u/f_y = 1.6)

Table 5.12 Performance parameters of BRB models with different properties of core steel

Material model	ω, -	β, -	$\omega\beta$, -	CID/Δ_{by}, -	Cycles completed	E_{dis}, kNm
mat-1	1.15	1.24	1.43	145	7	312
mat-2	1.49	1.25	1.86	265	9	688
mat-3	1.19	1.25	1.49	196	8	430
mat-4	1.54	1.28	1.98	334	10	845

but less ductile (ε_r = 0.22 mm/mm) causes the dissipated energy to reduce with almost 19 % (case of BRB model *mat-2*). In the case of BRB models with f_u/f_y = 1.2 (*mat-1* and *mat-3*), the dissipated energy is almost 50 % less in comparison to the models with f_u/f_y = 1.6 [135].

It can be concluded that characteristics of the steel core are critical for the performance of BRBs. The tensile to yield strength ratio is by far the most important. Larger f_u/f_y values allow for redistribution of plastic strains over a longer portion of the core (Fig. 5.32), increasing the overall ductility of the BRB. They also lead to a significant improvement of energy-dissipation capacity. As a downside, larger f_u/f_y values of steel requires stronger non-dissipative components. Based on numerical simulations, but also on experimental results, values of f_u/f_y = 1.3 and ε_r = 0.30 are required to fulfil the qualification protocol from Fig. 5.25. It has to be reminded that the protocol is quite "severe", the design inter-storey drift Δ_{bm} being equal to 2% of the storey height. Further studies are needed to generalise this conclusion for other BRB geometries, capacities, and loading protocols [135].

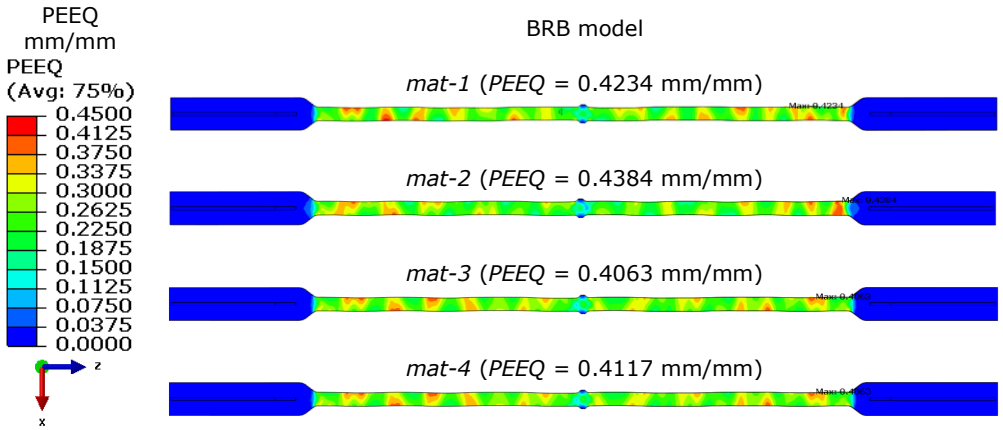

Fig. 5.32. State of cumulative plastic strain in core at peak compression during the first cycle at $1.5\Delta_{bm}$

5.2.3.4 *Gravity loading*

This numerical study aims at investigating the influence of gravity loading on the evolution of the plastic deformations in the plastic segments of the core. The top segment corresponds to the BRB end where the cyclic loading is applied, while the bottom segment to the fixed end [135].

For this investigation, four BRB models corresponding to specimens *CR73-2* and *CS73-2* were cyclically tested with and without gravity loading. The cyclic

response of the tested BRBs expressed as reaction force (N) and core end displacement (D), are presented in Fig. 5.33.a for *CR73-2* models and in Fig. 5.33.b for *CS73-2* models. No significant differences can be observed for the cases where the gravity loading was included [135].

However, if analyzing the time-history of the displacements between the tube and the top/bottom end of the core, D_{bt} / D_{bb}, in comparison to the core deformation, D_c, significant differences between the models can be observed. In the case of both *CR73-2* and *CS73-2* models, see Fig. 5.34.a and Fig. 5.34.c, the presence of gravity loading causes the top segment of the core to undergo larger deformations during the tensile loading in comparison to the bottom segment, which undergoes larger

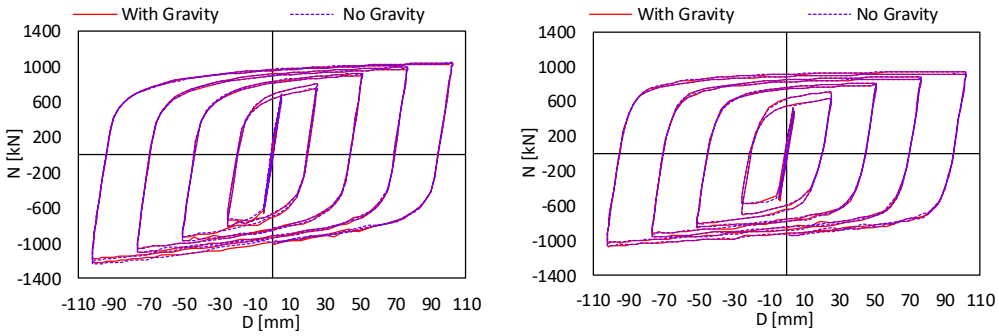

a) *CR73-2* b) *CS73-2*

Fig. 5.33. Influence of gravity loading on the cyclic response of BRB models

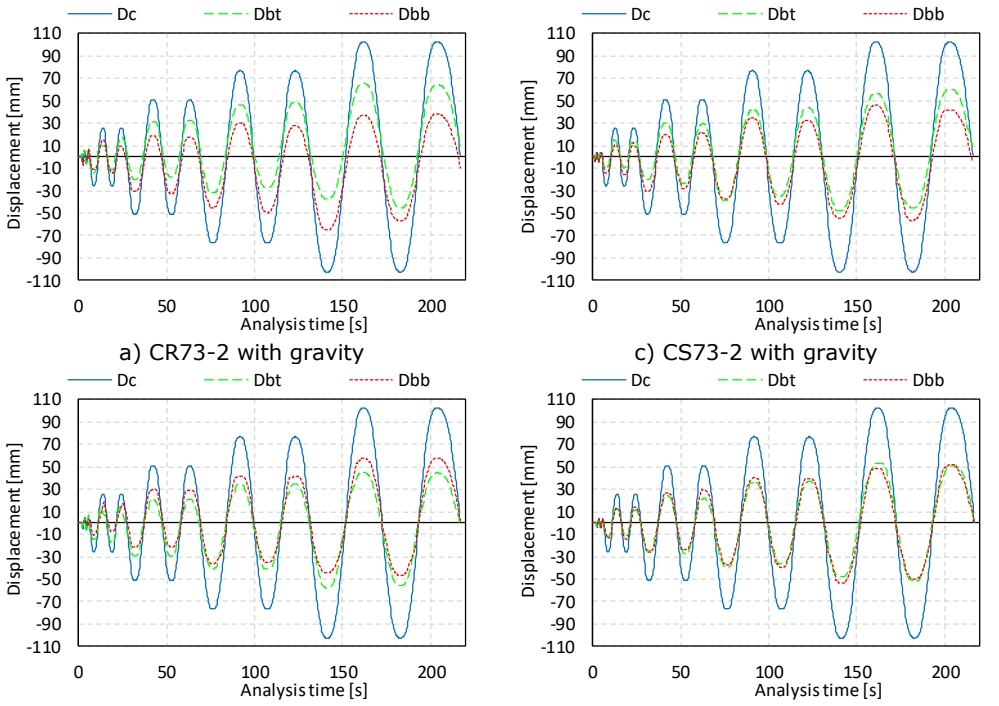

a) CR73-2 with gravity c) CS73-2 with gravity

b) CR73-2 no gravity d) CS73-2 no gravity

Fig. 5.34. FEM relative displacements: tube-to-core (D_{bt}, D_{bb}) vs. core end-to-end (D_c)

deformations during the compressive loading. Therefore, the evolution of the plastic deformations in the plastic segments of the core under the presence of gravity loading is unsymmetrical [135].

In the case of the BRB models where the gravity loading was not included, see Fig. 5.34.b and Fig. 5.34.d, the evolution of the plastic deformations in the plastic segments of the core is more uniform in comparison to the models with gravity loading. In the case of *CR73-2* model, the asymmetry is still more pronounced with respect to *CS73-2* [135].

To quantify this effect, maximum deformation ratios in the top (R_t) and bottom (R_b) parts of the core were determined for the $2.0\Delta_{bm}$ cycles [135]:

$$R_t = D_{bt}/D_c \quad (5.32)$$

$$R_b = D_{bb}/D_c \quad (5.33)$$

Maximum deformation ratios R_t and R_b are summarized in Table 5.13. Ideally, for a symmetrical response, both rations would be equal to 0.5. For all except one model (*CR73- 2- noG*), the deformation ratios in the top segment of the core are larger in tension (R_t = 0.52-0.64), while in the bottom part of the core the deformation ratios are larger in compression (R_b = 0.52-0.63) [135].

In the case of *CR73-2* models (with gravity, *CR73-2-G*, and without gravity, *CR73-2-noG*) the asymmetry is more pronounced in comparison to *CS73* models, with deformation ratios varying between R_t = 0.44-0.64 and R_b = 0.37-0.63. In the case of *CS73-2* models (*CS73-2-G* and *CS73-2-noG*), a more uniform distribution of plastic deformations is obtained, with deformation ratios varying between R_t = 0.47-0.59 and R_b = 0.45-0.55 [135].

The absence of gravity loading causes the deformation ratios R_t and R_b to approach to 0.5 [135].

Table 5.13 Maximum deformation ratios R_t and R_b

BRB model	R_t		R_b	
	Tension	Compression		Tension
CR73-2-G	0.64	0.44	0.37	0.63
CR73-2-noG	0.44	0.56	0.56	0.45
CS73-2-G	0.59	0.47	0.45	0.55
CS73-2-noG	0.52	0.51	0.51	0.52

5.2.3.5 Frame effect

The influence of the frame effect, in addition to the uniaxial cyclic loading (see chapter 5.2.2.2), on the BRB cyclic performance was investigated on two models corresponding to specimen *CR71-1*. The models are similar, except for the loading scheme, see Fig. 5.35.a. In the case of the first model (*Uniaxial*), only the axial load U_z was applied. For the second model (*Uniaxial + Frame eff.*) axial U_z, transversal U_y, and rotational UR_x loads were applied. Based on the results presented in Fig. 5.35.b, it can be observed that the additional frame effect leads to slightly lower resistance to overall buckling. In comparison to the maximum compression force experimentally recorded for *CR71-1*, C_{max} = 1258 kN, a closer prediction is obtained in the case of modelling both uniaxial and the frame effect, C_{max} = 1260 kN, while in the case of the uniaxially loaded model the maximum compression force is slightly larger, C_{max} = 1296 kN [135].

It is concluded that modelling the cyclic loading as uniaxial and frame effect leads to closer FEM predictions [135].

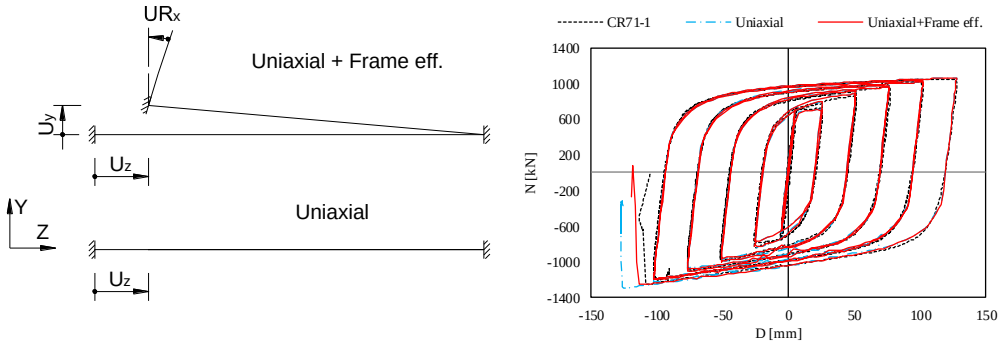

a) Cyclic loading scheme b) BRB response

Fig. 5.35. Influence of the loading scheme on the response of the BRB model

5.3 Concluding remarks

The proposed modelling technique of the cyclic response of structural steel for FEM analyses using the Abaqus "built-in" material models proved to assure reliable predictions. The material model can properly simulate the main features of mild carbon steel S355.

The calibration of the elastic and plastic behaviour is based on experimental results. Five coupons were tested: one uniaxial monotonic test and four uniaxial cyclic tests (three tests under symmetric strain control and one under variable strain control). The dependency of the cyclic hardening with respect to the strain range was experimentally observed.

The combined isotropic-kinematic hardening model is used to model metal plasticity under cyclic loading. The kinematic hardening definition is consistent for all loading cases. The isotropic hardening definition is not consistent for all loading cases, therefore is loading history dependent. The FEM results closely predict the experimental results with respect to the cyclic behaviour and the failure mode.

A calibration procedure of the material parameters for the combined hardening material model using uniaxial monotonic tensile tests is proposed and validated agains experimental tests. Predictions with an acceptable level of correlation is observed with respect to the monotonic (tensile) and cyclic experimental results.

A complex nonlinear numerical model of the buckling restrained brace was developed in the finite element environment Abaqus. The calibration against experimental data was performed at both component level (material models: steel, concrete, unbonding material) and BRB level (loading, geometrical initial imperfections). Geometrically and materially nonlinear analyses including imperfections (GMNIA) were performed on BRB models under cyclic loading. Close predictions were obtained for all FEM models. The calibrated models were further used to perform a parametric study aiming at understanding some phenomena related to BRB cyclic behaviour. Five main aspects were numerically investigated by running cyclic analyses and assessing the performance of the BRB models: the strength of the buckling restraining mechanism, concrete class of the infill material, mechanical properties of steel used for the core, gravity loading and frame effect.

The design procedure of the buckling restraining mechanism was validated based on FEM results. The analytical procedure proposed by Watanabe et al. (1988), with a minimum ratio of the critical elastic force of the BRM to the plastic resistance of the core, $N_{cr}/N_p > 1.5$, showed to be too simplistic and sometimes unconservative.

It was found that the analytical design procedure proposed by Takeuchi and Wada [1] is more appropriate.

Concrete class of the infill has little influence on the global performance of the BRB. However, to keep low levels of damage in concrete, it is prudent to use a concrete class of at least *C30/37*.

Characteristics of the steel core are critical for the performance of BRBs. Based on numerical simulations, but also on experimental results, values of $f_u/f_y \geq 1.3$ and $\varepsilon_r \geq 0.30$ are required to fulfil the qualification protocol. Further studies are needed to generalise this conclusion for other BRB geometries, capacities, and loading protocols.

The presence of gravity loading leads to unsymmetrical evolution of deformations in the plastic segments of the core. This phenomenon is more pronounced in the case of BRB model of *type A* (core with a rectangular cross-section) in comparison to BRB model of *type B* (core with square cross-section).

If BRB-column sub-assemblage setup is used for experimental tests, when performing FEM analyses the cyclic loading applied to the BRB model should consider both uniaxial and frame effect loading to achieve close predictions.

6 DESIGN RECOMMENDATIONS

6.1 Limits of applicability

Based on the conclusions from chapter 4.5, the "convetional" solution of *type A* was recommended as the prequalified BRB. Its conceptual composition is presented in Fig. 6.1. It consists of: a variable cross-section steel core wrapped with acrylic tape, polystyrene parts positioned in extension to the transition zone and stiffeners, and a circular steel tube filled with a ready-mix cement mortar and 4-8 mm aggregates.

The design procedure presented in this chapter considers only the prequalified BRB solution. These design recommendations were elaborated based on both experimental and (post-test) numerical results. The limits of applicability for the

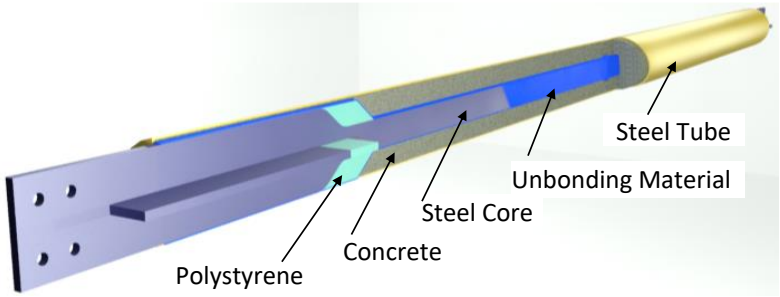

Fig. 6.1. Conceptual composition of the qualified BRB solution

Table 6.1 Applicability limits of the BRB prequalification

Applicability limits	Observations
Capacity ($N_p = A_p \cdot f_{y,m}$): 150 kN ≤ N_p ≤840 kN.	The experimentally prequalified BRBs had nominal capacities of 300 kN and 700 kN. The range of applicability for the experimental prequalification (ANSI/AISC 341-10 [100]): 0.5·300 kN = **150 kN** ≤ N_p ≤ 1.2·700 kN = **840 kN**
Core steel grade: S235, S275, S355.	The steel used for manufacturing the core of the BRB must comply with the requirements from P100-1/2013 [5] regarding the ductility of the steel, specifications 6.2.(1)-(2), and the fracture energy (Table 6.2).
Core ratio h_p/t_p: 4.0 ≤ h_p/t_p ≤ 5.0.	The ratios h_p/t_p experimentally tested: • BRB 300 kN: 60mm/14mm = 4.3; • BRB 700 kN: 99mm/20mm = 5.0
Maximum core strain: $\varepsilon_{c,max}$ = ± 4%.	The axial strain in the plastic zone of the core, ε_c, is limited to the value that was experimentally validated ($\varepsilon_{c,max}$ = 4%), which corresponds to twice the design inter-storey drift at ULS ($2 \cdot d_r^{SLU}$).
Minimum class of concrete/mortar: C30/37	The minimum class of concrete/mortar is based on the material used for experimental qualifications and is confirmed by numerical post-test simulations.

design procedure resulted from the dimensions and the materials used for manufacturing the prequalified BRB specimens. The use of other materials, geometries, technological processes or design procedures requires an experimental qualification program according to P100-1/2013 [5] and SR EN 15129 [4]. To obtain similar cyclic performances with the ones of the prequalified specimens, when designing new BRBs the limitations from Table 6.1 must be followed.

6.2 Design procedure

The design procedure of a BRB has several steps, as presented below [151].

6.2.1 Initial data

In this step several parameters describing the frame braced with BRBs (Fig. 6.2) are defined:

- the length *L* and height *H* of the frame;
- the dimensions of the beams and columns;
- the layout of the BRBs;
- the insertion angle of BRB, α;
- the required strength of BRB, $N_{p,req}$;
- the relative inter-storey displacements, d_r^{SLU}.

Having the geometry of the frame defined (beams, columns, gussets), the geometry of the BRB can be defined, see Fig. 6.3.

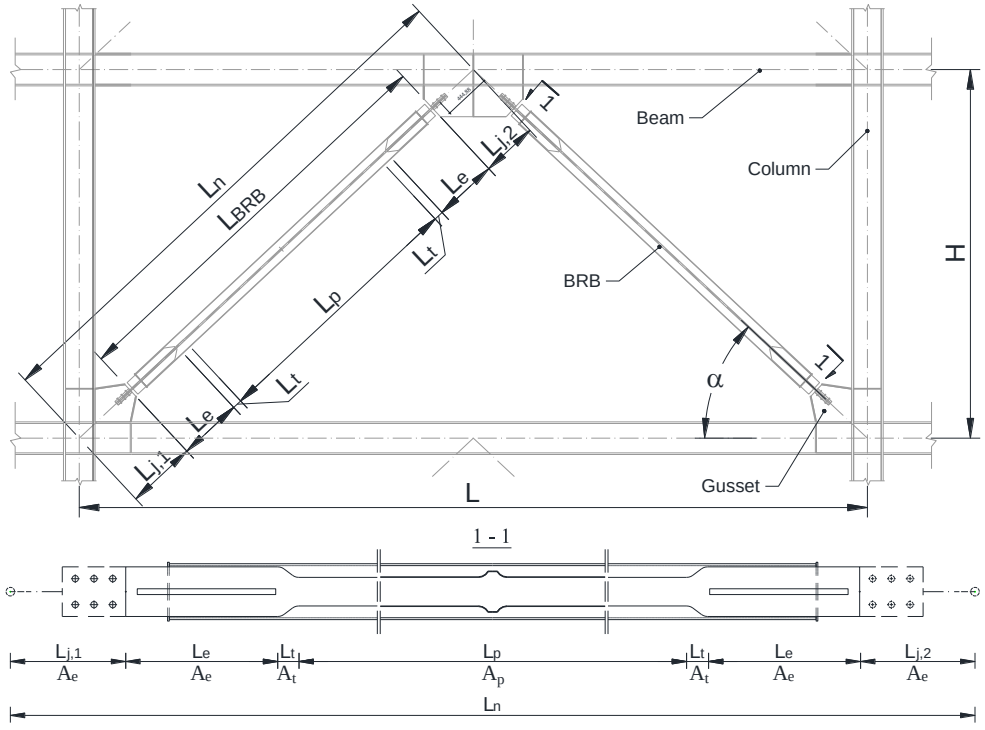

Fig. 6.2. Geometry of BRBF

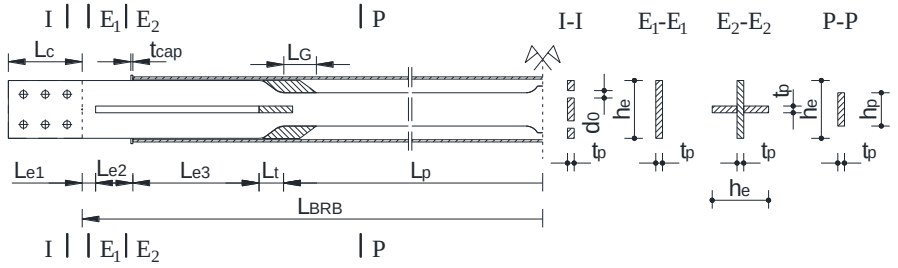

Fig. 6.3. Geometry of BRB

6.2.2 The length of longitudinal gap

The norm P100-1/2013 [5] specifies that the BRB must be capable to develop deformations corresponding to twice the design inter-storey drift at ULS ($2 \cdot d_r^{SLU}$). The design value of the axial deformation of the core (the stroke), δ_{Ed}, can be approximated as (see also Fig. 6.4):

$$\delta_{Ed} = 2 \cdot d_r^{SLU} \cdot \cos \alpha \tag{6.1}$$

To allow the core for free movement under compression loading, a longitudinal gap (polystyrene) of length L_G is provided in extension to the transition zone and stiffeners. Due to the unsymmetrical deformations in the two plastic segments of the core, the length of the longitudinal gap is considered 70% of the stroke:

$$L_G = 0{,}7 \cdot \delta_{Ed} \tag{6.2}$$

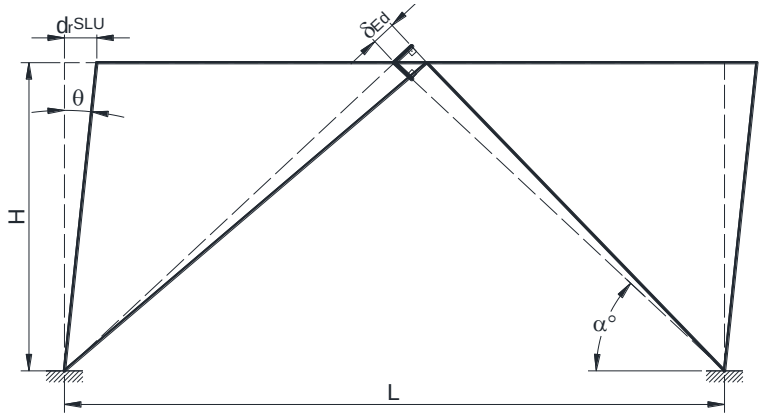

Fig. 6.4. The required axial deformation (the stroke) of BRB, δ_{Ed}

6.2.3 Plastic zone

The cross-sectional area of the core in the plastic zone is determined based on the required strength of the BRB:

$$A_p \geq N_{p,req}/f_{y,m} \tag{6.3}$$

where:

- $N_{p,req} = N_{p,Rd} \cdot \gamma_{M0}$ – the required strength of BRB supplied by the designer of BRBF.

- $N_{p,Rd}$ – the design strength of BRB.
- A_p – the nominal cross-sectional area of the core in the plastic zone.
- $f_{y,m}$ – the yield strength of the steel used for core manufacturing, it is experimentally determined as the mean value of three samples, extracted parallel with the core.
- $\gamma_{M0} = 1.1$ – the partial safety coefficient for steel (P100-1/2013 [5]).

According to SR EN 15129 [4], the BRB manufacturer must check the conformity of the steel used for the core by performing tensile tests. Thus, the cross-sectional area of the core in the plastic zone can be determined based on the experimentally determined yield strength of the steel ($f_{y,m}$). Consequently, a more economic design is obtained at both the BRB and (especially) the structure level. In principle, the option of using the nominal yield strength of the steel (f_y) can be adopted, but a less economical design at both BRB and structure levels is obtained.

The ratio between the height h_p and the thickness t_p of the cross-section must be in the between the limits used for the prequalified BRBs:

$$4.0 \leq h_p / t_p \leq 5.0 \tag{6.4}$$

To prevent the excessive buckling of the unconstrained segment of the plastic zone (Fig. 6.5) with respect to the minimum axis of inertia, the relative slenderness $\bar{\lambda}_p$ is limited. This limitation prevents possible wedging of the core in the longitudinal gap. The maximum length of the unconstrained segment appears after the maximum deformation during the tensile loading, being estimated as:

$$L_{g,cr} \leq 2 \cdot L_G \tag{6.5}$$

The value of the relative slenderness of the unconstrained segment with respect to the minimum axis of inertia is limited according to EN 1993- 1-1 [149]:

$$\bar{\lambda}_p \leq 0{,}2 \tag{6.6}$$

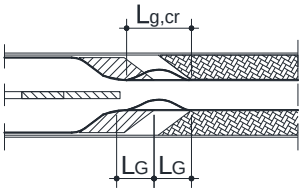

Fig. 6.5. Determination of buckling length of the unconstrained segment

Based on the results from the experimental prequalification tests, the (maximum) values for the strength adjustment factors are ω = 1.45 and $\omega\beta$ = 1.7 (resulting β = 1.17).

To design the non-dissipative zones of the core (elastic zone, connection cone), the BRM and the BRB-to-gusset connections, it is required to determine the nominal strength N_p, and the adjusted maximum capacities for tension T_{max}, and compression, C_{max}. The adjusted capacities consider the strain hardening effect (ω) and the additional hardening in compression ($\omega\beta$) as a cause of core-BRM interaction (friction):

$$N_p \geq A_p \cdot f_{y,m} \tag{6.7}$$

$$T_{max} \geq \omega \cdot N_p \tag{6.8}$$

$$C_{max} \geq \omega\beta \cdot N_p \tag{6.9}$$

The stopper represents a local enlarged region of the plastic zone, being positioned in the mid-span of it. It prevents the slippage of the BRM relative to the

core and prevents the unsymmetrical deformation of the plastic zone. The dimensions of the stopper can be determined as ratios of the core height h_p: height $h_0 = 0.1h_p$, width $b_0 = 0.5h_p$, fillet radius $R_0 = 0.2h_p$.

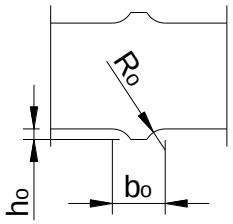

Fig. 6.6. Geometry of stopper

6.2.4 Elastic zone

The elastic zone L_e consists of three distinctive segments (Fig. 6.3): the elastic ("$2t_e$") zone of rectangular cross-section starting from the face of the gusset to the face of the stiffeners – L_{e1}, the elastic zone of cruciform cross-section positioned outside the BRM – L_{e2}, and the elastic zone of cruciform cross-section positioned inside the BRM – L_{e3}. The absence of the stiffeners on the "$2t_e$" zone limits the bending moment transmitted to the BRB ends due to the frame effect.

$$L_e = L_{e1} + L_{e2} + L_{e3} \tag{6.10}$$

$$L_{e1} = 2 \cdot t_e = 2 \cdot t_p \tag{6.11}$$

$$L_{e2} = 0.7 \cdot \delta_{Ed} + 20\ mm \tag{6.12}$$

$$L_{e3} = 2 \cdot h_e + 0.7 \cdot \delta_{Ed} \tag{6.13}$$

The cross-sectional area (A_{e1}) of the elastic zone of the core is determined based on the resistance check in the zone of minimum area (section E1-E1, see Fig. 6.3). The section is checked to the maximum compression force developed by BRB:

$$C_{max}/N_{c,e1,Rd} \leq 1.0 \tag{6.14}$$

where:

- $N_{c,e1,Rd} = A_{e1} \cdot f_{y,m}/\gamma_{M0}$ – the design resistance of the elastic zone.

Considering the thickness t_p for the cross-section of the elastic zone, the height h_e is computed as $h_e = A_{e1}/t_p$.

A class check of the core cross-section is performed in the section E2-E2 (Fig. 6.3) by limiting the ratio $c/t \leq 14\varepsilon$ (class section 3), according to EN 1993- 1-1 [149], Table 5.2.

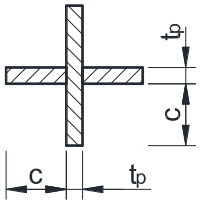

Fig. 6.7. Determining the class of cross-section of L_{e2} elastic segment

To prevent the buckling of the elastic zone, the relative slenderness $\bar{\lambda}_e$ is limited. The maximum length of the unconstrained segment appears after the maximum deformation during the tensile loading, being estimated as:

$$L_{e,cr} = 1.2 \cdot (L_{e1} + L_{e2} + 0.7 \cdot \delta_{Ed}) \quad (6.15)$$

Due to the fact that the elastic zone is of variable cross-section, the buckling length $L_{e,cr}$ is considered in a simplified way, and also the properties of the cross-section of the core (moment of inertia and radius of gyration), which are taken as the maximum ones from the zone L_{e1}.

The value of the relative slenderness of the unconstrained segment with respect to the minimum axis of inertia is limited according to EN 1993- 1-1 [149]:

$$\bar{\lambda}_e \leq 0{,}2 \quad (6.16)$$

6.2.5 Transition zone

The gradual increase of the cross-sectional area from the reduced (plastic) to the enlarged (elastic) zone is realized through the transition zone (Fig. 6.8) of length L_t. The gradual transition is assured by the fillet radius R_t, which also reduces the risk of stress concentrations which might cause premature failure of the core.

$$L_t = h_e - h_p \quad (6.17)$$

$$R_t = (h_e - h_p)/2 \quad (6.18)$$

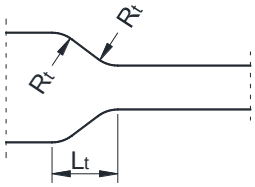

Fig. 6.8. Detail of transition zone

6.2.6 Connection zone

Bolted connections were provided for the experimental BRB specimens. A special detail was used as to limit the bending moments transmitted to the BRB ends due to the frame effect (opening and closing of the beam-to-column angle). As presented in Fig. 6.9, the stiffeners of the core are missing on a "$2t_p$" zone, as to limit the demand rotations. The gusset is welded to the beam and column and stiffeners are welded on the free edges to prevent local buckling, thus preventing a global failure mode of the BRB.

The connection zone of the core (of length L_c, see Fig. 6.3) and the stiffened gusset (of thickness $t_g = t_p$) are designed using the following design forces (P100-1/2013 [5]):

$$N_{c,i,Ed} = 1.1 \cdot C_{max} \quad (6.19)$$

$$N_{t,i,Ed} = 1.1 \cdot T_{max} \quad (6.20)$$

For the experimental specimens, according to the EN 1993- 1-8 [153] Table 3.2, the BRB-to-gusset connection is of category A (bearing type). Therefore, the design of the connection will obey the criteria specified in Table 3.2 [153].

Other connection details can also be used, but experimental validation is required as to assure a good cyclic performance for the BRBs.

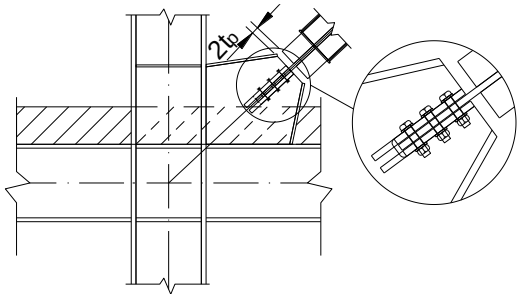

Fig. 6.9. Detail of bolted connection

6.2.7 Core axial deformation

Based on the results from the experimental tests, the axial strain in the core of the prequalified BRBs reached a maximum value of $\varepsilon_{c,max}$ = ± 4%. Having the length of the plastic zone L_p determined, the value of the axial deformation that can be developed by the core δ_{Rd} results as:

$$\delta_{Rd} = \varepsilon_{b,max} \cdot L_p \tag{6.21}$$

where:

- $L_p = L_n - L_{j,1} - L_{j,2} - 2L_e - 2L_t$ – the length of the plastic zone, including the stopper.
- L_n – the node-to-node length of the BRB (Fig. 6.2).
- $L_{j,1}, L_{j,2}$ – the length of the lower and upper joint zone (it includes the connection zone of the core, L_c), respectively (Fig. 6.2).

It needs to be mentioned that the length L_p can be adjusted as to satisfy the requirements regarding the axial stiffness and axial strain. Thus, a shorter L_p length will increase the axial stiffness but it will decrease the axial deformation capability.

The design value of the core axial deformation (the stroke), δ_{Ed}, must be less equal to the capacity of the BRB to axially deform, δ_{Rd}:

$$\delta_{Ed} \leq \delta_{Rd} \tag{6.22}$$

6.2.8 Buckling restraining mechanism

Based on the experimental and numerical results, the design of the buckling restraining mechanism (BRM) will consider the elastic critical force N_{cr} of the BRM be at least 3.0 times the nominal resistance of the core N_p:

$$N_{cr}/N_p \geq 3.0 \tag{6.23}$$

where:

- $N_{cr} = \pi^2 E_s I_s / L_{cr}^2$ – the elastic critical force of the BRM, without the contribution of the infill-concrete.
- E_s = 210000 N/mm^2 – the elastic modulus of the steel.
- I_s – the moment of inertia of the steel tube.
- $L_{cr} = L_{BRB}$ – the (in plane of the frame) buckling length of the BRM, considered for the tested BRB specimens equal to the length of the BRB, L_{BRB}, due to the special connection detail.

The length of the BRM can be determined as:

$$L_{BRM} = L_p + 2 \cdot L_t + 2 \cdot L_{e,3} \tag{6.24}$$

The interior diameter D_i of the tube must be greater than the height of the elastic zone plus four thicknesses of the unbonding material, t_{um}:

$$D_i \geq h_e + 4 \cdot t_{um} \tag{6.25}$$

This condition (6.25) prevents the contact between the core and the tube and allow for an easy insertion of the core into the tube.

6.2.9 Effective stiffness

The effective axial stiffness of the BRB, K_{eff}, is determined as the sum of the core components considered as springs in series:

$$K_{eff} = \frac{1}{\sum \frac{1}{K_j} + \sum \frac{1}{K_e} + \sum \frac{1}{K_t} + \frac{1}{K_p}} \tag{6.26}$$

where:

- $K_j = EA_j/L_j$ – the stiffness of one connection. For simplification, the effective area of the connection can be taken equal to the area of the elastic zone of the core ($A_j = A_{e,2}$). Usually, the length of the lower and upper connection are different ($L_{j,1} \neq L_{j,2}$).
- $K_e = EA_e/L_e$ – the stiffness of an elastic zone of length $L_e = L_{e1} + L_{e2} + L_{e3}$. The area $A_e = t_p(2 \cdot h_e - t_p)$ is computed in cross-section E2-E2, see Fig. 6.3.
- $K_t = EA_t/L_t$ – the stiffness of a transition zone, with $A_t = t_p(h_e + h_p)/2$.
- $K_p = EA_p/L_p$ – the stiffness of the plastic zone.

At the basis of the calculus of K_{eff} there are several simplifying hypotheses: the disregard of the additional stiffness from the stopper, the consideration of the elastic zone as having constant cross-section, the approximation of the area of connection zones as equal to the area of the elastic zone.

6.3 Concluding remarks

Design recommendations are given for the prequalified BRB solution ("convetional" BRB of *type A*).

Applicability limits (BRB capacity, steel grade, core aspect ratio, maximum core strain, minimum concrete class) of the design procedure are set based on experimental data from prequalification of BRBs.

A procedure is developed for the design of the BRBs according to P100-1/2013 [5], EN 1993- 1-1 [149] and EN 1993- 1-8 [153]: the plastic zone of the core is designed as the dissipative component, while all the other components are designed to work in the elastic domain.

A procedure to estimate the effective axial stiffness of the BRB is also proposed.

7 PERFORMANCE-BASED DESIGN OF BRBF

7.1 Introduction

The frames equipped with BRBs are known as Buckling Restrained Braced Frames (BRBF). Application of BRBFs can be seen for both new or retrofit project, steel or concrete buildings, as presented in chapter 2.5. Different design approaches consider the BRBFs as either the main lateral force-resisting system in the structure (Romania), or as a secondary system to provide additional damping to the main system (Japan). The use of BRBFs in Romania is regulated by the seismic design code P100-1/2013 [5], but no design regulations are provided for determining the optimal geometry of the main dissipative component, the steel core.

The main objective of this chapter is to provide additional guidelines to the existing design methodology of BRBs available in P100-1/2013 [5]. The additional guidelines refer to the optimization of the geometry of the main component of the BRB, the dissipative steel core. For a certain level of the demand force, several geometries can be provided for the core within the range from the lower bound to the upper bound of the geometrical constraints. All the resulting BRBs can have the same strength (N_p), stiffness (K_{eff}), but different values for the level of axial strain in the plastic zone of the core (ε_p). For this study, three different core configurations were investigated, resulting the following strain levels in the plastic zone: 1.66%, 1.75% and 2.00%.

The optimization process was based on the assessment of the seismic response of a reference structure equipped with BRBs of different core configurations. The seismic performance was investigated for a seismic action corresponding to Ultimate Limit State (ULS). 7 artificial accelerograms were used to simulate the ULS earthquake. Nonlinear dynamic and static analyses were performed in OpenSees [152] finite element framework. The seismic performance was assessed in terms of inter-story drifts, residual drifts, top displacements and maximum strains in the core. Based on results, the reference structure designed by the current methodology available in P100-1/2013 [5] fails the check for the inter-storey relative displacement (drift) at Ultimate Limit State (ULS). Therefore, discussions are made, and two solutions are proposed for improving the current design methodology.

7.2 FEM modelling

7.2.1 Reference structure

The reference structure (Fig. 7.1) is a low-rise multi-story steel building located in Bucharest that was designed according to P100-1/2013 [5] within the frame of IMSER research project [6]. The plan layout (Fig. 7.2.a) consists of 3 by 5 equal bays of 7.5 m, having perimetral buckling restrained braced frames as lateral resisting system. The vertical layout of the structure consists of 3 stories of 3.5m each. Within the initial design, pinned connections were provided for beam-to-column joints, BRBs, and unbraced columns. The columns forming the braced frames were fixed connected to the ground. The live loads were established as for an office building. The site

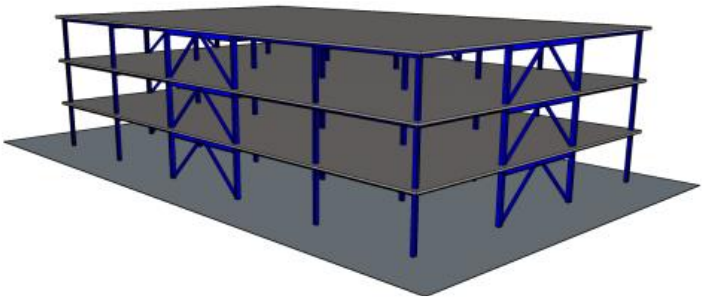

Fig. 7.1. Reference structure *BL16:* 3D view

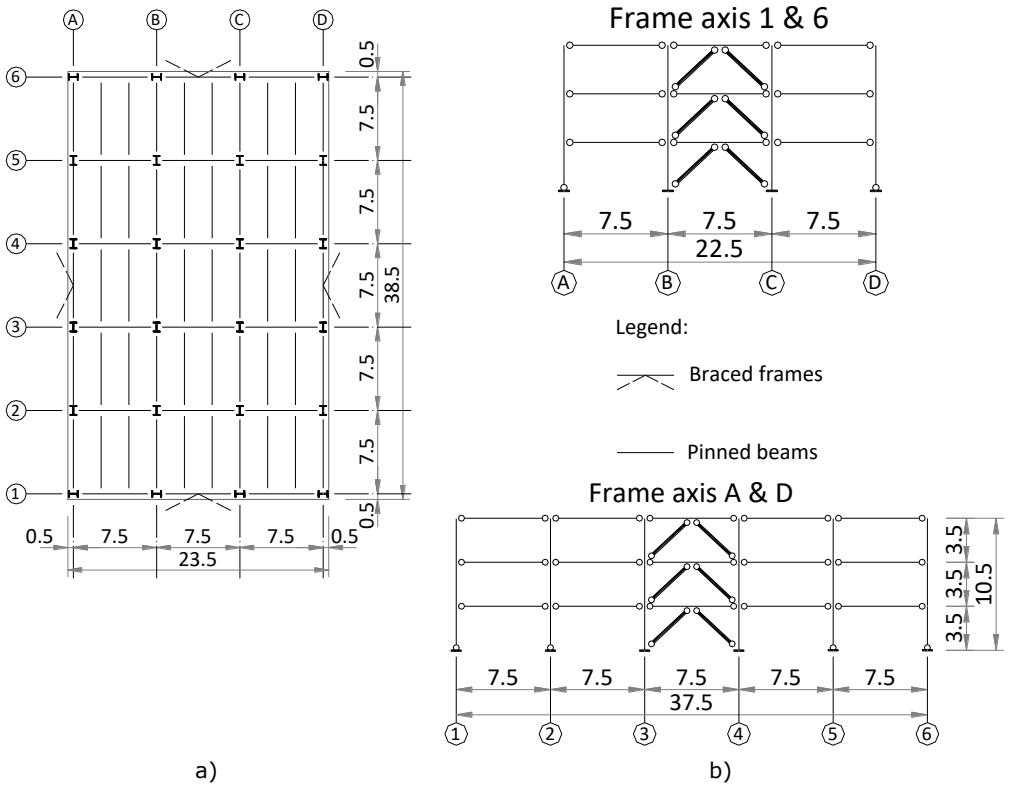

a) b)

Fig. 7.2. Reference structure *BL16:* a) plan and b) vertical layout

location, Bucharest, is characterized by T_B = 0.32 s, T_C = 1.6 s, T_D =2s, a_g = 0.3 g. The lateral resisting frames on the *X* direction of the building are frames axis 1 and 6, and frames axis *A* and *D* on *Y* direction (Fig. 7.2.b).

In this study, only the behaviour of the building in the *X* direction was investigated by considering the planar frame from axis 1. In Fig. 7.3 the sections resulted from the initial elastic design are presented.

As regarding the BRBs, three different solutions corresponding to the different levels of axial strain in the core (1.66%, 1.75%, 2.00%) were designed following the recommendations from chapter 6 for each brace capacity (*BRB-1*, *BRB-2*, *BRB-3*). In Fig. 7.4 the geometry configurations are presented for the BRBs used in the second floor (*BRB-2*). Using S355 steel grade and the same cross-sectional dimensions of the

core in section A-A, the same capacity (N_p) was provided for all three solutions. By adjusting the geometry (in the section B-B), the same effective stiffness (K_{eff}) was also assured. A special detail was used in the case of BRBs with the axial strain in the core equal to 1.66% due to stiffness requirement.

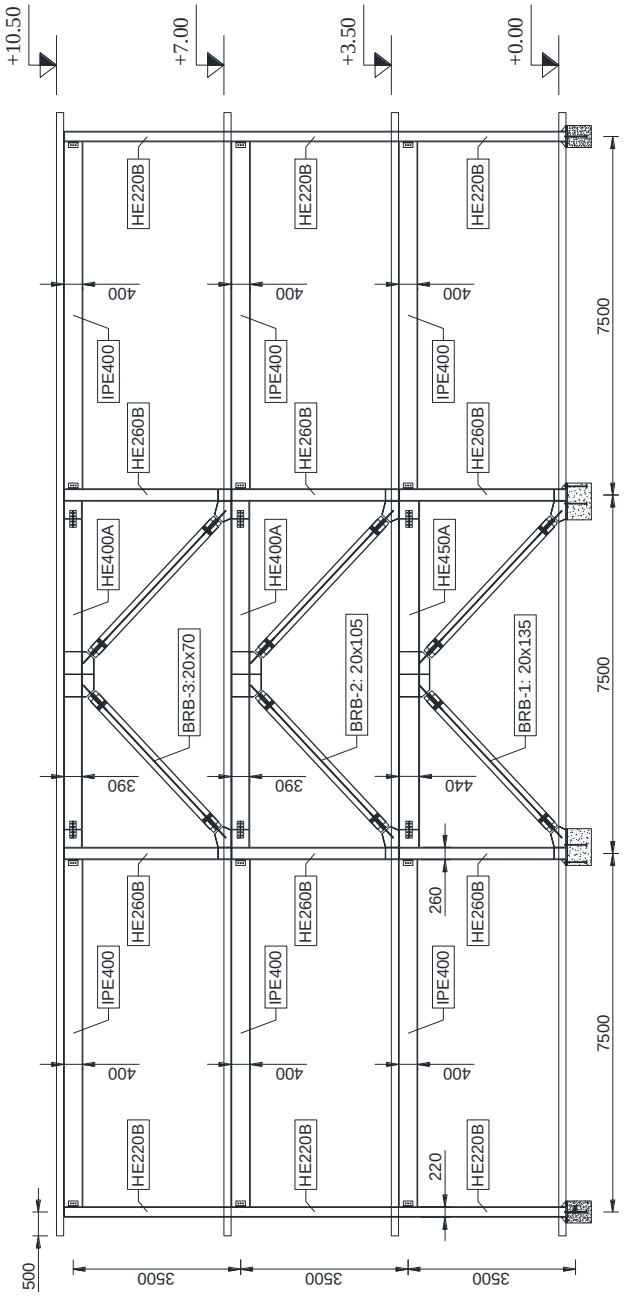

Fig. 7.3. Planar frame axis 1: sections and connectivity

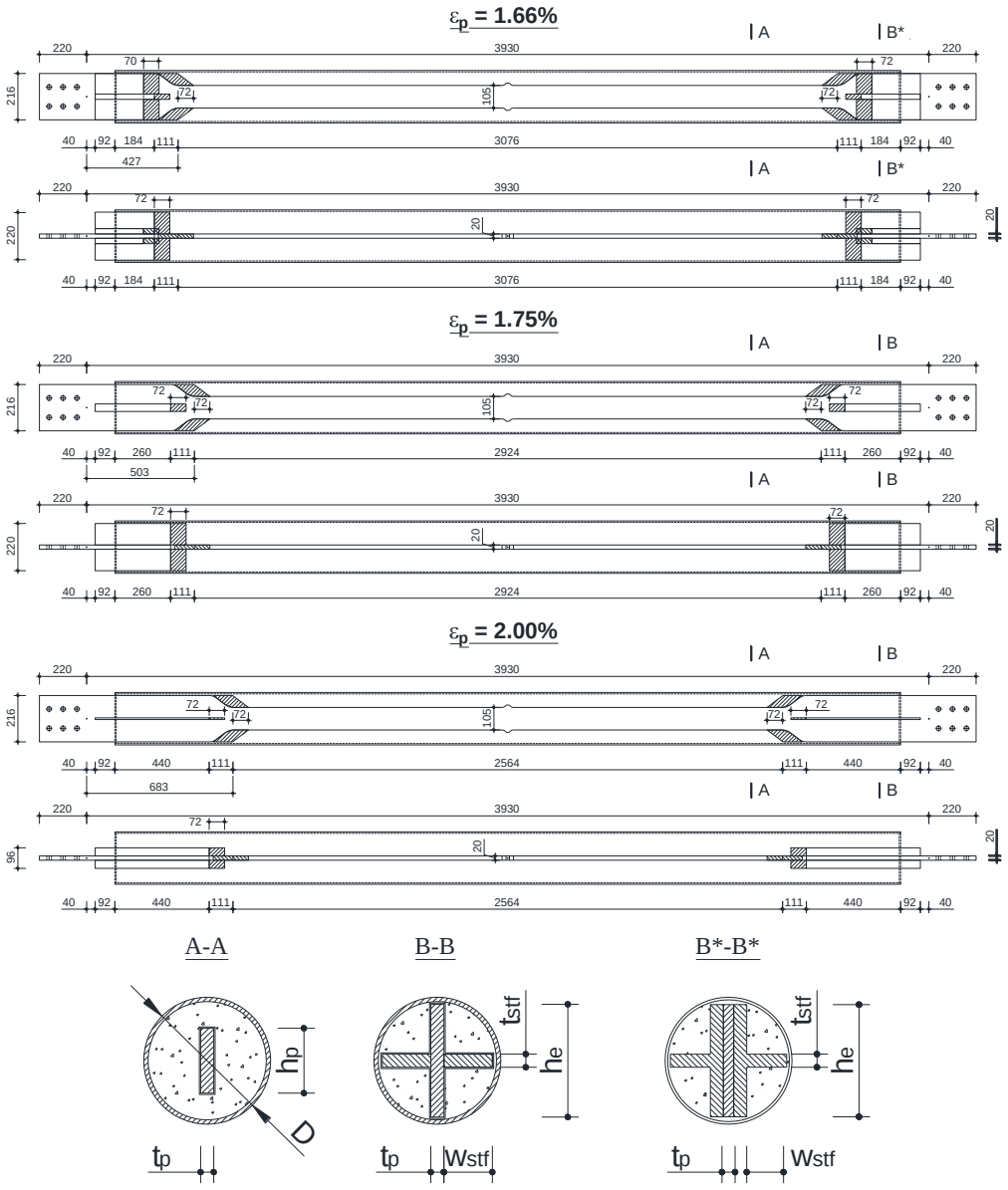

Fig. 7.4. The geometry of *BRB-2* for the three levels of axial strain: 1.66 %, 1.75%, 2.00%

7.2.2 Numerical model

OpenSees (2.5.0) [152] finite element code environment was chosen for the nonlinear analyses. The 3D structure was simplified based on the code provisions from P100-1/2013 [5] to two planar frames on the main directions of the building. For the assessment of the seismic performance of the building with respect to BRB solutions only the *X* direction was considered for the seismic action. Therefore, the frame presented in Fig. 7.3 was simplified to a numerical model including only the steel

elements (Fig. 7.5), thus the slabs were not modelled. Since pinned beam-to-column connections were provided, within the OpenSees model the location of the connections was considered at the face of the columns for the unbraced bays, and at certain distance from the axis of the column for the braced bay. This distance was set equal to the horizontal projection of the lower rigid zone of the BRB-to-gusset connection (Fig. 7.5). To account for the *P-d* effects, a leaning column was connected to the main structure by rigid truss elements.

All the beam and columns were modelled using elastic finite elements having three degrees of freedom per node (two translations and one rotation), identified as "elasticBeamColumn". No offsets of the sections were considered for beams.

A special interest was given to BRB modelling. As it can be observed from Fig. 7.5, between the insertion nodes of a BRB there are several zones: rigid zone (*i* and *j*), elastic zone and plastic zone. Therefore, different finite elements were used for modelling. For the rigid zones "elasticBeamColumn" elements were used having the geometrical properties obtained as follows: area was set equal to the area of the plastic zone multiplied by 1000 to assure axial rigid behaviour of the finite element; the inertial moment was set equal to the inertial moment of the plastic zone multiplied by 1000 to assure a rigid flexural behaviour of the stiffened gusset-to-beam-to-column connection. Similar finite elements were used to model the elastic zones, but only the inertial moment was obtained in a similar way to simulate the buckling restraining mechanism of the BRB. Area was computed from the cross-sectional properties of the core in the elastic zone. The plastic zone was modelled using a "nonlinearBeamColumn" element with two integration points along the length. Two different behaviours were assigned to this finite element by using the "section Aggregator" command: a nonlinear elastic-plastic behaviour was defined for the axial component (P) and an elastic behaviour for the flexural component (M_z). By using this procedure, both the core and the buckling restraining mechanism can be modelled. The plastic behaviour was defined using "Steel01" material type. The yield force was set equal to F_y = 355 N/mm^2·A_p, and a slope of b = 0.018 was considered for the second stiffness of the BRB. The slope was determined based on experimental data (Fig. 7.6).

Regarding the connectivity of the finite elements used to model the BRB (between the insertion nodes), pinned connections were provided only between the rigid and elastic segments, all the others being continuous.

Spring elements were used to connect the leaning columns and a very small value (K = 1e-14 N/mm) was assigned to the rotational material direction about Z axis (6) for the "zeroLength" element.

To account for geometrical nonlinearities (*P-d* effects), the "PDeltaTransf" command was used within the definition of all the finite elements, except the trusses.

The rigid diaphragm effect of the slabs was simulated in OpenSees by using multi-point constraint between the frame nodes ("equalDOF" command).

Two configurations were used for the definition of the column-base supports: *BRBF-1* and *BRBF-2* (Fig. 7.7). In The case of *BRBF-1*, the external columns have pinned supports, while the internal column have fixed supports, as described in [6]. Using this configuration, the structure is not truly BRBF, the contribution of the two fixed-base columns being further determined. In the case of the second configuration, *BRBF -2*, all the columns have pinned supports, thus assuring that only the BRBs will resist the lateral forces. This configuration is needed to evaluate de influence of the fixed columns to the seismic performance in the case of *BRBF-1*.

Based on the above assumptions, the models created in OpenSees uses concentrated plasticity theory to describe the nonlinear behaviour of the structure.

The idealized schematic of the numerical models are presented in Fig. 7.7, where the numbering and labelling of the nodes, finite elements and boundary conditions are graphical represented.

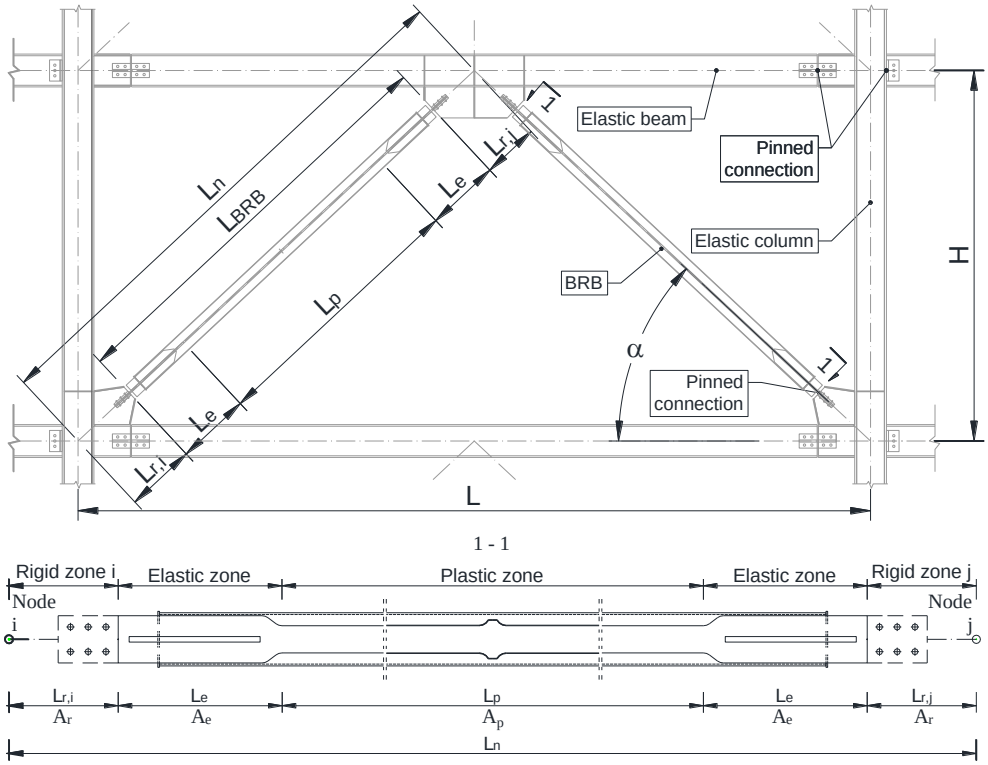

Fig. 7.5. Assumptions used for modelling the BRBF in OpenSees

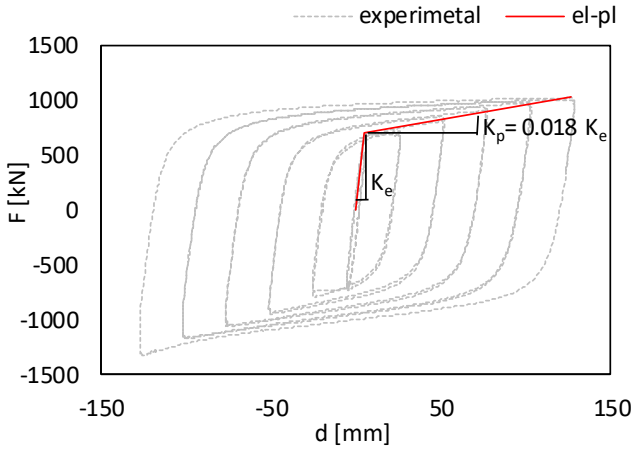

Fig. 7.6. Determination of the plastic stiffness for the analysed BRBs

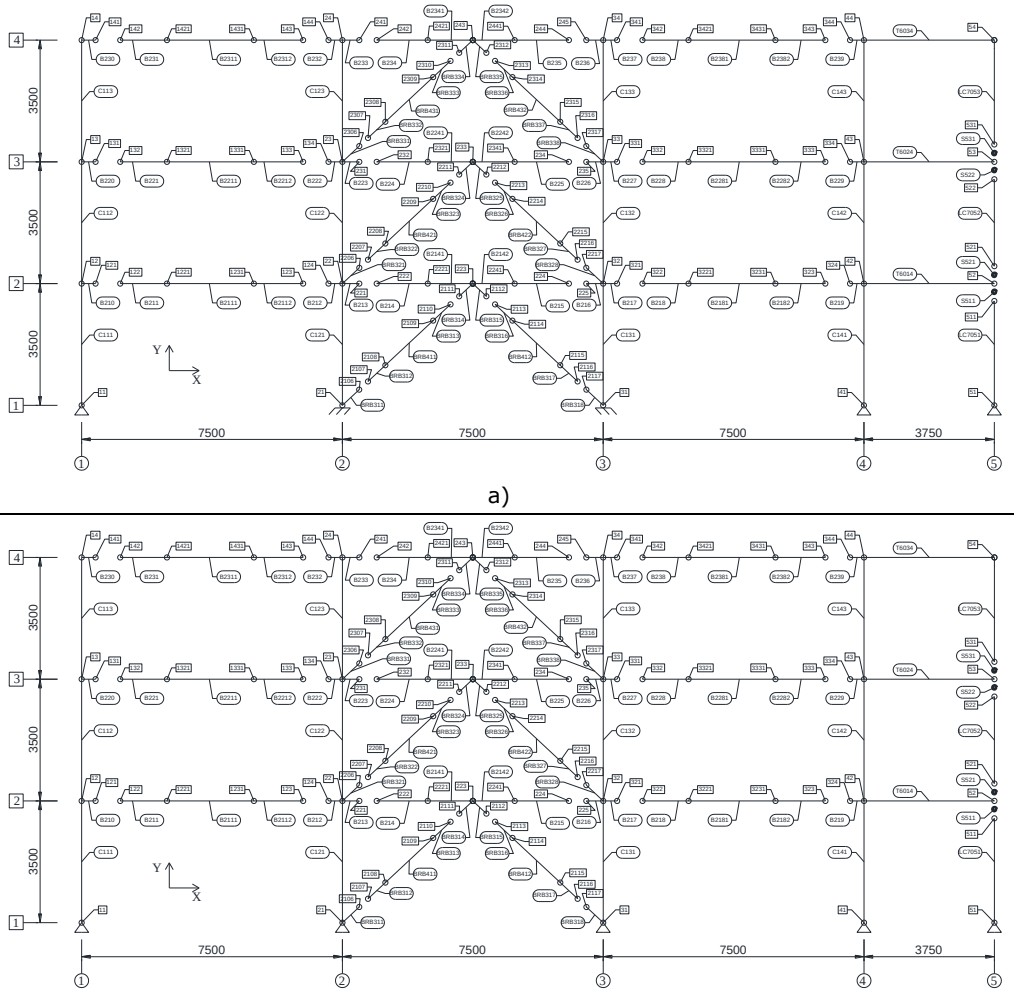

Fig. 7.7. Schematics of numerical BRBFs models in OpenSees: a) pinned-fixed column base supports - *BRBF-1*; b) pinned column base supports - *BRBF-2*

Both nonlinear static and dynamic analyses have two steps. In the first step, a load-controlled static analysis is performed using the gravity loads from the seismic combination (1.0·Dead_Load + 0.3·Live_Load). Tributary loads are applied on the BRBF as follows. Concentrated forces coming from the secondary beams are assigned to the intermediate nodes of the beams, while uniform distributed loads are assigned to the beams. The remaining loads from the rest of the half structure are assigned to the nodes of the leaning columns. The global imperfections of the reference structure were taken into consideration by applying a set of lateral loads according to EN 1993- 1-1 [149]. Further details regarding the loads can be found in [6] and centralized in Table 7.1. Having the gravity loads maintained constant, the nonlinear analysis is performed in the second step.

For the eigen analysis, the numerical model included lumped floor masses, distributed only to the frame nodes (Table 7.1).

Table 7.1 Loads and seismic masses assigned to BRBF models

	Dead Loads			Live		Imperf.	Masses
Floor #	Self weight [kN/m^2]	Super Dead [kN/m^2]	Facade [kN/m^2]	Live [kN/m^2]	Part. walls [kN/m^2]	Lateral loads [kN]	1*DL+ 0.3*LL [kNs^2/m]
3	3.0	2.5	1.0	2.5		9.4	317.211
2	3.0	2.0	1.0	2.5	0.8	18.5	308.705
1	3.0	2.0	1.0	2.5	0.8	27.7	309.916

The OpenSees BRBF models containing the code lines are presented in Annex A.

7.2.3 Calibration

To assure that reliable results are provided, the numerical model was check by performing eigen and pushover analyses. The pinned-base model, *BRBF-2*, was chosen for checks since lateral resistance is given only by the BRBs. Linear transformation of the finite elements was used in this case.

Within the eigen analysis, the OpenSees two-dimensional finite element model and its assigned masses were check against the results reported in [6] for three-dimensional FEM model. As it can be observed from Fig. 7.8, almost similar

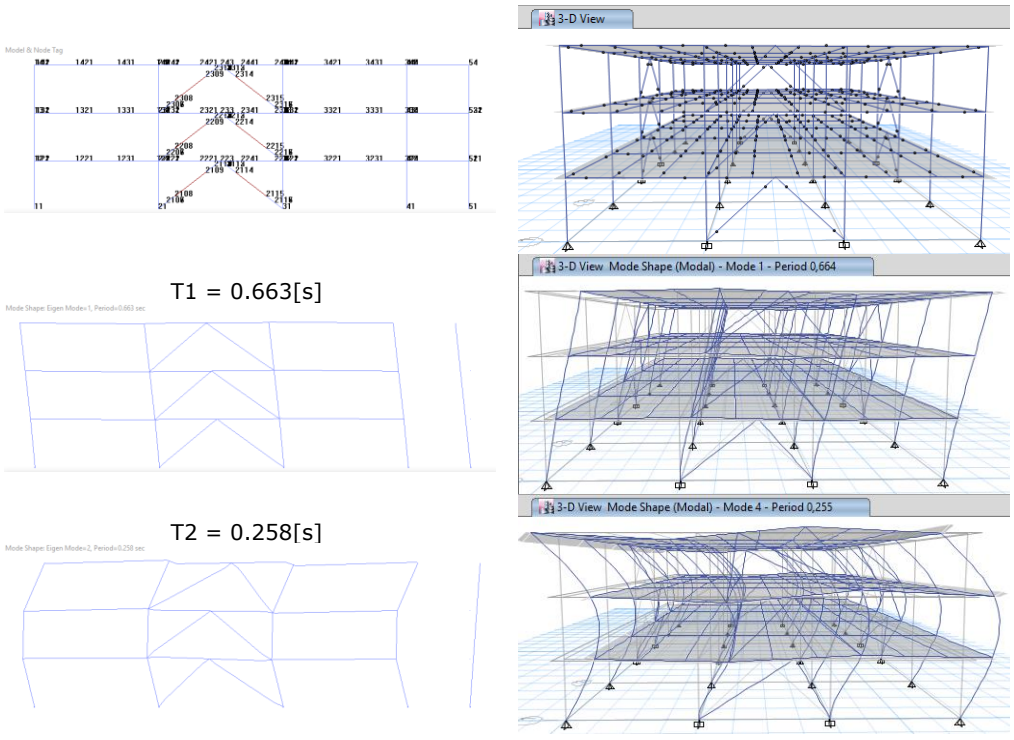

a) b)

Fig. 7.8. Comparison of eigen analysis results: a) OpenSees model, b) Etabs model

results were obtained for both models with respect and eigen values. Therefore, the finite element two-dimensional model was declared calibrated.

The second check relates to the lateral resisting system – the BRBs. Two checks were performed at this stage: the story lateral stiffness and the story lateral yield force. The results obtained from the pushover analysis performed in OpenSees were checked against the characteristic values of the stiffness and the yield force of the BRBs ($F_{y,k}^{BRB} = 2 \cdot f_{y,k} \cdot A_p \cdot \cos(\alpha)$, α = BRB insertion angle). The axial stiffness of the BRBs was computed considering the connection zones as rigid. The results related to this check are summarized in Fig. 7.9. It can be observed that the yield forces are in good agreement at all stories.

As regarding the lateral stiffness, several explanations must be gives since the results are not in close agreement at all floors. At the first floor, since all the connections are pinned and there are no other elements to resist to lateral forces, the stiffness of the story is the horizontal component of the stiffness of the two BRBs. At the second and third floor, due to vertical displacements of nodes forming the braced bay, the stiffness of the story is smaller than the stiffness of the two BRBs, considering its horizontal component. Based on these results, the OpenSees finite element model was considered calibrated and appropriate to use within the numerical program.

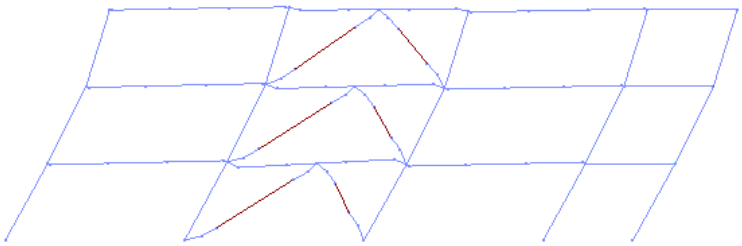

a)

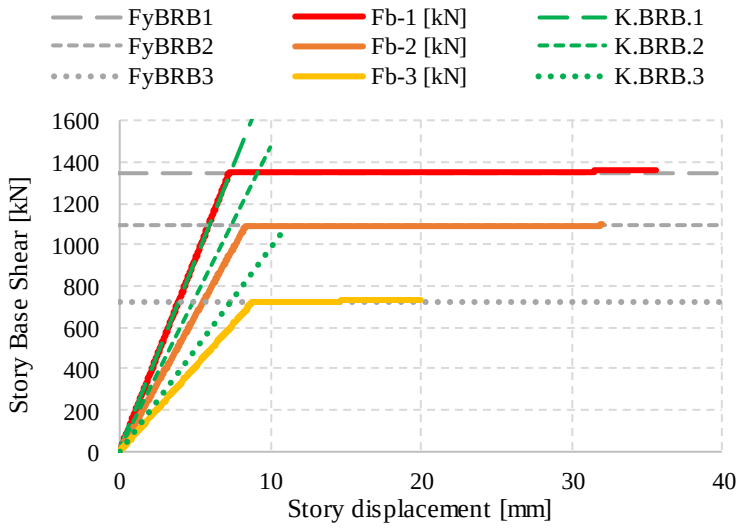

b)

Fig. 7.9. Pushover results used in calibration: a) failure mechanism, a) story capacity curves

7.3 Numerical program

Performance-based evaluation of the reference building frames equipped with BRBs was performed for a level of seismic action corresponding to Ultimate Limit State, ULS.

Within this parametric study, nonlinear static and dynamic analyses were performed. A total of eight BRBF models were created and analysed in OpenSees. Six BRBF models were used for nonlinear dynamic analyses (Time History, TH) and two BRBF models for static nonlinear analyses (Pushover, PO).

FEM models were created for each of the BRB configuration corresponding to pinned and pinned-fixed column base supports. For all six models, nonlinear time history analyses were performed using seven artificial accelerograms created for Bucharest (a_g = 0.3 g, T_B = 0.32 s, T_C = 1.6 s, T_D = 2 s), see Fig. 7.10 and Annex B. Mean values for the inter-story and relative displacements (drift), maximum residual drift, top displacement and maximum strain in the plastic zone of the core were used to assess the seismic performance of the analysed structures.

The nonlinear static analyses were used to observe the influence of using different column base supports and to asset the contribution of the fixed columns (axis 2 and 3) to the lateral stiffness of the BRBF frames.

The numerical program is summarized in Table 7.2.

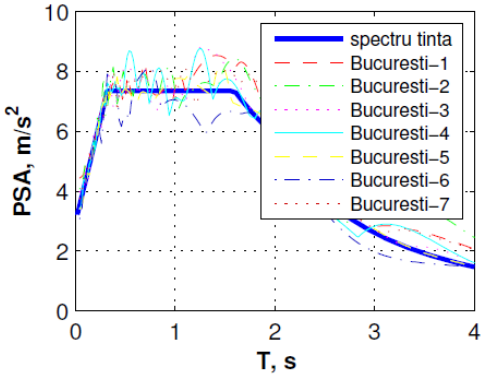

Fig. 7.10. Artificial accelerograms used for time history analyses

Table 7.2 BRBF - numerical program

ID FEM model	Analysis type	Strain level in core plastic zone			Column base supports	
		1.66%	1.75%	2.00%	Pinned	Pinned-fixed
BRBF_1.66p	TH	✓			✓	
BRBF_1.66pf	TH	✓				✓
BRBF_1.75p	TH		✓		✓	
BRBF_1.75pf	TH		✓			✓
BRBF_2.00p	TH			✓	✓	
BRBF_2.00pf	TH			✓		✓
PO_BRBF_2.00p	PO			✓	✓	
PO_BRBF_2.00pf	PO			✓		✓

7.4 Parametric study

7.4.1 Inter-storey drift

The assessment of the seismic performance of the analysed BRBF frames in terms of inter-storey drift is graphically presented in Fig. 7.11. As a general observation, all the frames failed the inter-storey drift check (drift limit 2.5%), even though in the case of *BRBF-2* (pinned-fixed column base supports) all the columns were modelled using finite elements with elastic properties. Also, it can be observed that by using pinned-fixed supports the maximum values of the inter-story drift recorded at the first floor are reduced by almost 40%. As regarding the use of different BRB configurations, a small reduction in terms of inter-story drift can be noticed if using BRBs with higher strain levels in the plastic zone of the core.

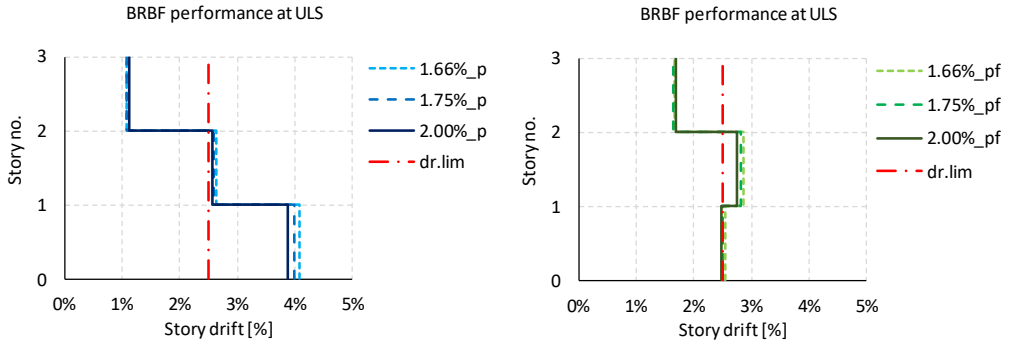

Fig. 7.11. Inter-storey drifts: a) BRBFs-1 (pinned), b) BRBFs-2 (pinned-fixed)

7.4.2 Maximum residual drift

Since BRBs dissipate seismic energy by undergoing plastic deformations, significant residual drifts may occur if no system with re-centering capacity is provided. To evaluate this aspect, in Fig. 7.12 are presented the maximum values of the residual inter-storey drifts corresponding to the frames *BRBF-1* (pinned column base supports) and *BRBF-2* (pinned-fixed column base supports). It can be observed a 35% reduction of the maximum residual drift if using pinned-fixed supports. Small reductions can be observed if using BRBs designed for higher values of the axial strain in the plastic zone.

7.4.3 Top displacement

As it can be observed in Fig. 7.13, in the case the frames provided with pinned-fixed column base supports a 20% reduction in the top displacement was noticed. Also, using BRBs with higher design axial strains in the plastic zone leads to slightly lower values for the top displacement.

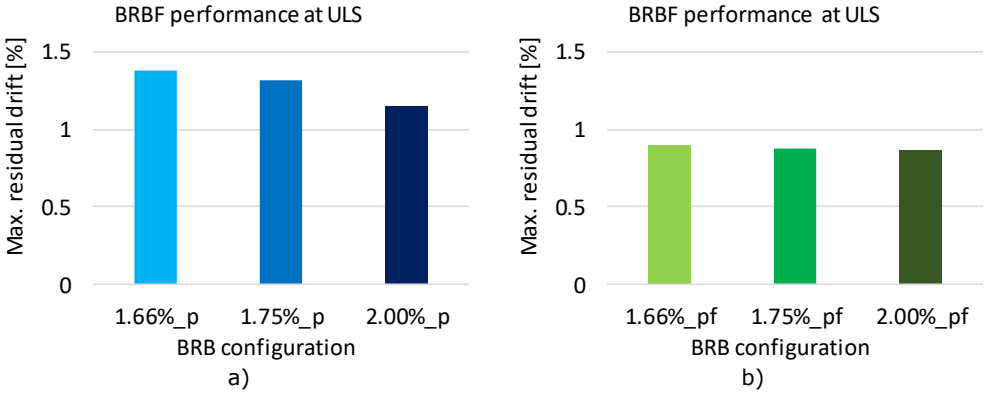

Fig. 7.12. Maximum residual drifts: a) BRBFs-1 (pinned), b) BRBFs-2 (pinned-fixed)

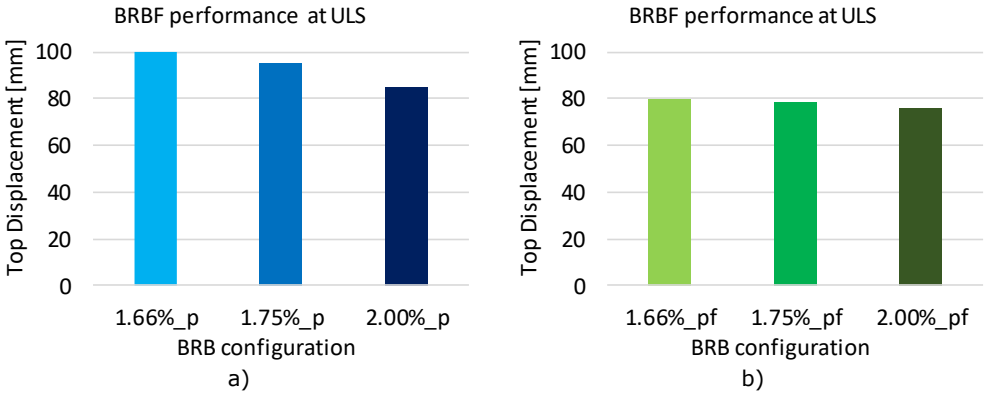

Fig. 7.13. Top displacements: a) BRBFs-1 (pinned), b) BRBFs-2 (pinned-fixed)

7.4.4 Maximum axial strain

By monitoring the displacements of the nodes delimiting the plastic zone of the core, the values of the axial strains with respect to initial plastic length were determined. The maximum values ($\varepsilon_{p,max}$) recorded for each BRBF model are centralized in Fig. 7.14. It can be observed that lower values are obtained for pinned-fixed configurations and for BRBF frames equipped with BRBs having longer plastic zones, thus lower axial strains.

The BRB configurations used within this study were experimentally qualified for a level of axial strain in the plastic zone of the core equal to 2.0% (see chapter 4). Based on the results from Fig. 7.14, all BRBs are failing the check related to the maximum allowable strain in the plastic zone.

In Fig. 7.15 it can be observed that by dividing the maximum recorded values ($\varepsilon_{p,max}$) to the design values ($\varepsilon_{p,d}$) of the axial strain in the plastic segment of the core, the ratios are larger than 1.0 in all BRBF cases. In the case of pinned BRBFs (*BRBF- 1*), the ration $\varepsilon_{p,max}/\varepsilon_{p,d}$ reaches values close to 2, while in the case of BRBFs with pinned-fixed supports (*BRBF- 2*) the ratio $\varepsilon_{p,max}/\varepsilon_{p,d}$ reaches values close 1.3.

Based on the above observations, the structures need to be re-designed.

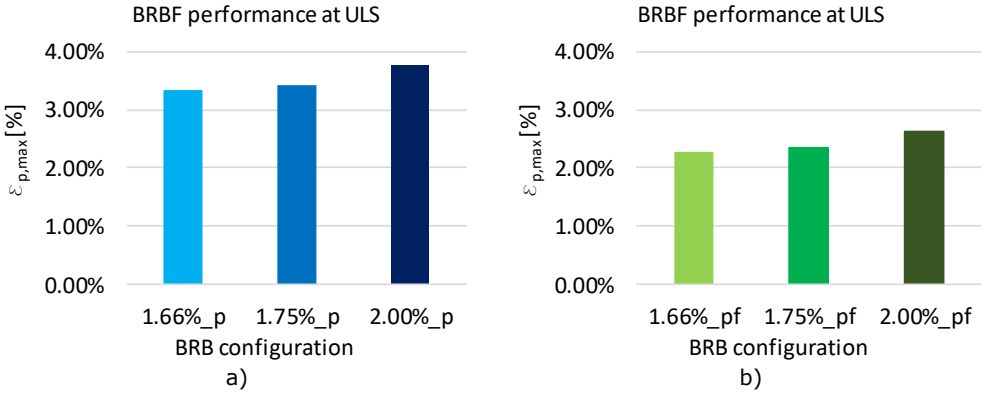

Fig. 7.14. Maximum axial strains in plastic zone of the core: a) BRBFs-1 (pinned), b) BRBFs-2 (pinned-fixed)

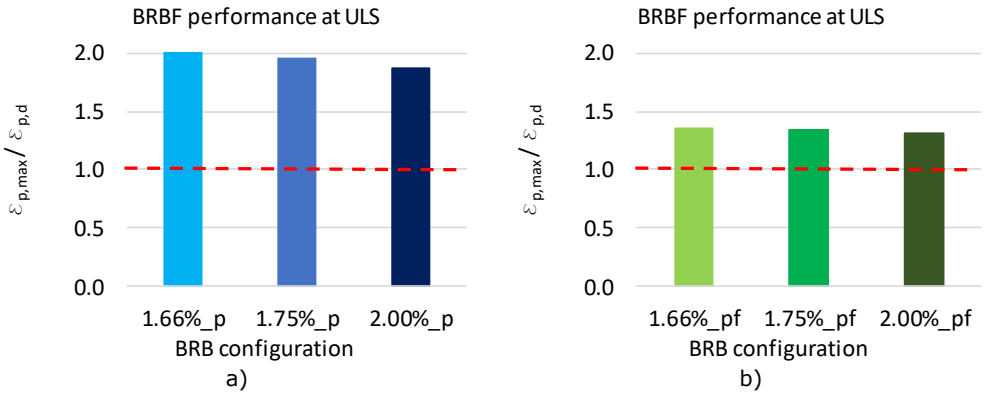

Fig. 7.15. Demand to design axial strain ratios in the plastic zone of the core: a) BRBFs-1 (pinned), b) BRBFs-2 (pinned-fixed)

7.4.5 Boundary conditions

Based on the time history analyses results, the structures having pinned supports (*BRBF- 1*) are undergoing large inter-story relative displacements, especially at the first floor (almost 4%). This may suggest a soft story mechanism. By using pinned-fixed supports (*BRBF- 2*), this problem is solved.

To evaluate the contribution of the fixed columns to the lateral stiffness of the reference structure, four pushover analyses were performed on the following models using modal and uniform lateral load configuration, as specified in P100-1/2013 [5]:

- *BRBF-1* (pinned), $\varepsilon_{p,d}$ = 2.0%:
  - Modal lateral load configuration: *Modal_P-d_pin*;
  - Uniform lateral load configuration: *Uniform_P-d_pin*.
- *BRBF-2* (pinned-fixed), $\varepsilon_{p,d}$ = 2.0%:
  - Modal lateral load configuration: *Modal_P-d_pin-fix*;
  - Uniform lateral load configuration: *Uniform_P-d_pin-fix*.

Significant contribution of fixed columns (axis 2 and 3) to the plastic stiffness is recorded in the case of pinned-fixed column base (Fig. 7.16). As previously

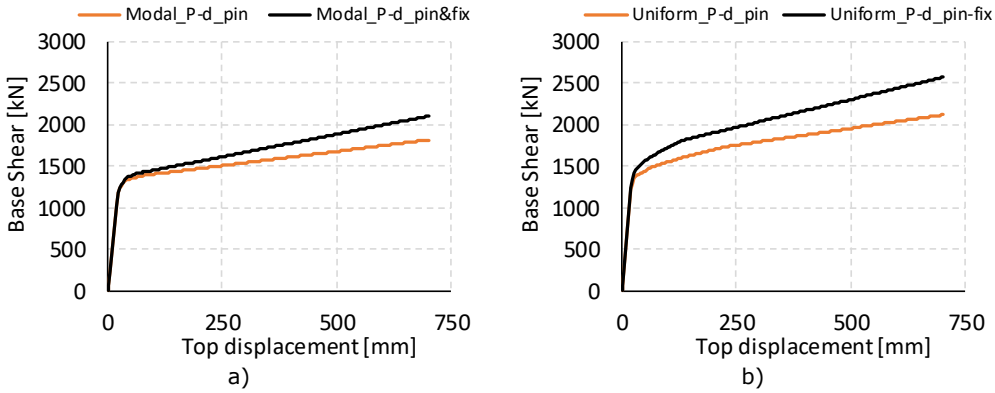

Fig. 7.16. Capacity curves of BRBFs_$\varepsilon_{p,d}$ = 2.00% for different column-base boundary conditions and lateral loads

mentioned, the fixed columns were modelled using elastic elements and, therefore, the second stiffness have a constant slope.

Based on the times history analyses results, all the BRBF frames with pinned-fixed supports have larger drifts than maximum allowable by P100-1/2013 [5] for ULS (drift max = 2.5%). If using "nonlinearBeamColumn" finite elements to model the fixed columns, even larger drift would be obtained. Therefore, the reference building initially designed by following the provisions from P100-1/2013 [5] needs to be re-designed by increasing the lateral stiffness of the structure.

7.5 Concluding remarks

The optimization process of the geometry of the BRB core involved using three different geometries with the same capacity, N_p, axial effective stiffness, K_{eff}, but different levels of axial strain in the plastic zone, $\varepsilon_{p,d}$ = 1.66 / 1.75 / 2.00 %. The optimization was carried out by running time history analyses and assessing the seismic behaviour of the BRBF frames equipped with the designed BRBs. Based on results, using different core geometries has a relatively small influence on the behaviour of the structure. Also, the frames equipped with BRBs having $\varepsilon_{p,d}$ = 2.00% proved to have smaller inter-storey relative displacements, residual drifts and top displacements.

A big influence in terms of global behaviour of the analysed frames was noticed if using different column base supports. Within the initial design of the reference structure [6], pinned supports were provided for external columns (axis 1 and 4) while fixed supports for internal columns (axis 2 and 3), all other connections being pinned. By using this configuration of supports, the two-dimensional frame model is not a truly BRBF frame anymore. Time history and pushover analyses showed that the fixed columns have a big contribution to the lateral stiffness of the structure. The maximum value of the inter-story drift was reduced by almost 30% if using pinned-fixed supports. Thus, if fixed supports are provided for the braced columns, then the framing effect needs to be considered and the necessary stiffness of the fixed columns should be determined.

All analysed BRBF frames failed the drift check at ultimate limit state. Therefore, further investigations are required.

The following future research topics derive from the second conclusion:

- To pass the drift check at ULS, the structure can be redesigned by using stiffer BRBs and pinned supports for all columns. This will assure that only the BRBs are the lateral resisting system.
- The second option consists in using slightly stiffer BRBs (than actual BRBs) and fixed supports for the braced columns. In this case, the required stiffness of the columns needs to be determined to assure an elastic behaviour.
- The third option also considers using slightly stiffer BRBs and fixed supports for the braced columns, but it allows for plastic hinges to appear at the base of the braced columns. In this case, the required stiffness of the column and the plastic bending moment need to be determined.

8 CONCLUSIONS

8.1 Synthesis of concluding remarks

The main conclusions of each chapter are presented bellow.

Chapter 1: Introduction

The motivation of this thesis finds its basis on the necessity to clear the way for a rapid and wide adoption of buckling restrained braces for seismic protection of building framed structures located in Romania.

A list of objectives is set aiming at providing pre-qualified BRBs and at transferring the "know-how" on designing such elements to the industry.

The main research framework of the thesis is a National research grant, entitled: "Implementation into Romanian seismic resistant design practice of buckling restrained braces", acronym IMSER. Knowledge and experience on characterising the behaviour of carbon steels were achieved within the frame of an international research project, entitled: "European pre-qualified steel joints", acronym EQUALJOINTS.

Chapter 2: BRB – state of knowledge

A state of knowledge on buckling restrained braces (BRBs) is presented, with the emphasis on the principle of work, history of development and applicability.

Since their initial development in Japan in the mid 1980's, BRBs have been intensively used for the last 30 years in earthquake-prone countries. Limited applications are recorded in Europe, and no applications in Romania.

From the point of view of cost savings, buckling restrained brace frames (BRBF) are more economical than conventional braced frames (CBF).

The critical evaluation of the existing BRB solutions reveales the optimal technical details to be used for the development of new BRB solutions.

Although several countries introduced regulations for BRBs/BRBFs in their design codes, no regulations for BRBFs are available in the European norm EN 1998-1 [3]. In this context, Romania is the only country in Europe that regulated the use of BRBF system starting with January 1st, 2014.

It is this thesis aim to develop, in the framework of the "IMSER" grant [6], a set of pre-qualified BRBs to be used for low-rise and mid-rise framed buildings located in Romania. The pre-qualification will eliminate the necessity of project-based experimental validation for future projects. Both "conventional" and "dry" BRBs are intended to be developed. Comprehensive (further) research and development is required to assure the new BRB solutions with a high level of reliability.

Chapter 3: Development of technical solutions

Two values of resistance (300 kN and 700 kN) are selected for the pre-qualification of BRBs. These values are representative for low-rise and mid-rise steel framed structures located in Romania.

The development of the technical BRB solutions involved iterative procedures: numerical and experimental pre-tests on several conceptual details of the transition zone, and numerical pre-test simulations on several proposed BRB concepts. The

outcome of the pre-test program is the four conceptual BRB solutions: (1) *type A* – "conventional" BRB with milled rectangular core; (2) *type B* – "conventional" BRB with hot rolled square profile core; (3) *type C* – "dry" BRB with milled rectangular core and steel-only buckling restraining mechanism (BRM); (4) *type D* – "dry" BRB with milled rectangular core and composite steel-concrete BRM.

The BRBs are equipped with bolted connections and a special detail is used to limit the bending moments transmitted to the ends of the BRB due to the frame effect.

Chapter 4: Experimental tests for pre-qualification of BRBs

The experimental program includs both pre-qualification tests on BRBs and tests on component materials (steel and concrete).

A set of 14 full-scale BRBs were cyclically tested using the ANSI/AISC 341-10 [100] loading protocol in view of prequalification. Detailing of BRBs aimed at investigating the core aspect ratio, gap size, strength of the buckling restraining mechanism, and the unbonding material. Most of the specimens performed well, with stable hysteretic response, and ultimate core strains larger than 4%.

Based on performance criteria, the "conventional" solution with milled core encased in concrete-filled tube is recommended as the qualified BRB solution for the strength range of 150-840 kN.

The distribution of deformations in the two segments of the core and the response of the bolted connection is assessed, and specific design recommendations are given.

Chapter 5: Post-test numerical simulations

Two sets of simulations were performed as to assess: (1) the accuracy of different material models in reproducing the behaviour of the steel material under motononic and cyclic loading; (2) the influence of several parameters (that could not be observed/measured during experimental tests) on the cyclic response of BRBs.

A modelling technique of the cyclic response of structural mild carbon steel was proposed using the Abaqus "built-in" material models, and and close predictions were obtained. The modelling technique involves calibration of material parameters based on test data with similar loading history as in the case of BRB (in terms of strain ranges).

An alternative calibration procedure of the material parameters for the combined hardening model is proposed using only tensile test data. Predictions with an acceptable level of accuracy are obtained for both monotonic and cyclic loading regime.

A complex nonlinear three-dimensional finite element model of the buckling restrained brace was developed in Abaqus. Close predictions were obtained for all FEM models with respect to the experimental results. The calibrated models were further used to perform a parametric study. Five parameters were investigated: the strength of the buckling restraining mechanism, concrete class of the infill material, mechanical properties of steel used for the core, gravity loading and frame effect. The outcome of the parametric study was used: to validate the design procedure of the buckling restraining mechanism (N_{cr}/N_p = 3.0); to recommend *C30/37* as minimum class for the infill-concrete; to recommend as material for the core steels with of $f_u/f_y \geq 1.3$ and $\varepsilon_r \geq 0.30$; to determine the gravity force as the main responsible for the unsymmetrical deformations in the plastic segment of the core; to show the proper modelling of loadings (both uniaxial and frame effect loading) when BRB-column sub-assemblage setup is used for experimental tests.

Chapter 6: Design recommendations

Design recommendations and applicability limits are given for the prequalified BRB solution. The design procedure developed for the BRBs considers the plastic zone of the core as the dissipative component, while all the other segments/components are designed to work in the elastic domain.

Chapter 7: Performance-based design of BRBF

No design provisions are given in P100-1/2013 [5] for determining the optimal geometry of the core of BRB. Optimization of core geometry can be attained by performing nonlinear time history analyses and assessing the seismic performance of BRBF frames equipped with BRBs having cores with different geometries (different lengths of plastic segment). For the BRBF study case, using BRBs with cores designed for $\varepsilon_{p,d}$ = 2.00% proved to have smaller inter-storey relative displacements, residual drifts and top displacements in comparison with the cases where the levels of axial strain in the plastic zone were 1.66 % or 1.75 %.

As the reference BRBF had the internal columns provided with fixed instead of pinned supports, it is shown that there is a big influence in terms of global behaviour of the reference BRBF if using different support configurations (pinned vs. pinned-fixed): the maximum value of the inter-story drift was reduced by almost 30% if using pinned-fixed supports. However, all analysed BRBF frames failed the drift check at ultimate limit state. Based on these facts, further investigations are suggested.

8.2 Contributions of the author

Based on the experimental and numerical analyses performed by the author as summarized in chapter 8.1, the following results are presented as the personal contributions.

(1) Sinthesis of previous research on BRBs into a comprehensive **state-of-knowledge**. The emphasis was on critical evaluation of existing BRB technical solutions and identification of needs for further research and development. On this basis, conceptual BRB solutions were developed using numerical simulations and experimental pre-tests.

(2) Development of the **experimental tests** for the pre-qualification of BRBs. The author was involved in: designing the technical solutions of the BRB specimens, designing the specimens for material tests, assisting and quality control of the technological process for manufacturing the BRBs and material samples, performing monotonic and cyclic tests on base materials, designing and instrumentation of the experimental setup used for BRB testing, monitoring the testing of BRB specimens. After testing, the experimental data was evaluated, failure modes of BRBs were identified and their cyclic performance, as to determine the pre-qualified solutions.

(3) Elaboration in collaboration with the BRB manufacturer of the **technical-economic studies on tested BRBs** as to evaluate the total cost of production per BRB typology and to determine a cost-estimation ecuation.

(4) Development of a **cyclic material model** used to simulate the nonlinear cyclic response of mild carbon steels with yield plateau. Uniaxial cyclic tests were performed by the author to characterize the cyclic response of steel under different loading conditions. An accurate calibration procedure of material parameters was

developed using cyclic test data. As an alternative, a less accurate calibration procedure using monotonic test data was developed.

(5) Development of a **complex nonlinear FEM model for BRB**. The calibrated models were used to perform a parametric study aiming at assessing the influence of several parameters on the cyclic response of BRBs.

(6) Development of a **design procedure for BRBs**. The design of the different zones of the core is following a capacity design approach. A similar approach is applied for the design of the buckling restraining mechanism and the connections with respect to the maximum forces developed by the core.

(7) Development of a **numerical model of buckling restrained braced framed** steel structure in OpenSees framework. Optimization of the geometry of the core was performed as to reduce the displacements of the structure under a ULS seismic event. Additional design provisions for BRBs were proposed in order to optimize the seismic response of BRBF systems.

(8) **Transfer of "know-how" to industry**. The author participated at two dissemination workhops held at Bucharest and Timisoara where he presented the numerical and experimental results of BRBs. Also, he is co-author of a book containing design guidelines for buckling restrained braced braces, which addresses to structureal engineers and BRB manufacturers.

8.3 Valorisation of research

The experimental and numerical results presented in this thesis related to the pre-qualification of the BRBs were disseminated within the frame of IMSER research project through a series of opensource research reports (four annual reports and one final report), two workshops (held at Bucharest, Timisoara) and a book with design recommendations for buckling restrained braced frames. Details about the IMSER project are available at https://www.ct.upt.ro/centre/cemsig/imser.htm. There are also some other research results obtained outside the frame of IMSER project which were made publicly available throught research reports, national and international conferences. A list with the main published results is presented below:

ISI Journals:

- **Zub, C.I.**, Stratan, A., Dogariu, A. and Dubina, D. (2018), "Development of a finite element model for a buckling restrained brace", Proceedings of the Romanian Academy Series A, (accepted for publication in Vol. 4/2018).
- Stratan, A., **Zub, C.I.** and Dubina, D. (in press). "Prequalification of a set of buckling restrained braces: Part I – experimental tests". Steel and Composite Structures, (in print).
- **Zub, C.I.**, Stratan, A. and Dubina, D. (in press). "Prequalification of a set of buckling restrained braces: Part II – numerical simulations". Steel and Composite Structures, (in print).

ISI conference proceedings:

- **Zub, C.I.**, Stratan, A. and Dubina, D. (in press), "Modelling the cyclic response of structural steel for FEM analyses", Proc. 1st Int. Conf. on Computational Methods and Applications in Engineering, Timisoara, Romania, May.

BDI journals:

- Stratan, A., **Zub, C.I**. and Dubina, D. (2018), "Experimental Tests for Pre-Qualification of a Set of Buckling-Restrained Braces", Key Engineering Materials, 763, 450–457.
- Florența, I., Pruteanu, M., **Zub, C.I.** (2016). "FEM Analysis of a Platform Framing Timber Structure". Intersections, vol. 13, no. 2, ISSN 1582-3024.

BDI international conferences:

- **Zub, C.I.**, Dogariu, A., Stratan, A. and Dubina, D. (2017), "Pre-test numerical simulations for development of prequalified buckling restrained braces", DOI: 10.1002/cepa.395, CE/Papers, Ernst& Sohn/Wiley, Vol.1, Issue 2-3, 3404-3413.
- Both, I., **Zub, C.**, Stratan, A. and Dubina, D. (2017), "Cyclic behaviour of European carbon steels", DOI: 10.1002/cepa.370, CE/Papers, Ernst& Sohn/Wiley, Vol.1, Issue 2-3, 3173-3180.

National conferences:

- **Zub, C.I.**, Stratan, A., Dogariu, A., Vulcu, C. and Dubina, D. (2018), "Development of two types of buckling restrained braces using finite element modelling", In Seismic Hazard and Risk Assessment, 373-387, Springer, Cham, Switzerland (indexed BDI).
- Stratan, A., Voica, F., Marcu, D., **Zub, C.** and D. Dubina (2015), "Design of steel structures with buckling restrained braces according to P100-1/2013" (in Romanian), Proc. 14-th National Conference on Steel Structures, Cluj-Napoca, Romania.

Books:

- Stratan, A., **Zub, C.I.**, Dogariu, A., Dinu, F., Dubina, D., Voica, T.F., Ganea, M.A., Marcu., A.D., Coman, M., Badea, I.C. and Todea, A. (2017), "Design Recommendations for Buckling Restrained Braced Frames", Editor Stratan A., Orizonturi Universitare, Timisoara, Romania (in Romanian).
- Stratan, A., Dogariu, A., **Zub, C.**, Dinu, F., Dubina, D. (2015). "Consolidarea cadrelor din beton armat folosind contravântuiri cu flambaj împiedicat: generalități și studiu de caz". Lucrările seminarului "Tehnici de consolidare anti-seismică a clădirilor existente bazate pe utilizarea oțelului", Timișoara, 23 Noiembrie 2015. Editura Orizonturi Universitare, Editor: Dan Dubina, ISBN: 978-973-638-608-4, pp. 100-137.
- D'Aniello, M., Costanzo, S., Tartaglia, R., Stratan, A., Dubina, D., Vulcu, C., Maris, C., **Zub, C.**, Da Silva, L., Rebelo, C., Augusto, H., Shahbazian, A., Gentili, F., Jaspart, J.P., Demonceau, J.F., Van Hoang, L., Elghazouli, A., Tsitos, A., Vassart, O. , Nunez, E.M., Dehan, V. and Hamreza, C. (2016), "European pre-QUALified steel JOINTS (EQUALJOINTS)", Editor Raffaele Landolfo, Final report RFSR-CT-2013-00021, University of Naples Federico II, Italy.

Others:

- Stratan, A., Voica, F. and **Zub, C.** (2015), "Capacity, stiffness and ductility demands of BRB's in relation with the target application". Workshop on "Steel for industrial and commercial buildings in earthquake prone regions", Tampere, Finland, 25 September.
- Stratan, A., Dubina, D., Voica, F., Dogariu, A. and **Zub, C.** (2015), "Design requirements for buckling restrained braces for different target applications". Workshop on "Structural steel solutions in earthquake-prone areas: design and retrofitting", The University of Thessaly, Volos, Greece, 4 December.
- **Zub, C.**, Stratan, A., Dogariu, A. and Dubina, D. (2015), "Numerical simulation of cyclic behaviour of buckling restrained braces". Eleventh International Miklós

Iványi PhD & DLA Symposium, University of Pécs Pollack Mihály Faculty of Engineering and Information Technology, Pécs, Hungary, 19-20 October.

8.4 Needs for further research

Based on the results and conclusions of this thesis, several needs for further research were identified, as follows:

- Further research and development of the "dry" BRBs as to obtain a cost effective and reliable steel-only solution. Numerical investigations should be performed using three-dimensional finite element models of the tested "dry" BRBs as to investigate de cause of unsatisfactory performance and to optimize the design concepts.
- Numerical investigations using three-dimensional finite element models of the BRB geometries used in chapter 7 and validation of the optimal solution (BRBs having $\varepsilon_{p,d}$ = 2.00 %).
- Numerical investigations using three-dimensional finite element models of the influence of the BRB-to-gusset connection (bolted-rigid versus bolted–flexible, the connection detail "2t_e" used in pre-qualification tests) on the cyclic performance of BRBs.
- Numerical investigations of the seismic performance of the study case BRBF structure using nonlinear models to describe the response of BRBs. Additional studies are required to enhance the seismic response of the BRBFs by redesigning the structures considering or not the contribution of the fixed-base inner columns.
- Numerical investigations on the recentering capacity of the BRBF. The following systems might be compared: dual system (MRF + BRBF) – European design approach, versus MRF + dampers (BRBs) – Japanese design approach.
- Validation based on experimental results of the simplified calibration procedure (that uses tensile test results) of material parameters. A consistent experimental program will include different steel grades (S235, S275, S355, S460) and different loading histories as to sets of kinematic parameters for different steel grades and to propose analytical formulas to determine the cyclic (isotropic) hardening parameters as function of loading history.
- Development of user material subroutine (UMAT and VUMAT) for mild carbon steel with yield plateau. The UMAT (VUMAT) should take into account the Baushinger effect, the yield plateau, the dependency of the cyclic hardening as a function of strain range, energy-based failure criterium (obtained based on fatigue strain/stress – life curves). This UMAT (VUMAT) is intended to be a loading history independent material model and to be used within Abaqus simulations.

8.5 Acknowledgement

The research leading to the results related to the pre-qualification of BRBs has received founding from the MEN-UEFISCDI grant Partnerships in Priority Areas PN II, contract no. 99/2014 IMSER (code project: PN-II-PT-PCCA-2013-4-2091). This support is gratefully acknowledged.

The research leading to the results from chapter 7 has received founding from the Erasmus+ Programme, which made possible a research stage of three months at the host institution: Nagoya Institute of Technology, NITech, Japan.

REFERENCES

[1] Takeuchi, T. and Wada, A. (2017), Buckling-Restrained Braces and Applications, The Japan Society of Seismic Isolation (JSSI), Jingumae Shibuyaku, Tokyo, Japan.

[2] Xie, Q. (2005), "State of the art of buckling-restrained braces in Asia", Journal of Constructional Steel Research. **61**, 727–748.

[3] EN 1998-1 (2004), Eurocode 8: Design of structures for earthquake resistance - Part 1: General rules, seismic actions and rules for buildings, European Committee for Standardization; Brussels, Belgium.

[4] EN 15129 (2010), Anti-seismic devices, European Committee for Standardization; Brussels, Belgium.

[5] P100-1/2013 (2014), Code for seismic design – Part I – Design prescriptions for buildings, Official Journal of Romania; Bucharest, Romania (in Romanian).

[6] IMSER project website (last visited 15 August 2018): http://www.ct.upt.ro/centre/cemsig/imser.htm.

[7] D'Aniello, M., Costanzo, S., Tartaglia, R., Stratan, A., Dubina, D., Vulcu, C., Maris, C., Zub, C., Da Silva, L., Rebelo, C., Augusto, H., Shahbazian, A., Gentili, F., Jaspart, J.P., Demonceau, J.F., Van Hoang, L., Elghazouli, A., Tsitos, A., Vassart, O. , Nunez, E.M., Dehan, V. and Hamreza, C. (2016), European pre-QUALified steel JOINTS (EQUALJOINTS), Editor Raffaele Landolfo, Final report RFSR-CT-2013-00021, University of Naples Federico II, Italy.

[8] Both, I., Zub, C., Stratan, A. and Dubina, D. (2017), "Cyclic behaviour of European carbon steels", DOI: 10.1002/cepa.370, CE/Papers, Ernst& Sohn/Wiley, Vol.1, Issue 2-3, 3173-3180.

[9] Robinson K. (2014), "Advances in design requirements for buckling restrained braced frames", *Proceedings of the 2014 NZSEE*, Auckland, New Zealand, March.

[10] Tremblay, R., Bolduc, P., Neville, R., DeVall, R. (2006), "Seismic testing and performance of buckling-restrained bracing systems, Can. J. Civ. Eng. **33**(2),183–198.

[11] Stratan, A., Zub, C.I. and Dubina, D. (2018), "Experimental Tests for Pre-Qualification of a Set of Buckling-Restrained Braces", Key Engineering Materials, **763**, 450–457.

[12] Tinker, J. and Dusicka, P. (2012), "Challenges in designing ultra-lightweight buckling restrained brace". STESSA 2012 – Mazzolani & Herrera (eds), Taylor & Francis Group, London, UK.

[13] Tsai, K.C., Lai, J.W., Hwang, Y.C., Lin, S.L., Weng, C.H. (2004). "Research and implementation of double-core buckling restrained braces in Taiwan". 13th World Conference on Earthquake Engineering, Vancouver, B.C., Canada, august 1-6, 2004, Paper no. 2179.

[14] Mazzolani, F.M., Della Corte, G. and D'Aniello, M. (2009), "Experimental analysis of steel dissipative bracing systems for seismic upgrading", Journal of Civil Engineering and Management, 2009, **15**(1), 7-19.

[15] BSLJ-2000 (2000), The Building Standard Law of Japan, Ministry of Construction and The Building Center of Japan; Tokyo, Japan.

[16] Shidhara, B.N., Ramaswamy, M.A. (1982), Sleeved Column as Compression Member, Unpublished Report, Bangalore, India.
[17] Sridhara, B.N. (1990)."Sleeved column as a basic compression member", Proceedings of the 4th International Conference on Steel Structures & Space Frames, Singapore, 181-188.
[18] Uang, C.M. and Nakashima, M. (2004). "Steel Buckling-Restrained Braced Frames". Earthquake Engineering: From Engineering Seismology to Performance-Based Engineering, Chapter 16, Y. Bozorgnia and Bertero, (eds.) CRC Press, Boca Raton, Fl;
[19] Escudero, E. O. (2003), "Comparative parametric study on normal and buckling restrained steel braces", Master Dissertation, European School of Advanced Studies in Reduction of Seismic Risk, Rose School.
[20] Watanabe, A., Hitomi, Y., Saeki, E., Wada, A. and Fujimoto, M. (1988), "Properties of brace encased in buckling restraining concrete and steel tube", Proceedings of 9th World Conf. Earthquake Engineering, Tokyo, Japan, August.
[21] Tsai, K.C., Lin, Y.C., Lin, J.L., Lin, S.L. and Hsiao, P.C. (2008), High Performance Steel Material and Structures for Earthquake Resistant Buildings, In C. Shi, & Y. L. Mo, *High-Performance Construction Materials* (pp. 155-206), World Scientific publishing Co. Pte. Ltd, Singapore.
[22] Blomgren, H.E., Koppitz, J.P., Valdés, A.D., Ko, E. (2016), "The heavy timber buckling-restrained braced frame as a solution for commercial buildings in regions of high seismicity", *Proceedings of World Conference on Timber Engineering - WCTE 2016*, Vienna, Austria, August.
[23] Zhou, Z., Xie, Q., Lei, X. C., He, X.T. and Meng, S.P. (2015), "Experimental investigation of the hysteretic performance of dual-tube self-centering buckling-restrained braces with composite tendons", *J. Compos. Constr.*, **19**(6), 04015011.
[24] Ko, E., and Field, C. (1988), "The Unbonded Brace™: From Research to Californian Practice", Technology, February.
[25] Tremblay, R., Dehghani, M., Fahnestock, L., Herrera, R., Canales, M., Clifton, C. and Hamid, Z. (2016), "Comparison of seismic design provisions for buckling restrained braced frames in Canada, United States, Chile, and New Zealand", *Structures*, **8**, 183-196.
[26] Chen, C.C., Chen, S.Y., Liaw, J.J. (2001), "Application of low yield strength steel on controlled plastification ductile concentrically braced frames", *Canadian Journal of Civil Engineering*, **28**, 823-836.
[27] Kim, J., Choi, H. (2004), "Behavior and design of structures with buckling-restrained braces", *Engineering structures*, **26**, 693-706.
[28] Ju, Y.K., Kim, M.H., Kim, J., and Kim, S.D. (2009), Component tests of buckling-restrained braces with unconstrained length", *Engineering Structures*, **31**(2), 507-516.
[29] Della Corte, G., D'Aniello, M., Mazzolani, F.M. (2005), "Seismic upgrading of RC buildings using buckling restrained braces: full-scale experimental tests", *Proceedings of the XX Italian Congress on Steel and Composite Structures*, Ischia, Italy, September.
[30] Bordea, S. (2010), "Dual frame systems of buckling restrained braces", PhD Thesis, Politehnica University of Timisoara, Politehnica, Romania.
[31] Dunai, L., Zsarnóczay, A., Kaltenbach, L., Kálló, M., Kachichian, M., Halász, A. (2011), "Type testing of Buckling Restrained Braces according to EN 15129 – EWC800 – Final report", Department of Structural Engineering, Budapest University Technology and Economics.

[32] Antonucci, R., Balducci, F, Castellano, M.G., Donà, F. (2006): "Precast RC buildings with buckling restrained braces: the example of the new building of the Faculty of Engineering in Ancona", *Proceedings of the 2nd International fib Congress*, Naples, Italy, June.
[33] Star Seismic Europe Ltd., http://www.starseismic.eu (accessed on 29 August 2018).
[34] Ma, N., Wu, B., Zhao, J., Li, H., Ou, J. and Yang, W. (2009), "Full scale tests of all-steel buckling restrained braces", *Proceedings of the 14th World Conference on Earthquake Engineering,* Beijing, China, October.
[35] Karimi, S. and Arbabi, F. (2008), "Seismic evaluation and cyclic testing of buckling restrained braces manufactured in Iran", *Proceedings of the 14th World Conference on Earthquake Engineering,* Beijing, China, October.
[36] Eryasar, E. (2009), "Experimental and numerical investigation of buckling restrained braces", Master Thesis, Middle East Technical University, Ankara, Turkey.
[37] Karatas, C. (2012), "Design, Fabrication, and Cyclic Behavior of Steel and Aluminum Alloy Core Buckling Restrained Braces (BRBs)", PhD Thesis, Istanbul Technical University, Istanbul, Turkey.
[38] Civelek, K.B. (2017), "Analysis of uniaxial and system performance tests of buckling-restrained braces with different designs", *European Int. Journal of Science and Technology*, **6**(2), 80-93.
[39] Erdik, M.O. (2017), " State of the Art on Application, R&D and Design Rules for Seismic Isolation and Energy Dissipation for Buildings, Bridges and Viaducts, Cultural Heritage and Chemical Plants in Turkey", *Proceedings of the 2017 NZSEE Conference,* Wellington, New Zealand, April.
[40] Wijanto, S. (2012), "Behaviour and Design of Generic Buckling Restrained Brace Systems". Master Thesis, University of Auckland, Auckland, New Zealand.
[41] Bruneau, M., and MacRae, G.A. (2017), "Reconstructing Christchurch: a seismic shift in building structural systems", Quake Centre Report, University of Canterbury, Christchurch, New Zealand.
[42] Rojas, P.P., Aguaguiña, M.E. and Herrera, R.A. (2015), "Seismic design of CFT-MRF and BRBF structural systems for steel buildings in Ecuador", *Proceedings of the 8th Int. Conf. on Behaviour of Steel Structures in Seismic Areas – STESSA 2015,* Shanghai, China, July.
[43] Medalla, M., Peña, C., Hidalgo, P., and Bravo, M.E. (2015), "Aplicación industrial de riostras de pandeo restringido (BRB) en Chile", *Proceedings of XI Congreso Chileno de Seismologia e Ingineria Sismica ACHISINA 2015,* Santiago de Chile, Chile, March.
[44] Wada, A., Connor, J.J., Kawai, H., Iwata, M. and Watanabe, A. (1992), "Damage Tolerant Structure", *Proc. 5th U.S.-Japan Workshop on the Improvement of Building structural design and Construction Practice, ATC-15-4*, San Diego, California, September.
[45] Fahnestock, L.A., Ricles, J.M. and Sause, R.P. (2007), "Experimental evaluation of a large-scale buckling-restrained braced frame", *Journal of Structural Engineering*, **133**(9),1205 – 1214.
[46] Kiggins, S. and Uang, C.M. (2006), "Reducing residual drift of buckling restrained braced frames as a dual system", *Eng. Struct.*, **28**, 1525-1532.
[47] Dasse (2009), "Cost Advantages of Buckling Restrained Braced Frame Buildings", Dasse Design Inc., San Francisco, CA, USA.
[48] StarSeismic (2010), " Cost advantages of buckling restrained braced frame buildings in accordance with Eurocode", StarSeismic™ Europe Ltd.

[49] Connor, J.J., Wada, A., Iwata, M. and Huang, Y.H. (1997), "Damage-controlled structures. I: Preliminary design methodology for seismically active regions", *J. Struct. Eng. ASCE*, **123**(4), 423-431.
[50] Wu, A.C., Lin, P.C. and Tsai, K.C., (2014), "High-mode buckling responses of buckling-restrained brace core plates", *Earthq. Eng. Struct. Dyn.*, **43**, 375-393.
[51] Fujimoto, M, Wada, A., Saeki, E., Takeuchi, T. and Watanabe, A. (1990), "Development of Unbonded Braces", *Quarterly Column*, **115**(1), 91-96.
[52] FIP INDUSTRIALE S.p.A (2018), https://www.fipindustriale.it/index.php?area=108&menu=99&page=251&lingua=1&idsession=1279200649 (accessed on 29 August 2018).
[53] Nagoya Lucent Tower (2007), http://www.taisin-net.com/library/casestudy/seisin/b0da0e000000ccec.html (accessed on 29 August 2018).
[54] Webb Tower, owner: University of Southern California, retrofitted by Saiful Bouquet Structural Engineers, http://www.saifulbouquet.com/portfolio/project/webb-tower-usc (accessed on 29 August 2018).
[55] Takeuchi, T. (2013), "Retrofit of damaged gymnasia and towers according to response control concept", *Proceedings of 10 Int. Conf. on Urban Earthquake Eng., 10CUEE*, Tokyo, Japan, March.
[56] CoreBrace LLC Company, http://www.corebrace.com/ (accessed on 29 August 2018).
[57] Nippon Steel Engineering USA, Inc., http://www.unbondedbrace.com/ (accessed on 29 August 2018).
[58] Changzhou Road Structure Damping Co., Ltd. http://www.roadjz.com/en/ (accessed on 29 August 2018).
[59] Seismic Bracing Company, https://www.thesbcllc.com (accessed on 29 August 2018).
[60] Lin, P.C., Tsai, K.C., Wang, K.J., Yu, Y.J., Wei, C.Y., Wu, A.C., Tsai, C.Y., Lin, C.H., Cen, J.C., Schellenberg, A.H., Mahin, S.A. and Roeder, C.W. (2012), "Seismic design and hybrid tests of a full-scale three-story buckling-restrained braced frame using welded end connections and thin profile", *Earthquake Eng Struct Dynam*, **41**(5), 1001-1020.
[61] Razavi, S.A., Mirghaderi, S.R., Seini, A. and Shemshadian, M.E. (2012), "Reduced length buckling restrained brace using steel plates as restraining segment", *Proc. 15th World Conf. on Earthq. Eng.*, Lisbon, Portugal, September.
[62] Sugisawa, M., Nakamura, H., Ichikawa, Y., Hokari, M., Saeki, E., Hirabayashi, R. and Ueki, M. (1995), "Development of Earthquake-Resistant, Vibration Control, and Base Isolation Technology for Building Structures". Nippon Steel technical Report No. 66, July 1995.
[63] Atlayan, O. (2013), "Hybrid Steel Frames", PhD Dissertation, Virginia Polytechnic Institute and State University, Blacksburg, VA, USA.
[64] Wang, C.L., Usami, T., Funayama, J. and Imase, F. (2013), "Low-cycle fatigue testing of extruded aluminium alloy buckling-restrained braces", *Engineering Structures*, **46**, 294-301.
[65] Zhao, J., Wu, B., Li, W. and Ou, J. (2014), "Local buckling behavior of steel angle core members in buckling-restrained braces: Cyclic tests, theoretical analysis, and design recommendations", *Eng. Struct.*, **66**, 129-145.
[66] Black, C.J., Makris, N. and Aiken, I.D. (2002), "'Component testing, stability analysis and characterization of buckling restrained braces",' Rep. No. PEER 2002/08, Univ. of California, Berkeley, California, USA.

[67] Tsai, C.S., Lin, Y., Chen, W., Su, H.C. (2009), "Mathematical modelling and full-scale shaking table tests for multi-curve buckling restrained braces", *Earthquake Engineering and Engineering Vibration*, **8**(3), 359-371;
[68] Oda H. and Usami, T. (2010), "Fabricating buckling-restrained braces from existing H-section bracing members: experimental study", *J. Struct. Eng. Japan Soc Civil Eng,* **56A**(3), 499–510.
[69] Piedrafita, D., Cahis, X., Simon, E. and Comas, J. (2015), "A new perforated core buckling restrained brace", *Engineering Structures*, **85**, 118-126.
[70] Zub, C.I., Stratan, A., Dogariu, A., Vulcu, C. and Dubina, D. (2018), "Development of two types of buckling restrained braces using finite element modelling", In *Seismic Hazard and Risk Assessment*, 373-387, Springer, Cham, Switzerland.
[71] Wang, C.L., Usami, T. and Funayama, J. (2012), "Improving low-cycle fatigue performance of high-performance buckling-restrained braces by toe-finished method", *J. Earthquake Eng.*, **16**, 1248-1268.
[72] Talebi, E., Tahir, M., Zahmatkesh, F. and Kueh, A. (2015), "A numerical analysis on the performance of buckling restrained braces at fire-study of the gap filler effect", *Steel and Composite Structures*, **19**(3), 661-678.
[73] Lai J.W. and Tsai, K.C. (2004), "Research and application of buckling restrained braces in Taiwan", *Proc. ANCER Annual Meeting*, Honolulu, Hawaii, USA.
[74] Xie, Q., Zhou, Z., Huang, J.H., Zhu, D.P., and Meng, S.P. (2016), "Finite-element analysis of dual-tube self-centering buckling-restrained braces with composite tendons", *J. Comp. for Constr.*, **21**(3), 04016112.
[75] Iwata, M., Kato, T., and Wada, A. (2000), "Buckling-restrained braces as hysteretic dampers". *Proc. 3rd Int. Conf. on Behaviour of Steel Structures in Seismic Areas – STESSA 2000*, Montreal, Canada, August.
[76] Nakamura, H., Maeda, Y., Sasaki, T., Wada, A., Takeuchi, T., Nakata, Y. and Iwata, M. (2000), "Fatigue properties of practical-scale unbonded braces" Nippon Steel technical Report No. 82 July 2000.
[77] Nippon Steel & Sumikin Engineering USA, INC http://nseusa-unbondedbrace.com, (accessed on 29 August 2018).
[78] Star Seismic LLC, http://www.starseismic.net (accessed on 29 August 2018).
[79] Hussain, S., Van Benschoten, P., Al Satari, M. and Lin, S. (2006), "Buckling Restrained Braced Frame (BRBF) structures: analysis, design and approvals issues", *Proceedings of the 75th SEAOC Annual Convention*, Sacramento, CA, USA.
[80] Usami, T., Wang, C.L. and Funayama, J (2012), "Developing high-performance aluminium alloy buckling-restrained braces based on series of low-cycle fatigue tests", *Earthq Eng Struct Dyn*, **41**, 643–61.
[81] Karats, C. and Celik, O.C. (2013), "Cyclic testing of aluminium alloy core buckling restrained braces (BRBs)", *Proc. 10th Int. Conf. on Urban Earthq. Eng.*, Tokyo, Japan, March.
[82] Singh, V.P. and Rai, D.C. (2014), "Aluminum buckling restrained braces for seismic resistance of truss moment frames", *Proc. Tenth US National Conf. on Earthq. Eng. (Frontiers of Earthquake Engineering)*, Anchorage, Alaska, July.
[83] Chen, C.C. (2002), "Recent Advances of Seismic Design of Steel Buildings in Taiwan", Int. Training Programs for Seismic Design of Building Structures – ITP 2002, Taipei, Taiwan.
[84] Ma, N., Ou, J.P. and Li, H. (2012), "Experimental study of low-cycle strength steel buckling restrained brace", ", *Proc. 15th World Conf. on Earthq. Eng.*, Lisbon, Portugal, September.

[85] Wu, A.C., Lin, P.C. and Tsai, K.C. (2012), "A type of buckling restrained brace for convenient inspection and replacement", *Proc. 15th World Conf. on Earthq. Eng.*, Lisbon, Portugal, September.
[86] Huang, Y.H., Wada, A., Iwata, M., and Watanabe, A. (1995), "Inelastic behavior of high strength steels under cyclic gradient stress", *Structural Steel, PSSC, 95*, 367-374.
[87] Inoue, K., Sawaizumi, S. and Higashibata, Y. (2001), "Stiffening requirements for unbonded braces encased in concrete panels", *Journal of structural engineering*, **127**(6), 712-719.
[88] Tsai, K.C., Wu, A.C., Wei, C.Y., Lin, P.C., Chuang, M.C., and Yu, Y.J. (2014), "Welded end-slot connection and debonding layers for buckling-restrained braces", *Earthquake Engineering & Structural Dynamics*, **43**, 1785-1807.
[89] Midorikawa, M., Asari, T., Iwata, M., Murai, M., and Tanaka, Y. (2012), "Cyclic behaviour of buckling-restrained braces using steel mortar planks; buckling mode number and strength ratio", *Proc. 15th World Conf. on Earthq. Eng.*, Lisbon, Portugal, September.
[90] Wu, J., Liang, R.J., Wang, C.L. and Ge, H.B. (2012), "Restrained buckling behaviour of core component in buckling-restrained braces", *Adv. Steel Constr.*, **8**(3), 212-225.
[91] Chen, Q., Wang, C.L., Meng, S. and Zeng, B. (2016), "Effect of the unbonding materials on the mechanic behavior of all-steel buckling-restrained braces", *Eng. Structures*, **111**, 478-493.
[92] ANSI/AISC 341-16 (2016), Seismic Provisions for Structural Steel Buildings, American Institute of Steel Construction; Chicago, IL, USA.
[93] ASCE/SEI 41-17 (2017), Seismic Evaluation and Retrofit of Existing Buildings, American Society of Civil Engineers; Reston, Virginia.
[94] ABRI 2005 (2005), Recommended Provisions for Building Seismic Regulations, Architecture Buildings Research Institute; Taipei.
[95] CSA S16-14 (2014), Design of Steel Structures, Canadian Standards Association; Mississauga, ON.
[96] NBCC (2015), National Building Code of Canada 2015, 14th ed., National Research Council of Canada; Ottawa, ON.
[97] EN 15129 (2010), Anti-seismic devices, European Committee for Standardization; Brussels, Belgium.
[98] NCh 433.Of1996 (2012), Diseño sísmico de Edificios, Norma Chilena Oficial, Modificada en 2012, Instituto Nacional de Normalizacion; Santiago, CH.
[99] NZS1170.5:2004 (2004), Structural Design Actions — Part 5: Earthquake Actions — New Zealand, Standards New Zealand; Wellington, New Zealand.
[100] ANSI/AISC 341-10 (2010), Seismic Provisions for Structural Steel Buildings, American Institute of Steel Construction; Chicago, IL, USA.
[101] Vaduva, M.G. and Cretu, D.I. (2013), "The use of buckling restrained braces for new and existing structures situated in seismic areas", PhD Thesis, Technical University of Civil Engineering, Bucharest (in Romanian).
[102] Stratan, A., Voica, F., Marcu, D., Zub, C. and D. Dubina (2015), "Design of steel structures with buckling restrained braces according to P100-1/2013" (in Romanian), *Proc. 14-th National Conference on Steel Structures*, Cluj-Napoca, Romania.
[103] Dehghani M. (2016), "Seismic design and qualification of all-steel buckling-restrained braced frames for Canadian applications". PhD dissertation, Département des Génies Civil, Géologique, et des Mines, École Polytechnique de Montréal, Montréal, Québec, Canada.

[104] Dassault (2014), Abaqus 6.14 - Abaqus Analysis User's Manual, Dassault Systèmes Simulia Corp.
[105] Zub, C.I., Dogariu, A., Stratan, A. and Dubina, D. (2017), "Pre-test numerical simulations for development of prequalified buckling restrained braces", DOI: 10.1002/cepa.395, CE/Papers, Ernst& Sohn/Wiley, Vol.1, Issue 2-3, 3404-3413.
[106] Kaufmann, E.J., Metrovich, B. and Pense, A.W. (2001), "Characterization of cyclic inelastic strain behavior on properties of A572 Gr. 50 and A913 Gr. 50 rolled sections". ATLSS Report No. 01-13, to American Institute of Steel Construction, by Lehigh University, USA.
[107] Iwata, M. and Murai, M. (2006), "Buckling-restrained brace using steel mortar planks; performance evaluation as a hysteretic damper", *Earthquake Engineering and Structural Dynamics*, **35**, 1807-1826.
[108] Stratan, A., Zub, C.I. and Dubina, D. (in press). "Prequalification of a set of buckling restrained braces: Part I – experimental tests". *Steel and Composite Structures*, (in print).
[109] CEMSIG Laboratory website, https://www.ct.upt.ro/centre/cemsig/index.htm (accessed on 29 August 2018).
[110] SR EN ISO 6892-1:2016 (2016), Metallic materials — Tensile testing — Part 1: Method of test at room temperature, ASRO, Bucharest, Romania (in Romanian).
[111] ASTM E606/E606M-12 (2012), Standard Test Method for Strain-Controlled Fatigue Testing, ASTM International, West Conshohocken, PA, USA.
[112] Zub, C.I., Stratan, A. and Dubina, D. (in press), "Modelling the cyclic response of structural steel for FEM analyses", *Proc. 1st Int. Conf. on Computational Methods and Applications in Engineering*, Timisoara, Romania, May.
[113] Hall, E.O. (1970), *Yield Point Phenomena in Metals and Alloys*, Plenum Press, New York, USA.
[114] Zub, C.I., Stratan, A., Dogariu, A. and Dubina, D. (2018), "Development of a finite element model for a buckling restrained brace", *Proceedings of the Romanian Academy Series A*, (accepted for publication in Vol. **4**/2018).
[115] Lemaitre, J. and Chaboche, J.L. (1990), *Mechanics of Solid Materials*, Cambridge University Press, UK.
[116] Park, J., Lee, J. and Kim, J. (2012), "Cyclic test of buckling restrained braces composed of square steel rods and steel tube", *Steel and Composite Structures*, **13**(5), 423-436.
[117] Razavi, S.A., Kianmehr, A., Hosseini, A. and Mirghaderi, S.R. (2018), "Buckling-restrained brace with CFRP encasing: Mechanical behavior & cyclic response", *Steel and Composite Structures*, **27**(6), 675-689.
[118] Korzekwa, A. and Tremblay, R. (2009), *Numerical Simulation of the Cyclic Inelastic Behaviour of Buckling Restrained Braces*, Taylor & Francis Group, London, UK, 653-658.
[119] Inoue, K., Sawaizumi S., Higashibata, Y., and Inoue, K. (1992), "Buckling stiffening design of reinforced concrete wall panel with built-in unbonded flat steel bar braces", *J. Struct. Constr. Eng.*, **432**, 41–49.
[120] Saeki, E., Iwamatu, K., and Wada, A. (1996a), "Analytical study by finite element method and comparison with experiment results concerning buckling-restrained unbonded braces", *J. Struct. Constr. Eng.*, **484**, 111–120.
[121] Saeki, E., Maeda, Y., Iwamatsu, K., Wada, A. (1996b), "Analytical study on unbonded braces fixed in a frame", *J. Struct. Constr. Eng.*, **489**, 95–104.

[122] Matsui, R., Takeuchi, T., Hajjar, J.F., Nishimoto, K., and Aiken, I. (2008), "Local buckling restraint condition for core plates in buckling-restrained braces", *Proc. 14th World Conf. on Earthquake Eng.*, Beijing, China, October.
[123] Rahai, A., Alinia, M. and Salehi, S. (2009), "Cyclic performance of buckling restrained composite braces composed of selected materials", *International Journal of Civil Engineering*, **1**(7), 1-8.
[124] Tinker, J.A. (2011), "Development of an Ultra-Lightweight Buckling Restrained Brace Using Analytical and Numerical Methods", Master dissertation, Portland State Univ., OR, USA.
[125] Rahai, A. and Mortazavi, M. (2014), "Experimental and numerical study on the effect of core shape and concrete cover length on the behavior of BRBs." *Int. J. Civil Engineering*, **12**(4 A), 379-395.
[126] Yazdi, H.M., Mosalman, M. and Soltani, A.M. (2018), "Seismic study of buckling restrained", *International Journal of Steel Structures*, **18**(1), 153-162.
[127] Pandikkadavath, M.S. and Sahoo, D.R. (2016), "Analytical investigation on cyclic response of buckling-restrained braces with short yielding core segments", *Int. J. Steel Struct.*, **16**(4), 1273-1285.
[128] AlHamaydeh, M., Abed, F. and Mustapha, A. (2016), "Key parameters influencing performance and failure modes for BRBs", *J. Constr. Steel Res.*, **116**, 1–18.
[129] Razavi, S.A., Mirghaderi, S.R., seini, A. and Shemshadian, M.E. (2012), "Reduced length buckling restrained brace using steel plates as restraining segment", Proc. 15th World Conf. Earthq. Eng., Lisbon, Portugal, September.
[130] Dusika, P. and Tinker, J. (2013), "Global Restraint in Ultra-Lightweight Buckling-Restrained Braces", *J. Compos. Constr.*, **17**, 139-150.
[131] Wu, A.C., Lin, P.C., Tsai, K.C. (2014), "High-mode buckling responses of buckling-restrained brace core plates", *Earthq. Eng. Str. Dyn.*, **43**(3), 375–393.
[132] Xie, Q., Zhou, Z., Huang, J.H., Zhu, D.P., and Meng, S.P. (2016), "Finite-element analysis of dual-tube self-centering buckling-restrained braces with composite tendons", *J. Comp. for Constr.*, **21**(3), 04016112.
[133] Talebi, E., Tahir, M., Zahmatkesh, F., Yasreen, A. and Mirza, J. (2014), "Thermal behavior of cylindrical buckling restrained braces at elevated temperatures", *The Sci. World J.*, **2014**, 1-13.
[134] Talebi, E., Tahir, M., Zahmatkesh, F. and Kueh, A. (2015), "A numerical analysis on the performance of buckling restrained braces at fire-study of the gap filler effect", *Steel and Composite Structures*, **19**(3), 661-678.
[135] Zub, C.I., Stratan, A. and Dubina, D. (in press). "Prequalification of a set of buckling restrained braces: Part II – numerical simulations". Steel and Composite Structures, (in print).
[136] Eryasar, E. (2009), "Experimental and numerical investigation of buckling restrained braces", Master Thesis, Middle East Technical University, Ankara, Turkey.
[137] Genna, F. and Gelfi, P. (2012), "Analysis of the lateral thrust in bolted steel buckling-restrained braces. I: experimental and numerical results", *J. Struct. Eng.*, **138**(10), 1231–1243.
[138] Budaházy, V., and Dunai, L. (2015), "Numerical analysis of concrete filled Buckling Restrained Braces", *J. of Constructional Steel Research*, **115**, 92-105.
[139] Mostafa, A.A. (2013), "Nonlinear finite element modeling of the load-carrying and energy dissipation capacities for buckling-restrained braces", Master dissertation, Faculty of the American University of Sharjah, College of Engineering, Sharjah, United Arab Emirates.

[140] Montazerian, L. and Mohammadreza, N.S. (2015), " Finite element simulation of the energy dissipation capacities for buckling restrained braces", *Can. J. Basic & Applied Sc.*, **03**(11), 290-295.
[141] Chou, C.C. and Chen, S.Y. (2010), "Subassemblage tests and finite element analyses of sandwiched buckling-restrained braces", *Eng. Struct.*, **32**(8), 2108–2121.
[142] Hoveidae, N., Rafezy, B. (2012), "Overall buckling behavior of all-steel buckling restrained braces", *J. Constr. S. Res.*, **79**, 151–158.
[143] Razavi Tabatabaei, S.A., Mirghaderi, S.R. and Hosseini, A. (2014), "Experimental and numerical developing of reduced length buckling-restrained braces", *Eng. Struct.*, **77**, 143–160.
[144] Guo, Y.L., Tong, J.Z., Wang, X.A., and Zhang, B.H. (2017), "Subassemblage tests and numerical analyses of buckling-restrained braces under pre-compression", *Eng. Structures*, **138**, 473-489.
[145] Dehghani M, Tremblay R. (2017), "An analytical model for estimating restrainer design forces in bolted buckling-restrained braces", *J. Constr. Steel Res.*, **138**, 608-620.
[146] Hadianfard, M.A., Eskandari, F. and JavidSharifi, B. (2018), "The effects of beam-column connections on behavior of buckling-restrained braced frames", *Steel Composite Str.*, **28**(3), 309-318.
[147] Lemaitre, J. and Chaboche, J.L. (1990), *Mechanics of Solid Materials*, Cambridge University Press, Cambridge, U.K.
[148] EN 1992-1-1 (2004), Eurocode 2: Design of concrete structures – Part 1-1: General rules and rules for buildings, European Committee for Standardization; Brussels, Belgium.
[149] EN 1993-1-1 (2005), Eurocode 3: Design of steel structures – Part 1- 1: General rules and rules for buildings, European Committee for Standardization; Brussels, Belgium.
[150] Hu F., Shi G. and Shi, Y. (2016), "Constitutive model for full-range elasto-plastic behavior of structural steels with yield plateau: Calibration and validation", *Eng. Structures*, **118**, 210-227.
[151] Stratan, A., Zub, C.I., Dogariu, A., Dinu, F., Dubina, D., Voica, T.F., Ganea, M.A., Marcu., A.D., Coman, M., Badea, I.C. and Todea, A. (2017), *Design Recommendations for Buckling Restrained Braced Frames*, Editor Stratan A., Orizonturi Universitare, Timisoara, Romania (in Romanian).
[152] McKenna F. and Feneves G.L. (2012), "Open system for earthquake engineering simulation", Pacific Earthquake Engineering Research Center.
[153] EN 1993-1-8 (2005), Eurocode 3: Design of steel structures – Part 1- 8: Design of joints, European Committee for Standardization; Brussels, Belgium.

ANNEXES

Annex A

Annex A presents the numerical models (source code) developed in the OpenSees framework for BRBF frames equipped with BRBs designed for $\varepsilon_{p,d}$ = 2.0%, having pinned-fixed connections. For the other BRBF models, the length of the elastic, L_e, and plastic zone, L_p, must be modified accordingly, and the ratio (r_{AeAp}) between the area of the elastic zone A_e and the area of the plastic zone A_p:

- BRB $\varepsilon_{p,d}$ = 1.66%, r_{AeAp} = Ae/Ap = 9.05714;
- BRB $\varepsilon_{p,d}$ = 1.75%, r_{AeAp} = Ae/Ap = 5.39048;
- BRB $\varepsilon_{p,d}$ = 2.00%, r_{AeAp} = Ae/Ap = 2.34667.

The OpenSees framework is open-source and its specific subroutines are available at [152].

```
################START##################################
# Updated:      02 April 2018
# Structure:    3-Story 3-Bay Steel BRBF Frame with Concentrated Plasticity in BRB
#               Centerline Model with pinned Beam-Column Joints; pinned BRBs
# FEM Model: Simplified modelling of BRBs: 1 finite element between working points
#               BRB axial stiffness: K_BRB=1.6*Ap*E/L
# CASE STUDY: BRB_eps_p = 2.0%
# Units: N, mm, seconds, (Ns^2)/mm=kg
#
# Element and Node ID conventions:
# Node:     a) main frame nodes: ex. 32, 3=X axis, 2=Y axis
#           b) extra nodes:    ex. 32i, i=1, 2, until reaching the next main node 42
#
# Element:  1) columns          /element elasticBeamColumn:          ex. 1xy
#           2) beams            /element elasticBeamColumn:          ex. 2xy
#           3) BRB (rig.& el)   /element elasticBeamColumn:          ex. 3xy
#           4) BRB(pl)          /element nonlinearBeamColumn:        ex. 4xy
#           5) springs K=0      /rotLeaningCol:                      ex. 5xy
#           6) rigid links      /element truss:                      ex. 6xy
#           7) P-delta columns /element elasticBeamColumn:           ex. 7xy
#############################################################
#         1. Set Up & Source Definition
#############################################################
        wipe;                           # clear memory of all past model definitions
        model BasicBuilder -ndm 2 -ndf 3; # define the model builder,
ndm=#dimension, ndf=#dofs
        set dataDir Data;# set up name of data directory (you can remove this)
        file mkdir $dataDir;                    # create data directory
        # set GMdir "../GMfiles/";              # ground-motion file directory
        source LibUnits.tcl;                    # define units
```

```
        source DisplayModel2D_n.tcl; # procedure for displaying the nodes for 2D
model
        source DisplayModel2D.tcl; # procedure for displaying a 2D perspective of
model
        source DisplayPlane.tcl; # procedure for displaying a plane in a model
        source rotLeaningCol.tcl; # procedure for defining a rotational spring (zero-
length element) with very small stiffness

########################################################
#       2. Define Analysis Type
########################################################
# Define type of analysis:  "pushover" = pushover; "dynamic" = dynamic
        set analysisType "dynamic";
        if {$analysisType == "pushover"} {
        set dataDir Concentrated_Pushover_Output;     # name of output folder
        file mkdir $dataDir;                          # create output folder
        }
        if {$analysisType == "dynamic"} {
        set dataDir Concentrated_Dynamic_Output;      # name of output folder
        file mkdir $dataDir;                          # create output folder
        }

########################################################
#       3. Define Building Geometry, Nodes, and Constraints
########################################################
# # Define structure-geometry parameters
        set LCol [expr 3500.0];                       # column height
        set LBeam [expr 7500.0];                      # beam length
        set alfa [expr atan($LCol/(0.5*$LBeam))];     # BRB insertion angle with
horizontal axis X
        set Lwp [expr sqrt(pow($LCol,2.0)+pow(0.5*$LBeam,2.0))]; # BRB length
working point to working point
#                           BRB geometry
#     node i (inferior)                                   node j (superior)
#     o-----------|------|-------------------------|------|-----------o
#     |<---Lri---->|<-Le->|<-----------Lp---------->|<-Le->|<----Lrj--->|
#                |<-----------------LBRB---------------->|
#     |<-----------------------------Lwp------------------------------>|
#
        set LBRB [expr 3930.0];         # mm, BRB length
        set Lri [expr 665.0];           # mm, BRB length rigid inferior node i
        set Le [expr 683.0];            # mm, BRB length elastic (variable,
depending on BRB eps_p)
# Le=Le1+Le2+Le3+Lt
        set Lp [expr 2564.0];              # mm, BRB length plastic (variable,
depending on BRB eps_p)
        set Lrj [expr $Lwp-$Lri-$LBRB]; # BRB length rigid superior node j
        set LriX [expr $Lri*cos($alfa)];    # BRB length rigid inferior node i, X
component
        set LriY [expr $Lri*sin($alfa)];    # BRB length rigid inferior node i, Y
component
```

```
        set LeX [expr $Le*cos($alfa)]; # BRB length elastic, X component
        set LeY [expr $Le*sin($alfa)]; # BRB length elastic, Y component
        set LpX [expr $Lp*cos($alfa)]; # BRB length plastic, X component
        set LpY [expr $Lp*sin($alfa)];      # BRB length plastic, Y component
        # Note: all lengths were checked and were OK!

# # Set lump floor masses at frame nodes
#       m3 = 634422.91 kg = 634.42291 (Ns^2)/mm # mass floor 3
#       m2 = 617410.94 kg = 617.41094 (Ns^2)/mm # mass floor 2; (from Etabs)
#       m1 = 619831.19 kg = 619.83119 (Ns^2)/mm # mass floor 1;
#       there are two BRBFs on X direction, therefore mass(floor.i)*0.5
        set m3  [expr 0.5*634.42291/4.0];   #4 main nodes per floor
        set m2  [expr 0.5*617.41094/4.0];   #4 main nodes per floor
        set m1  [expr 0.5*619.83119/4.0];   #4 main nodes per floor
        set mNegligible 1e-13; #a very small number to avoid problems with zero

# # Main nodal coordinates
# Calculate locations of beam/column intersections
        set X1 0.;
        set X2 [expr $X1 + $LBeam];
        set X3 [expr $X2 + $LBeam];
        set X4 [expr $X3 + $LBeam];
        set Y1 0.;
        set Y2 [expr $Y1 + $LCol];
        set Y3 [expr $Y2 + $LCol];
        set Y4 [expr $Y3 + $LCol];
# Nodes
        node 11 $X1 $Y1
        node 12 $X1 $Y2 -mass $m1 $mNegligible $mNegligible
        node 13 $X1 $Y3 -mass $m2 $mNegligible $mNegligible
        node 14 $X1 $Y4 -mass $m3 $mNegligible $mNegligible
        node 21 $X2 $Y1
        node 22 $X2 $Y2 -mass $m1 $mNegligible $mNegligible
        node 23 $X2 $Y3 -mass $m2 $mNegligible $mNegligible
        node 24 $X2 $Y4 -mass $m3 $mNegligible $mNegligible
        node 31 $X3 $Y1
        node 32 $X3 $Y2 -mass $m1 $mNegligible $mNegligible
        node 33 $X3 $Y3 -mass $m2 $mNegligible $mNegligible
        node 34 $X3 $Y4 -mass $m3 $mNegligible $mNegligible
        node 41 $X4 $Y1
        node 42 $X4 $Y2 -mass $m1 $mNegligible $mNegligible
        node 43 $X4 $Y3 -mass $m2 $mNegligible $mNegligible
        node 44 $X4 $Y4 -mass $m3 $mNegligible $mNegligible

# # Define extra nodes for pinned-beam releases and BRBs:
# Unbraced bays: connection is located at the face of the column @ wC/2
        set wC1 [expr 220.0]; # mm, width column axis 1
        set wC2 [expr 260.0]; # mm, width column axis 2
        set wC3 [expr 260.0]; # mm, width column axis 3
        set wC4 [expr 220.0]; # mm, width column axis 4
```

```
# 1st Floor:
        set X2106 [expr $LBeam +    $LriX];
        set X2107 [expr $LBeam +    $LriX];
        set X2108 [expr $LBeam +    $LriX+$LeX];
        set X2109 [expr $LBeam +    $LriX+$LeX+$LpX];
        set X2110 [expr $LBeam +    $LriX+$LeX+$LpX+$LeX];
        set X2111 [expr $LBeam +    $LriX+$LeX+$LpX+$LeX];
        set X2112 [expr 2.0*$LBeam - $LriX-$LeX-$LpX-$LeX];
        set X2113 [expr 2.0*$LBeam - $LriX-$LeX-$LpX-$LeX];
        set X2114 [expr 2.0*$LBeam - $LriX-$LeX-$LpX];
        set X2115 [expr 2.0*$LBeam - $LriX-$LeX];
        set X2116 [expr 2.0*$LBeam - $LriX];
        set X2117 [expr 2.0*$LBeam - $LriX];
        set Y2106 [expr 0.0   +    $LriY];
        set Y2107 [expr 0.0   +    $LriY];
        set Y2108 [expr 0.0   +    $LriY+$LeY];
        set Y2109 [expr 0.0   +    $LriY+$LeY+$LpY];
        set Y2110 [expr 0.0   +    $LriY+$LeY+$LpY+$LeY];
        set Y2111 [expr 0.0   +    $LriY+$LeY+$LpY+$LeY];
        set Y2112 [expr 0.0   +    $LriY+$LeY+$LpY+$LeY];
        set Y2113 [expr 0.0   +    $LriY+$LeY+$LpY+$LeY];
        set Y2114 [expr 0.0   +    $LriY+$LeY+$LpY];
        set Y2115 [expr 0.0   +    $LriY+$LeY];
        set Y2116 [expr 0.0   +    $LriY];
        set Y2117 [expr 0.0   +    $LriY];
        node 2106 $X2106 $Y2106
        node 2107 $X2107 $Y2107
        node 2108 $X2108 $Y2108
        node 2109 $X2109 $Y2109
        node 2110 $X2110 $Y2110
        node 2111 $X2111 $Y2111
        node 2112 $X2112 $Y2112
        node 2113 $X2113 $Y2113
        node 2114 $X2114 $Y2114
        node 2115 $X2115 $Y2115
        node 2116 $X2116 $Y2116
        node 2117 $X2117 $Y2117

# 2nd Floor:
        set X121 [expr $wC1/2.0];
        set X122 [expr $wC1/2.0];
        set X123 [expr $LBeam - $wC2/2.0];
        set X124 [expr $LBeam - $wC2/2.0];
        node 121 $X121 $Y2
        node 122 $X122 $Y2
        node 123 $X123 $Y2
        node 124 $X124 $Y2
        set X221 [expr $LBeam + $LriX];
        set X222 [expr $LBeam + $LriX];
        set X223 [expr $LBeam + $LBeam/2.0];
        set X224 [expr 2.0*$LBeam -$LriX];
```

```
set X225 [expr 2.0*$LBeam -$LriX];

node 221 $X221 $Y2
node 222 $X222 $Y2
node 223 $X223 $Y2
node 224 $X224 $Y2
node 225 $X225 $Y2
set X2206 [expr $LBeam +    $LriX];
set X2207 [expr $LBeam +    $LriX];
set X2208 [expr $LBeam +    $LriX+$LeX];
set X2209 [expr $LBeam +    $LriX+$LeX+$LpX];
set X2210 [expr $LBeam +    $LriX+$LeX+$LpX+$LeX];
set X2211 [expr $LBeam +    $LriX+$LeX+$LpX+$LeX];
set X2212 [expr 2.0*$LBeam - $LriX-$LeX-$LpX-$LeX];
set X2213 [expr 2.0*$LBeam - $LriX-$LeX-$LpX-$LeX];
set X2214 [expr 2.0*$LBeam - $LriX-$LeX-$LpX];
set X2215 [expr 2.0*$LBeam - $LriX-$LeX];
set X2216 [expr 2.0*$LBeam - $LriX];
set X2217 [expr 2.0*$LBeam - $LriX];
set Y2206 [expr $LCol +    $LriY];
set Y2207 [expr $LCol +    $LriY];
set Y2208 [expr $LCol +    $LriY+$LeY];
set Y2209 [expr $LCol +    $LriY+$LeY+$LpY];
set Y2210 [expr $LCol +    $LriY+$LeY+$LpY+$LeY];
set Y2211 [expr $LCol +    $LriY+$LeY+$LpY+$LeY];
set Y2212 [expr $LCol +    $LriY+$LeY+$LpY+$LeY];
set Y2213 [expr $LCol +    $LriY+$LeY+$LpY+$LeY];
set Y2214 [expr $LCol +    $LriY+$LeY+$LpY];
set Y2215 [expr $LCol +    $LriY+$LeY];
set Y2216 [expr $LCol +    $LriY];
set Y2217 [expr $LCol +    $LriY];
node 2206 $X2206 $Y2206
node 2207 $X2207 $Y2207
node 2208 $X2208 $Y2208
node 2209 $X2209 $Y2209
node 2210 $X2210 $Y2210
node 2211 $X2211 $Y2211
node 2212 $X2212 $Y2212
node 2213 $X2213 $Y2213
node 2214 $X2214 $Y2214
node 2215 $X2215 $Y2215
node 2216 $X2216 $Y2216
node 2217 $X2217 $Y2217
set X321 [expr 2.0*$LBeam + $wC3/2.0];
set X322 [expr 2.0*$LBeam + $wC3/2.0];
set X323 [expr 3.0*$LBeam - $wC4/2.0];
set X324 [expr 3.0*$LBeam - $wC4/2.0];
node 321 $X321 $Y2
node 322 $X322 $Y2
node 323 $X323 $Y2
node 324 $X324 $Y2
```

```
# 3rd Floor:
        set X131 [expr $wC1/2.0];
        set X132 [expr $wC1/2.0];
        set X133 [expr $LBeam - $wC2/2.0];
        set X134 [expr $LBeam - $wC2/2.0];
        node 131 $X131 $Y3
        node 132 $X132 $Y3
        node 133 $X133 $Y3
        node 134 $X134 $Y3
        set X231 [expr $LBeam + $LriX];
        set X232 [expr $LBeam + $LriX];
        set X233 [expr $LBeam + $LBeam/2.0];
        set X234 [expr 2.0*$LBeam -$LriX];
        set X235 [expr 2.0*$LBeam -$LriX];
        node 231 $X231 $Y3
        node 232 $X232 $Y3
        node 233 $X233 $Y3
        node 234 $X234 $Y3
        node 235 $X235 $Y3
        set X2306 [expr $LBeam +    $LriX];
        set X2307 [expr $LBeam +    $LriX];
        set X2308 [expr $LBeam +    $LriX+$LeX];
        set X2309 [expr $LBeam +    $LriX+$LeX+$LpX];
        set X2310 [expr $LBeam +    $LriX+$LeX+$LpX+$LeX];
        set X2311 [expr $LBeam +    $LriX+$LeX+$LpX+$LeX];
        set X2312 [expr 2.0*$LBeam - $LriX-$LeX-$LpX-$LeX];
        set X2313 [expr 2.0*$LBeam - $LriX-$LeX-$LpX-$LeX];
        set X2314 [expr 2.0*$LBeam - $LriX-$LeX-$LpX];
        set X2315 [expr 2.0*$LBeam - $LriX-$LeX];
        set X2316 [expr 2.0*$LBeam - $LriX];
        set X2317 [expr 2.0*$LBeam - $LriX];
        set Y2306 [expr 2.0*$LCol+  $LriY];
        set Y2307 [expr 2.0*$LCol+  $LriY];
        set Y2308 [expr 2.0*$LCol+  $LriY+$LeY];
        set Y2309 [expr 2.0*$LCol+  $LriY+$LeY+$LpY];
        set Y2310 [expr 2.0*$LCol+  $LriY+$LeY+$LpY+$LeY];
        set Y2311 [expr 2.0*$LCol+  $LriY+$LeY+$LpY+$LeY];
        set Y2312 [expr 2.0*$LCol+  $LriY+$LeY+$LpY+$LeY];
        set Y2313 [expr 2.0*$LCol+  $LriY+$LeY+$LpY+$LeY];
        set Y2314 [expr 2.0*$LCol+  $LriY+$LeY+$LpY];
        set Y2315 [expr 2.0*$LCol+  $LriY+$LeY];
        set Y2316 [expr 2.0*$LCol+  $LriY];
        set Y2317 [expr 2.0*$LCol+  $LriY];
        node 2306 $X2306 $Y2306
        node 2307 $X2307 $Y2307
        node 2308 $X2308 $Y2308
        node 2309 $X2309 $Y2309
        node 2310 $X2310 $Y2310
        node 2311 $X2311 $Y2311
        node 2312 $X2312 $Y2312
        node 2313 $X2313 $Y2313
```

```
        node 2314 $X2314 $Y2314
        node 2315 $X2315 $Y2315
        node 2316 $X2316 $Y2316
        node 2317 $X2317 $Y2317
        set X331 [expr 2.0*$LBeam + $wC3/2.0];
        set X332 [expr 2.0*$LBeam + $wC3/2.0];
        set X333 [expr 3.0*$LBeam - $wC4/2.0];
        set X334 [expr 3.0*$LBeam - $wC4/2.0];
        node 331 $X331 $Y3
        node 332 $X332 $Y3
        node 333 $X333 $Y3
        node 334 $X334 $Y3

# Roof:
        set X141 [expr $wC1/2.0];
        set X142 [expr $wC1/2.0];
        set X143 [expr $LBeam - $wC2/2.0];
        set X144 [expr $LBeam - $wC2/2.0];
        node 141 $X141 $Y4
        node 142 $X142 $Y4
        node 143 $X143 $Y4
        node 144 $X144 $Y4
        set X241 [expr $LBeam + $LriX];
        set X242 [expr $LBeam + $LriX];
        set X243 [expr $LBeam + $LBeam/2.0];
        set X244 [expr 2.0*$LBeam -$LriX];
        set X245 [expr 2.0*$LBeam -$LriX];
        node 241 $X241 $Y4
        node 242 $X242 $Y4
        node 243 $X243 $Y4
        node 244 $X244 $Y4
        node 245 $X245 $Y4
        set X341 [expr 2.0*$LBeam + $wC3/2.0];
        set X342 [expr 2.0*$LBeam + $wC3/2.0];
        set X343 [expr 3.0*$LBeam - $wC4/2.0];
        set X344 [expr 3.0*$LBeam - $wC4/2.0];
        node 341 $X341 $Y4
        node 342 $X342 $Y4
        node 343 $X343 $Y4
        node 344 $X344 $Y4

# # Define extra nodes for leaning column
        set X5 [expr 3.5*$LBeam];
        node 51 $X5 $Y1;
        node 511 $X5 $Y2;
        node 52 $X5 $Y2;
        node 521 $X5 $Y2;
        node 522 $X5 $Y3;
        node 53 $X5 $Y3;
        node 531 $X5 $Y3;
        # node 532 $X5 $Y4;
```

```
        node 54 $X5 $Y4;
# # Diaphragm effect:
# Constrain frame nodes/floor to have the same lateral displacement using the
"equalDOF" command.
# command: equalDOF $MasterNodeID $SlaveNodeID $dof1 $dof2...
        set dof1 1;       # constrain movement in dof 1 (x-direction)
# Floor 1
        equalDOF 12 22 $dof1;
        equalDOF 12 223 $dof1;
        equalDOF 12 32 $dof1;
        equalDOF 12 42 $dof1;
        equalDOF 12 52 $dof1;
# Floor 2
        equalDOF 13 23 $dof1;
        equalDOF 13 233 $dof1;
        equalDOF 13 33 $dof1;
        equalDOF 13 43 $dof1;
        equalDOF 13 53 $dof1;
# Floor 3
        equalDOF 14 24 $dof1;
        equalDOF 14 243 $dof1;
        equalDOF 14 34 $dof1;
        equalDOF 14 44 $dof1;
        equalDOF 14 54 $dof1; # problems if using the addtional lower point 532

# # BOUNDARY CONDITIONS
        # command:  fix nodeID dxFixity dyFixity rzFixity
        # fixity values: 1 = constrained; 0 = unconstrained
        fix 11 1 1 0;
        fix 21 1 1 1;
        fix 31 1 1 1;
        fix 41 1 1 0;
        fix 51 1 1 0; # P-delta column is pinned

# Define constraints for pined beam-to-column connection
        equalDOF 121 122 1 2;
        equalDOF 124 123 1 2;
        equalDOF 221 222 1 2;
        equalDOF 225 224 1 2;
        equalDOF 321 322 1 2;
        equalDOF 324 323 1 2;
        equalDOF 2106 2107 1 2;
        equalDOF 2111 2110 1 2;
        equalDOF 2112 2113 1 2;
        equalDOF 2117 2116 1 2;
        equalDOF 131 132 1 2;
        equalDOF 134 133 1 2;
        equalDOF 231 232 1 2;
        equalDOF 235 234 1 2;
        equalDOF 331 332 1 2;
        equalDOF 334 333 1 2;
```

```
        equalDOF 2206 2207 1 2;
        equalDOF 2211 2210 1 2;
        equalDOF 2212 2213 1 2;
        equalDOF 2217 2216 1 2;
        equalDOF 141 142 1 2;
        equalDOF 144 143 1 2;
        equalDOF 241 242 1 2;
        equalDOF 245 244 1 2;
        equalDOF 341 342 1 2;
        equalDOF 344 343 1 2;
        equalDOF 2306 2307 1 2;
        equalDOF 2311 2310 1 2;
        equalDOF 2312 2313 1 2;
        equalDOF 2317 2316 1 2;

##########################################################
#         Define Section Properties and Elements
##########################################################
# # Define material properties
        set Es 210000.0;                        # steel Young's modulus
# # Define column sections
# Axis 1 & 4, column = HE220B
        set A_colAx1 9100.0;            # cross-sectional area, mm^2
        set I_colAx1 80910000.0;        # moment of inertia, mm^4
# Axis 2 & 3, column = HE260B
        set A_colAx2 11840.0;           # cross-sectional area, mm^2
        set I_colAx2 149200000.0;       # moment of inertia, mm^4
# # Define beam sections
        set A_IPE400 8450.0;            # cross-sectional area, mm^2
        set I_IPE400 231300000.0;       # moment of inertia, mm^4
        set A_HE400A 15900.0;                   # cross-sectional area, mm^2
        set I_HE400A 450700000.0;       # moment of inertia, mm^4
        set A_HE450A 17800.0;                   # cross-sectional area, mm^2
        set I_HE450A 637200000.0;       # moment of inertia, mm^4
# # Set up geometric transformations of element
        set PDeltaTransf 1;
        geomTransf PDelta $PDeltaTransf;        # PDelta transformation

# # Define elastic column elements using "element" command
# command: element elasticBeamColumn $eleID $iNode $jNode $A $E $I $transfID
# eleID convention:  "xyz" where x=1=column; y=floor #; z = left to write
numbering, 1; 2 ...
# Columns Axis 1
        element elasticBeamColumn 111 11 12 $A_colAx1 $Es $I_colAx1
$PDeltaTransf; # Floor 1
        element elasticBeamColumn 112 12 13 $A_colAx1 $Es $I_colAx1
$PDeltaTransf; # Floor 2
        element elasticBeamColumn 113 13 14 $A_colAx1 $Es $I_colAx1
$PDeltaTransf; # Floor 3
# Columns Axis 2
```

```
        element elasticBeamColumn 121 21 22 $A_colAx2 $Es $I_colAx2
$PDeltaTransf; # Floor 1
        element elasticBeamColumn 122 22 23 $A_colAx2 $Es $I_colAx2
$PDeltaTransf; # Floor 2
        element elasticBeamColumn 123 23 24 $A_colAx2 $Es $I_colAx2
$PDeltaTransf; # Floor 3
# Columns Axis 3
        element elasticBeamColumn 131 31 32 $A_colAx2 $Es $I_colAx2
$PDeltaTransf; # Floor 1
        element elasticBeamColumn 132 32 33 $A_colAx2 $Es $I_colAx2
$PDeltaTransf; # Floor 2
        element elasticBeamColumn 133 33 34 $A_colAx2 $Es $I_colAx2
$PDeltaTransf; # Floor 3
# Columns Axis 4
        element elasticBeamColumn 141 41 42 $A_colAx1 $Es $I_colAx1
$PDeltaTransf; # Floor 1
        element elasticBeamColumn 142 42 43 $A_colAx1 $Es $I_colAx1
$PDeltaTransf; # Floor 2
        element elasticBeamColumn 143 43 44 $A_colAx1 $Es $I_colAx1
$PDeltaTransf; # Floor 3
# # Define elastic beam elements
#       eleID convention:  "2xy" where 2=beam #; y=floor #; z = left to write
numbering, 1; 2 ...
# Beams Floor 1
        # # Additional nodes for secondary beams
        set Xadd_bay1_nod1 [expr 1.0/3.0*$LBeam];
        set Xadd_bay1_nod2 [expr 2.0/3.0*$LBeam];
        set Xadd_bay2_nod1 [expr 1.0/3.0*$LBeam + $LBeam];
        set Xadd_bay2_nod2 [expr 2.0/3.0*$LBeam + $LBeam];
        set Xadd_bay3_nod1 [expr 1.0/3.0*$LBeam + $LBeam*2.0];
        set Xadd_bay3_nod2 [expr 2.0/3.0*$LBeam + $LBeam*2.0];
        node 1221 $Xadd_bay1_nod1 $Y2;     node 1231 $Xadd_bay1_nod2 $Y2;
        node 1321 $Xadd_bay1_nod1 $Y3;     node 1331 $Xadd_bay1_nod2 $Y3;
        node 1421 $Xadd_bay1_nod1 $Y4;     node 1431 $Xadd_bay1_nod2 $Y4;
        node 2221 $Xadd_bay2_nod1 $Y2;     node 2241 $Xadd_bay2_nod2 $Y2;
        node 2321 $Xadd_bay2_nod1 $Y3;     node 2341 $Xadd_bay2_nod2 $Y3;
        node 2421 $Xadd_bay2_nod1 $Y4;     node 2441 $Xadd_bay2_nod2 $Y4;
        node 3221 $Xadd_bay3_nod1 $Y2;     node 3231 $Xadd_bay3_nod2 $Y2;
        node 3321 $Xadd_bay3_nod1 $Y3;     node 3331 $Xadd_bay3_nod2 $Y3;
        node 3421 $Xadd_bay3_nod1 $Y4;     node 3431 $Xadd_bay3_nod2 $Y4;
        element elasticBeamColumn 210 12 121 $A_IPE400 $Es $I_IPE400
$PDeltaTransf;
        element elasticBeamColumn 211 122 1221 $A_IPE400 $Es $I_IPE400
$PDeltaTransf;
        element elasticBeamColumn 2111 1221 1231 $A_IPE400 $Es $I_IPE400
$PDeltaTransf;
        element elasticBeamColumn 2112 1231 123 $A_IPE400 $Es $I_IPE400
$PDeltaTransf;
        element elasticBeamColumn 212 124 22 $A_IPE400 $Es $I_IPE400
$PDeltaTransf;
```

```
        element elasticBeamColumn 213 22 221 $A_HE450A $Es $I_HE450A
$PDeltaTransf;
        element elasticBeamColumn 214 222 2221 $A_HE450A $Es $I_HE450A
$PDeltaTransf;
        element elasticBeamColumn 2141 2221 223 $A_HE450A $Es $I_HE450A
$PDeltaTransf;
        element elasticBeamColumn 2142 223 2241 $A_HE450A $Es $I_HE450A
$PDeltaTransf;
        element elasticBeamColumn 215 2241 224 $A_HE450A $Es $I_HE450A
$PDeltaTransf;
        element elasticBeamColumn 216 225 32 $A_HE450A $Es $I_HE450A
$PDeltaTransf;
        element elasticBeamColumn 217 32 321 $A_IPE400 $Es $I_IPE400
$PDeltaTransf;
        element elasticBeamColumn 218 322 3221 $A_IPE400 $Es $I_IPE400
$PDeltaTransf;
        element elasticBeamColumn 2181 3221 3231 $A_IPE400 $Es $I_IPE400
$PDeltaTransf;
        element elasticBeamColumn 2182 3231 323 $A_IPE400 $Es $I_IPE400
$PDeltaTransf;
        element elasticBeamColumn 219 324 42 $A_IPE400 $Es $I_IPE400
$PDeltaTransf;
# Beams Floor 2
        element elasticBeamColumn 220 13 131 $A_IPE400 $Es $I_IPE400
$PDeltaTransf;
        element elasticBeamColumn 221 132 1321 $A_IPE400 $Es $I_IPE400
$PDeltaTransf;
        element elasticBeamColumn 2211 1321 1331 $A_IPE400 $Es $I_IPE400
$PDeltaTransf;
        element elasticBeamColumn 2212 1331 133 $A_IPE400 $Es $I_IPE400
$PDeltaTransf;
        element elasticBeamColumn 222 134 23 $A_IPE400 $Es $I_IPE400
$PDeltaTransf;
        element elasticBeamColumn 223 23 231 $A_HE400A $Es $I_HE400A
$PDeltaTransf;
        element elasticBeamColumn 224 232 2321 $A_HE400A $Es $I_HE400A
$PDeltaTransf;
        element elasticBeamColumn 2241 2321 233 $A_HE400A $Es $I_HE400A
$PDeltaTransf;
        element elasticBeamColumn 2242 233 2341 $A_HE400A $Es $I_HE400A
$PDeltaTransf;
        element elasticBeamColumn 225 2341 234 $A_HE400A $Es $I_HE400A
$PDeltaTransf;
        element elasticBeamColumn 226 235 33 $A_HE400A $Es $I_HE400A
$PDeltaTransf;
        element elasticBeamColumn 227 33 331 $A_IPE400 $Es $I_IPE400
$PDeltaTransf;
        element elasticBeamColumn 228 332 3321 $A_IPE400 $Es $I_IPE400
$PDeltaTransf;
        element elasticBeamColumn 2281 3321 3331 $A_IPE400 $Es $I_IPE400
$PDeltaTransf;
```

```
        element elasticBeamColumn 2282 3331 333 $A_IPE400 $Es $I_IPE400
$PDeltaTransf;
        element elasticBeamColumn 229 334 43 $A_IPE400 $Es $I_IPE400
$PDeltaTransf;
# Beams Floor 3
        element elasticBeamColumn 230 14 141 $A_IPE400 $Es $I_IPE400
$PDeltaTransf;
        element elasticBeamColumn 231 142 1421 $A_IPE400 $Es $I_IPE400
$PDeltaTransf;
        element elasticBeamColumn 2311 1421 1431 $A_IPE400 $Es $I_IPE400
$PDeltaTransf;
        element elasticBeamColumn 2312 1431 143 $A_IPE400 $Es $I_IPE400
$PDeltaTransf;
        element elasticBeamColumn 232 144 24 $A_IPE400 $Es $I_IPE400
$PDeltaTransf;
        element elasticBeamColumn 233 24 241 $A_HE400A $Es $I_HE400A
$PDeltaTransf;
        element elasticBeamColumn 234 242 2421 $A_HE400A $Es $I_HE400A
$PDeltaTransf;
        element elasticBeamColumn 2341 2421 243 $A_HE400A $Es $I_HE400A
$PDeltaTransf;
        element elasticBeamColumn 2342 243 2441 $A_HE400A $Es $I_HE400A
$PDeltaTransf;
        element elasticBeamColumn 235 2441 244 $A_HE400A $Es $I_HE400A
$PDeltaTransf;
        element elasticBeamColumn 236 245 34 $A_HE400A $Es $I_HE400A
$PDeltaTransf;
        element elasticBeamColumn 237 34 341 $A_IPE400 $Es $I_IPE400
$PDeltaTransf;
        element elasticBeamColumn 238 342 3421 $A_IPE400 $Es $I_IPE400
$PDeltaTransf;
        element elasticBeamColumn 2381 3421 3431 $A_IPE400 $Es $I_IPE400
$PDeltaTransf;
        element elasticBeamColumn 2382 3431 343 $A_IPE400 $Es $I_IPE400
$PDeltaTransf;
        element elasticBeamColumn 239 344 44 $A_IPE400 $Es $I_IPE400
$PDeltaTransf;

# # Define rigid links
        set TrussMatID 600;                     # define a material ID
        set Arigid [expr 100.0*$A_HE450A];    # define area of truss section (make
much larger than A of frame elements)
        set Irigid [expr 100.0*$I_HE450A];     # moment of inertia for p-delta
columns (make much larger than I of frame elements)
        uniaxialMaterial Elastic $TrussMatID $Es;       # define truss material
# Rigid truss elemnts to assure that the beam nodes move horizontaly together
#       command: element truss $eleID $iNode $jNode $A $materialID
#       eleID convention:  614, 6=rigid truss, 1=floor#, 4= elem.#
        element truss 6014 42 52 $Arigid $TrussMatID;         # Floor 1
        element truss 6024 43 53 $Arigid $TrussMatID;         # Floor 2
        element truss 6034 44 54 $Arigid $TrussMatID;         # Floor 3
```

```
# # Define P-delta columns
#       eleID convention:  751, 7=P-d column; 5=X axis; 1=floor#.
        element elasticBeamColumn 7051 51 511 $Arigid $Es $Irigid $PDeltaTransf;
        # Story 1
        element elasticBeamColumn 7052 521 522 $Arigid $Es $Irigid
$PDeltaTransf;  # Story 2
        element elasticBeamColumn 7053 531 54   $Arigid $Es $Irigid
$PDeltaTransf;  # Story 3 ### problems if using node 532 intead of 54

#########################################################
#         Define zero-stiffness elastic rotational spring
#                 to model pinned connections
#########################################################
#       Spring ID: "5xy" where 5=spring; x=Floor; y=el.# bottom to top
#       rotLeaningCol ElemID ndR ndC ## master=frame node, slave=end column
node
# P-delta column
        rotLeaningCol 511 52 511;
        rotLeaningCol 521 52 521;
        rotLeaningCol 522 53 522;
        rotLeaningCol 531 53 531;
        # rotLeaningCol 532 54 532; # problems if active and (equaldDof 14 54)
also active
#########################################################
#               Define BRB elements
#       BRB is pinned connected to the gussets.
#       BRB is composed of several segments between working points:
#
# (wp_i)*-- Lrigid_i -o- Lelastic -- Lplastic -- Lelastic -o- Lrigid_j --*(wp_j)
#                   |<---------------LBRB--------------->|
#       |<----------------------------Lwp----------------------------->|
#########################################################
# # Define BRB properties
        set tp3 20.0; set hp3 70.0; # tp=core thickness @ plastic zone # Floor 3
        set tp2 20.0; set hp2 105.0; # hp=core hight     @ plastic zone # Floor 2
        set tp1 20.0; set hp1 130.0;                                    # Floor 1
#!!! rAeAp    to be modified when using other BRBs
        set rAeAp     2.34667;                  # ration= Ae / Ap (variable,
depending on BRB_e=?%)
        set Ap_BRB3 [expr $tp3*$hp3];         # cross-sectional area of the plastic
zone, mm^2
        set Ae_BRB3 [expr $rAeAp*$Ap_BRB3]; # cross-sectional area of the elastic
zone, mm^2
        set I_BRB3 [expr $tp3*$tp3*$tp3*$hp3/12.0];# moment of inertia of
plastic zone, mm^4
        set Ap_BRB2 [expr $tp2*$hp2];
        set Ae_BRB2 [expr $rAeAp*$Ap_BRB2];
        set I_BRB2 [expr $tp2*$tp2*$tp2*$hp2/12.0];
        set Ap_BRB1 [expr $tp1*$hp1];
        set Ae_BRB1 [expr $rAeAp*$Ap_BRB1];
```

```
        set I_BRB1 [expr $tp1*$tp1*$tp1*$hp1/12.0];
# Define modification factors
        set mfA 1000.0; # to affect axial stiffness of the RIGID zones
        set mfI 1000.0; # to affect bending stiffness of the entire BRB = BRM

# BRB Floor 1
#       eleID convention:  314, 3=elastic BRB component, 1=floor#,  4= elem.#
#left BRB
        element elasticBeamColumn 311 21 2106 [expr $mfA*$Ap_BRB1] $Es [expr
$mfI*$I_BRB1] $PDeltaTransf; # segment rigid, node i
        element elasticBeamColumn 312 2107 2108     $Ae_BRB1 $Es [expr
$mfI*$I_BRB1] $PDeltaTransf; # segment elastic, node i
   #... segment plastic
        element elasticBeamColumn 313 2109 2110     $Ae_BRB1 $Es [expr
$mfI*$I_BRB1] $PDeltaTransf; # segment elastic, node j
        element elasticBeamColumn 314 2111 223 [expr $mfA*$Ap_BRB1] $Es
[expr $mfI*$I_BRB1] $PDeltaTransf;    # segment rigid, node j
#right BRB
        element elasticBeamColumn 315 2112 223 [expr $mfA*$Ap_BRB1] $Es
[expr $mfI*$I_BRB1] $PDeltaTransf;    # segment rigid, node j
        element elasticBeamColumn 316 2114 2113     $Ae_BRB1 $Es [expr
$mfI*$I_BRB1] $PDeltaTransf; # segment elastic, node j
   #... segment plastic
        element elasticBeamColumn 317 2116 2115     $Ae_BRB1 $Es [expr
$mfI*$I_BRB1] $PDeltaTransf; # segment elastic, node i
        element elasticBeamColumn 318 31   2117 [expr $mfA*$Ap_BRB1] $Es
[expr $mfI*$I_BRB1] $PDeltaTransf;    # segment rigid, node j

# BRB Floor 2
#left BRB
        element elasticBeamColumn 321 22 2206 [expr $mfA*$Ap_BRB2] $Es [expr
$mfI*$I_BRB2] $PDeltaTransf; # segment rigid, node i
        element elasticBeamColumn 322 2207 2208     $Ae_BRB2 $Es [expr
$mfI*$I_BRB2] $PDeltaTransf; # segment elastic, node i
   #... segment plastic
        element elasticBeamColumn 323 2209 2210     $Ae_BRB2  $Es [expr
$mfI*$I_BRB2] $PDeltaTransf; # segment elastic, node j
        element elasticBeamColumn 324 2211 233 [expr $mfA*$Ap_BRB2] $Es
[expr $mfI*$I_BRB2] $PDeltaTransf;    # segment rigid, node j
#right BRB
        element elasticBeamColumn 325 2212 233 [expr $mfA*$Ap_BRB2] $Es
[expr $mfI*$I_BRB2] $PDeltaTransf;    # segment rigid, node j
        element elasticBeamColumn 326 2214 2213     $Ae_BRB2 $Es [expr
$mfI*$I_BRB2] $PDeltaTransf; # segment elastic, node j
   #... segment plastic
        element elasticBeamColumn 327 2216 2215     $Ae_BRB2 $Es [expr
$mfI*$I_BRB2] $PDeltaTransf; # segment elastic, node i
        element elasticBeamColumn 328 32   2217 [expr $mfA*$Ap_BRB2] $Es
[expr $mfI*$I_BRB2] $PDeltaTransf;    # segment rigid, node j

# BRB Floor 3
```

```
#left BRB
        element elasticBeamColumn 331 23   2306 [expr $mfA*$Ap_BRB3] $Es
[expr $mfI*$I_BRB3] $PDeltaTransf;    # segment rigid, node i
        element elasticBeamColumn 332 2307 2308      $Ae_BRB3 $Es [expr
$mfI*$I_BRB3] $PDeltaTransf; # segment elastic, node i
   #... segment plastic
        element elasticBeamColumn 333 2309 2310      $Ae_BRB3 $Es [expr
$mfI*$I_BRB3] $PDeltaTransf; # segment elastic, node j
        element elasticBeamColumn 334 2311 243 [expr $mfA*$Ap_BRB3] $Es
[expr $mfI*$I_BRB3] $PDeltaTransf;    # segment rigid, node j
#right BRB
        element elasticBeamColumn 335 2312 243 [expr $mfA*$Ap_BRB3] $Es
[expr $mfI*$I_BRB3] $PDeltaTransf;    # segment rigid, node j
        element elasticBeamColumn 336 2314 2313      $Ae_BRB3 $Es [expr
$mfI*$I_BRB3] $PDeltaTransf; # segment elastic, node j
   #... segment plastic
        element elasticBeamColumn 337 2316 2315      $Ae_BRB3 $Es [expr
$mfI*$I_BRB3] $PDeltaTransf; # segment elastic, node i
        element elasticBeamColumn 338 33   2317 [expr $mfA*$Ap_BRB3] $Es
[expr $mfI*$I_BRB3] $PDeltaTransf;    # segment rigid, node j

# Define ELEMENTS & SECTIONS
# Floor 1
        set BRB1_secTag 410; # assign a tag number to the BRB section tag
        set BRB1_matTagAxial 411; #assign a tag number to the BRB axial behavior
        set BRB1_matTagFlex 412; # assign a tag number to the BRB flexural
behavior
# Floor 2
        set BRB2_secTag 420;  # assign a tag number to the BRB section tag
        set BRB2_matTagAxial 421; #assign a tag number to the BRB axial behavior
        set BRB2_matTagFlex 422; #assign a tag number to the BRB flexural
behavior
# Floor 3
        set BRB3_secTag 430; # assign a tag number to the BRB section tag
        set BRB3_matTagAxial 431; #assign a tag number to the BRB axial behavior
        set BRB3_matTagFlex 432; # assign a tag number to the BRB flexural
behavior
# MATERIAL parameters
        # set Es 210000.0; #steel Young's modulus (previously defined) [N/mm^2]
        set fy 355.0;             # steel yield strength [N/mm^2]
        set b 0.0184;             # strain-hardening ratio (ratio between post-yield
tangent and initial elastic tangent)
# BRB section
#   calculated stiffness parameters
        set EAp_BRB1 [expr $Es*$Ap_BRB1];   # EAp, for axial-force-strain
relationship
        set Fy_BRB1 [expr $fy*$Ap_BRB1];     # BRB yield force
        set EI_BRB1 [expr $Es*$mfI*$I_BRB1];          # EI, for moment-curvature
relationship
        uniaxialMaterial Steel01 $BRB1_matTagAxial $Fy_BRB1 $EAp_BRB1 $b;
        # bilinear behavior for axial
```

```
        uniaxialMaterial Elastic $BRB1_matTagFlex $EI_BRB1;  # elastic behavior for
flexure
        section Aggregator $BRB1_secTag $BRB1_matTagAxial P
$BRB1_matTagFlex Mz;          # combine axial & flexural behavior into one section
(no P-M interaction here)

        set EAp_BRB2 [expr $Es*$Ap_BRB2];   # EAp, for axial-force-strain
relationship
        set Fy_BRB2 [expr $fy*$Ap_BRB2];     # BRB yield force
        set EI_BRB2 [expr $Es*$mfI*$I_BRB2];          # EI, for moment-curvature
relationship
        uniaxialMaterial Steel01 $BRB2_matTagAxial $Fy_BRB2 $EAp_BRB2 $b;
                # bilinear behavior for axial
        uniaxialMaterial Elastic $BRB2_matTagFlex $EI_BRB2;  # elastic behavior for
flexure
        section Aggregator $BRB2_secTag $BRB2_matTagAxial P
$BRB2_matTagFlex Mz;          # combine axial & flexural behavior into one section
(no P-M interaction here)

        set EAp_BRB3 [expr $Es*$Ap_BRB3];           # EAp, for axial-force-strain
relationship
        set Fy_BRB3 [expr $fy*$Ap_BRB3];            # BRB yield force
        set EI_BRB3 [expr $Es*$mfI*$I_BRB3];        # EI, for moment-curvature
relationship
        uniaxialMaterial Steel01 $BRB3_matTagAxial $Fy_BRB3 $EAp_BRB3 $b;
                # bilinear behavior for axial
        uniaxialMaterial Elastic $BRB3_matTagFlex $EI_BRB3;          # elastic
behavior for flexure
        section Aggregator $BRB3_secTag $BRB3_matTagAxial P
$BRB3_matTagFlex Mz;          # combine axial & flexural behavior into one section
(no P-M interaction here)

# Element connectivity:
#   element nonlinearBeamColumn $eleTag $iNode $jNode $numIntgrPts $secTag
$transfTag
        set numIntgrPts 2; # number of integration points for force-based element
        element nonlinearBeamColumn 411 2108 2109 $numIntgrPts
$BRB1_secTag $PDeltaTransf;
        element nonlinearBeamColumn 412 2115 2114 $numIntgrPts
$BRB1_secTag $PDeltaTransf;
        element nonlinearBeamColumn 421 2208 2209 $numIntgrPts
$BRB2_secTag $PDeltaTransf;
        element nonlinearBeamColumn 422 2215 2214 $numIntgrPts
$BRB2_secTag $PDeltaTransf;
        element nonlinearBeamColumn 431 2308 2309 $numIntgrPts
$BRB3_secTag $PDeltaTransf;
        element nonlinearBeamColumn 432 2315 2314 $numIntgrPts
$BRB3_secTag $PDeltaTransf;

##########################################################
#           Eigenvalue Analysis
```

```
        set pi [expr 2.0*asin(1.0)];                    # Definition of pi
        set nEigenI 1;                                  # mode i = 1
        set nEigenJ 3;                                  # mode j = 2
        set lambdaN [eigen [expr $nEigenJ]];            # eigenvalue analysis for
nEigenJ modes
        set lambdaI [lindex $lambdaN [expr 0]];         # eigenvalue mode i = 1
        set lambdaJ [lindex $lambdaN [expr $nEigenJ-2]]; # eigenvalue mode j = 2
        set w1 [expr pow($lambdaI,0.5)];        # w1 (1st mode circular frequency)
        set w2 [expr pow($lambdaJ,0.5)];        # w2 (2nd mode circular frequency)
        set T1 [expr 2.0*$pi/$w1];              # 1st mode period of the structure
        set T2 [expr 2.0*$pi/$w2];              # 2nd mode period of the structure
        puts "Check-2:  Eigenvalue Analysis         - DONE!";
        puts "          T1 = $T1 sec";   # display the first mode period in the
command window
        puts "          T2 = $T2 sec";   # display the second mode period in the
command window

#########################################################
#           Display the model
#########################################################
# create display for mode shapes
set x [expr 1.75*$LBeam]; set xx [expr 2.*$LBeam]; set xxx [expr 2.*$LBeam];
set y [expr 1.5*$LCol]; set yy [expr 1.6*$LCol]; set yyy [expr 2.*$LCol];
set ViewScale1 20000; # scale factor for deformed shape
#                   $windowTitle $xLoc $yLoc $xPixels $yPixels
        recorder display "Model & Node Tag" 720 1 870 300 -wipe; # display
Recorder pg 321 pdf
        prp $x $y 1;
        vup 0 1 0;
        vpn 0 0 1;
        viewWindow -$xxx $xxx -$yy $yyy; # display command in opensees @ help
363 pg / book
        display 1 -1 0; # display a b c; a<0 eigen mode plot (ex: -1; -2) # a=1 plot
shape of frame;
#                       b=-1 plot nod tags # b=>0 SF for nodes;
#                       c=0 undeformed shape # c>0 view scale factor;
        set fmt1 "Mode Shape: Eigen Mode=%.1i, Period=%.3f %s "
        set windowTitle1 [format $fmt1 1 $T1 $TunitTXT]
        recorder display $windowTitle1 720 301 870 300 -wipe
        prp $xx $yy 1;  # projection reference point; defines the center of projection
(viewer eye)
        vup 0 1 0;                  # view-up vector (vup)
        vpn 0 0 1;                  # view-plane normal (vpn)
        viewWindow -$xxx $xxx -$yy $yyy; # coordiantes of the window relative to
prp (-x, x, -y, y)
        display -1 2 $ViewScale1;       # the 1st arg. is the tag for display mode
(ex. -1 is for the first mode shape)
#                               # the 2nd arg. is magnification factor for nodes,
#                               # the 3rd arg. is magnif. factor of deformed shape
        set fmt2 "Mode Shape: Eigen Mode=%.1i, Period=%.3f %s "
        set windowTitle2 [format $fmt2 2 $T2 $TunitTXT]
```

```
        recorder display $windowTitle2 720 601 870 300 -wipe
        prp $xx $yy 1;
        vup 0 1 0;
        vpn 0 0 1;
        viewWindow -$xxx $xxx -$yy $yyy;
        display -2 2 $ViewScale1;
# Procedures OpenSees wiki: display the model with the node numbers
        # DisplayModel2D_n NodeNumbers; # Options: ModeShape , NodeNumbers
, DeformedShape (used for nodes)
        # DisplayModel2D        ModeShape; # Options: ModeShape , NodeNumbers
, DeformedShape        (used for modes)
# Checking
        puts "Check-3:  Display Model & Eigen Modes   - DONE!";

##########################################################
#           Gravity Loads & Gravity Analysis
##########################################################
#       Load = 1.0 x DEAD + 0.3 x LIVE
# # Apply gravity loads
#       command: pattern PatternType $PatternID TimeSeriesType
        pattern Plain 101 Linear {
# Loads on BRBF
#       Floor 3
        set Fe_fl_3 [expr -5.329e+4];  # N, concentrated load from exterior sec.
beam
        set Fi_fl_3 [expr -5.737e+4];   # N, concentrated load from interior sec.
beam
        set Fd_fl_3 [expr -6.56]; #N/mm, uniformly distributed load on princ. beam
#       Floor 2
        set Fe_fl_2 [expr -5.158e+4];  # N, concentrated load from exterior sec.
beam
        set Fi_fl_2 [expr -5.494e+4];   # N, concentrated load from interior sec.
beam
        set Fd_fl_2 [expr -6.43]; #N/mm, uniformly distributed load on princ. beam
#       Floor 1
        set Fe_fl_1 [expr -5.158e+4];  # N, concentrated load from exterior sec.
beam
        set Fi_fl_1 [expr -5.494e+4];   # N, concentrated load from interior sec.
beam
        set Fd_fl_1 [expr -6.43]; #N/mm, uniformly distributed load on princ. beam
# Distribution of loads on nodes and beam elements
#       command: eleLoad -ele $eleTag1 <$eleTag2 ....> -type -beamUniform $Wz
<$Wx>
#       command: eleLoad -ele $eleTag1 $eleTag2 -type -beamPoint $Pz $xL
<$Px>
#       command: load node Fx Fy Mz
#       Floor 1
        load 12    0.0 $Fe_fl_1 0.0; # external sec. beam
        load 1221 0.0 $Fi_fl_1 0.0; ##
        load 1231 0.0 $Fi_fl_1 0.0; #
        load 22    0.0 $Fi_fl_1 0.0; #
```

```
        load 2221 0.0 $Fi_fl_1 0.0; #
        load 2241 0.0 $Fi_fl_1 0.0; # internal sec. beam
        load 32   0.0 $Fi_fl_1 0.0; #
        load 3221 0.0 $Fi_fl_1 0.0; #
        load 3231 0.0 $Fi_fl_1 0.0; ##
        load 42   0.0 $Fe_fl_1 0.0; # external sec. beam
        eleLoad -ele 210 211 2111 2112 212    -type -beamUniform $Fd_fl_1;
        eleLoad -ele 213 214 2141 2142 215 216 -type -beamUniform $Fd_fl_1;
        eleLoad -ele 217 218 2181 2182 219    -type -beamUniform $Fd_fl_1;
#       Floor 2
        load 13   0.0 $Fe_fl_2 0.0; # external sec. beam
        load 1321 0.0 $Fi_fl_2 0.0; ##
        load 1331 0.0 $Fi_fl_2 0.0; #
        load 23   0.0 $Fi_fl_2 0.0; #
        load 2321 0.0 $Fi_fl_2 0.0; #
        load 2341 0.0 $Fi_fl_2 0.0; # internal sec. beam
        load 33   0.0 $Fi_fl_2 0.0; #
        load 3321 0.0 $Fi_fl_2 0.0; #
        load 3331 0.0 $Fi_fl_2 0.0; ##
        load 43   0.0 $Fe_fl_2 0.0; # external sec. beam
        eleLoad -ele 220 221 2211 2212 222    -type -beamUniform $Fd_fl_2;
        eleLoad -ele 223 224 2241 2242 225 226 -type -beamUniform $Fd_fl_2;
        eleLoad -ele 227 228 2281 2282 229    -type -beamUniform $Fd_fl_2;
#       Floor 3
        load 14   0.0 $Fe_fl_3 0.0; # external sec. beam
        load 1421 0.0 $Fi_fl_3 0.0; ##
        load 1431 0.0 $Fi_fl_3 0.0; #
        load 24   0.0 $Fi_fl_3 0.0; #
        load 2421 0.0 $Fi_fl_3 0.0; #
        load 2441 0.0 $Fi_fl_3 0.0; # internal sec. beam
        load 34   0.0 $Fi_fl_3 0.0; #
        load 3421 0.0 $Fi_fl_3 0.0; #
        load 3431 0.0 $Fi_fl_3 0.0; ##
        load 44   0.0 $Fe_fl_3 0.0; # external sec. beam
        eleLoad -ele 230 231 2311 2312 232    -type -beamUniform $Fd_fl_3;
        eleLoad -ele 233 234 2341 2342 235 236 -type -beamUniform $Fd_fl_3;
        eleLoad -ele 237 238 2381 2382 239    -type -beamUniform $Fd_fl_3;
# Loads from geometrical imperfections, X direction
        set F_imp_3 [expr 0.5*18812.0];       # N, Floor 3
        set F_imp_2 [expr 0.5*37090.0];       # N, Floor 2
        set F_imp_1 [expr 0.5*55426.0];       # N, Floor 1
        load 14 $F_imp_3 0.0 0.0;             # Floor 3
        load 13 $F_imp_2 0.0 0.0;             # Floor 2
        load 12 $F_imp_1 0.0 0.0;             # Floor 1
# Point loads on leaning column nodes
#   (tributarry area is less than 1/2 od the building...
#    ...exterior principal beams also take gravity loads)
        set F_linCol_3 [expr -2.262e+6];      # Floor 3
        set F_linCol_2 [expr -2.171e+6];      # Floor 2
        set F_linCol_1 [expr -2.171e+6];      # Floor 1
        load 54   0.0 $F_linCol_3 0.0;        # Floor 3
```

```
        load 53   0.0 $F_linCol_2 0.0;            # Floor 2
        load 52   0.0 $F_linCol_1 0.0;            # Floor 1
        }
# # recorde disp at node 14 (top, left) and reactions at the bottom nodels
        if {$analysisType == "pushover"} {
        recorder Node -file "$dataDir/Pushover_Node_Disp_14.out" -time -node 14 -
dof 1 disp;
        recorder Node -file "$dataDir/Pushover_Reactions_Floor_1.out" -time -node
11 21 31 41 51 -dof 1 reaction;
        }
# """""""""""""""""""""""""""""""""""""""""""""""""""""""""""""""""""""""""""""""
# # Display deformed shape
        set ViewScale2 1;                                   # to be modified by user
        DisplayModel2D DeformedShape $ViewScale2; # display deformed shape,
the scaling factor needs to be adjusted for each model
# Large display window
        set fmt3 "Deformed Shape: Top Displ.=%.1i, Period=%.3f %s  "; #
"Deformed Shape: Top Displ.=%.1i, Period=%.3f %s  ";
        set windowTitle3 [format $fmt3 1 $T1  $TunitTXT];
        recorder display $windowTitle3 10 10 1580 880 -wipe;
        prp $xx $yy 1;
        vup 0 1 0;
        vpn 0 0 1;
        viewWindow -$xxx [expr $xxx+1000.] -$yy [expr $yyy-1000.];
        display 1 2 $ViewScale2;
# """""""""""""""""""""""""""""""""""""""""""""""""""""""""""""""""""""""""""""""
# # Gravity-analysis: load-controlled static analysis
        constraints Plain;        # how it handles boundary conditions
        numberer RCM; # renumber dof's to minimize band-width (optimization)
        system BandGeneral;   # how to store and solve the system of equations in
the analysis (large model: try UmfPack)
        # system UmfPack;               # large model
         set iter 200;    # the max number of iterations to check before returning
failure condition
         set tol 1.0e-6;          # convergence tolerance for test
        test NormDispIncr $tol $iter;    # determine if convergence has been
achieved at the end of an iteration step (initial =10)
        algorithm Newton;               # use Newton's solution algorithm: updates
tangent stiffness at every iteration
         set NstepGravity 10;            # apply gravity in 10 steps
         set DGravity [expr 1.0/$NstepGravity];         # load increment
        integrator LoadControl $DGravity;       # determine the next time step for
an analysis
        analysis Static;          # define type of analysis: static or transient
        analyze $NstepGravity;          # apply gravity
# Maintain constant gravity loads and reset time to zero
        loadConst -time 0.0
        puts "Check-4:  Gravity Load Applied        - DONE!"
#####################################################
#           Pushover Analysis
#####################################################
```

```
        if {$analysisType == "pushover"} {
                puts "  "
                puts "     Running Pushover Anlysis..."
# # Assign lateral loads and create load pattern:  use P100-1/2013 distribution
# MODAL distribution              (loads are divided to 4 frame nodes per floor)
        # set latLoad3 [expr 1.0/4.0]; set latLoad2 [expr 0.649/4.0]; set latLoad1
[expr 0.326/4.0];
# UNIFORM distribution          (loads are divided to 4 frame nodes per floor)
# (also it might be applied only to the master node of the floor diaphragm)
        set latLoad3 [expr 1.0/4.0]; set latLoad2 [expr 0.973/4.0]; set latLoad1
[expr 0.977/4.0];
        pattern Plain 200 Linear {
                load 14 $latLoad3 0.0 0.0; load 24 $latLoad3 0.0 0.0; load 34
$latLoad3 0.0 0.0; load 44 $latLoad3 0.0 0.0; # Floor 3
                load 13 $latLoad2 0.0 0.0; load 23 $latLoad2 0.0 0.0; load 33
$latLoad2 0.0 0.0; load 43 $latLoad2 0.0 0.0; # Floor 2
                load 12 $latLoad1 0.0 0.0; load 22 $latLoad1 0.0 0.0; load 32
$latLoad1 0.0 0.0; load 42 $latLoad1 0.0 0.0; # Floor 1
        }
# record displacement at node 14 (top, left) and reactions at the bottom nodes
        recorder Node -file "$dataDir/Node_Disp_14.out" -time -node 14 -dof 1
disp;
        recorder Node -file "$dataDir/Node_Disp_13.out" -time -node 13 -dof 1
disp;
        recorder Node -file "$dataDir/Node_Disp_12.out" -time -node 12 -dof 1
disp;
        recorder Node -file "$dataDir/Reactions_Floor_1.out" -time -node 11 21 31
41 51 -dof 1 reaction;
        recorder Node -file "$dataDir/Reactions_Floor_2.out" -time -node 12 22 32
42 52 223 -dof 1 reaction;
        recorder Node -file "$dataDir/Reactions_Floor_3.out" -time -node 13 23 33
43 53 233 -dof 1 reaction;
# columns Floor 3
        recorder Element -file "$dataDir/Force_Column_113.out" -time -ele 113
force;
        recorder Element -file "$dataDir/Force_Column_123.out" -time -ele 123
force;
        recorder Element -file "$dataDir/Force_Column_133.out" -time -ele 133
force;
        recorder Element -file "$dataDir/Force_Column_143.out" -time -ele 143
force;
        recorder Element -file "$dataDir/Force_Column_753.out" -time -ele 753
force;
# columns Floor 2
        recorder Element -file "$dataDir/Force_Column_112.out" -time -ele 112
force;
        recorder Element -file "$dataDir/Force_Column_122.out" -time -ele 122
force;
        recorder Element -file "$dataDir/Force_Column_132.out" -time -ele 132
force;
```

```
        recorder Element -file "$dataDir/Force_Column_142.out" -time -ele 142
force;
        recorder Element -file "$dataDir/Force_Column_752.out" -time -ele 752
force;
# columns Floor 1
        recorder Element -file "$dataDir/Force_Column_111.out" -time -ele 111
force;
        recorder Element -file "$dataDir/Force_Column_121.out" -time -ele 121
force;
        recorder Element -file "$dataDir/Force_Column_131.out" -time -ele 131
force;
        recorder Element -file "$dataDir/Force_Column_141.out" -time -ele 141
force;
        recorder Element -file "$dataDir/Force_Column_751.out" -time -ele 751
force;
        recorder Element -file "$dataDir/Force_BRB_331.out" -time -ele 331 force;
# BRB FLoor 3
        recorder Element -file "$dataDir/Force_BRB_338.out" -time -ele 338 force;
# BRB FLoor 3
        recorder Element -file "$dataDir/Force_BRB_321.out" -time -ele 321 force;
# BRB FLoor 2
        recorder Element -file "$dataDir/Force_BRB_328.out" -time -ele 328 force;
# BRB FLoor 2
        recorder Element -file "$dataDir/Force_BRB_311.out" -time -ele 311 force;
# BRB FLoor 1
        recorder Element -file "$dataDir/Force_BRB_318.out" -time -ele 318 force;
# BRB FLoor 1
# record drift histories
        # drift recorder command: recorder Drift -file $filename -iNode $NodeI_ID -
jNode $NodeJ_ID -dof $dof -perpDirn $Record.drift.perpendicular.to.this.direction
        recorder Drift -file "$dataDir/Drift_Floor_3.out" -iNode 13 -jNode 14 -dof 1 -
perpDirn 2; # Floor 3
        recorder Drift -file "$dataDir/Drift_Floor_2.out" -iNode 12 -jNode 13 -dof 1 -
perpDirn 2; # Floor 2
        recorder Drift -file "$dataDir/Drift_Floor_1.out" -iNode 11 -jNode 12 -dof 1 -
perpDirn 2; # Floor 1

# displacement parameters
        set IDctrlNode 14;      # node where disp is read for disp control
        set IDctrlDOF 1;        # degree of freedom read for disp control (1 = x
displacement)
        set Dmax [expr 0.2*$LCol]; # maximum displacement of pushover;
0.025*H=code drift limit
        set Dincr [expr $Dmax/200.];  # displacement increment
# pushover analysis commands
        constraints Plain;              # how it handles boundary conditions
        numberer RCM; # renumber dof's to minimize band-width (optimization)
        system BandGeneral;             # how to store and solve the system of
equations in the analysis (large model: try UmfPack)
        test NormUnbalance 1.0e-6 1000;       # type of convergence criteria with
tolerance, max iterations (ex = 400 iter.)
```

```
        algorithm Newton;       # use Newton's solution algorithm: updates tangent
stiffness at every iteration
        integrator DisplacementControl $IDctrlNode $IDctrlDOF $Dincr;          #
use displacement-controlled analysis
        analysis Static;          # define type of analysis: static for pushover
        set ok 0
        set currentDisp 0.0
        while {$ok == 0 && $currentDisp < $Dmax} {
                set ok [analyze 1]
                if {$ok != 0} {
                test NormDispIncr 1.0e-6 1000 1;       # text for convergence,
convg. tol., maxNumIter; 1 print information on each step
                algorithm Newton –initial
                set ok [analyze 1]
                test NormDispIncr 1.0e-6 10
                algorithm Newton
                }
                set currentDisp [nodeDisp $IDctrlNode 1]
                }

        puts "  node14disp: [nodeDisp 14 1]"
        puts "  node24disp: [nodeDisp 24 1]"
        puts "  node34disp: [nodeDisp 34 1]"
        puts "  node44disp: [nodeDisp 44 1]"
        puts "  TargetDisp:          $Dmax mm"
        puts " "
        puts "Check-5:  Pushover Anlysis            - DONE!"
        }
#####################################################
#           Transient Analysis
#####################################################
        if {$analysisType == "dynamic"} {
                puts "        Running Transient analysis..."
        # record drift histories
                # drift recorder command: recorder Drift -file $filename -iNode
$NodeI_ID -jNode $NodeJ_ID -dof $dof -perpDirn
$Record.drift.perpendicular.to.this.direction
                # recorder Drift -file "$dataDir/$subDir1/Drift.out" -iNode 1 -jNode
3 -dof 1 -perpDirn 2;
                recorder Drift -file "$dataDir/TH_Drift_Floor_3.out" -iNode 13 -jNode
14 -dof 1 -perpDirn 2; # Floor 3
                recorder Drift -file "$dataDir/TH_Drift_Floor_2.out" -iNode 12 -jNode
13 -dof 1 -perpDirn 2; # Floor 2
                recorder Drift -file "$dataDir/TH_Drift_Floor_1.out" -iNode 11 -jNode
12 -dof 1 -perpDirn 2; # Floor 1
                recorder Node -file "$dataDir/TH_Node_Disp_14.out" -node 14 -dof
1 disp;

        # record displacements at the nodes of the BRB-plastic-segment
                recorder Node -file "$dataDir/TH_Node_Disp_BRB_1L.out" -node
2108 2109 -dof 1 2 disp;
```

```
                recorder Node -file "$dataDir/TH_Node_Disp_BRB_1R.out" -node
2115 2114 -dof 1 2 disp;
                recorder Node -file "$dataDir/TH_Node_Disp_BRB_2L.out" -node
2208 2209 -dof 1 2 disp;
                recorder Node -file "$dataDir/TH_Node_Disp_BRB_2R.out" -node
2215 2214 -dof 1 2 disp;
                recorder Node -file "$dataDir/TH_Node_Disp_BRB_3L.out" -node
2308 2309 -dof 1 2 disp;
                recorder Node -file "$dataDir/TH_Node_Disp_BRB_3R.out" -node
2315 2314 -dof 1 2 disp;

        # record basic deformations of the BRB-plastic-segment element (for
checking the results obtained with "recorder Node")
                recorder Element -file
"$dataDir/TH_basicDeformation_BRB_1L_elem.out" -ele 411 basicDeformation;
                recorder Element -file
"$dataDir/TH_basicDeformation_BRB_1R_elem.out" -ele 412 basicDeformation;
                recorder Element -file
"$dataDir/TH_basicDeformation_BRB_2L_elem.out" -ele 421 basicDeformation;
                recorder Element -file
"$dataDir/TH_basicDeformation_BRB_2R_elem.out" -ele 422 basicDeformation;
                recorder Element -file
"$dataDir/TH_basicDeformation_BRB_3L_elem.out" -ele 431 basicDeformation;
                recorder Element -file
"$dataDir/TH_basicDeformation_BRB_3R_elem.out" -ele 432 basicDeformation;
                source DynamicEQ_BRB.tcl
        puts "Check-5:  Transient Anlysis            - DONE!"
        }
# ------------------------------------------------------------------------
# Dynamic Earthquake Analysis
# Created by:  Vesna Terzic, UC Berkeley, 2013
# execute this file after you have built the model, and after you apply gravity
# ------------------------------------------------------------------------
# source in procedures
        source ReadSMDfile.tcl;# procedure for reading GM file and converting it to
proper format
# Uniform Earthquake ground motion (uniform acceleration input at all support
nodes)
        set GMdirection 1;                      # ground-motion direction
        set GMfileH "Bucuresti_7";              # ground-motion filenames:
horizontal component
        set GMfact 1.0;                         # ground-motion scaling factor
        puts "          Using the accelerogram: $GMfileH."
#########################################################
#                Define & Apply Damping
#########################################################
# # RAYLEIGH damping parameters
#       C=$alphaM*M + $betaKcurr*Kcurrent + $betaKcomm*KlastCommit +
$beatKinit*$Kinitial
############ TRIAL 1 (analysis not converging all the way)###########
        # set betaK 0.05; # factor applied to elements current stiffness matrix
```

```
	# # critical damping ratio = 2% in Japan for steel structures
# # Assign tangent stiffness proportional damping to columns, beams, braces and gusset plate of a braced frame
	# region 1 -eleRange 111 2382 -rayleigh 0. $betaK 0. 0.;		# frame columns, beams, BRB, NOT rigid-trusses, NOT leaning columns

########## TRIAL 2	(analysis converging all the way) #############
	set xDamp 0.05; # damping ratio
	set betaKcomm [expr 2.*$xDamp*$T1/(2.*$pi)];
	#assign tangent stifness proportional damping to columns, beams, braces and gusset plate of a braced frame
	region 1 -eleRange 111 2382 -rayleigh 0. 0. 0. $betaKcomm; #columns
#########################################################
#	Perform Dynamic Ground-Motion Analysis for Horizonal Component of Ground Motion
#########################################################
# # Uniform EXCITATION: acceleration input
	set IDloadTag 400;	# for uniform support excitation
	set inFileH $GMfileH.acc
	set outFileH $GMfileH.g3
	ReadSMDFile $inFileH $outFileH dt nPt;		# call procedure to convert the horizontal ground-motion file
	set GMfatt [expr $g*$GMfact];		# data in input file is in g Unifts -- ACCELERATION TH
	timeSeries Path 10 -dt $dt -filePath $outFileH -factor $GMfatt;		# horizonatal time series information
	pattern UniformExcitation $IDloadTag $GMdirection -accel 10;		# create Uniform excitation for horizontal GM

# # Record absolute floor accelerations
	# recorder Node -file "$dataDir/$subDir1/FloorAcc.out" -time -timeSeries 10 -node 3 -dof 1 accel

# # Define analysis objects and performe analysis
	set tFinal	[expr $dt*$nPt];	# maximum duration of ground-motion analysis
	constraints Plain
	numberer RCM
	system BandGeneral
	test NormDispIncr 1.0e-6 10
	algorithm Newton
	integrator Newmark 0.5 0.25
	analysis Transient

	set deltaT 0.001
	set ok 0.0
	set currentTime 0.0
	while {$ok == 0 && $currentTime < $tFinal} {
		set ok [analyze 1 $deltaT]
		if {$ok != 0} {
			test NormDispIncr 1e-4 2000
```

```
                        algorithm Newton -initial
                        set ok [analyze 1 $deltaT]
                        test NormDispIncr 1.0e-6 10
                        algorithm Newton
                }
        if {$ok != 0} {
                        test NormDispIncr 1.0e-6 200 1
                        algorithm NewtonLineSearch 0.8
                        set ok [analyze 1 $deltaT]
                        test NormDispIncr 1.0e-6 10
                        algorithm Newton
                }
                if {$ok != 0} {
                        test NormDispIncr 1.0e-4 2000
                        algorithm Newton -initialThenCurrent
                        set ok [analyze 1 $deltaT]
                        test NormDispIncr 1.0e-6 10
                        algorithm Newton
                }
                set currentTime [getTime]
        }

        puts "Ground Motion Done. End Time: [getTime]. tFinal: $tFinal."

#########################################################
# ReadSMDFile $inFilename $outFilename $dt
#########################################################
# read gm input format
# Written: MHS
# Date: July 2000
# A procedure which parses a ground motion record from the PEER
# strong motion database by finding dt in the record header, then
# echoing data values to the output file.
# Formal arguments
#   inFilename -- file which contains PEER strong motion record
#   outFilename -- file to be written in format G3 can read
#   dt -- time step determined from file header
# Assumptions
#   The header in the PEER record is, e.g., formatted as follows:
#    PACIFIC ENGINEERING AND ANALYSIS STRONG-MOTION DATA
#     IMPERIAL VALLEY 10/15/79 2319, EL CENTRO ARRAY 6, 230
#     ACCELERATION TIME HISTORY IN UNITS OF G
#     NPTS = 3930, DT= .00500 SEC

proc ReadSMDFile {inFilename outFilename dt nPt } {
        # read gm input format

  # Pass dt by reference
  upvar $dt DT
  upvar $nPt NPTS
```

```
  # Open the input file and catch the error if it can't be read
  if [catch {open $inFilename r} inFileID] {
    puts stderr "Cannot open $inFilename for reading"
  } else {
    # Open output file for writing
    set outFileID [open $outFilename w]

    # Flag indicating dt is found and that ground motion
    # values should be read -- ASSUMES dt is on last line
    # of header!!!
    set flag 0
          set j 0
          set k 0
    # Look at each line in the file
    foreach line [split [read $inFileID] \n] {
      if {[llength $line] == 0} {
        # Blank line --> do nothing
        continue
      } elseif {$flag == 1} {
        # Echo ground motion values to output file
        puts $outFileID $line
      } else {
              incr j 1
        # Search header lines for dt
        foreach word [split $line] {
          # Read in the time step
          if { $j == 7 } {
                  incr k 1
                  if { $k == 1 } {
                          set NPTS $word
                  }
                  if { $k == 2 } {
                                  set DT $word
                          }
          }
#           if {$flag == 1} {
#             set DT $word
#             break
#           }
          # Find the desired token and set the flag
          if {[string match $word "DT"] == 1} {set flag 1}
        }
      }
    }
    # Close the output file
    close $outFileID
    # Close the input file
    close $inFileID
  }
};
####################END#########################
```

Annex B

Annex B presents the artificial accelerograms of Bucharest site location (a_g = 0.3g, T_B = 0.32s, T_C = 1.6s, T_D = 2.0s) used for nonlinead dynamic analyses.

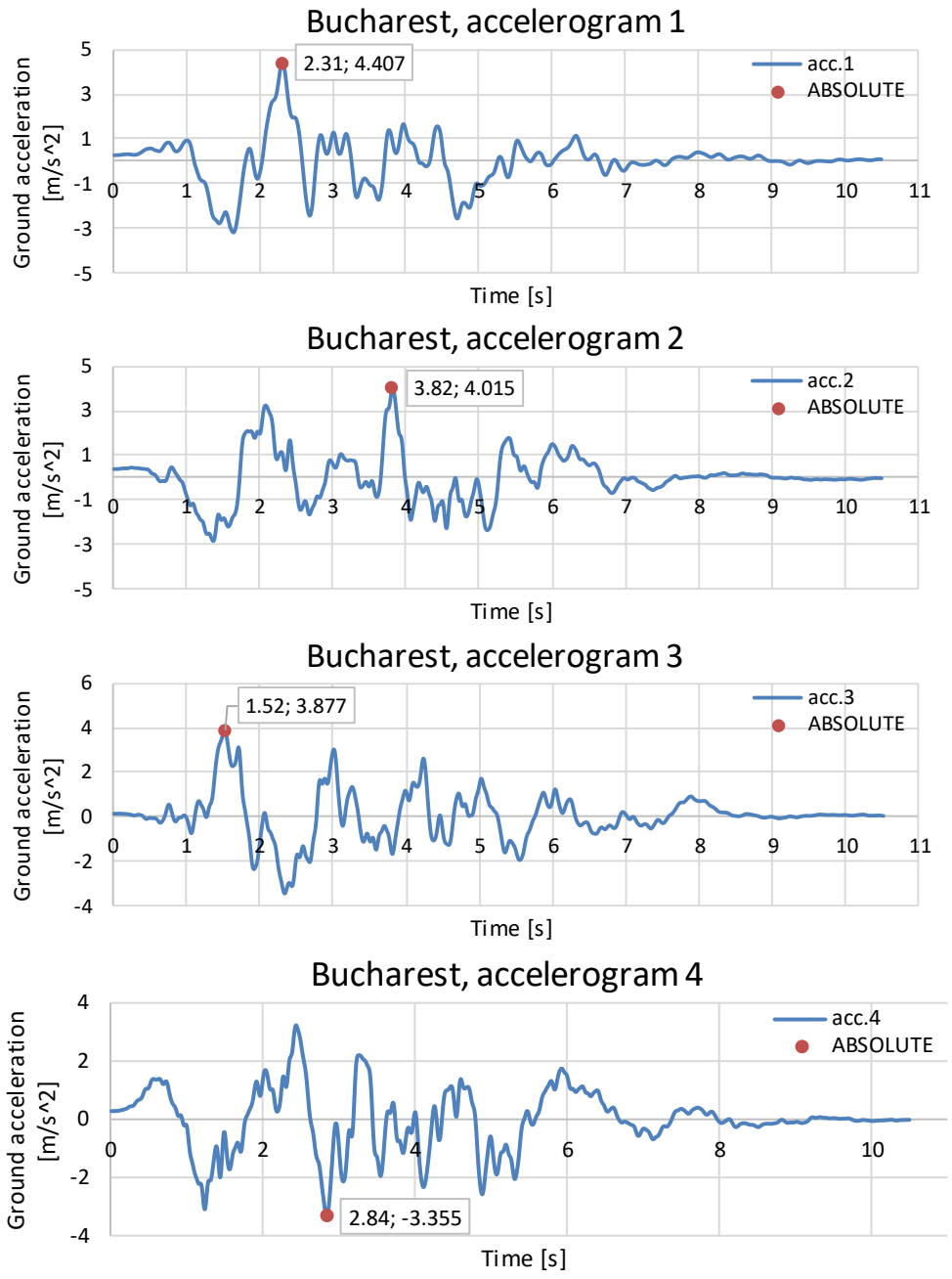

Fig.B. 1 Artificial accelerograms used for nonlinear dynamic analyses

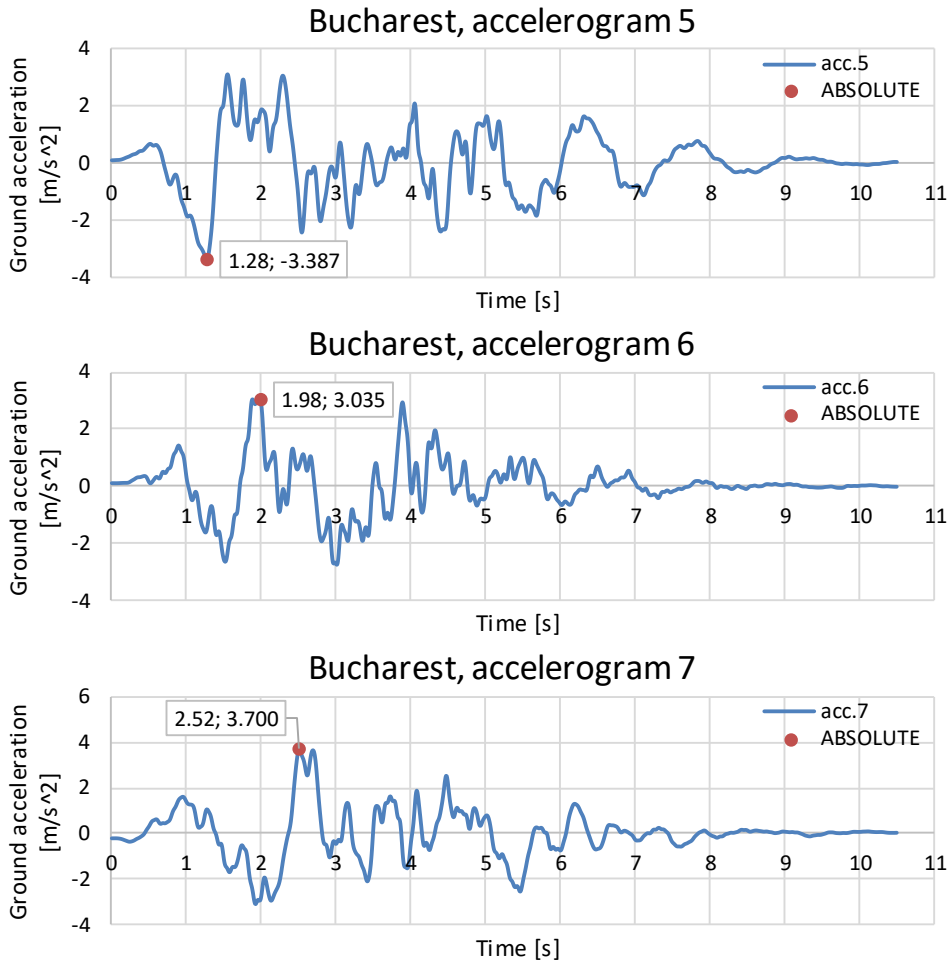

Fig.B. 1 Artificial accelerograms used for nonlinear dynamic analyses (continued)